University of Sheffield

Rough Surface Reconstruction with Machine Learning Methods

Michael-David Johnson

A thesis submitted in partial fulfilment of the requirements for the degree of

Doctor of Philosophy

The University of Sheffield

Faculty of Engineering

Department of mechanical engineering

Submission Date

Autumn 2023

Dedicated to my Nan,
thank you for making me the person I am today.

Acknowledgements

Firstly, I would like to acknowledge my supervisors, Dr. Anton Krynkin and Dr. Artur Gower. Anton, I highly appreciated working with you throughout my years as a PhD student, the countless hours standing over a whiteboard will be missed greatly. Artur, thank you for being a good friend, and for keeping me sane. I would also like to acknowledge all the people that I have collaborated with. Special mention to Jacques Cuenca, Timo Lahivaara, Fabio Muraro, Simon Tait, and Giulio Dolcetti. Thank you all for the great discussions and patience that all of you have had with me, you truly have made my experience throughout my PhD an enjoyable one.

I would like to thank my friends and family who have supported me throughout my PhD, especially due to the extra strain that COVID caused on all of our health. I would especially like to thank Joanna and the entire Watts household. Your care, sympathy, and willingness to listen has been fundamental in giving me the support to be able to complete this research.

Abstract

This article-based thesis consists of a collection of four journal papers (one accepted, one submitted pending reviews, two in the process of submission), and one conference paper (accepted and presented at InterNoise 2022). Each article relates to a chapter written and formatted in manuscript form. The purpose of this work is to investigate the validity of using Machine Learning to deal with recovering parameters non-intrusively. These parameters range from estimating the amplitudes, wavelengths and phases for direct surface reconstruction for static surface recovery, and the average surface velocity, and water depth for dynamic river free-surfaces. This is done both acoustically on a rough surface, and optically on dynamic rough surfaces. Treating the inverse problem with a machine learning approach allows for further analysis of the problem. For example, getting spatial uncertainty for a given reconstruction, or analysing the behaviour of the trained model as opposed to more traditional approaches. Within this thesis, the Kirchhoff Approximation is used as the underlying acoustic scattering model due to the types of surfaces investigated, the accuracy of the model, and the fast computation time. This model is then used to generate the data required for training. Further to this, the frequency-wavenumber spectrum of dynamic free-surface fluctuations of shallow turbulent flow is exploited.

Firstly, a random forest is trained on data generated from the Kirchhoff approximation in order to recover parameters of a harmonic surface at a given acoustic frequency. It is shown that this generalises well to unseen surfaces, and out-competes methods that utilise the small amplitude assumption. Different metrics are presented to show the applicability of the random forest framework over different source incident angles, and source frequencies.

An acoustic source with a broadband nature was exploited to get some estimation of prediction error. For each frequency, data was generated and models were trained. This allowed for the spread of predicted parameters to be estimated.

In order to recover a wider range of rough surfaces, as well as to get statistical information, a stochastic method named Metropolis-Hastings was introduced to the problem. This competed well with the random forest predictions for the single harmonic, while giving spatial uncertainty. This was extended to a more complicated roughness profile consisting of a summation of many harmonics at different wavelengths. It was found that the profile was recovered well in a region of approximately 33% of the full profile. In this region, the credible interval decreased substantially. This fact can be used to infer the region of interest, without needing to know the underlying truth of the surface.

Finally, the recovery of the velocity and the depth of shallow-turbulent flows through the application of Metropolis-Hastings and the frequency-wavenumber spectrum to series of images of the flow surface, obtained in laboratory and in-field experiments, was attempted. First, the surface frequency-wavenumber spectrum recovered from a Digital Image Correlator was analysed. This, and data from a CCTV camera over the River Sheaf, was used in the Metropolis-Hastings algorithm. It was found that the velocity was well recovered, and the resulting distributions of the velocity were useful in the extraction of reliable credible intervals. However, the method struggled to recover the depth.

The work presented in this thesis provide an approach to increase the accuracy of recovery from static surface acoustic recovery, while also including a highly informative representation of uncertainty in the spatial domain. Further, this thesis paves the way in new inversion methods using cameras to get information such as the mean surface velocity and can be used to automatically extract the gravity-capillary waves from the captured video leaving a representation that is ready to be exploited.

Statement of Originality

I, the author, Michael-David Johnson, confirm that the work submitted is my own, except where work that has formed part of a jointly authored publication has been included. The contribution of the candidate and the other authors to this work has been explicitly given below. I confirm that appropriate credit has been given within the thesis where reference has been made to the work of others.

Examples:

Chapter 4: I, the candidate, planned and wrote the manuscript. The co-authors reviewed, provided comments on the manuscript. The section entitled "Experimental testing data" the first two paragraphs were written by Dr. Giulio Dolcetti. Dr. Anton Krynkin edited figures.

Chapter 5: I, the candidate, planned and wrote the manuscript. The co-authors reviewed and provided comments on the manuscript.

Chapter 6: I, the candidate, planned and wrote the manuscript. The co-authors reviewed and provided comments on the manuscript. The section entitled "Data collection" was written by Dr. Giulio Dolcetti.

Chapter 7: I, the candidate, planned and co-wrote the manuscript with Fabio Muraro and Simon Tait. The section entitled "Introduction" was written by Simon Tait, the section entitled "Experiment Setup" was written by Fabio Muraro. The sections entitled "Theory, Feature extraction method, Results, Conclusion" were written by I, the candidate.

Chapter 8: I, the candidate, planned and wrote the manuscript. The co-authors reviewed and provided comments on the manuscript.

I, the candidate, Michael-David Johnson confirm that, aside from the collaboration mentioned, this thesis is my own work and that this work has not been previously presented for an award at this, or any other, university.

Publications

Journal Publications

- Johnson, M. D., Krynkin, A., Dolcetti, G., Alkmim, M., Cuenca, J., and De Ryck, L. (2022). Surface shape reconstruction from phaseless scattered acoustic data using a random forest algorithm. The Journal of the Acoustical Society of America, 152(2), 1045-1057.

Journal Publications in Progress

- Johnson, M. D., Cuenca, J., Lahivaara, T., Krynkin, A., Dolcetti, G., Alkmim, M., and De Ryck, L. Bayesian reconstruction of surface shape from phaseless scattered acoustic data.
- Johnson, M. D., Muraro, F., Tait, S., Dolcetti, G., and Krynkin, A. Recovering the free surface frequency-wavenumber spectra of shallow turbulent open channel flows using Digital Image Correlation (DIC).
- Johnson, M. D., Muraro, F., Tait, S., Dolcetti, G., and Krynkin, A. Using Metropolis-Hastings to estimate parameters of shallow turbulent flow from the free-surface elevation.

Conference Proceedings

- Johnson, M. D., Krynkin, A., Dolcetti, G., Alkmim, M., Cuenca, J., De Ryck, L., and Li, Y. (2023, February). Data-driven reconstruction of rough surfaces from acoustic scattering. In INTER-NOISE and NOISE-CON Congress and Conference Proceedings (Vol. 265, No. 1, pp. 6188-6198). Institute of Noise Control Engineering.

- Johnson, M. D., Lahivaara, T., Cuenca, J., Alkmim, M., de Ryck, L., Dolcetti, G., and Krynkin, A. (2022). Bayesian Recovery of Sinusoidal Rough Surface from Scattered Acoustic Pressure on a Linear Microphone Array. In Proceedings of the 24th International Congress on Acoustics. International Commission for Acoustics (ICA).
- Cuenca, J., Lahivaara, T., Dolcetti, G., Alkmim, M., de Ryck, L., Johnson, M. D., and Krynkin, A. (2022). Deterministic and Statistical Reconstruction of Rough Surfaces from Acoustic Scattering. In Proceedings of the International Congress on Acoustics. International Commission for Acoustics (ICA).

Contents

List of Figures

List of Tables

Chapter 1

Introduction

Rivers provide a freshwater resource that sustains ecosystems, supports biodiversity, and serve as vital sources for agricultural, industrial, and domestic water requirements. The United Kingdom, along with many other countries, faces unprecedented challenges arising from changing climate patterns, population growth, and increased urbanisation. These factors have placed immense pressure on the nation's river systems. Along with providing an essential resource, rivers represent a hazard due to their potential to flood: floods are one of the leading causes of naturally occurring damage to property in the United Kingdom. Floods can occur in winter due to the presence of atmospheric rivers [3] or due to extreme rainfall events [4]. During the winter of 2015/2016, the estimated cost due to property damage and effects on business by Storm Desmond was "likely to be >£1.3 billion" [5]. In November 2019, estimated insurance payouts as a consequence of flooding "would reach £110 million" [6]. The prediction and prevention of floods is an area of active research [7] [8] [9] since, clearly, it is of great importance to mitigate damage as much as possible from these events. The first step in understanding river behaviour is developing an observation network, after which the key properties of the systems can be monitored and models developed to predict future behaviour. These models must be generic enough to cope with the changing behaviour of rivers due to climate change.

A key metric that is used in order to understand the flow of water in rivers and seas is the discharge, which is a measure of how much water flows over a given volume. For rivers, this can be calculated as [10]:

$$Q = \sum_i B_i D_i V_i. \tag{1.1}$$

Thinking of this in the context of the trapezoidal method of numerical integration B_i can be seen as the width of a rectangle such that the sum of all B_i is the width of the river, and D_i is the average depth in this band. V_i is then defined as the depth average velocity.

When using non-contact sensing measurements V_i cannot be found directly. In this case it is inferred from the surface velocity, V_{si}, using the relation:

$$V_i = \alpha V_{si}. \tag{1.2}$$

Discharge has been used to monitor a vast range of conditions, one such example is [11] which investigated the river discharge into the Arctic Ocean. It has also been applied to other oceans around the world, yielding reference texts such as [12]. Discharge rates are affected by climate change [13] so it can be used as a metric for understanding and mitigating the effects of climate change.

Getting a measure of discharge is fairly straightforward, first, the width needs to be measured, then the depth and finally, the depth averaged velocity. Traditionally, the sensors that are used in order to calculate this are installed underwater. There are issues with this approach, because underwater maintenance is needed, and there is a cost to that. Because they are underwater, there is a limit to where they can be located, due to river depth and/or width. This causes a spatial sparsity, and can be dangerous for personnel [14]. In order to measure outside the underwater stations, Acoustic Doppler Current Profiler boats [15] can be moved along the surface of rivers, but there are limitations again in depth ranges and these cannot be deployed in dangerous conditions.

It is clear that a noncontact approach is favourable. Avoiding the need to be in the water allows for cheap, rapid deployment along the majority of the system. Such a density of sensors is essential in order to drive high data based analysis. A very popular method for measuring surface velocity is Particle Image Velocimetry (PIV), of which an excellent reference text is [16]. PIV relies on particles - known as tracers - either artificially introduced or naturally occurring, to move with the surface velocity. These features are then tracked via video and various methods are used to estimate velocity. There are issues with this approach, mainly the complications arising from the need for tracers: artificial tracers allow for good coverage but entail environmental concerns. Naturally occurring tracers are uncontrolled and so cannot guarantee consistent data coverage.

An attractive alternative to PIV is to analyse the structure of the flow directly, this can be done acoustically or optically through the investigation of the frequency-wavenumber spectrum. This type of analysis has been used extensively in analysing ocean waves, with reference texts such as [17]. However, due to the effects of turbulence and the presence of gravity-capillary waves, this has not been applied often up to now for rivers and other shallow watercourses. Recent work [18] has shown that in certain conditions the turbulent structures can be approximated to move proportionally to the mean flow velocity. In these conditions, a frequency-wavenumber spectrum can be used to analyse the flow of the river.

The work in this thesis comprises two main problems, both looking at river dynamics analysis as a rough surface reconstruction problem. First, a simplification is made of the dynamic rough surface where motion is not taken into account. The essence of this problem is finding the elevation of a rough surface comprised of a superposition of multiple harmonics. In this case, the surface is probed using a non-contact airborne acoustic approach, and the elevation estimated from the scattered field. Secondly, dynamic rough surfaces are investigated, in which case it is the velocity and depth which need to be recovered. This problem is probed using an airborne optical approach: the parameters of interest are recovered from analysing CCTV footage, and the reconstruction from a Digital Image Correlator. Both of these represent "inverse problems" since they are trying to find the input parameters given observed data.

Inverse problems are typically difficult to solve. For example, in acoustic scattering, usually one has to invert a Fredholm integral equation of the second kind [19], or further simplifications have to be made in order to generate a linearised system to solve numerically. Machine Learning is an attractive alternative due to its ability to handle complicated inversion, as has been demonstrated with image reconstruction from MRI images [20] [21]. A clear benefit of Machine Learning is that no further approximations need to be made to the numerical models: the approximations are left to the Machine Learning algorithm. In fact, issues that typically are a problem in standard optimization approaches can be leveraged to ascertain uncertainty, through the application of Bayesian approaches such as Markov-Chain Monte Carlo and Gaussian Processes. This measure of uncertainty yields substantially more information to the implementer, allowing for interpretable measures of confidence in the prediction, even when there is no labelled data to test against.

1.1 Aims and Objectives

The main aim for this thesis is to investigate and build a platform for the application of deterministic and stochastic data-driven / machine learning based approaches for rough surface reconstruction with the aim of inferring characteristics of the dynamic free-surface from shallow turbulent flows. This large task has been subdivided into the following objectives:

- To investigate the validity of data-driven machine learning based approaches for the inverse problem of acoustic scattering from a rough surface, and compare against more standard approaches.
- To provide a measure of uncertainty in the reconstruction, allowing for reasonable interpretation for when the model is accurate or not.
- To extend this inversion methodology to reconstruction of a dynamic rough surface i.e. the free-surface of rivers.
- Validate against experimental data.

1.2 Thesis Layout

The thesis is presented in a publication-based format, where each chapter relates to a published work or a publication in the process of submission. Supplementary data can be found in the chapter under the heading 'Supplementary data' or in an appendix when necessary.

Chapter 2 provides a literature review on the topic of inverse problems, with some emphasis to inverse acoustic scattering and the application of machine learning for this problem. Further to this, Markov-Chain Monte Carlo (MCMC) schemes will be investigated as well as free-surface wave theory.

Chapter 3 presents the relevant theory that underpins the majority of the work presented in the thesis. Starting with the Navier-Stokes equations and the Helmholtz equation, the Kirchhoff-Helmholtz integral formula is derived with particular interest in the application of the Green's second identity. The Kirchhoff (or tangent plane) approximation is derived, this model is the main acoustic scattering model used throughout the thesis, therefore there is some empirical analysis on the sensitivity to surface roughness changes the model has. Following this, relevant free-surface water wave phenomena are presented, the gravity-wave dispersion curve is

derived from separation of variables with Laplace's equation and Bernoulli's equation. The dispersion curves underpinning shallow-turbulent motion i.e. as can be found in rivers is presented and a sensitivity analysis to the parameters is shown. Following this, random forests, and the Metropolis-Hastings are presented.

Chapters 4-6 present papers on the inversion of surface roughness with respect to the application of using random forests on single frequency source excitation. This is tested with experimental data in Chapter 4. Chapter 5 investigates how a broadband signal can be leveraged to get some information about model error. Chapter 6 uses an adaptive Metropolis-Hastings scheme to recover more complicated experimental surfaces while giving very clear spatial information about the model's credible region.

The thesis then proceeds onto investigating if parameters from moving rough surfaces, generated from shallow-turbulent flow, can be recovered. Chapter 7 presents the analysis of the frequency-wavenumber spectrum recovered using a Digital Image Correlation (DIC) based approach. This gets a space-time estimate of the free-surface elevation directly from the tracers, and investigates the viability of fitting the advection dispersion curves and the gravity capillary dispersion curves. Chapter 8 aims to link the methodology provided in Chapter 6 to this new problem. Given the DIC measurement, and the measurements of a real river from CCTV footage, can MCMC be used to get an estimate on the posterior of the velocity and the depth?

Chapter 9 presents the conclusions of the thesis, as well as highlighting future work in this area.

Chapter 2

Literature Review

This chapter aims to present the literature relevant to rough surface reconstruction methods using machine learning. It begins generally, then focus onto the specific research question as the literature review develops. It will evaluate previous methods, and discuss the issues and approximations used. By the conclusion, the gap in the literature and the novelty of this work will have been presented. It is important to note that this is not the only literature review present in the text: chapter specific literature reviews are provided in each chapter. That is, in Chapter 4.2 the research surrounding inverse acoustic scattering for a rough surface is discussed with a focus on recovering the phaseless acoustic pressure. Chapter 6.4 presents an introduction of Bayesian methods for the acoustic scattering problem, in order to reframe the problem of this work as a Bayesian one. Finally, in Chapter 8.2 the issues with respect to shallow turbulent flow are presented, as well as the shortcomings of PIV measurements and the transition to frequency-wavenumber spectra.

This literature review begins with the study of acoustics and some general uses, before moving on to discuss in more detail the specific use case that underpins this work. It initially focuses on scattering theory, introducing this in a general sense then introducing the Tangent Plane Approximation (also known as the Kirchhoff Approximation) which is pivotal to this work. It moves on to look at inverse problems in general, followed by inverse problems in acoustic scattering. The general concept of Machine Learning is introduced briefly, before looking at the use of Machine Learning for inverse problems, focusing on acoustic inverse problems. Stochastic Methods and Markov-chain Monte Carlo is introduced and examples in acoustics are presented. Finally, the theory of free-surface water waves are introduced with a focus on dispersion relations, which underpin the latter sections of this work.

2.1 Acoustics

Sound has always been a crucial means of communicating information, not least since it was the first major communication method used by humans. Acoustics, that is the study of sound, is an important topic in many fields, reference texts include [22] [23], [24]. Morse [24] is an essential text in the understanding of the derivation of wave motion, culminating in acoustic motion, radiation, and almost everything of interest to acoustics.

Beyond short distance interpersonal communication, acoustics is used for longer distance transmission, probing of structures and room design, among other things. These each have their own challenges, [25] is a reference book on using acoustics for long distance communication underwater, where radio waves are ineffective and the salinity, density and temperatures encountered must be accounted for. [26] introduces acoustics for building design, [27] discusses techniques using perforations in pipe for acoustic attenuation in pipes.

2.2 Scattering

Characterising the behaviour of scattered sound has been of historical importance, especially during the second world war. In 1945, Foldy published a paper investigating the behaviour of multiple scattered waves from water droplets in air [28]. It's trivial to change the media to think of the same problem as bubbles underwater; Acoustic scattering from submarines is still an active part of research. With developments to submarine acoustic modelling in [29] [30], the analysis of the estimation of the hull scattered field based on the propeller as a noise source can be observed in [31].

It is inevitable that acoustic waves will make contact with objects and surfaces during the course of their path. When this happens, an acoustic wave is created with amplitude proportional to the incident acoustic wave and transmitted through the surface, and another wave is created that reflects from the surface. Fresnel highlighted that if the surface that the sound made contact with is perfectly flat, then the angle of reflection is the same as the angle of incidence [32]. This leads on to Snell's law [33], from which information about the reflected and transmitted waves can be found. However, the case where a surface is perfectly flat occurs very rarely in the real world. Instead, the acoustic wave will scatter in many directions, due to surface irregularities or the geometry of the scattering object. Investigating

how sound scatters in these situations is very useful to many applications. One of the main methods to tackle this issue is through the Kirchhoff-Helmholtz integral formulation.

The Kirchhoff-Helmholtz integral formulation was derived in [34] and translated in [35], it is shown in [24] [36] [37]. This approach utilises a Green's function, which is a fundamental solution to the (homogeneous) Helmholtz equation. Through subtraction and integration over a volume Green's second identity (See Chapter 3.2 for a derivation) can be applied to reduce the volume integral to surface integrals, where the surface integrals are taken over scattering object. This leaves an integral equation of the pressure based on the pressure and a known Green's function. Which is used in many Boundary Element Method approaches, sometimes called the direct method e.g. in [38].

Considering the case when there are multiple scattering objects, other methods can be used, especially where the scattered field from one particle affects the incident field on another. A key method is the T-matrix (or transition matrix) method, a significant contributor to this field is Martin, with excellent reference texts such as [39]. The key paper on the T-matrix method is [40] where the application of Graf's addition theorem and spherical wave functions, as well as the fact that the problem is linear, is exploited. This allows for the coefficients of the scattered field to be represented by some matrix T which contains information about the scattering properties, and the coefficients of the spherical wave representation of the incident field are combined to yield the T-matrix. If the scattering objects are simple, for example spheres, then elements of the T-matrix have an analytical form as in [41]. For more complicated shapes, the elements have to be found numerically, again from a boundary integral equation. The work in this thesis assumes that multiple scattering is not present, therefore T-matrices are not used.

This work considers the case when the scattering object is an infinitely long scattering surface. In this case, further approximations can be made. If the roughness is very small, one method that can be used is the Small Perturbation Method. In this case, the scattered field will be dominated by the flat surface. A detailed derivation is shown in [42] where the authors also show that the pressure becomes a series expansion. It is noted in [42] that it is not guaranteed that the series converges and so only a small amount of terms of the series are taken for the small perturbation method. Because of the further restrictions that the small perturbation method enforces on the scattering surface, the small perturbation method was not used in this work.

Instead, the Tangent Plane Approximation (or the Kirchhoff Approximation, they are used interchangeably) was used.

This method is explained in Chapter 7 of Bass F.G and Fuks I.M [36]. The Kirchhoff Approximation applies to a much larger set of surfaces than the small perturbation method, only requiring the radius of curvature of the scattering surface to be relatively smooth given the acoustic wavelength. The fundamental approximation that this method uses is that at a given point on the surface, the scattered field can be locally approximated as reflection from an infinite plane, this follows the law of reflection discussed earlier and is easy to calculate, thus causing large simplification of the problem (see the derivation in Chapter 3.3). This simplification allows for even the simplest of numerical integration schemes, Trapezium Rule, to be applied. In this work, the Simpson's rule is applied due to the increased accuracy. Nevertheless, the reduction in numerical complexity is significant.

An issue with the Kirchhoff Approximation is the loss of multiple-scattering effects, and the issue of shadow zones. These occur at low grazing angles, although they can be corrected slightly by introducing a shadowing function [43]. In this work the grazing angles are set high enough such that this does not occur.

2.3 Machine Learning

Machine Learning has become increasingly popular for many reasons, even though models such as Recurrent Neural Networks [44] were developed in the 1990s. One of the important reasons for this sudden explosion in interest is due to the substantial increase in computational power. This has allowed many different methods to be applied to very large data sets, providing significant improvements in the fields of object detection and speech recognition [45].

Machine Learning can roughly be categorised into three categories: supervised, unsupervised and reinforcement learning. In supervised learning, the data that the model is attempting to fit on has an associated output set of either labels or real numbers: these are called Classification (labels) and Regression (Real numbers). In contrast, unsupervised learning does not have an associated set of known outputs. Reinforcement learning can be seen as an iterative approach to optimise how agents make decisions, by maximising some reward function. Reinforcement learning is not considered in this thesis.

In this thesis, where parametrisations of rough surfaces and the properties of dynamic rough surfaces (velocity, depth) are considered, the data available is usually

best suited to applying supervised regression. An example of a machine learning supervised regression method is the decision tree, this is a component of the random forests used in Chapters 4 and 5.

A decision tree favours a greedy top-down approach to extracting information about the data [46]. A decision tree will constantly partition the dataset until the outputs at the bottom of the tree are perfectly fitted to the given training data. This can cause a problem in model performance as overfitting can occur, which is a failure to predict on new data due to models being trained too much on the data used for training. Random forests were specifically created to address this problem by applying ensemble methods. Random forests offer significant performance increases in comparison to standard decision trees, while also being efficient at tree generation with the use of parallelisation. Breiman also states in [47] that due to the strong law of large numbers [48], Random Forests do not overfit to data, which removes the main shortcoming of decision trees.

Machine Learning models can be parametric or non-parametric. Parametric models have a fixed number of parameters, whereas non-parametric models have a dynamic amount of parameters. Random Forests and K-Nearest Neighbours are examples of non-parametric models. There have been investigations into parametric against non-parametric model evaluations in different fields, an example of this is where Park H. [49] presented that non-parametric models were significantly more accurate in predicting the performance of various index options.

Due to the rising popularity of machine learning and deep learning, many popular programming frameworks have been produced for both researchers and developers, such as Scikit-learn [50] and TensorFlow [51]. The work in this thesis uses Scikit-learn for Random Forests, and K-Nearest Neighbours and uses author-created code for the Metropolis-Hastings, Adaptive Metropolis, and Linear regression algorithms.

2.4 Acoustics and Machine Learning

Before discussing the specific intersection of acoustic scattering and machine learning that underpins the work in this thesis, the author would like to present some influential literature under the more general heading of “Machine Learning and Acoustics" to show, much like Bianco in [52], that machine learning is becoming more prevalent in the field of acoustics.

Acoustics is a challenging environment to use machine learning in due to the sizes of the datasets required. For time dependent signals each individual sample is large, and cannot easily reduced due to the requirement for the data sampling rate to be twice the greatest frequency of interest (by Nyquist's theorem). For all these challenges it is still being attempted; one of the key review papers on machine learning in the context of acoustics is [52]. In this it becomes clear that a further issue when it comes to applying machine learning to acoustics is the requirement for lots of high quality, representative training data. Bianco presents some use cases where machine learning has proven successful, such as source localisation.

Bianco does not place much emphasis on stochastic methods, such as bayesian neural networks, MCMC, or Gaussian processes which is a shame because stochastic machine learning allows for a measure of confidence in prediction, giving more information than a standard 'black box' approach. The problem of representative data is prevalent in all machine learning based methods, and the need for accurate modelling to make up for the lack of available representative data is clear.

In [53] Elforjani aimed to compare three different machine learning techniques: support vector machines, artificial neural networks, and the Bayesian method of Gaussian process regression, for the problem of analysing the acoustic emission to predicting the remaining useful life of bearings from their acoustic emissions. The main use case presented in this work is to analyse the acoustic emission in real time, to estimate issues beforehand. The authors conclude that the artificial neural network performs the best as the errors are lower, discounting support vector machines and Gaussian processes. The issue with this conclusion is the primary metric of investigating the percentage error does not account for nuances in stochastic approaches such as Gaussian processes. The calculated error for the Gaussian processes was only selected on the mean prediction, with no account for the credible interval in time that the Gaussian process benefits from.

Using machine learning for acoustic emissions was also investigated in [54] where Das used unsupervised machine learning (where the data has no label or associated value) in order to replicate the idea of field measurements. Labelled data was created and then clustered with a Gaussian mixture model, then the separation of the clusters was found from support vector machines. Although this approach used labelled data, it was tested on unlabelled data, this allowed a separation to be found between tensile and shear cracking modes. Due to this separation, a support vector machine was used to classify the two modes. The main shortcoming of this

research was the lack of a measure of uncertainty for values of stress that are very close to the hyperplane separation lines.

A similar approach of comparing different machine learning models is discussed in [55] where Palaniappan investigated support vector machines and k nearest neighbours to classify pulmonary acoustic signals from a database of various lung sounds. Features were extracted from the dataset and the accuracy of the classifiers was very high. The authors show the validation of hyperparameters for both methods, which shows how the prediction dynamics change over parameters. An example of this is the increase of k, the number of neighbours, for k-nearest neighbours where, as k increases, the error decreases. This makes sense for k-nearest neighbours, as the predictions are based on the expectation of the k neighbours. Although the results are promising, there is minimal analysis on the cases that were predicted wrong, aside from a confusion matrix which merely describes the proportion of data that was misclassified. This does not give much information in what specifically caused this error, and therefore there isn't key insight for gaining confidence in prediction on truly unseen data.

Machine learning has been applied for speech processing, an example of this is the review paper by [56] where Jung explored the recent literature of the application of machine learning for speech processing. From a machine learning perspective, the authors did not delve too deeply in the issue of prediction uncertainty, data pruning, or comparison.

A specific paper on the combination of machine learning and speech recognition is found in [57]. Gonzalez tackles the problem of reconstructing the acoustical waveform of predicted speech from motion. Sensors were placed in various places on the lips and tongue. A database was used called the Carnegie Mellon University Arctic set of phonetically-rich sentences where six people spoke for roughly twenty minutes each to create a database of recorded speech with the sensors. Various models were tested such as recurrent neural networks, Gaussian mixture models, and deep neural networks with various loss functions tested. The authors present a metric of error bounds for their results. The authors are aiming to prioritise real-time speech restoration.

The work from Skowronski [58] utilised a Gaussian mixture model, and a hidden markov model to detect and classify various bats based on their vocalisations. The study also reported the errors with error bounds, which can be extracted from these methods, this is ideal as in real-world situations, one doesn't have labelled

data to compare against, and reporting error to the user is essential for widespread adoption of methods.

This approach is something that this thesis uses extensively in Chapters 5,6, and 8. A commonly raised complaint with machine learning methods is that they act as a 'black box' providing no real information about exactly what has been learned from the data. There are exceptions to this: random forests can get a measure of what features were important for the prediction through the aptly-named feature importances map. Those parameters can then be mined for information from the user. Gaussian processes are another key example of methods that provide an uncertainty metric. In the case of Gaussian processes, it is from the posterior covariance matrix.

2.5 Numerical Solution of Inverse Problems, Kirchhoff Integral

Along with the development of acoustic scattering theory, the inverse problem gained more interest. An inverse problem attempts to find the input parameters of a system (or the system if the input parameters are known) given some observed data. A key reference text on the inverse problem, sometimes called the 'indirect method', of acoustic and electromagnetic scattering is [59]. Colton names the forward problem the direct method and the inverse problem the indirect method. The methods in Colton can be split into as sampling methods and factorisation methods. One of the more popular sampling methods is the linear sampling method.

An example where the linear sampling method was used is in [60]. In this paper it was used to identify one open arc and the more complicated problem of two open arcs amounting to a problem of reconstructing multiply connected domains. In the course of solving these problems, they note that there is a limitation on the linear sampling method in that the complete far field data for all possible incident and observation directions is needed for accurate reconstruction. This was found earlier in [61] which formulated the inverse scattering problem for all observation directions.

In [62], an extension to three dimensions was investigated in the context of electromagnetic inverse scattering, they explored recovering a sphere, as well as more complicated domains such as a model of an aircraft. This work was focused on exploring the limitations due to the frequency, showing that typically the resolution increases with the frequency. The linear sampling method has been combined

with machine learning with the application of the linear sampling method and a neural network, found in [63]. First, the linear sampling method was used to give initial information about the shape of the obstacle, the shape was then parameterised and with the far-field data as input and the parameters as output the mean squared error was used as a metric to investigate errors. The cases of noisy far-field information, different wavenumbers, and limited apertures were presented. There was no discussion of model confidence, nor real-world experimental data, so the use case is unclear.

The work in [64] used COMSOL to generate acoustic scattered data from random geometries of a sound hard scatterer (steel object in water). This data was used to train various models, one of the more interesting was a Neural Network to be able to generate new scattered data in order to avoid using COMSOL or solving the Helmholtz equation. This was tested against COMSOL and showed good agreement, which is expected, as COMSOL was used to train the data in the first place. The approach to the inverse problem in [64] was to feed multi-frequency acoustic far-field phaseless data and yielded good results, for a range of observation angles.

The above related to the study of inverse problems from scattering objects, what is more relevant for this work is the scattering from a rough surface. Scattering from rough surfaces in acoustics is similar to that of optics (as seen in Kirchhoff's original paper discussed earlier). In [65], the method of perturbation was used with the covariant form of Maxwell's equations and then used an iterative inverse solver. This shows some promising results, although it is not clear how well it would behave in the presence of noise: the authors use an iterative scheme that updates the profile of the surface for the optimiser, but the behaviour of the change of surface is not tracked in the results which could be throwing information away. The iterative Markov-Chain Monte Carlo approach in this work in Chapter 6 uses the history of the surfaces to get a spatial metric of uncertainty, under noise. This allows for more analysis.

In [66], Krynkin proposed an airborne approach to recovering information about a shallow turbulent water system, it was shown that using the inversion method using stationary phase allowed Krynkin *et al.* to successfully recover the mean roughness height of the surface tested within a $\pm 5\%$ error. Krynkin further develops this idea in [67] where instead of attempting to invert the statistical parameters, they attempt to return the immediate surface height of the surface using a matrix / factorisation based approach with singular value decomposition in the inversion. It was shown that the inversion could successfully recover 2D surface roughness with

a maximum reduced mean square error of 20% when using the Kirchhoff Approximation. Krynkin, however, noted a need for improvement in larger scales of spatial wavelength. Noting that there needs to be improvement in the centimetre and sub-centimetre range, Krynkin highlighted in [68] that there is a relationship between the surface roughness of an open channel flow and hydraulic characteristics such as Reynolds number and mean flow depth. This is useful as in [69], Nichols presents a bidirectional relationship between the pattern of the surface pattern and the bulk flow.

Instead of using the Kirchhoff Approximation, [70] extends the scattering to be for unbounded rough surfaces. This is achieved by changing the forward model to be scattered near-field Cauchy data measured along a line above the surface. Also, different boundary conditions were investigated. Finally, they leave an iterative numerical model that utilises a mesh of the rough surface used in the calculation of the forward problem. They then apply an imaging function to this data. It is presented in [70] that the whole rough surface with 20% noise was accurately recovered for a large enough wavenumber using this method.

These have been a few examples of inversion methods, focused on those of relevance to this thesis, there are many others such as the distorted-wave Born approximation which is successful in various imaging applications [71].

Most of the results above, especially when considering inverse scattering, require the full complex field to be given. It is important to note that one can not always recover phase information. Klibanov points out in [72] that losing the phase information is common in the study of optics, stating that it is often impossible to recover, as opposed to the intensity. This is a major problem for methods that require full far-field information. Klibinov explores the Helmholtz equation in three-dimensions with the phaseless inverse scattering problem in [73], looking into incident plane wave scattering specifically for nanostructures, where the phase is not affected by the geometry of the scatterer. A limitation of this paper is that there is no numerical implementation of the proposed approach, as it is purely analytical.

The choice to use phaseless data in this thesis was driven by the limitation of the random forest approach, and to avoid issues with phase calibration, as well as to investigate how phaseless data can be used in the reconstruction. In Dolcetti et al.[74] phase uncertainty was found to have a stronger impact than amplitude uncertainty on the accuracy of the surface reconstruction, and imperfect wrapping of the phase was found to cause a multi-modal distribution of the reconstruction error,

especially at large roughness amplitudes (relative to the acoustic wavelength). This motivates further analysis in models that infer on amplitude only.

In [75], Xu uses a convolutional neural network in order to find unknown scatterers from phaseless data using electromagnetical waves. The convolutional neural network was trained to find cylinders , this work had an amusing approach in creating unseen data through an interesting use of the MNIST handwriting database [76]. When this work was tested on experimental data, they noticed an issue with higher nonlinearity when using a 8 GHz source vs a 6 GHz source, causing a larger spike in error for the recovery from experimental data. The authors looked at different methods of data processing before going into the model, and find that results were better when the model did not have to learn the underlying wave physics that would occur if the phaseless data alone was input to the model.

Another recent approach involves recovering a rough surface at grazing angles using single-frequency, phaseless acoustic pressure through the use of an iterative marching method approach derived from the parabolic wave approximation (forward-scattered wave propagation assumption) [77]. Although the inversion results were found to be relatively accurate, it is assumed that the forward-scattered approach is not applicable in the context of this thesis due to significant differences. For example, in the underlying theoretical assumptions, experimental setup and in the specific acoustic remote sensing application where the sound field is best described by a solution of the full Helmholtz equation [74]. This means that the parabolic wave equation is not sufficient to fully describe the dynamics.

2.6 Data Driven Inverse Problems, Machine Learning

A key benefit of machine learning approaches is their capability for instantaneous prediction, as opposed to classical iterative based methods. This was a benefit highlighted in the work by Qian [78] where a metamaterial was being produced in order to make a material invisible to microwaves. This was tested on the fly with various incident waves, and because the neural network was trained beforehand, allowing for predictions to be made much faster than typical iterative approaches. The authors highlight a potential issue in the time taken to make high quality data in order to train the model.

There is evidence in the literature that machine learning has successfully been used for inverse wave problems. For example, in [79] Antona applied Neural Networks to classify different species of fish to a similar level of accuracy in comparison

to the data based approach using significantly fewer samples. Another example is in [80] where Goldade investigated the application of various Machine Learning methods to generate sea-floor maps in real-time using sidescan sonar. It was discovered that Neural Networks can be used to classify every pixel with great accuracy. Another example is where Mendieta [81] investigated the use of classification and clustering models to recover a 3D recovery of the lumbar spine from an MRI. It was shown that although clustering methods worked fairly well, there were some limitations, such as the model resolving the 3D image 10 times larger than the actual image.

In [82] Adler proposes an approach to solving ill-posed inverse problems when the forward operator is not linear by introducing a gradient iterative scheme, where the gradient is learned by the use of a convolutional neural network. This method is then tested on tomographic inversion problems, such as identifying heads as well as random ellipses using simulated data. This paper highlights a difference between classical regularisation and machine learning: Machine learning forms a functional mapping from the output space to the input space whereas in classical regularisation everything is focused on minimising an objective function. The algorithm provided in this paper had a significant improvement over methods such as Total Variation Regularisation with improvements in accuracy as well as run-time. The method proposed in this paper is said to be able to work for any non-linear forward operator, as well as highlighting the key importance of having quality training data.

Other novel approaches have been introduced in order to not only attempt to solve the inverse problem, but solve it while maintaining a fast runtime. The paper by Wang [83] is an example of this. This paper provides a multi-resolution deep neural network which is then tested on different inverse problems. For example, recovering phases of a propagating wave from direct intensity measurements. The model that Wang provides shows highly accurate results for few epochs of model generation.

The application of using machine learning as the basis of a data-driven approach to solving these inverse problems span across many fields, notably in geophysics and medical imaging. In [84] Kim considered recovering reflectivity from seismic traces by using artificial neural networks and compared this against least-squares. The paper used noisy seismic traces as input data and reflectivity as the output data for the artificial neural network. The paper poses that the use of artificial neural networks generates a nonlinear mapping which is equivalent to the pseudo-inverse of the forward operator. Which is reasonable as artificial neural networks

are universal approximators [85]. The paper by Kim highlights that the neural networks contain better resolution to that of the least-squares method in recovering this reflectivity term, while also correctly resolving thin beds. Kim posed that quality training data is the key for success.

Success has been found in applying this approach to identifying structural damage [86] as well as predicting brain activity from functional MRI image data [87].

Fan *et al.* [88] successfully applied deep learning methodologies utilising the Helmholtz equation in the recovery of the shape and placement of multiple scatterers in two different settings, including a seismic imaging setting where the source and receivers were above the scatterers and receivers were in a linear array. The scatterers were placed randomly and formed from a number of shapes such as triangles, squares or ellipses. It was shown that for many receivers and sources, the locations and orientations of the scatterers were successfully recovered with various amounts of noise in the dataset, while the recovered boundaries of the scatterers became blurred as the noise level increased.

Other works that recovered the parameters of surfaces instead of the full surface include: recovering parameters of a sum of sine waves forming a rough surface [89], recovering coefficients of a parametric curve of an obstacle [90], and using a convolutional neural network to recover the root-mean-squared height and correlation length from a Gaussian rough surface through synthetic aperture radar [91]. The flexibility of data-driven approaches as compared to classical model inversion, in the presence of noise, stands as a central motivation of the thesis.

Applying machine learning methods to wave scattering problems can allow for more flexibility, opening up the choice for interaction between one or more models. For example, it has been shown that a combination of random forest and neural networks results in a robust method enabling reconstruction of geometrical features against noise [92]. This was achieved by first classifying training shapes with a random forest and then inverting the far-field scattered signal using neural networks to obtain geometrical features of different scattering objects.

2.7 Stochastic Methods and Markov-Chain Monte Carlo

A key issue when considering models that give a response, especially in the Machine Learning domain, is that the error metrics are usually given for some testing set, a set that is withheld from training in order to evaluate some metric of model generalisability. Such methods include the coefficient of determination defined in [93],

or the mean absolute error. This then gives some measure on how the model would behave on that set of data. However, this gives no further information on error for every new unlabelled sample when the model is being used for new predictions. This can be an issue as there is not a way to diagnose a given new sample; the predicted value of the sample must be taken as the true value with no appreciation of the underlying uncertainty in the sample.

Outside of machine learning, and the work in this thesis, this problem is being considered, forming a new branch of numerical analysis called probabilistic numerics (with reference text such as [94]). These have application in probabilistic ODE solutions (an example being [95]) and PDE solutions (an example being [95]).

Getting a measure of confidence (or credibility) for a given prediction is clearly more favourable than a prediction alone. One of the more popular methods for doing this in the machine learning domain is a Gaussian Process. A reference text on Gaussian Processes can be found in [96].

Fundamentally, a Gaussian Process is defined as a stochastic process such that any finite subcollection of random variables has a multivariate Gaussian distribution. A Gaussian Process is typically characterised by a mean function and a covariance function defined by a kernel. This leaves an analytic representation of the predictive equations (the predictive mean and the variance) and is found by matrix multiplication and inversion of given data with known inputs. There are limitations to the basic approach such as the requirement for inputs to be noise-free, there are approaches to handle this such as in [97] but they struggles with large amount of data. These limitations are why Gaussian processes were avoided in this work.

The approach used in this thesis is the iterative Markov Chain Monte Carlo (MCMC) method. An essential reference text can be found in [98], where Andieu introduced MCMC methods, providing key theoretical understanding and algorithms for many methods, including Metropolis-Hastings and Sequential Monte Carlo. More detail on the theory of Metropolis-Hastings can be found in the theory chapter of this thesis.

MCMC is a family of Bayesian methods. Bayesian methods have recently gained popularity in the field of acoustics, with applications such as recovering parameters from the seafloor using acoustic back-scattering [99], estimation of rough surface elevation using a Bayesian compressive sensing [100], and for acoustic holography [101] [102]. Li *et al.* [103] applied a Metropolis-Hastings MCMC scheme in order to reconstruct the locations and intensities of acoustic sources from both near-field and far-field information. Fouda in [100] used Bayesian compressive sensing with

the small perturbation approximation to acoustic scattering. However the error bars presented appear to be roughly constant in range, even in regions of bad agreement to the true surface. The receivers were spaced over distance (12m) considerably longer than the wave height of the surface, which makes the surface appear flatter and less illustrative for surfaces that behave like dynamic waves on the free-surface of water.

Application of a Bayesian approach for acoustic scattering with phaseless data was proposed by Yang *et al.* [104, 105]. In Yang *et al.* [104], the location and shape of a sound-soft scatterer were reconstructed, and the approach was tested on shapes such as kites, disks, and line cracks, all with positive results. The only note that should be made is that the number of parameters being recovered from the MCMC algorithm was less than 6, which limits the scope of this method. In Yang *et al.* [105], the method was extended to use a Gibbs sampling method in order to recover more parameters, with phaseless data and with point source excitation. Palafox *et al.* [106] also used a Bayesian formulation in order to perform shape reconstruction of a scattering object, through a reduction of the problem by a Fourier-based representation using a t-walk [107]. The effective dimension method was presented where, given a parametric representation of the solution of the inverse problem, the normalising constant can be approximated.

Bayesian methods have also been applied in inverse problems in other fields, such as for seismic waveform inversion [108], and automatic motion analysis in tagged magnetic resonance imaging scans [109][110].

Application of the adaptive Metropolis-Hastings scheme in relation to acoustical inverse problems can be seen in Niskanen *et al.* [111], where the Johnson–Champoux–Allard–Lafarge model was used in conjunction with a Metropolis-Hastings method in order to recover the model parameters of a homogeneous rigid frame porous media. The joint probability densities verified that the least-squares solution was close to the maximum a posteriori estimation from the MCMC method.

The choice of method used in this thesis was the Adaptive Metropolis method explained in [112] [113]. This extends the classical Metropolis-Hastings algorithm to allow for an adaptive step size. This method was chosen over the methods such as Hamiltonian Monte Carlo [114] due to the dimensionality of the problem not affecting the convergence, it may be important as the number of terms in the roughness recovery increase to switch to Hamiltonian Monte Carlo. The work in this thesis did not increase the terms to justify the switch to Hamiltonian Monte Carlo. Open source implementations of MCMC can be found in Python with PYMC3 [115] or the

language Stan [116]. Both of these libraries are powerful, but due to the desire of the author to have the flexibility to generate custom priors based on the Kirchhoff approximation, the algorithms were coded from scratch in Python and can be found at:

- https://github.com/michaeldavidjohnson/Kirchhoff-Approximation,
- https://github.com/michaeldavidjohnson/MetropolisHastings,
- https://github.com/michaeldavidjohnson/surfaceGen.

2.8 Free Surface Wave Theory and Dispersion Relations for Water Waves

The understanding of wave phenomena has been of great importance classically. Understanding the elevation of the free-surface of a body of water, and the underlying velocity field under the surface has applications in offshore wave loading, and tsunami prediction. In the linear case when the wave height of the free surface is much smaller than the depth, linear wave theory (Or Airy wave theory [117]) can be used. This theory allows for the application of separation of variables (See the derivation in Chapter 3.4) to be applied, and due to the nature of the solutions many terms can be found analytically such as the pressure, energy flux, particle displacement, and radiation stress [118]. The solutions only apply when a relationship between angular frequency (ω) and wavenumber (k) is enforced such that the dispersion relation is defined. Waves are typically classified as deep, intermediate, and shallow based on the relationship between the depth of the water d, and the wavelength of the waves λ according to the following classifications [118]: deep if $\frac{d}{\lambda} > 0.5$, shallow if $\frac{d}{\lambda} < \frac{1}{20}$ and intermediate else. A benefit of linear wave theory is that a linear composition of two solutions is itself a solution, allowing for easy modelling of complicated wave structures comprised of more than one frequency.

This dispersion relationship allows for the construction of solutions to the linear wave equation based on measurements of the frequency or the wavenumber, as long as a relationship between the frequency or wavenumber and surface elevation amplitude is known. This is seen often in the ocean domain, applied to finding power spectra over a frequency range. Examples of this are the JONSWAP spectrum [119], the Pierson–Moskowitz spectrum [120], and the Bretschneider spectrum [121]. Combined with a choice of spectrum, random ocean waves can easily be generated from the dispersion relation.

In this simple case, having knowledge of the underlying dispersion relation, and some way of relating the frequency or wavenumber to wave amplitude, allows a free surface to be recovered. This can be taken advantage of in the more complicated domain of shallow flow. In the case of shallow water flow, the power spectral density $S(f)$ can be related to frequency with the following equation [122]:

$$\log(S(f)) = \frac{1}{-0.0650 + 0.00518\sqrt{f}}, \tag{2.1}$$

which was found from optimising a line through empirical data from experimental data in a flume. They also found a spatial correlation, but this has been found to underestimate surface spectrum slopes when compared to measurements in real rivers [123]. The power spectra dependence as the wavenumber k increases has been found to be proportional to $k^{-\alpha}$ and has been used in [124] [125] [126]. Therefore, with this relation, waves can be numerically created.

Analysing the behaviour of the free-surface of open channel shallow turbulent flows (typical of shallow rivers) is very complex. A review paper by Muraro [127] summarises many of the phenomena that causes the domain to be complex. For example, the behaviour of the flow is sensitive to the shape of the bed, as well as the roughness of the bed. Turbulence-generated structures can be seen on the free surface. For example, bursts can appear by a disruption in the viscous sublayer from the bed roughness profile [128] among other effects such as scars and boils. The nonlinearity caused by introducing turbulence over rough beds cannot generally be solved analytically. Numerical schemes such as Reynolds Averaged Navier Stokes [129], and Large Eddy Simulation [130] have been employed. This can be seen with comparison papers in the domain of shallow turbulent flow such as [131]. The understanding of free-surface behaviour from experiments typically avoids numerical simulation and instead attempts to target a specific variable of interest.

There are issues when extending this understanding to field measurements of rivers, especially where they are shallow and turbulent. If intrusive measurement systems are in place, the local depth and the velocity could reduce the reliability of observations. A key non-intrusive evaluation method is Particle Image Velocimetry (PIV). PIV methods rely on “tracers" that are present through the video recording of the region. These tracers may be naturally occurring or may be introduced into the flow, the restriction on this is that the chosen tracers need to follow appropriately the movement of the flow. Many review papers have been released since its inception in 1984 [132] such as [133] [134] and most relevantly [135]. PIV has proven to be a powerful method for obtaining velocity field measurements over a

large region. This has been applied to measuring the velocities at the free surface of rivers. For example, [136] collates several different examples where this has been used for rivers.

A defining feature of PIV is the reliance on tracers in the flow that are either naturally present in the flow, or are artificially introduced into the flow, the motion of which is used to find the velocity field in space and time. This poses a significant issue when it comes to scaling up the process to more sites. Either, an investigator must rely only on natural tracers which could be inconsistent, or find a way to allow for a constant stream of environmentally friendly tracers to be introduced on a large scale.

Another approach is to investigate the motion of the flow directly. A method for this is optical flow, with examples in [137], [138], [139], [140]. Alternatively, Fourier analysis and the investigation of the frequency-wavenumber spectra can be used [18] [2]. This work will focus on the latter.

Using spectral analysis for ocean waves has been studied extensively, and has been explained clearly in [17], it has been extended to the study of shallow turbulent flows using wave probes in [18] and [127]. An airborne approach to estimate the velocity with the frequency-wavenumber spectra was shown in [141] although only the gravity-capillary dispersion curve was fit.

The key point of these papers was to investigate how the free-surface's dispersion relation changed with rough beds, which are a significant factor in the behaviour of shallow flows where boundary conditions have more of an effect [2]. The culmination of this was a non-invasive approach in [2] where an approximation of the dispersion relation due to advection was linked with the dispersion relation due to gravity capillary waves, allowing for three relations to be fit. Good agreement was found experimentally with these relations, then an optimizer was fit to be able to estimate the discharge and the depth.

There are some issues with this approach. The river Calder is much worse in the prediction of the method, due to the increase of noise in the frequency-wavenumber plots. The analysis of the spread of predictions was obtained by looking at the worst predicted samples from the optimiser. This is not an optimal method for obtaining the underlying noise in the data. This could be improved by using a stochastic model for the prediction, where the results can form a distribution that can be analysed with statistical methods. This can then probe the underlying noise in the signal, as well as how credible the results are. The behaviour of the optimizer-based

approach may not have been due to noise, and could merely have been stuck on a local minima.

Another issue that arises when considering an optimiser on Fourier transformed data is that only a single value for velocity and depth can be recovered. These values represent the spatial and temporal average of the system. However, as it is not true that the velocity and the depth are constant in space and time, the work in this thesis aims to extend the prediction by using a Bayesian framework through the application of MCMC, which has shown promise in gathering information from dispersion relations in the seismic domain [142]. The MCMC generates a posterior distribution of the depth and the velocity, which should capture the noise in the data from measurement noise and also the spread of velocities in the timeline of measurement.

Chapter 3

Theory

This chapter aims to introduce the relevant theory required for the work in the later chapters. When possible, derivations and definitions have been provided. This chapter begins with the Navier-Stokes equations from which the relation between pressure and velocity is obtained. Then the Helmholtz equation is introduced from the wave equation. Basics surrounding the application of Green's fundamental solutions for the non-homogeneous Helmholtz equation are presented. Then, the Kirchhoff-Helmholtz integral formulation is derived, followed by the derivation of the tangent plane approximation. A quick analysis on how the acoustic pressure changes due to various surface profiles are presented. Next, dispersion curves at the free-surface of an infinitely long wave tank is derived from separation of variables to get the water waves dispersion relation. Other dispersion relations are introduced, as well as the theory behind the construction of surfaces which contain this dispersion relation. Key models in Machine Learning and Markov-Chain Monte Carlo are also introduced.

3.1 Wave Equation, Helmholtz Equation, Green's functions and Delta functions

Starting with the Navier-Stokes equations for an inviscid fluid [143]

$$\frac{\partial \rho}{\partial t} + \nabla \cdot (\rho \mathbf{v}) = 0, \tag{3.1}$$

$$\rho \frac{\partial \mathbf{v}}{\partial t} + \nabla p + \rho \mathbf{v} \nabla \mathbf{v} = 0. \tag{3.2}$$

$$\nabla = \left(\frac{\partial}{\partial x}, \frac{\partial}{\partial y}, \frac{\partial}{\partial z} \right) \tag{3.3}$$

Where ρ is the density, p is the pressure, t is time, $\mathbf{v}$ is the vector representation of velocity. Assuming that the fluctuations in the fluid $\rho'(t), p'(t)$ are small compared to the background $\rho_0, \quad p_0$ then the linearised Euler equations can be found [143]

$$\frac{\partial \rho'}{\partial t} + \rho_0 \nabla \cdot \mathbf{v} = 0 \tag{3.4}$$

$$\rho_0 \frac{\partial \mathbf{v}}{\partial t} + \nabla p' = 0 \tag{3.5}$$

Taking the derivative in time of Equation (3.4) and taking the derivative with respect to space of Equation (3.5) and subtracting the two yields [143]

$$\frac{\partial^2 \rho'}{\partial t^2} - \nabla^2 p' = 0 \tag{3.6}$$

Assuming that there exists a functional relationship $p = p(\rho)$ and taking a Taylor expansion around ρ_0 [143]

$$p(\rho) = p(\rho_0) + (\rho - \rho_0) \frac{\partial p}{\partial \rho}\Big|_{\rho=\rho_0} + \ldots \tag{3.7}$$

$$p' = p - p_0 \approx (\rho - \rho_0) \frac{\partial p}{\partial \rho}\Big|_{\rho=\rho_0} = c^2 \rho' \tag{3.8}$$

$$\rho' = \frac{1}{c^2} p' \tag{3.9}$$

$$c^2 = \frac{\partial p}{\partial \rho}\Big|_{\rho=\rho_0} \tag{3.10}$$

The constant c is known as the speed of sound, and is related to the rate of change of pressure due to density. The above equation can be recognised as the wave equation. Considering only the pressure fluctuation and setting that value to p instead of p' one arrives at the homogeneous (source-free) wave equation is

$$\frac{1}{c^2} \frac{\partial^2 p}{\partial t^2} - \Delta p = 0, \quad \Delta = \nabla^2. \tag{3.11}$$

The inhomogeneous wave equation is

$$\frac{1}{c^2} \frac{\partial^2 p}{\partial t^2} - \Delta p = g(x, t), \tag{3.12}$$

where $g(x, t)$ describes the inhomogeneity.

The relationship between pressure and velocity can be found from Equation (3.5) and is used in Appendix A:

$$\mathbf{v}' = -\frac{1}{\rho_0}\int \nabla p' dt \tag{3.13}$$

Often it is useful to deal with the velocity potential rather than the velocity, the velocity potential is defined as [24]

$$\mathbf{v} = \nabla\psi. \tag{3.14}$$

This means that the pressure can be more succinctly described in terms of the velocity potential

$$p = -\rho_0 \frac{\partial\psi}{\partial t}. \tag{3.15}$$

The velocity potential is also a solution to the wave equation

$$\frac{1}{c^2}\frac{\partial^2\psi}{\partial t^2} - \Delta\psi = 0. \tag{3.16}$$

It is common to consider waves in the frequency, rather than time, domain. Recalling that the Fourier transform is defined as

$$\phi(\mathbf{x},\omega) = \int_{-\infty}^{\infty} \psi(\mathbf{x},t)\mathrm{e}^{\mathrm{i}\omega t} d\omega. \tag{3.17}$$

Where ω is the angular frequency $\omega = 2\pi f$. As a note, this can also be described as moving from the real domain to the reciprocal domain or moving from the real space to the frequency space. This is described in [144] although not directly.

Using the Fourier transform to move Equation (3.11) from the time domain to the frequency domain

$$\int_{-\infty}^{\infty} (\frac{1}{c^2}\frac{\partial^2\psi}{\partial t^2} - \Delta\psi)\mathrm{e}^{\mathrm{i}\omega t} d\omega = 0 \tag{3.18}$$

$$\Rightarrow \int_{-\infty}^{\infty} \frac{1}{c^2}\frac{\partial^2\psi}{\partial t^2}\mathrm{e}^{\mathrm{i}\omega t} d\omega - \int_{-\infty}^{\infty} \Delta\psi \mathrm{e}^{\mathrm{i}\omega t} d\omega = 0 \tag{3.19}$$

$$\Rightarrow -\frac{\omega^2}{c^2}\psi - \Delta\psi = 0 \tag{3.20}$$

$$\Rightarrow \Delta\psi + k^2\psi = 0, \quad k = \frac{\omega}{c} \tag{3.21}$$

This alternative form of the wave equation in the frequency domain is known as the Helmholtz equation.

Consider the inhomogeneous Helmholtz equation in 3D Cartesian co-ordinates

$$(\Delta + k^2)\psi(x,y,z) = -f(x,y,z), \quad k = \frac{\omega}{c}, \tag{3.22}$$

where $f(x,y,z)$ is the source term, k is the acoustic wave number, and ψ is the value of the acoustic field at any point in space.

Homogeneous partial differential equations are relatively easy to solve subject to boundary conditions, but inhomogeneous partial differential are significantly more complex. However, a key tool for doing so is the theory of Green's functions. A Green's function solution is a solution to

$$(\Delta + k^2)G(x-a, y-b, z-c) = -\delta(x-a)\delta(y-b)\delta(z-c). \tag{3.23}$$

$$\Rightarrow (\Delta + k^2)G(\mathbf{R}, \mathbf{R}') = -\delta(\mathbf{R} - \mathbf{R}'). \tag{3.24}$$

$$\mathbf{R} = (x,y,z) \tag{3.25}$$

$$\mathbf{R}' = (a,b,c) \tag{3.26}$$

The right-hand side of Equation (3.23) is a combination of delta functions. Delta functions are defined as

$$\int_{-\infty}^{\infty} \delta(x-a)dx = 1. \tag{3.27}$$

The delta function is not a typical function, and can be thought of as

$$\delta(x-a) = \begin{cases} 0 & x \neq a \\ \infty & x = a \end{cases}. \tag{3.28}$$

There is another highly useful property in the introduction of delta functions called the sifting property (Appendix C in [145]):

$$f(a) = \int_{-\infty}^{\infty} f(x)\delta(x-a)dx \tag{3.29}$$

Green's function solutions come up frequently in the study of inhomogenous partial differential equations. The main type of Green's function considered in this work are known as the free field Green's function. These typically represent sources

of sound in the absence of any reflecting boundaries. The free field is sometimes referred to as the fundamental solution. in 2 and 3 dimensions these can be defined as [24]

$$G_{free}(\mathbf{R},\mathbf{R}') = \begin{cases} -\frac{e^{ik|\mathbf{R}-\mathbf{R}'|}}{4\pi|\mathbf{R}-\mathbf{R}'|} & 3D \\ -\frac{i}{4}H_0^{(1)}(k|\mathbf{R}-\mathbf{R}'|) & 2D \end{cases}, \tag{3.30}$$

Where $H_0^{(1)}$ is the order 0 Hankel function of the first kind [146]. In general, a Green's function solution can be expressed as [24]

$$G(\mathbf{R},\mathbf{R}') = G_{free}(\mathbf{R},\mathbf{R}') + G(\mathbf{R}), \tag{3.31}$$

Where $G(\mathbf{R})$ is a general solution to the homogeneous Helmholtz equation. As $G_{free}(\mathbf{R},\mathbf{R}')$ has been defined in Equation (3.30) to be an outgoing wave in an unbounded medium, $G(\mathbf{R})$ can be set to be non-zero in situations where boundary conditions need to be applied [24].

Green's functions as well as delta functions adhere to reciprocity:

$$G(\mathbf{R},\mathbf{R}') = G(\mathbf{R}',\mathbf{R}) \quad \delta(x-a) = \delta(a-x) \tag{3.32}$$

This allows for the source location and the point of observation to be swapped, yielding the same result.

3.2 Kirchhoff - Helmholtz integral formulation

This section contains a derivation for the Kirchhoff-Helmholtz integral equation in 3 dimensions, assuming a point source. After the derivation, the 2D case and a directed case will be presented with citation.

In preparation for this derivation, the following results are provided:

Theorem 1 (Green's second identity) *If ψ and ν are both twice continuously differentiable on $U \subset \mathbb{R}^3$. Then*

$$\int_U \psi\Delta\nu - \nu\Delta\psi dV = \oint_{\partial U} (\psi\nabla\nu - \nu\nabla\psi)\cdot\mathbf{n}dS \tag{3.33}$$

Where $\mathbf{n}$ *is a unit normal vector and*

$$\Delta = \nabla^2 \tag{3.34}$$

Theorem 2 (Sommerfeld radiation condition [147] [19]) *If a solution u to the inhomogeneous Helmholtz equation is due to a source that has no sources at infinity, then the radiation has to satisfy the Sommerfeld radiation conditions.*

In 3D

$$r \to \infty, \quad u = \mathcal{O}(\frac{1}{r}), \quad \frac{\partial u}{\partial r} - \mathrm{i}ku = \wr(\frac{1}{r}) \tag{3.35}$$

In 2D

$$r \to \infty, \quad u = \mathcal{O}(\frac{1}{\sqrt{r}}), \quad \frac{\partial u}{\partial r} - \mathrm{i}ku = \wr(\frac{1}{\sqrt{r}}) \tag{3.36}$$

Consider a source contained inside a bounded region Γ, and consider evaluating the acoustic field at another point inside the bounded region. Suppose there a source lies at $\mathbf{R_0}$, and the point of observation is $\mathbf{R}$. Recalling the definition of the Helmholtz equation and an associated free field, Green's function solution.

$$(\Delta + k^2)\psi(\mathbf{R}') = -f(\mathbf{R}'), \quad k = \frac{\omega}{c}, \tag{3.37}$$

$$(\Delta + k^2)G(\mathbf{R}, \mathbf{R}') = -\delta(\mathbf{R} - \mathbf{R}') \tag{3.38}$$

It can be shown, ψ is also a solution to the homogeneous Helmholtz equation everywhere except at $\mathbf{R}' = \mathbf{R_0}$. Also, $G(\mathbf{R}, \mathbf{R}')$ is a solution to the homogenenous Helmholtz equation everywhere except at $R' = \mathbf{R}$. Multiplying Equation (3.37) by $G(\mathbf{R}, \mathbf{R}')$ and Equation (3.38) by $\psi(\mathbf{R})$ and subtracting (3.38) from (3.37)

$$G(\mathbf{R}, \mathbf{R}')(\Delta + k^2)\psi(\mathbf{R}') - \psi(\mathbf{R}')(\Delta + k^2)G(\mathbf{R}, \mathbf{R}') = -f(\mathbf{R}')G(\mathbf{R}, \mathbf{R}') + \delta(\mathbf{R} - \mathbf{R}')\psi(\mathbf{R}') \tag{3.39}$$

$$G(\mathbf{R}, \mathbf{R}')\Delta\psi(\mathbf{R}') - \psi(\mathbf{R}')\Delta G(\mathbf{R}, \mathbf{R}') = -f(\mathbf{R}')G(\mathbf{R}, \mathbf{R}') + \delta(\mathbf{R} - \mathbf{R}')\psi(\mathbf{R}') \tag{3.40}$$

Define a volume V such that there are spheres B_ϵ and B_δ, centred at $\mathbf{R}$ and $\mathbf{R}_0$ respectively, not contained inside the volume V. That is to say the volume contains points $\boldsymbol{\rho}$ such that

$$V = \{\boldsymbol{\rho} \in V \,||\boldsymbol{\rho} - \mathbf{R}| \geq \epsilon, \quad |\boldsymbol{\rho} - \mathbf{R}_0| \geq \delta\} \tag{3.41}$$

Because the volume has the points $\mathbf{R}$ and $\mathbf{R}_0$ removed, in the volume the right-hand side of Equation (3.40) is 0, because G and ψ are solutions to the homogeneous Helmholtz equation. Therefore, every point $\boldsymbol{\rho}$ in the volume V is free from discontinuities, they are both second order differentiable and Green's second identity can be applied. Consider a volume integral of Equation (3.40) with respect to the volume defined in Equation (3.41)

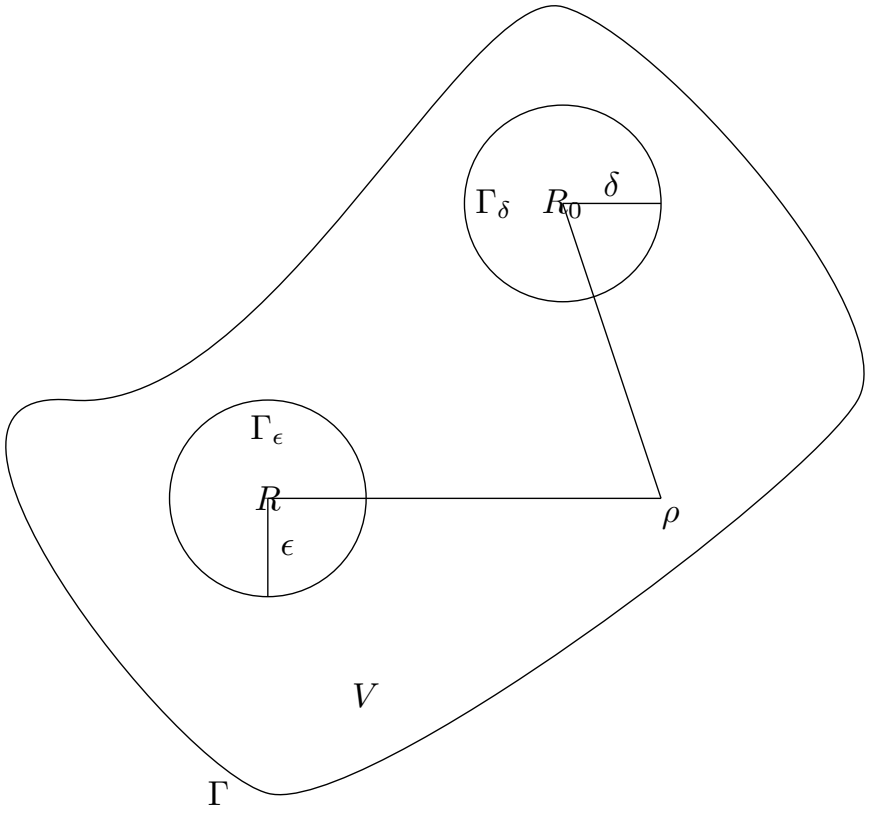

Figure 3.1: Pictorial representation of the formation of the volume integral V where two balls centred at the discontinuities in the volume have been omitted from the volume, leaving surfaces Γ, Γ_ϵ, and Γ_δ.

$$\int_V G(\mathbf{R},\boldsymbol{\rho})\Delta\psi(\boldsymbol{\rho}) - \psi(\boldsymbol{\rho})\Delta G(\mathbf{R},\boldsymbol{\rho})dV_{\boldsymbol{\rho}} = 0. \tag{3.42}$$

Where the subscript $\boldsymbol{\rho}$ indicates that the variable of integration is with respect to $\boldsymbol{\rho}$. The volume integral can be reduced to surface integrals of the boundary of the volume using Green's second identity, and the surfaces formed from the removal of the two balls

$$\int_V G(\mathbf{R},\boldsymbol{\rho})\Delta\psi(\boldsymbol{\rho}) - \psi(\boldsymbol{\rho})\Delta G(\mathbf{R},\boldsymbol{\rho})dV_{\boldsymbol{\rho}} = \int_{\Gamma+\Gamma_\epsilon+\Gamma_\delta} (G(\mathbf{R},\boldsymbol{\rho})\nabla\psi(\boldsymbol{\rho}) - \psi(\boldsymbol{\rho})\nabla G(\mathbf{R},\boldsymbol{\rho}))\cdot\mathbf{n}dS_{\boldsymbol{\rho}}. \tag{3.43}$$

Consider the surface integral Γ_ϵ, noting that as the ball is centred at R of distance ϵ then $|\mathbf{R}-\boldsymbol{\rho}| = \epsilon$ and $\frac{dG}{dn} = -\frac{dG}{d\epsilon}$. Hence

$$\int_{\Gamma_\epsilon} (G(\epsilon)\nabla\psi(\boldsymbol{\rho}))\cdot\mathbf{n} + \psi(\boldsymbol{\rho})\frac{dG(\epsilon)}{d\epsilon}dS_{\boldsymbol{\rho}} \tag{3.44}$$

$$= \frac{1}{4\pi}\int_{\Gamma_\epsilon} (\Big(\frac{e^{ikx}}{x}\Big)\nabla\psi(\boldsymbol{\rho}))\cdot\mathbf{n} + \psi(\boldsymbol{\rho})(e^{ik\epsilon}\Big(\frac{ik}{\epsilon} - \frac{1}{\epsilon^2}\Big))dS_{\boldsymbol{\rho}} \tag{3.45}$$

$$= \frac{1}{4\pi}\int_{\Gamma_\epsilon} (\Big(\frac{e^{ikx}}{x}\Big)\nabla\psi(\boldsymbol{\rho}))\cdot\mathbf{n}dS_{\boldsymbol{\rho}} + \int_{\Gamma_\epsilon}\psi(\boldsymbol{\rho})(e^{ik\epsilon}\Big(\frac{ik}{\epsilon} - \frac{1}{\epsilon^2}\Big))dS_{\boldsymbol{\rho}} \tag{3.46}$$

As the surface is over a sphere of radius ϵ, then

$$dS_{\boldsymbol{\rho}} = \epsilon^2\sin(\theta)d\theta d\phi \tag{3.47}$$

and

$$\int_{\Gamma_\epsilon} = \int_0^{2\pi}\int_0^{\pi}. \tag{3.48}$$

Therefore,

$$= \frac{1}{4\pi}\int_0^{2\pi}\int_0^{\pi} (\Big(\epsilon e^{ik\epsilon}\Big)\nabla\psi(\boldsymbol{\rho}))\cdot\mathbf{n}\sin(\theta)d\theta d\phi + \int_0^{2\pi}\int_0^{\pi}\psi(\boldsymbol{\rho})(e^{ik\epsilon}\Big(\epsilon ik - 1\Big))\sin(\theta)d\theta d\phi. \tag{3.49}$$

As $\epsilon \to 0$, $\boldsymbol{\rho} \to \mathbf{R}$,

$$\approx -\frac{\psi(\mathbf{R})}{4\pi}\int_0^{2\pi}\int_0^{\pi}\sin(\theta)d\theta d\phi. \tag{3.50}$$

$$= -\psi(\mathbf{R}) \tag{3.51}$$

Consider the surface integral Γ_δ, noting that as the ball is centred at R_0 of distance δ then $|\mathbf{R_0} - \boldsymbol{\rho}| = \delta$. Assuming that close to $\mathbf{R}_0$, ψ is close to the free field case and assuming the free-field is a point source i.e. $\psi(\delta) = \frac{e^{ik\delta}}{4\pi\delta}$, $\frac{d\psi}{dn} = -\frac{d\psi}{d\delta}$. Hence

$$\int_{\Gamma_\delta} G(\mathbf{R}, \boldsymbol{\rho}) \frac{d\psi(\delta)}{d\delta} - (\psi(\delta) \nabla G(\mathbf{R}, \boldsymbol{\rho})) \cdot \mathbf{n} dS_{\boldsymbol{\rho}} \tag{3.52}$$

$$= \frac{1}{4\pi} \int_{\Gamma_\delta} -G(\mathbf{R}, \boldsymbol{\rho}) \Big(\frac{ik}{\delta} - \frac{1}{\delta^2} \Big) e^{ik\delta} dS_{\boldsymbol{\rho}} - \frac{1}{4\pi} \int_{\Gamma_\delta} (\psi(\delta) \nabla G(\mathbf{R}, \boldsymbol{\rho})) \cdot \mathbf{n} dS_{\boldsymbol{\rho}} \tag{3.53}$$

By the same logic as above, as $\delta \to 0$,

$$\to G(\mathbf{R}, \mathbf{R}_0) \tag{3.54}$$

Substituting Equations (3.51) and (3.54) into (3.43). Then

$$0 = -\psi(\mathbf{R}) + G(\mathbf{R}, \mathbf{R}_0) + \int_\Gamma (G(\mathbf{R}, \boldsymbol{\rho}) \nabla \psi(\boldsymbol{\rho}) - \psi(\boldsymbol{\rho}) \nabla G(\mathbf{R}, \boldsymbol{\rho})) \cdot \mathbf{n} dS_{\boldsymbol{\rho}} \tag{3.55}$$

$$\psi(\mathbf{R}) = G(\mathbf{R}, \mathbf{R}_0) + \int_\Gamma (G(\mathbf{R}, \boldsymbol{\rho}) \nabla \psi(\boldsymbol{\rho}) - \psi(\boldsymbol{\rho}) \nabla G(\mathbf{R}, \boldsymbol{\rho})) \cdot \mathbf{n} dS_{\boldsymbol{\rho}} \tag{3.56}$$

Recalling the inhomogeneity in Equation (3.22), noting that if the source is a point source located at $\mathbf{R}_0$ then $f(\mathbf{R}) = \delta(\mathbf{R} - \mathbf{R}_0)$. Then by it can be observed that

$$G(\mathbf{R}, \mathbf{R}_0) = \int_{V'} \delta(\boldsymbol{\rho} - \mathbf{R}_0) G(\mathbf{R}, \boldsymbol{\rho}) dV'_{\boldsymbol{\rho}} = \int_{V'} f(\boldsymbol{\rho}) G(\mathbf{R}, \boldsymbol{\rho}) dV'_{\boldsymbol{\rho}}. \tag{3.57}$$

Which leaves

$$\psi(\mathbf{R}) = \int_{V'} f(\boldsymbol{\rho}) G(\mathbf{R}, \boldsymbol{\rho}) dV'_{\boldsymbol{\rho}} + \int_\Gamma (G(\mathbf{R}, \boldsymbol{\rho}) \nabla \psi(\boldsymbol{\rho}) - \psi(\boldsymbol{\rho}) \nabla G(\mathbf{R}, \boldsymbol{\rho})) \cdot \mathbf{n} dS_{\boldsymbol{\rho}} \tag{3.58}$$

This is the Kirchhoff-Helmholtz integral equation. Similar definitions can be found in [36] and [24].

This equation can be immediately simplified to the two dimensional case using the following insights:

$$\frac{d}{dx} \Big(\frac{i}{4} H_0^{(1)}(kx) \Big) = \frac{ik}{4} H_1^{(1)}(kx), \tag{3.59}$$

$$\lim_{x\to 0} \frac{x\mathrm{i}}{4} H_0^{(1)}(kx) = 0, \tag{3.60}$$

$$\lim_{x\to 0} \frac{x\mathrm{i}}{4} H_1^{(1)}(kx) = \frac{1}{2\pi}. \tag{3.61}$$

The 2π will get cancelled from the surface integral over circles, instead of balls.

3.3 Tangent Plane Approximation

Recalling the Kirchhoff-Helmholtz integral formulation

$$\psi(\mathbf{R}) = \psi_0(\mathbf{R}) + \int_\Gamma (G(\mathbf{R},\boldsymbol{\rho})\nabla\psi(\boldsymbol{\rho}) - \psi(\boldsymbol{\rho})\nabla G(\mathbf{R},\boldsymbol{\rho}))\cdot \mathbf{n} dS_{\boldsymbol{\rho}} \tag{3.62}$$

Where $\psi_0 = \int_{V'} f(\boldsymbol{\rho}) G(\mathbf{R},\boldsymbol{\rho}) dV'_{\boldsymbol{\rho}}$ is the incident field, the field due to the source absent from reflections.

This section will derive the Tangent Plane method, also known as the Kirchhoff Approximation [36]. The main idea of the tangent plane method is that the scattered field can be represented by an infinite number of monopoles radiating from the surface where the reflection at a given point is approximated by reflection from an infinite tangent plane. This yields a relationship between the incident field and the full field (as is described in Appendix A, derived from plane wave scattering and transmission from two media). That is, [36]

$$\psi(\mathbf{r}) = (1+\mathscr{V})\psi_0(\mathbf{r}) \tag{3.63}$$

$$\frac{\partial\psi(\mathbf{r})}{\partial n} = (1-\mathscr{V})\frac{\partial\psi_0(\mathbf{r})}{\partial n} \tag{3.64}$$

Where $\mathscr{V}$ is the reflection coefficient. The condition that the scattering surface must be “smooth enough" can be defined mathematically as [36]:

$$\frac{1}{(ka)^{\frac{1}{3}}} << 1, \tag{3.65}$$

which can be relaxed [148]

$$\frac{1}{(ka)^{\frac{1}{3}}} < 1. \tag{3.66}$$

Where k is the acoustic wavenumber and a is the local radius of curvature.

Assuming the Green's function is the free-field 3D Green's function in Equation (3.30) and substituting this, Equations(3.63) (3.64) into Equation (3.62)

$$\psi(\mathbf{R}) = \psi_0(\mathbf{R}) + \frac{1}{4\pi}\int_{S+S'+C_{R'}} [\frac{e^{ik|\mathbf{R}-\mathbf{r}|}}{|\mathbf{R}-\mathbf{r}|}\nabla\psi(\mathbf{r}) - \psi(\mathbf{r})\nabla\frac{e^{ik|\mathbf{R}-\mathbf{r}|}}{|\mathbf{R}-\mathbf{r}|}].\mathbf{n}d\mathbf{r} \tag{3.67}$$

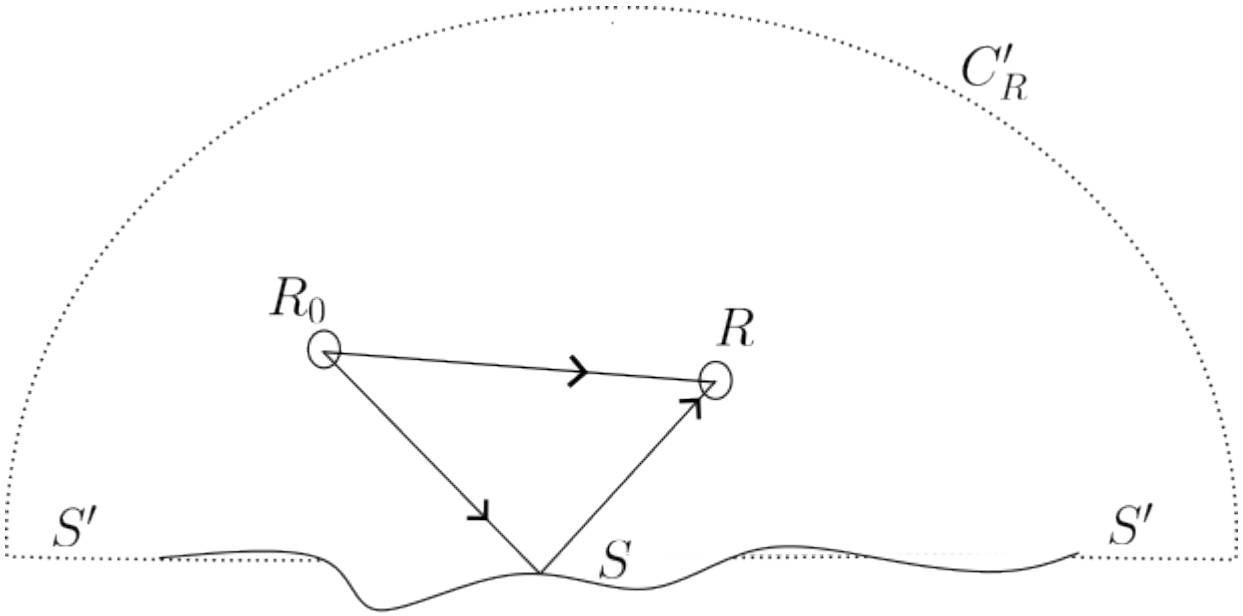

Figure 3.2: Pictorial representation of the setup used in the acoustic scattering, in order to set up the Kirchhoff Approximation. In order to transform the external domain problem into an internal domain, a hemisphere is formed that surrounds the surface and this hemisphere is then tended to infinity. From the Sommerfeld radiation condition, this does not contribute to the overall scattered signal.

Note that this is just the surface integral. However, the surface is formed by the surface S, part of the plane S', and hemisphere $C_{R'}$ as shown in Figure 3.2 to make a closed surface containing all field sources.

As there are no sources present on the surfaces then [36],

$$0 = \frac{1}{4\pi}\int_{S+S'+C_{R'}} [\frac{e^{ik|\mathbf{R}-\mathbf{r}|}}{|\mathbf{R}-\mathbf{r}|}\nabla\psi_0(\mathbf{r}) - \psi_0(\mathbf{r})\nabla\frac{e^{ik|\mathbf{R}-\mathbf{r}|}}{|\mathbf{R}-\mathbf{r}|}].\mathbf{n}d\mathbf{r} \tag{3.68}$$

Subtracting Equation (3.68) from Equation (3.67)

$$\psi(\mathbf{R}) = \psi_0(\mathbf{R}) + \frac{1}{4\pi}\int_{S+S'+C_{R'}} \left[\frac{e^{ik|\mathbf{R}-\mathbf{r}|}}{|\mathbf{R}-\mathbf{r}|}\frac{\partial}{\partial n}(\psi(\mathbf{r}) - \psi_0(\mathbf{r})) - (\psi(\mathbf{r}) - \psi_0(\mathbf{r}))\frac{\partial}{\partial n}\frac{e^{ik|\mathbf{R}-\mathbf{r}|}}{|\mathbf{R}-\mathbf{r}|}\right] d\mathbf{r} \tag{3.69}$$

Considering the hemisphere $C_{R'}$ and the surface S'. Firstly, $C_{R'}$ is removed by taking $R' \to \infty$, and enforcing the Sommerfeld Radiation condition. That is to say, for extremely far from the scattering rough surface, the field behaves as the free-field solution and thus decays. For the integral over S', at any point on S' then $\psi(\mathbf{r}) = \psi_0(\mathbf{r})$. Enforcing Equations (3.63) (3.64) into Equation (3.69)

$$\begin{aligned}\psi(\mathbf{R}) = \psi_0(\mathbf{R}) + \frac{1}{4\pi}\int_{S+S'+C_{R'}} [\frac{e^{ik|\mathbf{R}-\mathbf{r}|}}{|\mathbf{R}-\mathbf{r}|}\frac{\partial}{\partial n}((1+V)\psi_0(\mathbf{r}) - \psi_0(\mathbf{r})) \\ - ((1-V)\psi_0(\mathbf{r}) - \psi_0(\mathbf{r}))\frac{\partial}{\partial n}\frac{e^{ik|\mathbf{R}-\mathbf{r}|}}{|\mathbf{R}-\mathbf{r}|}]d\mathbf{r}\end{aligned} \tag{3.70}$$

$$= \psi(\mathbf{R}) = \psi_0(\mathbf{R}) + \frac{1}{4\pi}\int_{S+S'+C_{R'}} V[\frac{e^{ik|\mathbf{R}-\mathbf{r}|}}{|\mathbf{R}-\mathbf{r}|}\frac{\partial}{\partial n}(\psi_0(\mathbf{r})) + \psi_0(\mathbf{r})\frac{\partial}{\partial n}\frac{e^{ik|\mathbf{R}-\mathbf{r}|}}{|\mathbf{R}-\mathbf{r}|}]d\mathbf{r} \tag{3.71}$$

Applying the product rule of derivatives

$$\psi(\mathbf{R}) = \psi_0(\mathbf{R}) + \frac{1}{4\pi}\int_S V(\mathbf{r})\frac{\partial}{\partial n}[\frac{e^{ik|\mathbf{R}-\mathbf{r}|}}{|\mathbf{R}-\mathbf{r}|}\psi_0(\mathbf{r})]d\mathbf{r}. \tag{3.72}$$

Assuming the incident field is a point source

$$\psi(\mathbf{R}) = \psi_0(\mathbf{R}) + \frac{1}{4\pi}\int_S V(\mathbf{r})\frac{\partial}{\partial n}[\frac{e^{ik(R_1+R_2)}}{R_1R_2}]d\mathbf{r}, \tag{3.73}$$

where R_1 and R_2 are Euclidean distances from a point on the surface to the source and observation point. That is to say, if the surface roughness is defined by a function $\zeta(\mathbf{x})$, and the source location and receiver location are $(x_1, y_1, z_1), (x_2, y_2, z_2)$ respectively, then

$$R_1 = \sqrt{(x_1-x)^2 + (y_1-y)^2 + (z_1-\zeta(x,y))^2}, \tag{3.74}$$

$$R_2 = \sqrt{(x_2-x)^2 + (y_2-y)^2 + (z_2-\zeta(x,y))^2}. \tag{3.75}$$

Considering the normal derivative, and assuming that $kR_1, kR_2 >> 1$[36]

$$\frac{\partial}{\partial n}[\frac{e^{ik(R_1+R_2)}}{R_1R_2}] = -\mathrm{i}(\mathbf{n}\cdot\mathbf{q})\frac{e^{ik(R_1+R_2)}}{R_1R_2} + \mathcal{O}(\frac{1}{(R_1R_2)^2}) \tag{3.76}$$

$$\approx -\mathrm{i}(\mathbf{n}\cdot\mathbf{q})\frac{e^{ik(R_1+R_2)}}{R_1R_2} \tag{3.77}$$

Where $\mathbf{q} = -k\nabla_S(R_1+R_2)$ and ∇_S are the derivatives with respect to the dimensions of the surface. That is to say

$$\nabla_S = \begin{cases} (\frac{\partial}{\partial x}, \frac{\partial}{\partial y}, \frac{\partial}{\partial z}), & \text{3D} \\ (\frac{\partial}{\partial x}, \frac{\partial}{\partial y}), & \text{2D} \end{cases} \tag{3.78}$$

Therefore,

$$\psi(\mathbf{R}) = \psi_0(\mathbf{R}) + \frac{1}{4\pi\mathrm{i}}\int_S V(\mathbf{r})\frac{e^{ik(R_1+R_2)}}{R_1R_2}(\mathbf{n}\cdot\mathbf{q})d\mathbf{r}, \tag{3.79}$$

where

$$\mathbf{n} = \frac{\mathbf{i_z} - \nabla_r\zeta(x,y)}{\sqrt{1-(\nabla_r\zeta(x,y))^2}} \tag{3.80}$$

$$n_z = \frac{1}{\sqrt{1-(\nabla_r\zeta(x,y))^2}} \tag{3.81}$$

Where ∇_r removes the last element from ∇_s, and $\mathbf{i_z}$ is the unit vector in the z direction.

Utilising a change of variable

$$d\mathbf{r} = \frac{d\mathbf{r}}{n_z} = d\mathbf{r}\sqrt{1-(\nabla_r\zeta(x,y))^2}. \tag{3.82}$$

To project onto a flat plane centred at the mean value of the surface. Using Appendix B, the equation can be rearranged to

$$\psi(\mathbf{R})_s = \frac{1}{4\pi i}\int_{S_0}\frac{V(\mathbf{r})}{R_1R_2}e^{ik(R_1+R_2)}(q_z - \mathbf{q}\nabla_r\zeta(x,y))d\mathbf{r} \tag{3.83}$$

In 2D, due to the change of the free-field Green's function, the equation is [67]

$$\psi(\mathbf{R})_s = \frac{1}{2k\pi\mathrm{i}}\int_{S_0}\frac{V(\mathbf{r})}{\sqrt{R_1R_2}}e^{ik(R_1+R_2)}(q_y - q_x\nabla_r\zeta(x))d\mathbf{r} \tag{3.84}$$

If the source has a directivity pattern approximated by radiation from a baffled piston as in [24] centred around the angle of the source ϕ_0 in space then

$$\psi(\mathbf{R})_s = \frac{1}{4\pi i}\int_{S_0}\frac{A(\mathbf{r})V(\mathbf{r})}{R_1R_2}e^{ik(R_1+R_2)}(q_z - \mathbf{q}\nabla_r\zeta(x,y))d\mathbf{r}, \quad 3D \tag{3.85}$$

$$\psi(\mathbf{R})_s = \frac{1}{2k\pi \mathrm{i}} \int_{S_0} \frac{A(\mathbf{r})V(\mathbf{r})}{\sqrt{R_1 R_2}} e^{ik(R_1+R_2)}(q_y - q_x \nabla_r \zeta(x))d\mathbf{r}, \quad 2D \tag{3.86}$$

$$A(\mathbf{r}) = \frac{2J_1(ka\sin(\phi(\mathbf{r}) - (-\phi_0 + \pi/2)))}{ka\sin(\phi(\mathbf{r}) - (-\phi_0 + \pi/2))}. \tag{3.87}$$

Where a is the aperture, J_1 is the Bessel function of the first kind with $n = 1$, ϕ_0 is the angle of inclination of the source main axis to the Ox-axis, and $\phi(\mathbf{r})$ is the angle between the vector produced from the location of the source and the point $\mathbf{r}$ with the Oy-axis.

Throughout this work, a linear microphone array was simulated above the surface, using code based on the above equation and conditions, written by the author and provided in https://github.com/michaeldavidjohnson/Kirchhoff-Approximation, and the absolute scattered acoustic pressure was used as input to various models, both deterministic and stochastic. The primary hypothesis is that there is enough information about the structure of the surface contained in the scattered absolute pressure in the far-field that a model can be fitted to the data such that parameters of the surface can be recovered. Therefore, the far-field scattered field is visualised. In order to visualise the impact on the acoustic far-field due to the effect of surface roughness, different surfaces at different acoustic frequencies are presented.

Figures 3.4, 3.5, and 3.6 showcase the absolute scattered acoustic pressure in the far-field of the acoustic source, for scattering from a flat surface, at 4,000Hz, 14,000Hz, and 25,000Hz, respectively. From a flat surface, the angle of reflection is the same as the angle of incidence (Snell's law). As the frequency increases, the beam-width of the baffled-piston directivity pattern narrows, this can clearly be seem in the figures presented.

Figures 3.7, 3.8, and 3.9 showcase the absolute scattered acoustic pressure in the far-field of acoustic source, at the same frequencies. For a sinusoidal surface, the scattering surface is defined by:

$$\zeta(x) = 0.0015\sin\left(\frac{2\pi}{0.05}x\right) \tag{3.88}$$

Patterns can be observed for all frequencies. However, as the frequency increases the complexity of the patterns increases. This is a crucial insight when considering inputs to a machine learning model, as complexity typically (although not always) provides more useful information for prediction. The spatial scale of these observed patterns are due directly to the surface scattered. This is the main motivation to using acoustic scattering as an input in a machine learning based approach.

To show the effect of surface roughness on the acoustic far-field, the ensemble average and the ensemble standard deviation was investigated for different levels of surface roughness. The surface roughness was created by choosing a discrete collection of points in the x-direction $X = (x_0, x_1, ..., x_N)$. For each x, the corresponding y-value was determined by drawing a random value from a normal distribution with a given standard deviation σ and adding this random value to a constant translation of 0.0015. The value of σ chosen determines the roughness profile. To recover the full surface profile, cubic spline interpolation was used. The surface was generated from [-1m, 1m], 50 equally spaced values in this range were selected to be the finite collection of points. Cubic Spline interpolation was used to recover a spatial sampling rate of 0.002m. Figure 3.3 presents a single instance of a random surface generated with standard deviations of $0.001, 0.004, 0.009$ respectively.

20 instances of the random surfaces were created, for each standard deviation, and the ensemble average and ensemble standard deviation was obtained for each point in the far-field. Figures 3.10, 3.12, and 3.14 present the ensemble average. Figures 3.11, 3.13, and 3.15 presents the ensemble standard deviation.

In Figure 3.10, the surface roughness is negligible, and the ensemble means look like reflection from a flat surface, with minimal changes in the ensemble standard deviation in Figure 3.11. As the surface roughness increases to 0.004, the overall ensemble average in Figure 3.12 still has a main specular reflection, but outside this main region, there are values of varying absolute scattered field. This can be observed in the standard deviation shown in Figure 3.13, which highlights the overall variation in the ensemble. It is observed that there are changes in the field which are sensitive to the shape of surface roughness. This is highlighted further as the roughness scales increase in Figures 3.14 and 3.15 with the exception of the region close to $y = 0$ where some surfaces are large enough in amplitude to be observed directly in the figures.

These figures have highlighted the proof-of-concept that this work uses to infer true surface heights. There is information in the scattered far-field, and there is spatial dependence that can be used in a machine learning approach. This is expected. The scattered field is formed (at least, in situations where the tangent plane approximation holds), by infinite monopoles distributed along the surface, radiating with a directivity pattern. Classically, this has been leveraged to attempt to approximate the inverse problem directly (for example, attempting to use single value decomposition [67], to invert a transfer matrix from a point on the surface to a receiver).

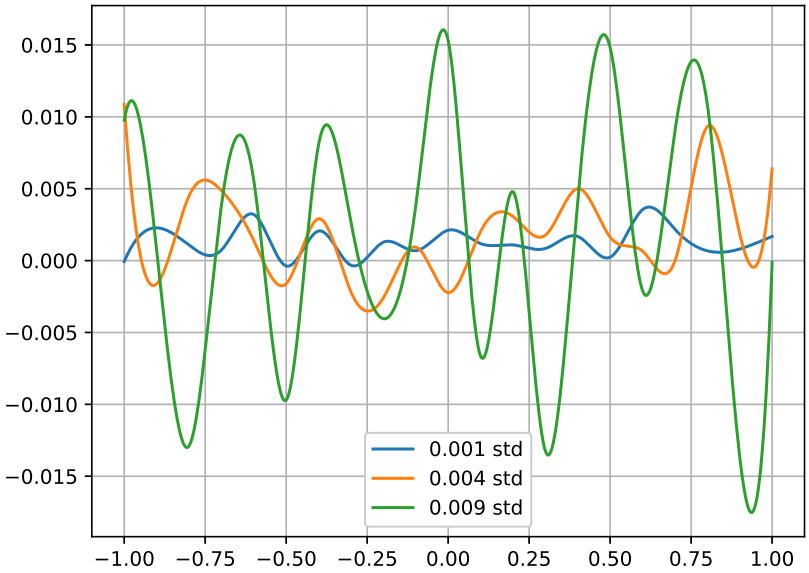

Figure 3.3: Single-instance realisations for rough surfaces at different standard deviations named std in the figure legend.

The code used throughout the later chapters was developed by the author and can be found at https://github.com/michaeldavidjohnson/Kirchhoff-Approximation

3.4 Free Surface Generation of Shallow Flow

This section aims to present information on the most relevant wave theory: dispersion relations. Once dispersion relations have been presented, a method of creating synthetic surfaces is introduced. Due to physical constraints in the system, different spatial wavelengths act at different frequencies. A derivation of the simplest water waves dispersion relation (which relates the frequency to the wavenumber) is included. This methodology has had a slight modification to the form used in later chapters. The fundamental approximations are that the fluid is irrotational (therefore, the fluid is not viscous), and that the free-surface amplitude is small. In these cases, the equations simplify. For example, consider an infinitely long tank with a fixed depth $z = -h$. Assuming plane wave propagation in the x direction, the following equations hold:

$$\nabla^2 \phi = 0 \tag{3.89}$$

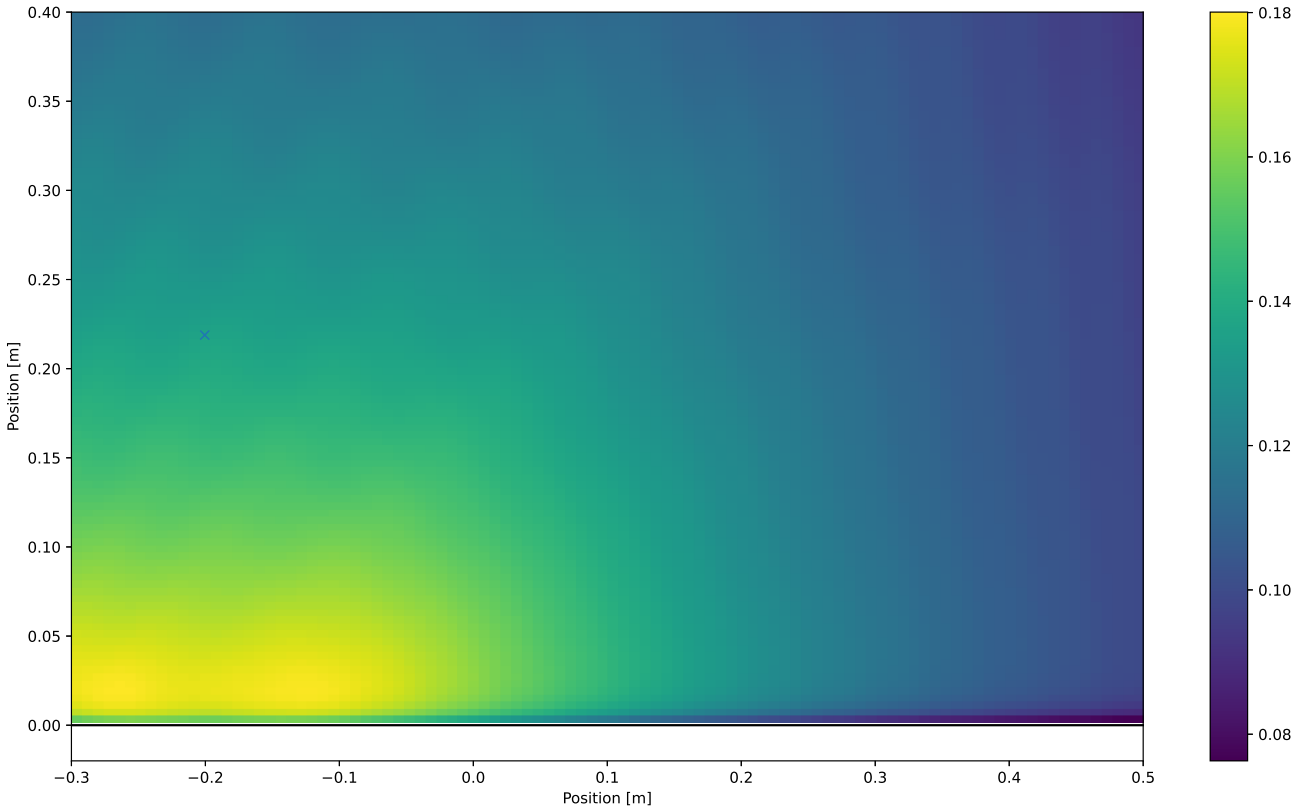

Figure 3.4: The absolute scattered field yielded from the Kirchhoff Approximation when scattering against a flat surface. Frequency 4000Hz

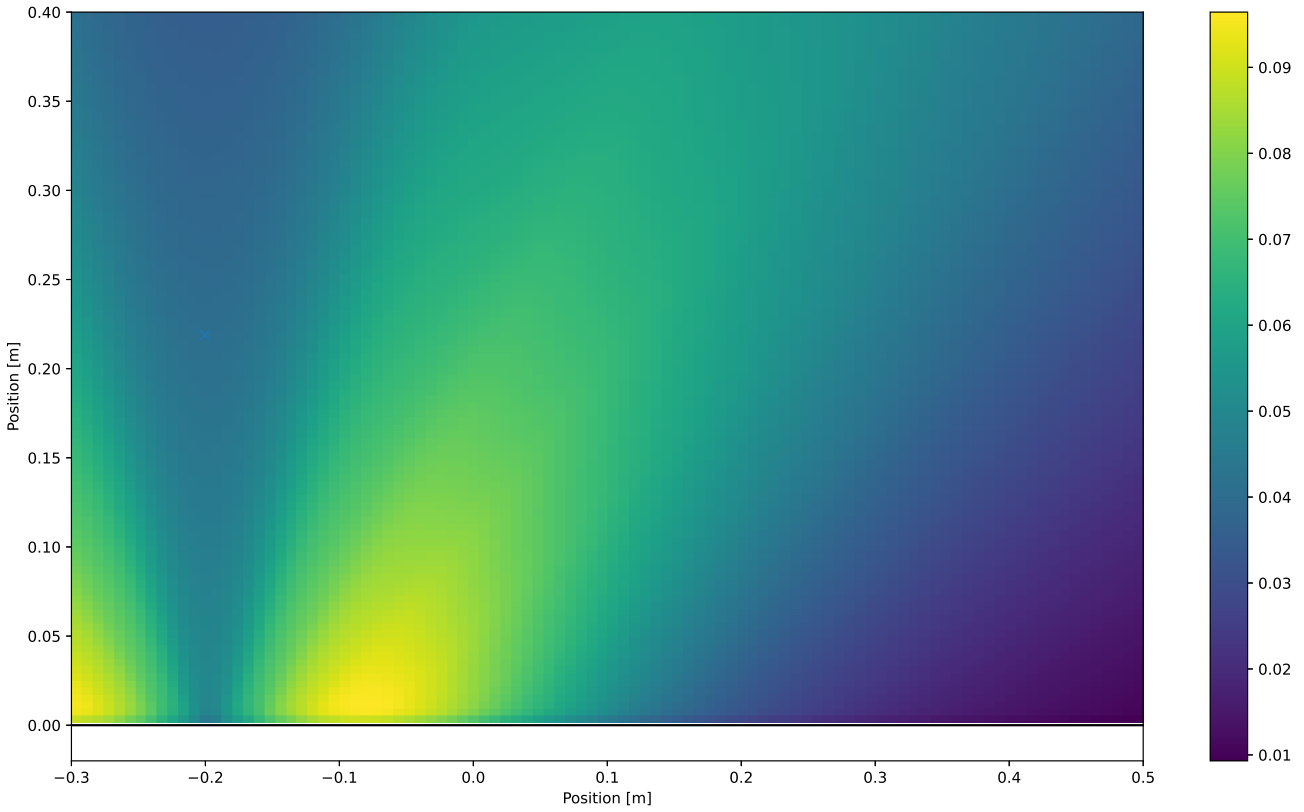

Figure 3.5: The absolute scattered field yielded from the Kirchhoff Approximation when scattering against a flat surface. Frequency 14000Hz

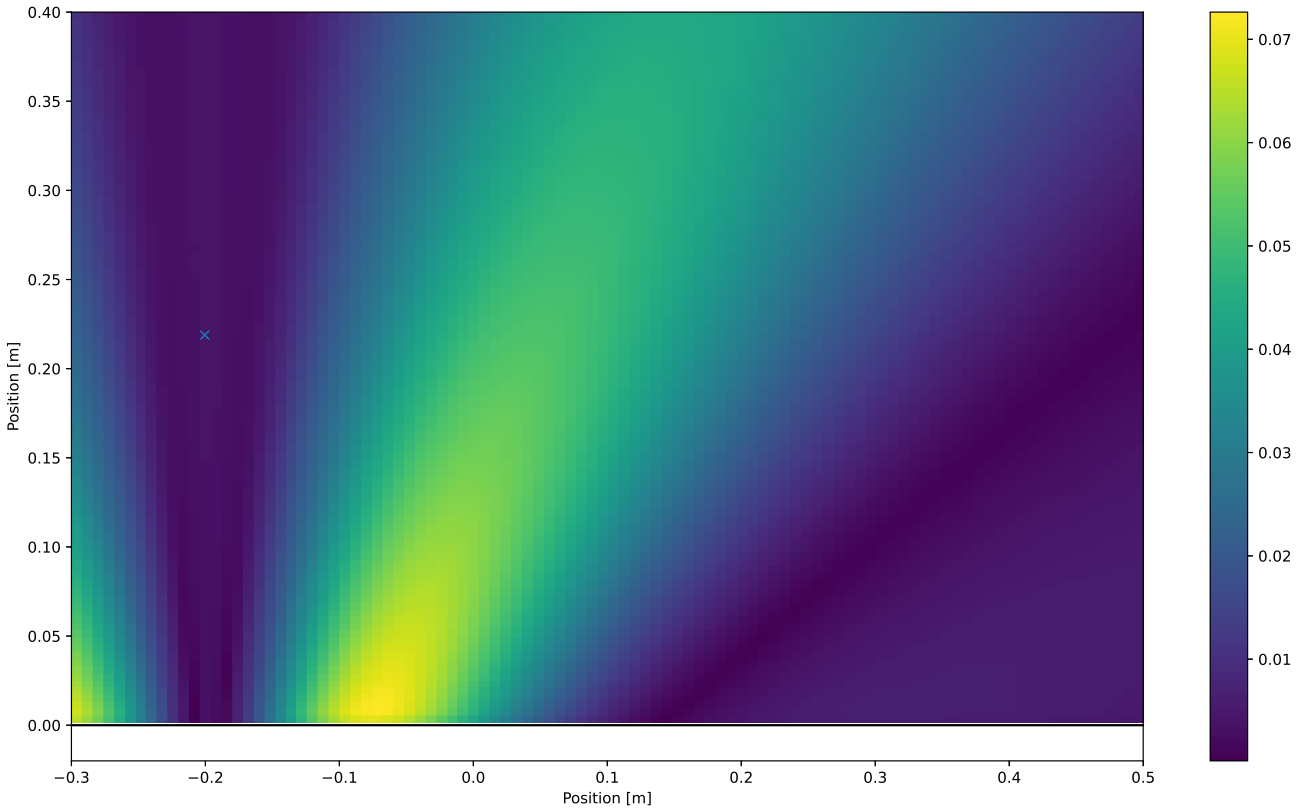

Figure 3.6: The absolute scattered field yielded from the Kirchhoff Approximation when scattering against a flat surface. Frequency 25000Hz

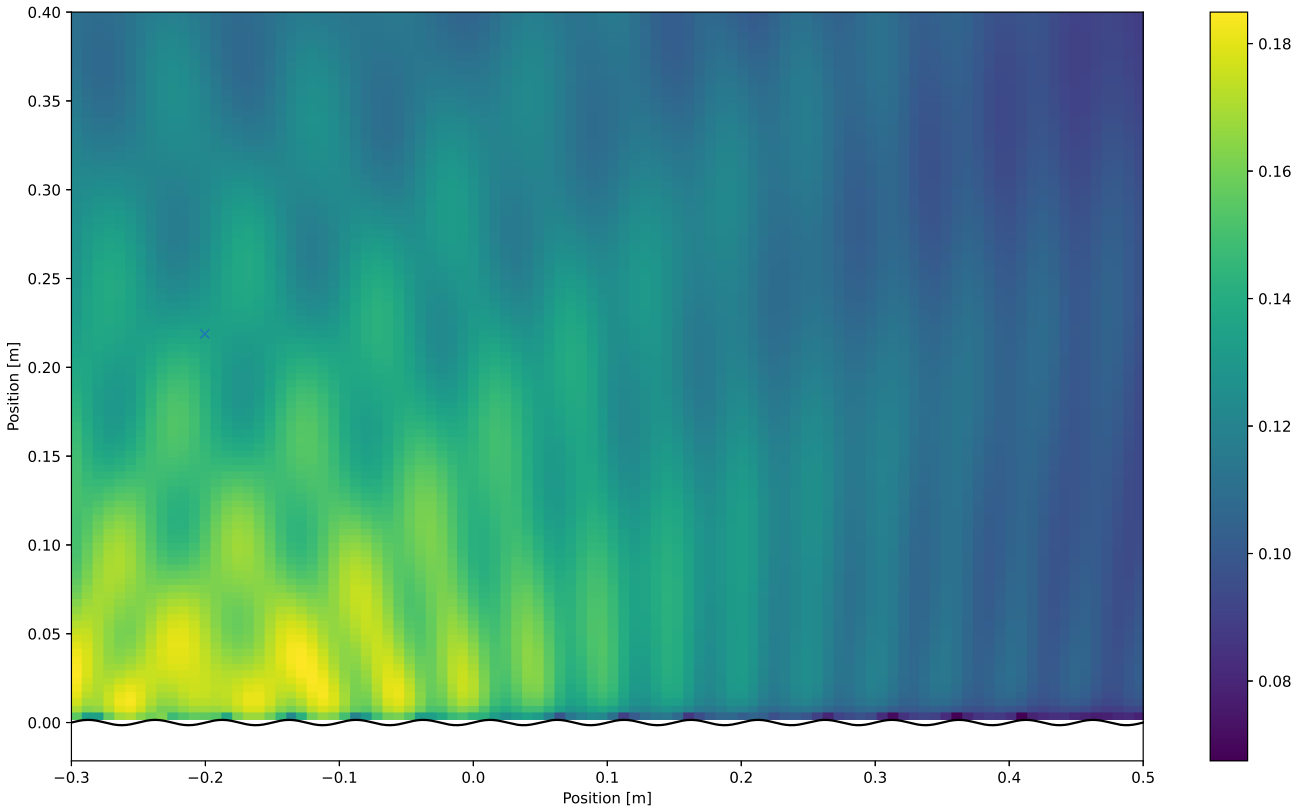

Figure 3.7: The absolute scattered field yielded from the Kirchhoff Approximation when scattering against a sinusoidal surface. Frequency 4000Hz

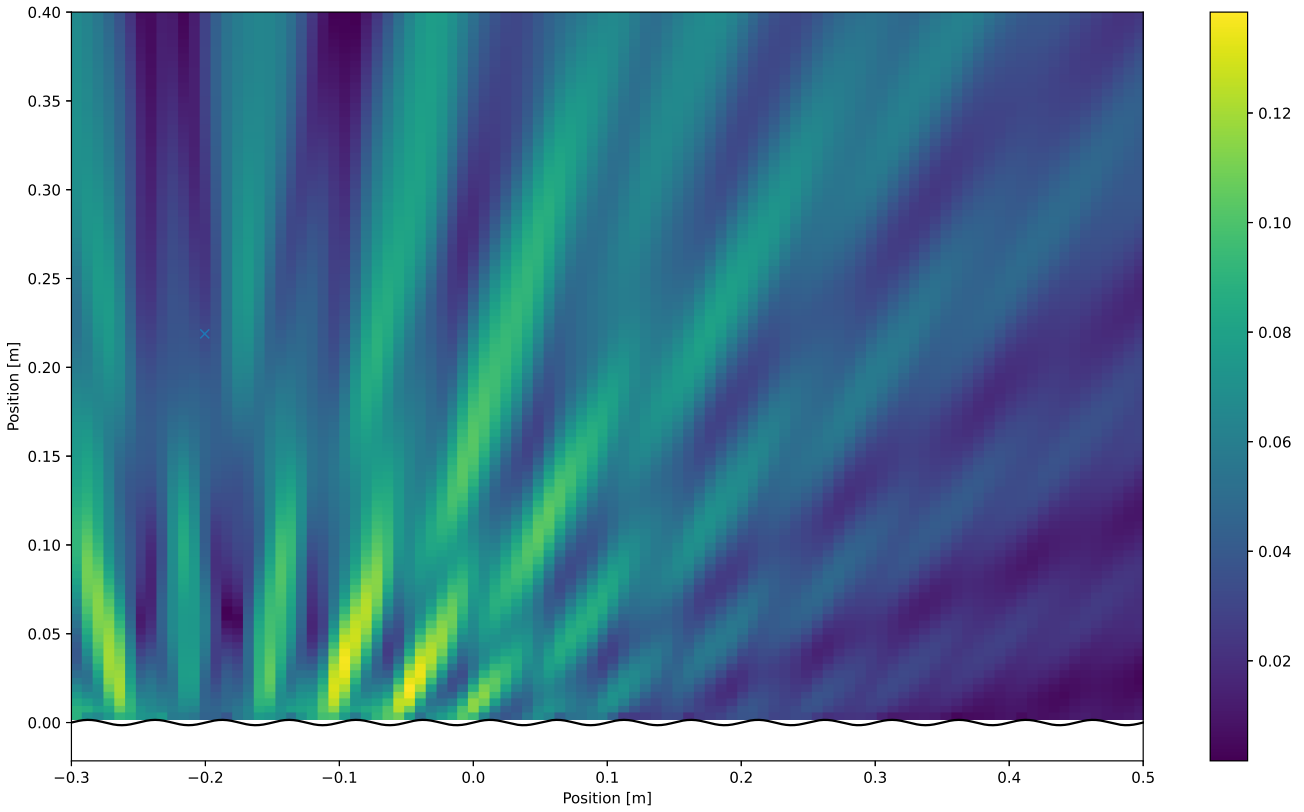

Figure 3.8: The absolute scattered field yielded from the Kirchhoff Approximation when scattering against a sinusoidal surface. Frequency 14000Hz

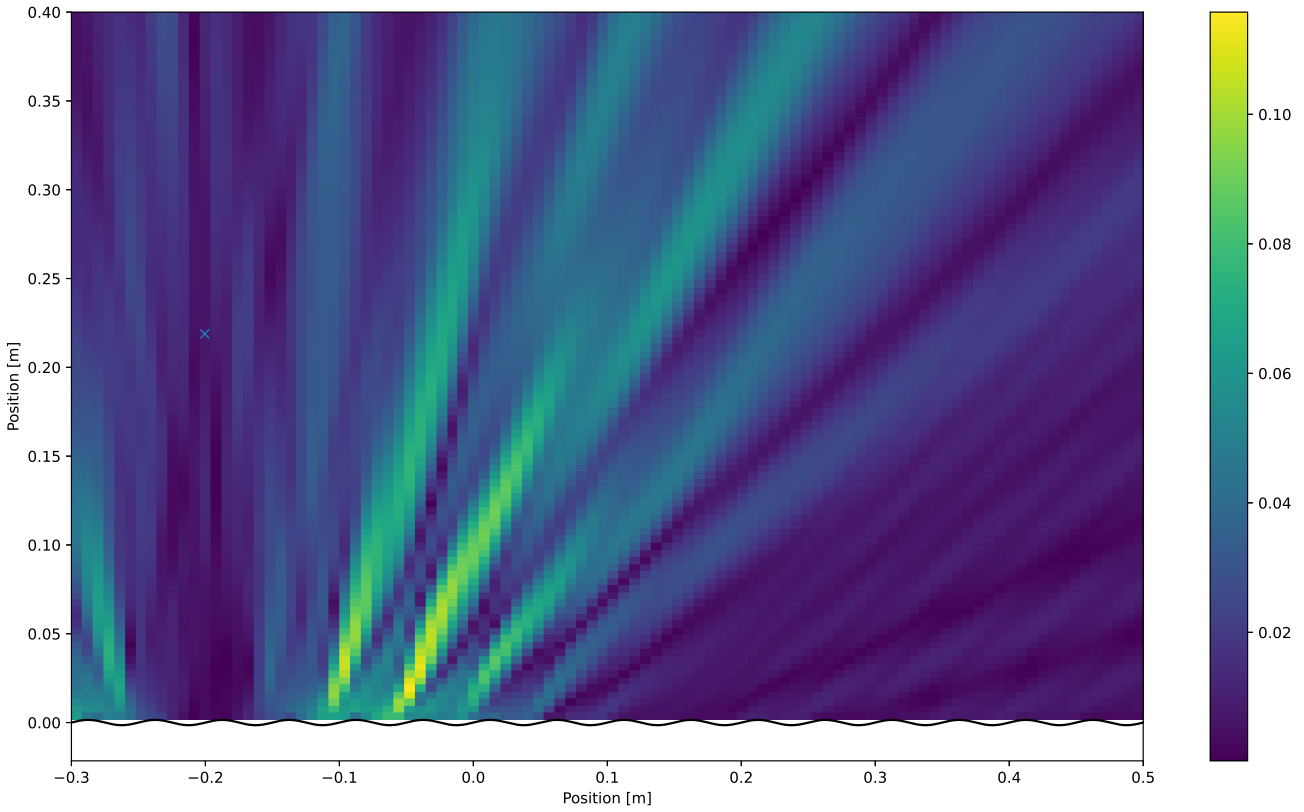

Figure 3.9: The absolute scattered field yielded from the Kirchhoff Approximation when scattering against a sinusoidal surface. Frequency 25000Hz

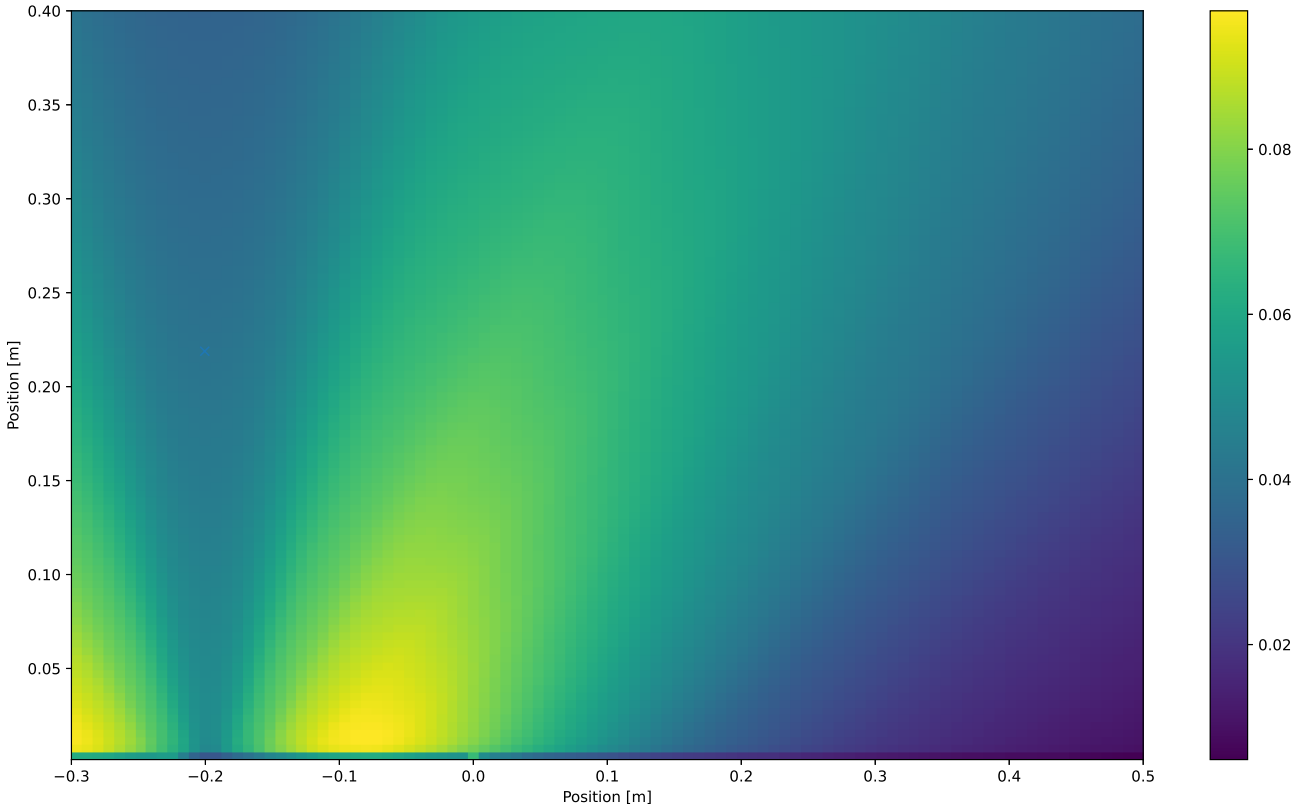

Figure 3.10: The expected absolute scattered field from an ensemble of twenty randomly generated rough surface, yielded from the Kirchhoff Approximation. Frequency, 14000Hz, roughness standard deviation 0.001

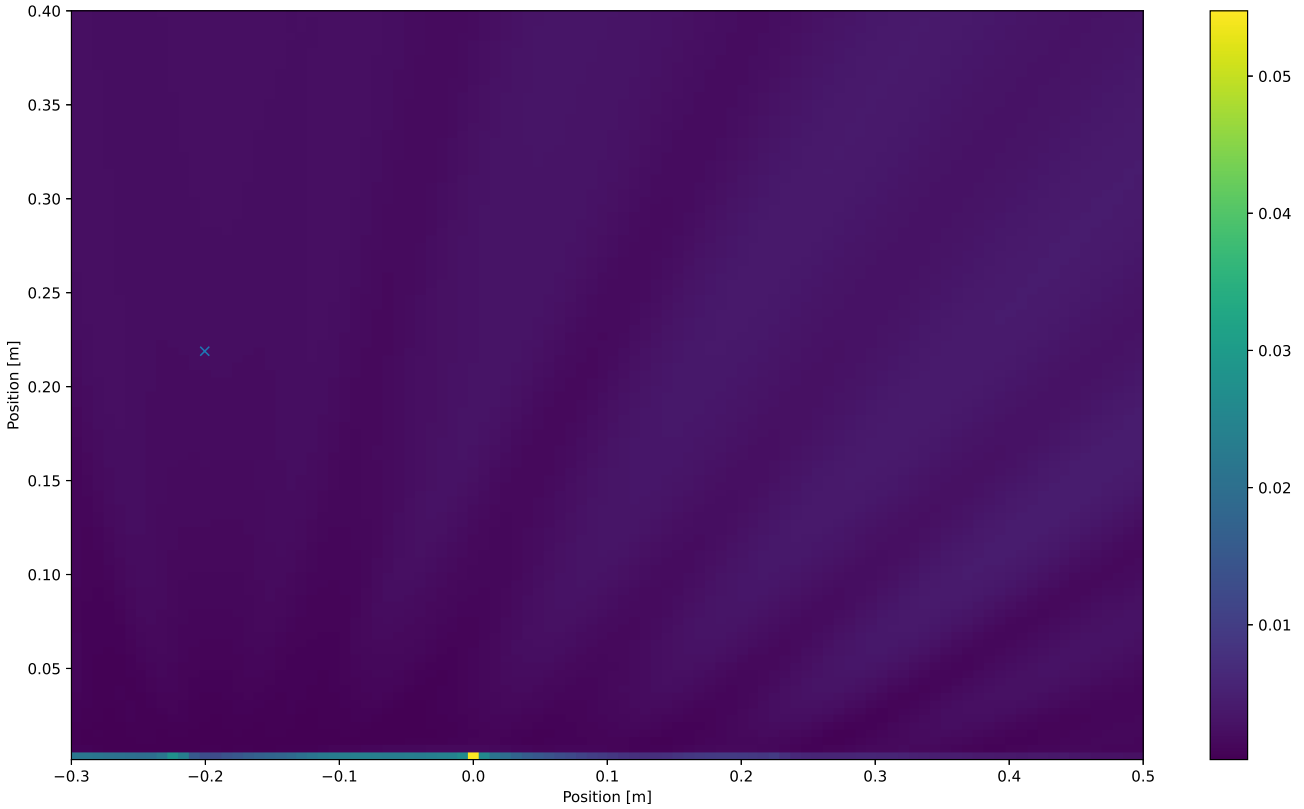

Figure 3.11: The standard deviation of the absolute scattered field from an ensemble of twenty randomly generated rough surface, yielded from the Kirchhoff Approximation. Frequency, 14000Hz, roughness standard deviation 0.001

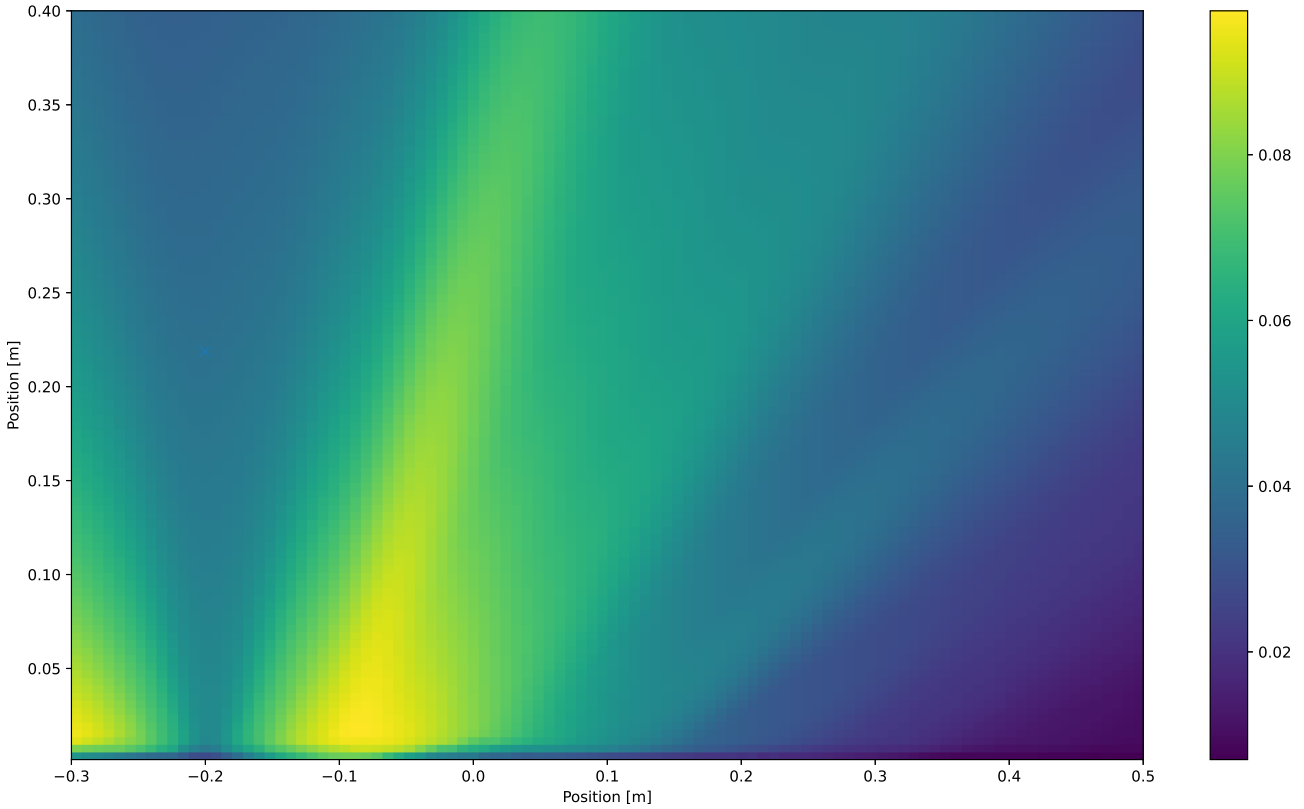

Figure 3.12: The expected absolute scattered field from an ensemble of twenty randomly generated rough surface, yielded from the Kirchhoff Approximation. Frequency, 14000Hz, roughness standard deviation 0.004

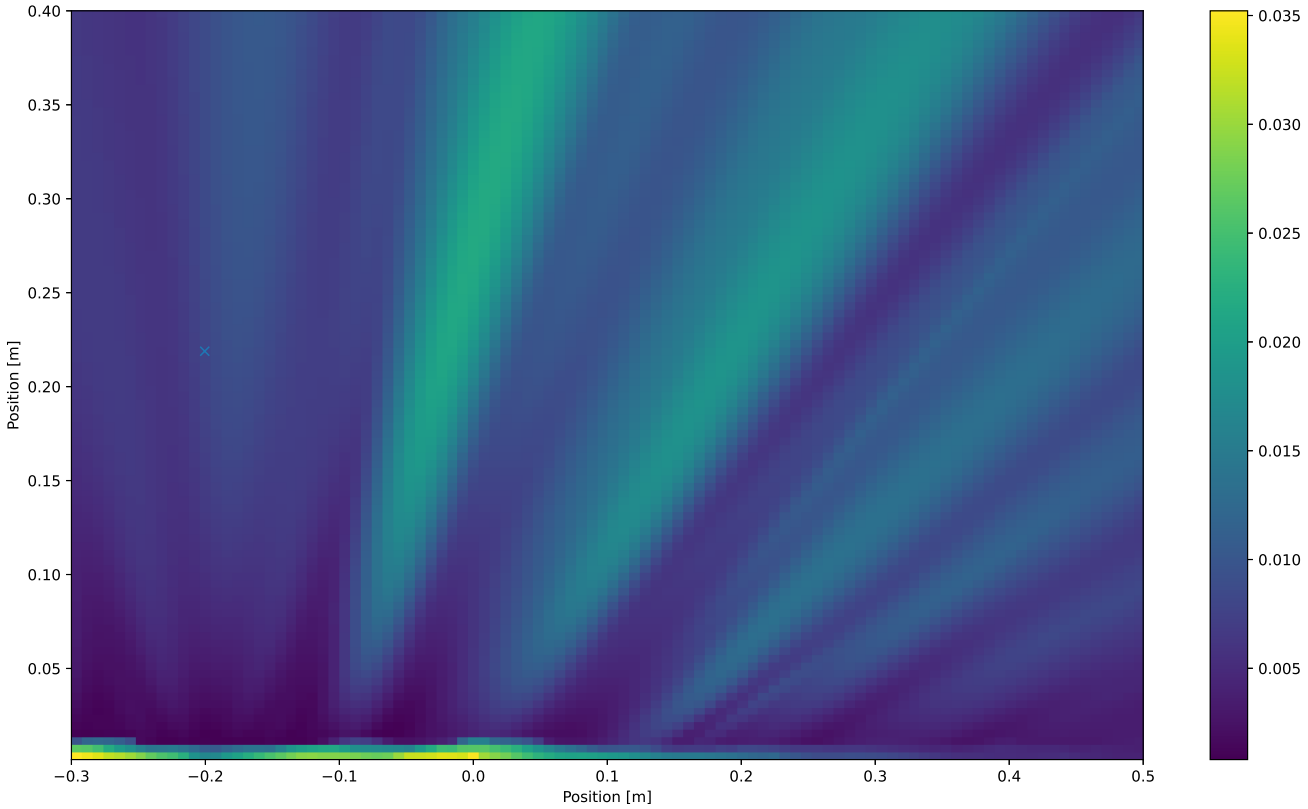

Figure 3.13: The standard deviation of the absolute scattered field from an ensemble of twenty randomly generated rough surface, yielded from the Kirchhoff Approximation. Frequency, 14000Hz, roughness standard deviation 0.004

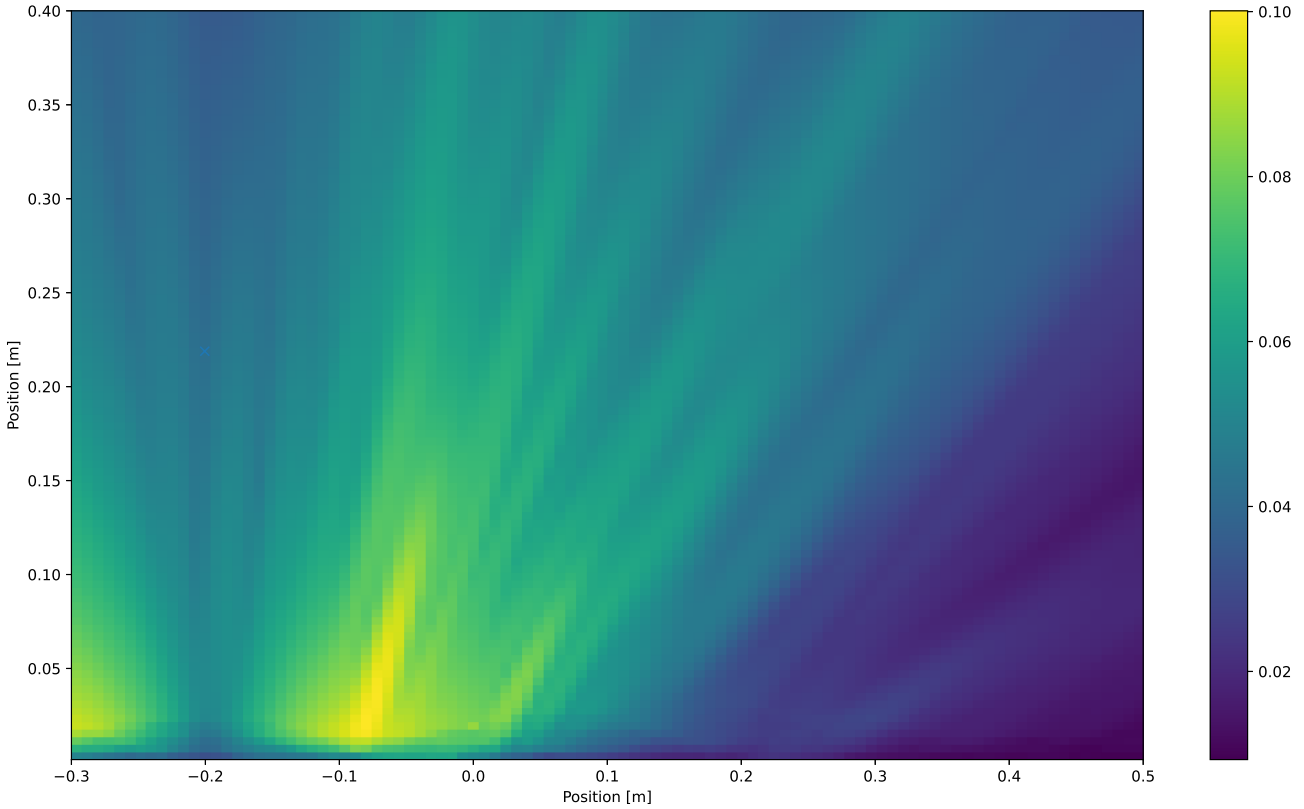

Figure 3.14: The expected absolute scattered field from an ensemble of twenty randomly generated rough surface, yielded from the Kirchhoff Approximation. Frequency, 14000Hz, roughness standard deviation 0.009

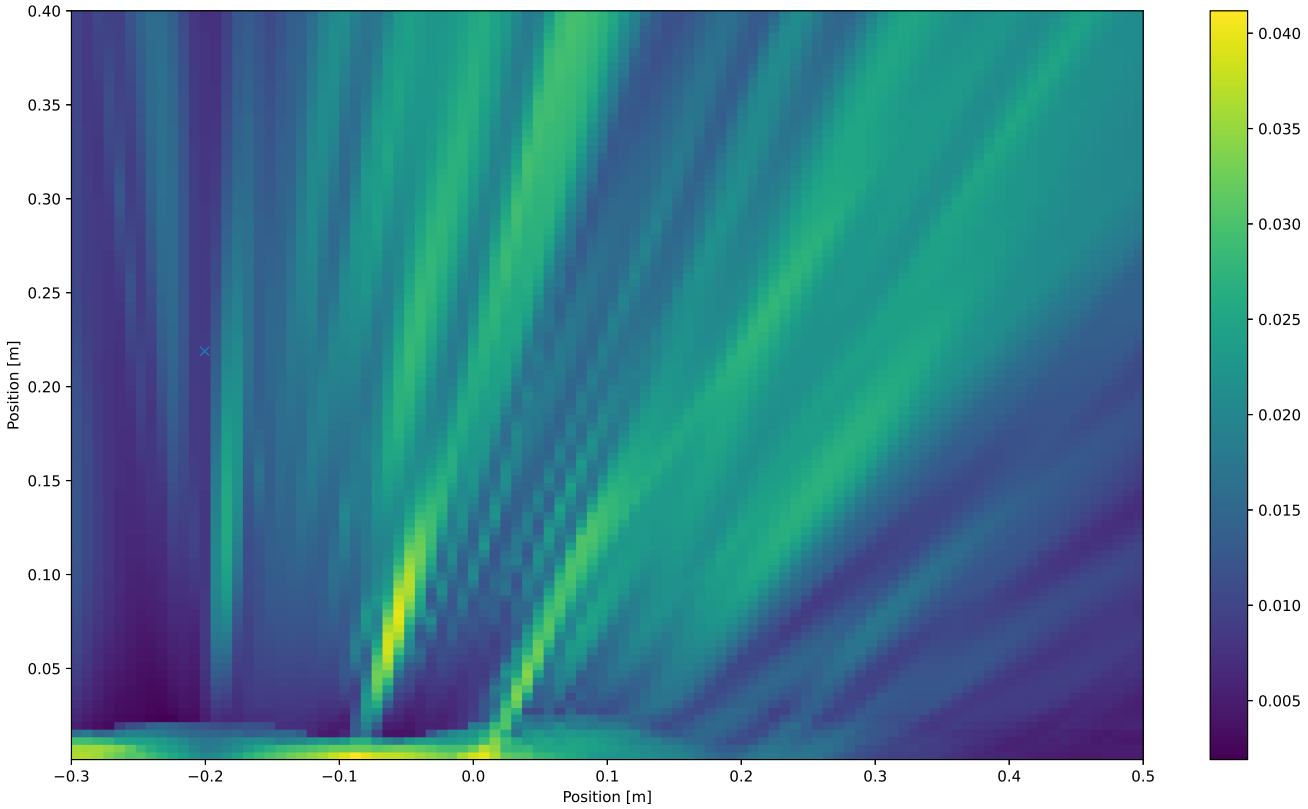

Figure 3.15: The standard deviation of the absolute scattered field from an ensemble of twenty randomly generated rough surface, yielded from the Kirchhoff Approximation. Frequency, 14000Hz, roughness standard deviation 0.009

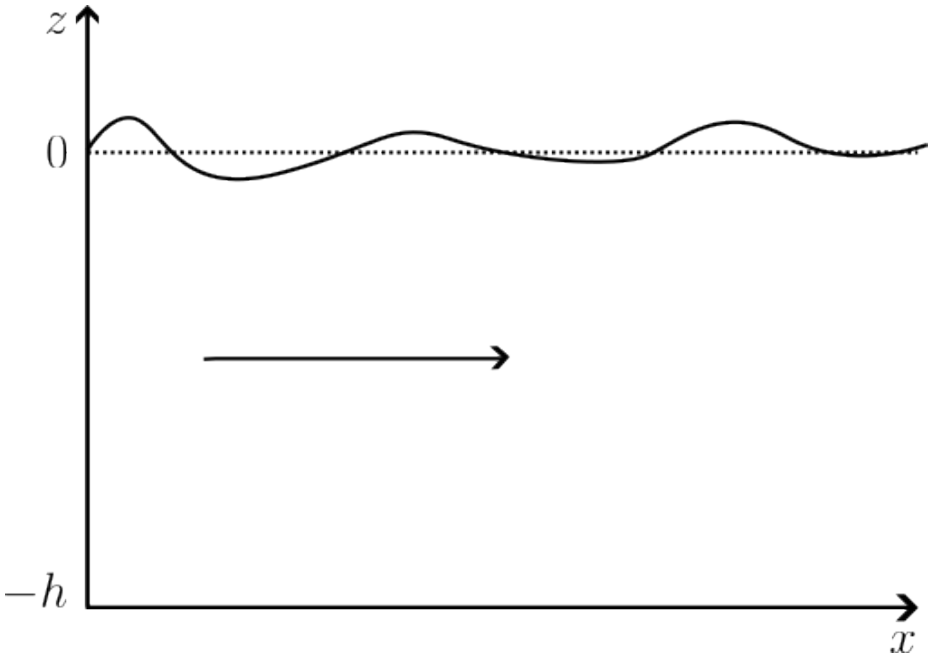

Figure 3.16: Graph representing the problem setup, a tank of water infinitely long in the x direction, bounded by a depth $z = -h$, and a mean surface at $z = 0$. The arrow inside the flow is indicating the propagation direction.

$$\left[\frac{\partial \phi}{\partial n}\right]_{boundary} = 0 \tag{3.90}$$

$$\left[\frac{\partial^2 \phi}{\partial t^2} + g\frac{\partial \phi}{\partial z}\right]_{z=0} = 0. \tag{3.91}$$

Where ϕ is defined as the velocity potential defined earlier, which exists due to irrotational flow [149] and g is the acceleration due to gravity.

To solve this set of equations, seek separable solutions of the form

$$\phi = X(x)Z(z). \tag{3.92}$$

Then, substituting into Equation (3.89)

$$X''Z + Z''X = 0. \tag{3.93}$$

Divide by XZ to find

$$-\frac{X''}{X} = \frac{Z''}{Z} \tag{3.94}$$

There must exist a separation constant, s_z such that

$$\frac{X''}{X} = s_z \tag{3.95}$$

$$\implies -(X'' - s_z X) = 0 \quad Z'' - s_z Z = 0 \tag{3.96}$$

There are three cases of s_z to consider. The case that allows for non-trivial solutions is the case where $s_z > 0$, define this constant to be $s_z = k^2$, $k \in \mathbb{R}$. In this case, and for the results in this section k is taken to become the spatial wavenumber. Substituting these gives:

$$Z'' - k^2 Z = 0, \tag{3.97}$$

$$\implies Z = A\mathrm{e}^{kz} + B\mathrm{e}^{-kz}. \tag{3.98}$$

Enforcing Equation (3.90) yields

$$\left.\frac{\partial \phi}{\partial z}\right|_{z=-h} = 0, \tag{3.99}$$

$$\implies Z'(-h) = 0, \tag{3.100}$$

$$\implies A\mathrm{e}^{kh} = B\mathrm{e}^{-kh}. \tag{3.101}$$

Where A, B are unknown constants. With some manipulation, one finds

$$Z = D\cosh(k(z+h)), \tag{3.102}$$

Where D is an unknown constant. The assumption of plane wave in the x-direction propagation gives

$$X = E\cos(kx + \psi) \tag{3.103}$$

This can be trivially checked that this is a valid assumption. So we have derived, assuming temporal harmonic motion in the x direction given by d'Alembert $f(x-ct)$ [150]:

$$\phi(x, y, t) = F\cos(k(x - ct) + \psi)\cosh(k(z+h)) \tag{3.104}$$

Where $F = DE$. Now, consider the boundary condition at the free-surface $z = 0$ from Equation (3.91)

$$\Big[\frac{\partial^2\phi}{\partial t^2} + g\frac{\partial\phi}{\partial z}\Big]_{z=0} = 0 \tag{3.105}$$

This boundary condition should yield the specific relationship between frequency and wavenumber and therefore the dispersion relation. Substituting in the values gives

$$F\cos(k(ct)[-c^2k^2\cosh(k(z+h)) + gk\sinh(k(z+h)))]_{z=0} = 0 \tag{3.106}$$

$$\implies -c^2k^2\cosh(kh) + gk\sinh(kh) = 0 \tag{3.107}$$

$$\implies c^2 = \frac{g}{k}\tanh(kh) \tag{3.108}$$

Using $c^2 = \frac{\omega^2}{k^2}$ one obtains a relationship between the angular frequency and the wavenumber.

$$\omega^2 = gk\tanh(kh) \tag{3.109}$$

This is known as a dispersion relation between ω and k and determines that the frequency of generated waves is gathered from the spatial wavelength of the waves. The free surface ζ (and the constant F) can be obtained from calculating [151][149]

$$\zeta = \Big[-\frac{1}{g}\frac{\partial\phi}{\partial t}\Big]_{z=0} \tag{3.110}$$

The simple dispersion relation due to gravity waves as shown in Lamb [151] and Stoker [149] has been derived. Having knowledge of the dispersion relation i.e. the relationship between frequency and wavenumber is of great importance when it comes to the analysis used later. This is because of the link between the harmonics present in Equations (3.104) and (3.110) and analysis methods, such as the application of the Fourier transform. This avoids the need for a full reconstruction based on numerically calculating the above equation. This is favorable as when boundary conditions such as the bed roughness becomes complex, the time taken to simulate is large. The only thing that is needed to synthetically generate surfaces that obey the dispersion relation, is the dispersion relation alone. The following dispersion relations are provided as cited results, without derivation and are used throughout the thesis.

If the mean speed of the flow is faster than pattern deformations, the fluctuations in time at a fixed point is primarily due to advection. The advectice dispersion relation is [2]:

$$\Omega_A(\mathbf{k}, \mathbf{U_0}) \approx \mathbf{k}\mathbf{U_0}. \tag{3.111}$$

Where $\mathbf{k} = (k_x, k_y)$ is the spatial wavenumber in the x and y dimension, and $\mathbf{U_0}$ is the surface velocity vector. The dispersion relation with surface tension due to gravity-capillary waves can be approximated as

$$\Omega_{GW}(\mathbf{k}, \mathbf{U_0}) \approx \Omega_A(\mathbf{k}, \mathbf{U_0}) \pm \sqrt{\left(g + \frac{\gamma}{\rho}k^2\right) k \tanh(kd)} \tag{3.112}$$

Where $g \approx 9.81 m/s$ is acceleration due to gravity, γ is the surface tension of water and air, ρ is the density of water, and d is the depth. This is the form of the gravity waves presented in Equation (3.109), but with terms representing the surface tension. Note that this equation contains the addition of the advection dispersion curve. This is due to the Doppler effect that occurs when there is a dispersion curve present with constant moving flow [152].

These two dispersion relations are mainly affected by the average surface velocity $\mathbf{U_0}$ and the depth of the flow d. However, the dispersion curve is substantially more sensitive to the velocity in comparison to the depth, as can be shown by taking the derivative:

$$\frac{\partial \Omega_{GW}}{\partial U_0} = k \tag{3.113}$$

$$\frac{\partial \Omega_{GW}}{\partial d} = \frac{(g + \frac{\gamma}{\rho}k^2)k^2(1 - \tanh(kd)^2)}{2\sqrt{(g + \frac{\gamma}{\rho}k^2)k \tanh(kd)}}. \tag{3.114}$$

Sensitivity analysis of the parameters are presented in Figures 8.1 and 8.2. Realisations of moving surfaces that exhibit the dispersion relations discussed were created.

Surfaces can now be created from the dispersion curves showcased earlier, and are created with the velocity and the depth as input, and after the reconstruction in space from the wavenumber domain. The surface elevation function that determines the surface state in space and time based on the advective, and gravity-capillary dispersion relations can be defined as

$$\Upsilon = \mathscr{F}_k^{-1}(\mathscr{C}_1 A(k) \mathrm{e}^{-\mathrm{i}\Omega_A(\mathbf{k},\mathbf{U_0})t}) + \mathscr{F}_k^{-1}(\mathscr{C}_2 A(k) \mathrm{e}^{-\mathrm{i}\Omega^+_{GW}(\mathbf{k},\mathbf{U_0})t}) + \mathscr{F}_k^{-1}(\mathscr{C}_3 A(k) \mathrm{e}^{-\mathrm{i}\Omega^-_{GW}(\mathbf{k},\mathbf{U_0})t}) \tag{3.115}$$

$$\zeta(x,t) = \delta \frac{\Upsilon}{std(\Upsilon)} \tag{3.116}$$

Where $A(k) = k^{\frac{-\beta}{2}}$ represents the surface spectrum slope decay for increasing k, $\mathscr{F}_k^{-1}$ is the inverse Fourier transform in the spatial dimension, std is the standard deviation, $\mathscr{C}_1, \mathscr{C}_2, \mathscr{C}_3$ are complex random numbers generated from Gaussian distributions in both the real and imaginary components, and δ is the amplitude scaling factor that determines the root mean square (rms) height of the overall rough surface. Surfaces that are created according to Equation (3.116) have a frequency-wavenumber spectrum that contains the three dispersion curves, this can be seen in Figure 3.17.

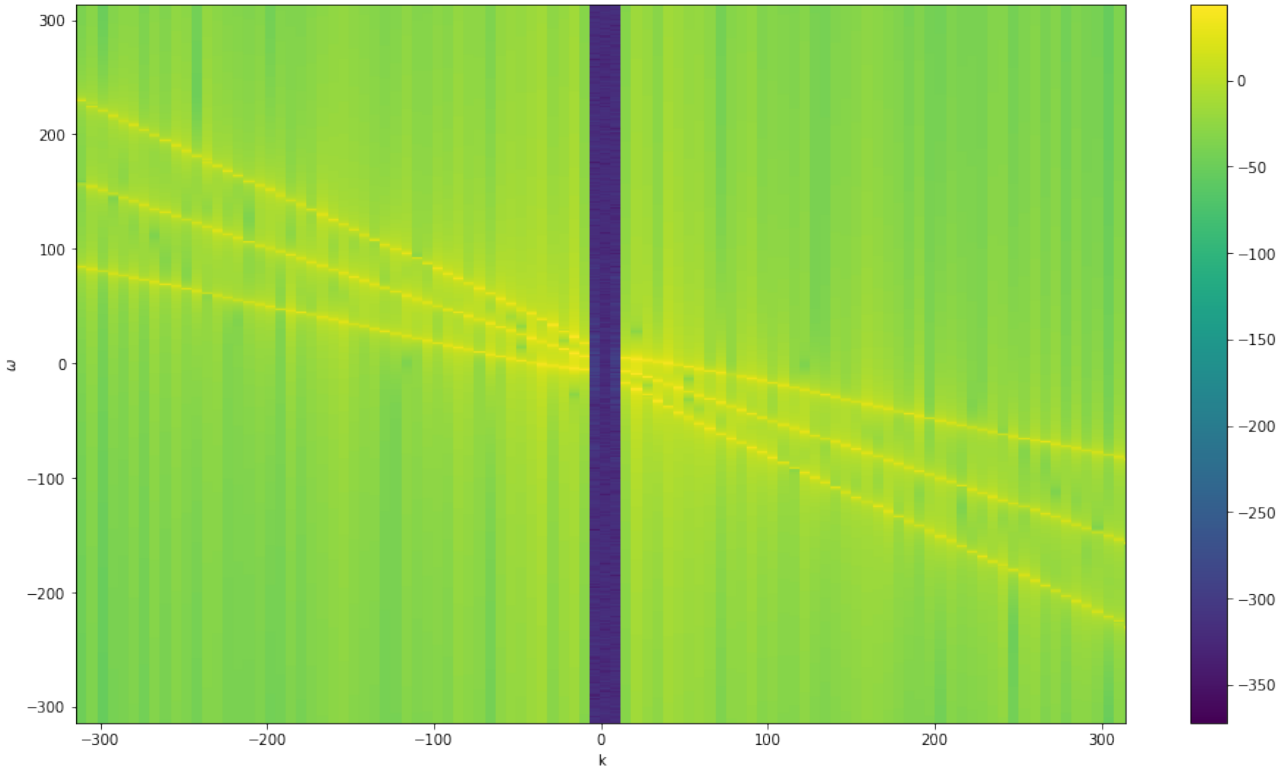

Figure 3.17: Absolute value $10\log_{10}$ frequency-wavenumber from a surface generated using Equation (3.116) for: depth = 0.4, velocity = 0.5, $\beta = 2$, temporal sample rate = 200, spatial sample rate = 1000

3.5 Machine Learning

This work aims to solve the inverse problem with data-driven approaches. Firstly, classical machine learning algorithms were tested. Random Forests, K-Nearest

Neighbors and Linear Regression were evaluated for this problem. Neural Network based architectures were avoided in this work due to the vast amount of hyperparameter tuning, as well as architecture tuning. It was concluded that the hyperparameters would need to be tuned for different surface problems, that is to say, the optimal hyperparameters for a three parameter harmonic surface (e.g. amplitude, wavelength and phase) could be different to the hyperparameters for a forty-parameter surface (e.g. a sum of sine waves where amplitude and phase can vary). Therefore, models that have fewer parameters were favoured.

This section contains some relevant theory and derivations for Random Forests, K-Nearest Neighbors, and Linear Regression. The application of which are seen in chapters 4, and 5.

3.5.1 Random forests

Random forests are a classification and regression model where the model predictions are formed from an average of multiple decision trees. A decision tree is a supervised machine learning model in which the resulting model is a tree-like structure, where queries on the data define the branches and predictions define the leaves. As the values of parameters in this study are real numbers, regression random forests are used. The composition of decision trees are discussed significantly by Breiman *et al.* [153].

3.5.1.1 Decision tree

Suppose a dataset $D = (\mathbf{\Omega}, \mathbf{Z})$, where $\mathbf{\Omega} = (\omega_{lj}) \in \mathbb{R}^{N_D \times M}$ and $\mathbf{Z} = (\zeta_{lj}) \in \mathbb{R}^{N_D \times N}$, are the matrices of input and output values, respectively with M the number of receivers and N the number of outputs to recover, and N_D denotes the number of samples in a dataset, with $l = 1..N_D$. Next, define a splitting criterion (j, S) where j is a column in $\mathbf{\Omega}$ and S is some value defined on an interval $[\min(\mathbf{\Omega}), \max(\mathbf{\Omega})]$.

A binary partition of D forms two datasets $D_1(j, S)$ and $D_2(j, S)$ via the following form,

$$D_1(j, S) = \left\{(\mathbf{\Omega}, \mathbf{Z}) | \omega_{lj} \leq S,\, l = 1..N_D,\, j = 1..M\right\}, \tag{3.117}$$

$$D_2(j, S) = D \setminus D_1(j, S). \tag{3.118}$$

Where $\setminus$ is the set minus operator. To find the best splitting criteria in the case of $\mathbf{Z}$ having one output (i.e. $i = 1$), one must minimise the following equation [154],

modified with weights:

$$\min_{(j,S)} \left[\frac{N_{D_1}}{N_D} \sum_{D_1} (\zeta_l - \bar{\zeta}_{D_1})^2 + \frac{N_{D_2}}{N_D} \sum_{D_2} (\zeta_l - \bar{\zeta}_{D_2})^2 \right], \tag{3.119}$$

where $\bar{\zeta}_D$ is an average of all outputs for a dataset. This process is then repeated recursively on D_1 and D_2 until the nodes are "pure", i.e. for an ideal case

$$\sum_{\omega_{lj} \in D_{\text{leaf}}} (\zeta_l - \bar{\zeta}_{D_{\text{leaf}}})^2 = 0 \tag{3.120}$$

for some partition D_{leaf}, or another stopping criterion is reached. The final partitions are names leaves and are the contributing factor for prediction. The decision tree's prediction at a leaf node will be the mean of all the outputs in that leaf node. In reality, for regression implementations a value of zero will never be obtained so other stopping criteria to make a leaf must be considered, such as the sum of squared errors becoming lower than a threshold or defining a minimal amount of elements (no less than 2) required to be in a sub-dataset.

This splitting is then done recursively by using Equations (3.117) and (3.118), until the tree is fully formed. Common algorithms to generate the decision trees include the Iterative Dichotomiser (ID) algorithm [155], and the Classification and Regression Trees algorithm (CART) [153]. The thesis uses the algorithm provided in scikit-learn [50].

Due to the nature of the decision tree algorithm, decision trees tend to overfit any given training data. Random forests attempt to solve this issue (seen in [47, 156]) where the overfitting issue is tackled through incorporating randomness. The fundamental approach a random forest takes is to produce many decisions trees, each individually trained on a random subset on the given dataset. Each tree is then used to make predictions, and the average behaviour of all trees in the forest are taken into account for the final prediction. A simple case of this is simply taking the mean value of all the decision tree's predictions. Comparisons of the performance over decision trees have been studied previously, i.e. [156] where in classification, random forests yielded an improved performance in 17 out of 20 datasets tested for the same amount of attributes over decision trees.

The random forests in this thesis were created using the Python library scikit-learn. [50]

3.5.2 K-Nearest Neighbors

This section contains a short mathematical explaination of the model. For more information, see [157]. Suppose that the problem is mapping a collection of D dimensional inputs which are associated to some output value. To compare a test input $\boldsymbol{x}_{test}$ to the collection a distance metric $d : \Gamma x \Gamma \to \mathbb{R}$, where Γ is any set, needs to be defined. If the collection of inputs are real valued, which is the case for the inverse scattering problem, the metric space can be seen as $(\mathbb{R}^D, d)$. An example metric could be the Euclidean distance. That is to say,

$$d(\boldsymbol{x}, \boldsymbol{y}) = \sqrt{(y_1 - x_1)^2 + (y_2 - x_2)^2 + \cdots + (y_d - x_d)^2}. \tag{3.121}$$

In reality, because this can be seen as a metric space, the only restrictions on the choice of d are as follows $\forall \boldsymbol{x}, \boldsymbol{y}, \boldsymbol{z} \in \Gamma$:

The distance from a point to itself is 0

$$d(\boldsymbol{x}, \boldsymbol{x}) = 0. \tag{3.122}$$

The distance is symmetric

$$d(\boldsymbol{x}, \boldsymbol{y}) = d(\boldsymbol{y}, \boldsymbol{x}). \tag{3.123}$$

The distance is positive if $\boldsymbol{x} \neq \boldsymbol{y}$

$$d(\boldsymbol{x}, \boldsymbol{y}) > 0. \tag{3.124}$$

The triangle inequality holds

$$d(\boldsymbol{x}, \boldsymbol{z}) \leq d(\boldsymbol{x}, \boldsymbol{y}) + d(\boldsymbol{y}, \boldsymbol{z}). \tag{3.125}$$

If these are true, then d is said to be a metric of Γ.

Once a metric is defined, the prediction of output y_{test} from the new test sample $\boldsymbol{x}_{test}$ is the following. Firstly, calculate all the distances $\boldsymbol{d}$ where $d_i = d(\boldsymbol{x}_i, \boldsymbol{x}_{test})$. Then find the shortest k distances (the value of k is user-provided). Once the results are found, the prediction is either a uniform average of the results, or a weighted average found from the inverse of the resultant distances.

3.5.3 Linear Regression

The aim is to fit the best straight line to a collection of data with inputs

$$\boldsymbol{X} = [x_0, x_1, \ldots, x_n]^T \tag{3.126}$$

$$\boldsymbol{Y} = [y_0, y_1, \ldots, y_n]^T. \tag{3.127}$$

In matrix form, linear regression can be seen as

$$\begin{pmatrix} y_1 \\ y_2 \\ \vdots \\ y_n \end{pmatrix} = \begin{pmatrix} 1 & x_1 \\ 1 & x_2 \\ & \vdots \\ 1 & x_n \end{pmatrix} \begin{pmatrix} \beta_0 \\ \beta_1 \end{pmatrix} + \begin{pmatrix} \epsilon_1 \\ \epsilon_2 \\ \vdots \\ \epsilon_n \end{pmatrix} \tag{3.128}$$

Where β_0, β_1 are constant coefficients which dictate the translation and gradient of the line, and $\epsilon_1, ..., \epsilon_n$ are the associated error values for a given combination of β_0, β_1. The problem is to choose the optimal value for β. This is found as [158]:

$$\hat{\boldsymbol{\beta}} = (\boldsymbol{X}^T\boldsymbol{X})^{-1}\boldsymbol{X}^T\boldsymbol{Y} \tag{3.129}$$

With estimation of error given as

$$\hat{\boldsymbol{\epsilon}} = \boldsymbol{Y} - \boldsymbol{X}(\boldsymbol{X}^T\boldsymbol{X})^{-1}\boldsymbol{X}^T\boldsymbol{Y} \tag{3.130}$$

3.6 Markov Chains Monte Carlo, Metropolis Hastings, Stochastic Approach

We take a brief tangent to present the ideas of Markov Chain Monte Carlo. Explicitly this is defined by the following definition

Definition 1 *[159] A Markov chain Monte Carlo (MCMC) method for the simulation of a distribution f is any method producing an ergodic Markov Chain (X^t) whose stationary distribution is f*

It is now pertinent to define precisely what a Markov-Chain is. This is defined in the sense of measure theory in order to rigorously define a transition kernel. Once this is defined, a lot of the formality will be loosened in order to present a more example-based approach.

Definition 2 *[160] A non-empty collection $\mathscr{E}$ of subsets of E is called an algebra on E provided that it is closed under finite unions and compliments, it is called a σ-algebra on E if it is closed under complements and countable unions.*

$$A \in \mathscr{E} \Rightarrow E - A \in \mathscr{E} \tag{3.131}$$

$$A_1, A_2, \ldots \in \mathscr{E} \Rightarrow \bigcup_n A_n \in \mathscr{E} \tag{3.132}$$

Definition 3 *[160] Let $(E, \mathscr{E})$ be a measurable space. A measure on $(E, \mathscr{E})$ is a mapping $\mu : \mathscr{E} \to [0, +\infty]$ such that*

- $\mu(\emptyset) = 0$,
- $\mu(\bigcup_n A_n) = \sum_n \mu(A_n)$ *for every disjointed sequence* $(A_n) \in \mathscr{E}$.

Therefore, a measure space is defined as a triplet $(E, \mathscr{E}, \mu)$ where $(E, \mathscr{E})$ is a measurable space and μ is a measure on this space.

Definition 4 *[160] Let $(E, \mathscr{E})$ and $(F, \mathscr{F})$ be measurable spaces. A mapping $\iota : E \to F$ is said to be measurable relative to $\mathscr{E}$ and $\mathscr{F}$ if $\iota^{-1}B \in \mathscr{E}$ for every B in $\mathscr{F}$.*

Definition 5 *[160] A numerical function on E is a mapping from E to $[-\infty, \infty]$. If this function is measurable relative to $\mathscr{E}$ and the Borel σ-algebra on $[-\infty, \infty]$ then it is said to be $\mathscr{E}$-measurable.*

Definition 6 *[160] A measurable space is a pair $(E, \mathscr{E})$ where E is a set, and $\mathscr{E}$ is a σ-algebra on E.*

Definition 7 *[160] Let $(E, \mathscr{E})$ and $(F, \mathscr{F})$ be measurable spaces. Let K be a mapping from $E \times \mathscr{F}$ into $[0, +\infty]$. Then, K is called a transition kernel from $(E, \mathscr{E})$ to $(F, \mathscr{F})$ if*

- *the mapping $x \to K(x, B)$ is $\mathscr{E}$-measurable for every set $B \in \mathscr{F}$*
- *the mapping $B \to K(x, B)$ is a measure on $(F, \mathscr{F})$ for every $x \in E$.*

Essentially, a transmission kernel allows for a probability measure to be formed from any element x which is in the set E on the measurable space $(F, \mathscr{F})$. Thinking about $K(x, B)$, this is allowing for a probability to be assigned when considering the move from state x to some state in the set B. We will assume throughout that $E = F, \mathscr{E} = \mathscr{F}$. This is because in this work, Markov chains are used to assign the probability of exploring the current state space.

Definition 8 *[159] Given a transition kernel K, a sequence $X_0, X_1, ..., X_n, \ldots$ of random variables is a Markov chain (X_n) if, for any t, the conditional distribution of X_t given $x_{t-1}, x_{t-2}, \ldots, x_0$ is the same as the distribution of X_t given x_{t-1}*

$$P(X_{t+1} \in A | x_0, x_1, \ldots, x_t) = P(X_{t+1} \in A | x_t) \tag{3.133}$$

Therefore, the main idea from the definition of a Markov chain is that the probability from moving to the next state, is only dependent on the current state. The history does not matter. Further, a Markov chain is time homogeneous if

$$P(X_{n+1} = j | X_n = i) = P(X_1 = j | X_0 = i) \tag{3.134}$$

holds, that is to say, that the transition kernel does not change in time.

Consider the following two examples. Firstly, a two-state problem. As the number of states is discrete, the transition kernel reduces to a transition matrix T with elements

$$P_{xy} = P(X_n = y | X_{n-1} = x) \tag{3.135}$$

For example, consider a set $E = 1, 2$ and $\mathscr{E} = \mathscr{P}(E) = \{\emptyset, \{1\}, \{2\}, \{1, 2\}\}$ the power set of E. A kernel that exhibits the Markovian nature described above is formed from the probability it assigns to the singletons $\{s\}, s \in E$. Defining a kernel that allows for the probability of moving from state 1 to itself as $P_{11} = 0.5$ and to state 2 as $P_{12} = 0.5$, and the probability of moving from state 2 to itself as $P_{22} = 0.5$ and to state 1 as $P_{21} = 0.5$ the following transition matrix can be formed

$$T = \begin{pmatrix} P_{11} & P_{12} \\ P_{21} & P_{22} \end{pmatrix} \tag{3.136}$$

$$T = \begin{pmatrix} 0.5 & 0.5 \\ 0.5 & 0.5 \end{pmatrix}. \tag{3.137}$$

Note that the probabilities P_{ij} were only defined as the probability of going to the next state j, from the current state i.

A state space diagram for this transition matrix can be drawn, as in Figure 3.18.

Next, consider the following random walk

$$x_0 = 0 \tag{3.138}$$

$$x_i = x_{i-1} + \mathscr{N}(0, \sigma), \quad i = 1, 2, \cdots \tag{3.139}$$

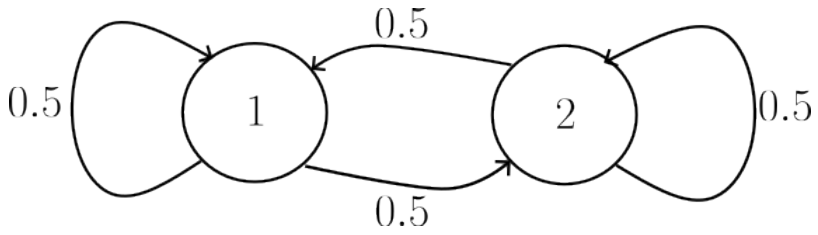

Figure 3.18: State space diagram for the transition matrix given in Equation 3.137.

Where $\mathcal{N}(0,\sigma)$ is a draw from a normal distribution of mean value 0 and standard deviation σ. The collection of these form a Markov Chain with probabilities

$$P(x_{n+1}|x_0,x_1,\ldots,x_n) = P(x_{n+1}|x_n) = \mathcal{N}(x_n,\sigma). \tag{3.140}$$

This is illustrated in Figure 3.19

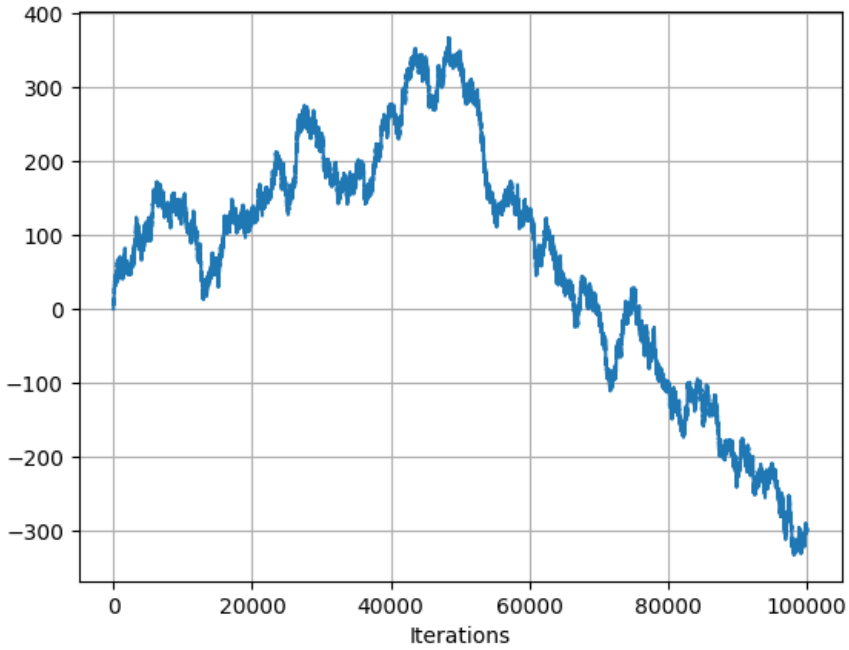

Figure 3.19: Gaussian random walk with initial value $x_0 = 0$ with standard deviation 1. The y axis represents the value.

Definition 9 *[161] An irreducible positive recurrent Markov chain is an ergodic Markov chain.*

Where recurrent means that the probability that going from a state i and never returning to this state is zero.

Definition 10 *[162] A Markov chain with transition kernel K satisfies the detailed balance condition if there exists a function p satisfying*

$$K(y,x)f(y) = K(x,y)f(x) \quad \forall(x,y) \tag{3.141}$$

More-or-less, this definition states that the probability to move from x to y is the same as the probability for moving from y to x, therefore the Markov Chain is said to be reversible. If the Markov Chain is irreducible, then f is a unique stationary distribution [163]. The required definitions are now in place.

3.6.1 Metropolis-Hastings

Suppose one is aiming to sample from a probability distribution $p(x)$ and suppose this cannot be evaluated. Assume that a probability distribution $f(x)$ can be calculated, and has the relation

$$p(x) = \frac{f(x)}{Z}. \tag{3.142}$$

Where Z is some constant. Recalling Definition 1, a MCMC method is any method to simulate a distribution f that produces an ergodic Markov chain, with stationary distribution p. Beginning with the detailed balance definition

$$K(y,x)p(y) = K(x,y)p(x) \tag{3.143}$$

The transition kernel is separated into two components, a proposal distribution $q(x,y)$ and an acceptance distribution $\alpha(x,y)$ which define the probability of moving from a state x to a state y, and the probability of this new state change being accepted. Substituting these values into Equation (3.143)

$$q(y,x)\alpha(y,x)p(y) = q(x,y)\alpha(x,y)p(x) \tag{3.144}$$

$$\Rightarrow \frac{\alpha(x,y)}{\alpha(y,x)} = \frac{p(y)q(y,x)}{p(x)q(x,y)} \tag{3.145}$$

$$\Rightarrow \frac{\alpha(x,y)}{\alpha(y,x)} = \frac{f(y)q(y,x)}{f(x)q(x,y)} \tag{3.146}$$

To find the relation for $\alpha(x,y)$, the cases of

$$q(y,x)\alpha(y,x)f(y) > q(x,y)\alpha(x,y)f(x) \tag{3.147}$$

and

$$q(y,x)\alpha(y,x)f(y) < q(x,y)\alpha(x,y)f(x) \tag{3.148}$$

need to be evaluated. Using this, and setting the corresponding $\alpha(\cdot,\cdot)$ in the greater than side to be 1 (as α is a probability distribution), the following relation can be found [162]:

$$\alpha(x,y) = Min\left(1, \frac{f(y)q(y,x)}{f(x)q(x,y)}\right) \tag{3.149}$$

If $q(x,y) = q(y,x)$ the proposal distribution is said to be symmetric, and the methodology is called Metropolis Scheme. A table representing the Algorithm is provided in Table 1.

Algorithm 1 Metropolis-Hastings Algorithm

```
Initialise x_0
for i = 0, ..., N − 1 do
    Sample u ∼ U(0, 1)
    Sample y ∼ q(y | x_i)
    x = x_i
    if u ≤ α then
        x_{i+1} = y                          ▷ Accept sample.
    else
        x_{i+1} = x                          ▷ Reject sample.
    end if
end for
```

This approach produces a Markov Chain [159]. Therefore, from any given input x_0 this Markov Chain will eventually reach the stationary distribution p, which is exactly the distribution that is aiming to be inferred.

3.6.2 Stochastic Approach

Consider a set of data collected from acoustic scattering from an infinite rough surface. This can be thought of as data generated from the simulation under a set of parameters θ such that

$$\boldsymbol{p} = [\psi_s(R_i|\theta)]_{i=1,..,n} + \epsilon \tag{3.150}$$

Where $\boldsymbol{p}$ represents the experimental array of scattered acoustic pressure.

$[\psi_s(R_i|\theta)]_{i=1,..,n}$ is an extension of Equation (3.85) where each R_i refers to a location R in Equation (3.85), centred at the location of a receiver, the θ term has

been included here indicating that some set of parameters θ will be able to be varied, in order to change the underlying surface ζ in Equation 3.85.

The question then becomes, how to find θ. From Bayes' rule, the posterior of θ can be found as proportional to

$$\mathscr{P}(\theta|\mathbf{p}) \propto \mathscr{P}(\mathbf{p}|\theta)\mathscr{P}(\theta). \tag{3.151}$$

Where $\mathscr{P}(\mathbf{p}|\theta)$ is the likelihood of the data being generated by a set of parameters θ and is called the likelihood function, and $\mathscr{P}(\theta)$ contains prior knowledge of the distribution of parameters θ called the prior distribution. It can immediately be seen that this proportional form can be immediately applied under the Metropolis Hastings framework. The algorithm used in this work is called the Adaptive Metropolis (AM) scheme, and is found in [113]. The main change in this reference is the manipulation of the proposal distribution. The main definition of the proposal distribution is a Gaussian distribution centred at a current state with an adaptive covariance matrix. To compute the covariance matrix at some step t, An index $t_0 > 0$ is selected, and the covariance matrix is formed by [164]:

$$C_t = \begin{cases} C_0, & t \leq t_0 \\ s_d cov(X_0, ..., X_{t-1}) + s_d \epsilon I_d, & t > t_0 \end{cases} . \tag{3.152}$$

Here, C_t is the covariance matrix at the time t, X_t is the state of the model at a time t, I_d is a d-dimensional identity matrix, $s_d = (2.4)^2/d$, $\epsilon > 0$ a small number. It can be seen that this covariance matrix is not Markovian, as the entire history need be considered. However, Haario et. al proved that the ergodic properties are sufficiently satisfied to be a valid proposal distribution [164].

As an example, consider some data $\boldsymbol{D} = [\boldsymbol{X}]_{i=0,...,n}$was generated from a two-dimensional Gaussian distribution

$$\boldsymbol{X} \sim \mathscr{N}_2(\boldsymbol{\mu}, \boldsymbol{\Sigma}) \tag{3.153}$$

with $\boldsymbol{\mu} = [\mu_1, \mu_2]^T$ and $\boldsymbol{\Sigma}$ is a covariance matrix where terms can be calculated as in [165]. Suppose that the data was generated from $\mu_1 = 0.5, \mu_2 = 0.5$. For this example, assume that the covariance matrix is known (this does not have to be true in general). Then Metropolis-Hastings can be used to infer the posterior of the parameters $\boldsymbol{\theta} = [\mu_1, \mu_2]$ with respect to the data. Figure 3.20 presents the results from using the Metropolis-Hastings scheme to find the value of $\boldsymbol{\mu}$. The plot showcases a contour plot of the density of the distribution that generated the data.

Then there is a line moving through $x = \mu_1, y = \mu_2$ starting at $[-1,-1]$. Very quickly, this line, made up from "traces" of values sampled from the Metropolis-Hastings scheme, moves towards the centre of the contour distribution and then, as it enters the stationary distribution, stays there. The line going to the stationary distribution is called the "burn in" period and is discarded in analysis.

The code used throughout the later chapters was developed by the author and can be found at https://github.com/michaeldavidjohnson/MetropolisHastings

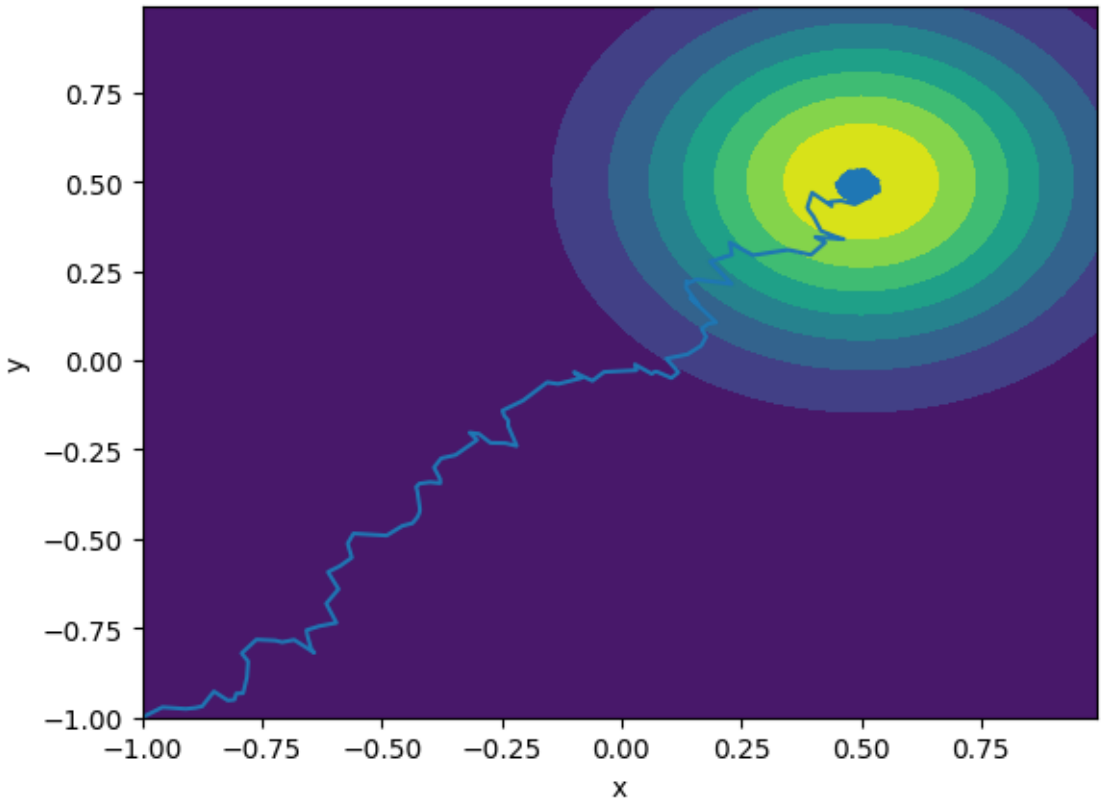

Figure 3.20: Overlay of the traces against the true density that made up some experimental data.

Chapter 4

Surface shape reconstruction from phaseless scattered acoustic data using a random forest algorithm

Reference

Johnson, M. D., Krynkin, A., Dolcetti, G., Alkmim, M., Cuenca, J., and De Ryck, L. (2022). Surface shape reconstruction from phaseless scattered acoustic data using a random forest algorithm. The Journal of the Acoustical Society of America, 152(2), 1045-1057.

Author Contributions

- Johnson, M.D., - Writing, model development, data analysis, editing, structure.
- Krynkin, A. - Figure editing, editing.
- Dolcetti, G. - Data collection, editing.
- Alkmim, M. - Data collection, editing.
- Cuenca, J. - Data collection, editing.
- De Ryck, L. - Data collection, editing.

Summary

This paper investigated the validity in using Machine Learning (specifically Random Forests) in order to solve the inverse problem of scattering from an infinite rough surface. Without using Machine Learning, this is a nonlinear problem unless some assumptions are made, such as the Bojarski Identity [59] which is a linearisation assuming that all wavenumbers are known. Because of the further approximations on the wavenumber all the wavenumbers cannot be recovered, and thus the problem is ill posed. Iterative methods can be applied, or a further approximation can be made to be able to perform a matrix inversion [66] [74]. In order to avoid these extra assumptions, a Random Forest model was fit to synthetic realisations of different single harmonic sine waves. This was also tested and trained on different proportions of noise in the data to be able to test for robustness.

The performance of the Random Forest approach was tested in three different ways. Firstly, the coefficient of determination was used to test the model performance in the recovery of each parameter under each noise condition for all data. To show further generalisability of this approach different incident angles from 20 degrees to 90 degrees were tested from 50Hz to 45,000Hz. These results were analysed to find how the performance varied with angle, given a fixed receiver layout.

Further to this, synthetic data was used as a dataset, and the error of the random forest prediction was tested against the Short Array method presented in [74]. What was found here is that both models perform well until the ratio of the surface amplitude to the acoustic wavelength rose above 0.1. In this case, the random forest still performs well, but the Short Array method's performance severely decreases. This is due to the breakdown of the linearisation, the amplitude is no longer significantly smaller than the wavelength, so the approximation breaks down. This highlights the applicability for Random Forests to be able to perform in a nonlinear inverse environment.

Further metrics were presented such as a heatmap of the true parameters against the predicted parameters, this was an illuminating figure as it quantified directly how much data was in the outlier region. Overwhelmingly, the data followed the predicted = true line, and this over many surface iterations highlighted the accuracy of the model.

To finish, an experimental sample was produced from laboratory experiments, and the random forest predicted this well over a large number of noise conditions. This was also with the underlying Kirchhoff Approximation code that generated

the synthetic data, was in 2D with an approximate directivity pattern. This further highlighted the validity of this approach.

4.1 Abstract

Recent studies have demonstrated that acoustic waves can be used to reconstruct the roughness profile of a rigid scattering surface. In particular, the use of multiple microphones placed above a rough surface as well as an analytical model based on the linearised Kirchhoff integral equations provide a sufficient base for the inversion algorithm to estimate surface geometrical properties. Prone to fail in the presence of high noise and measurement uncertainties, the analytical approach may not always be suitable in analysing measured scattered acoustic pressure. With the aim to improve the robustness of the surface reconstruction algorithms, here it is proposed to use a data-driven approach through the application of a random forest regression algorithm in order to reconstruct specific parameters of one-dimensional sinusoidal surfaces from airborne acoustic phase-removed pressure data. The data for the training set is synthetically generated through the application of the Kirchhoff integral in predicting scattered sound, and it is further verified with data produced from laboratory measurements. The surface parameters from the measurement sample were found to be recovered accurately for various receiver combinations and with a wide range of noise levels ranging from 0.1% to 30% of the average scattered acoustical pressure amplitude.

4.2 Introduction

Inverse acoustic scattering is concerned with the recovery of information about an object or a surface based on scattered acoustic data collected using sound sources and receivers. It has applications in fields such as non-intrusive damage testing as well as surface recovery.

A numerical method based on the boundary integral equations and Kirchhoff approximation to reconstruct the shape of a scattering surface was recently outlined[67, 68]. This approach was found to be highly sensitive to uncertainties, partly because of the strong dependence on the phase of the scattered signal [74]. The errors in the inversion results were associated with the underdetermined and ill-posed nature of the problem [74]. The range of applicability in reconstructing a surface is

also limited by the validity of a partial linearisation of the scattering problem, which is required in order to make the numerical inversion feasible.

Another recent approach includes recovering a rough surface at grazing angles using single-frequency, phaseless acoustic pressure through the use of an iterative marching method approach derived from the parabolic wave approximation (forward-scattered wave propagation assumption) [77]. Although the inversion results are found to be relatively accurate, it is assumed that the forward-scattered approach is not applicable in the context of this paper research due to significant differences in the assumptions and experimental setup and, in particular, acoustic remote sensing applications where the sound field is best described by a solution of the full Helmholtz equation [74].

Recent work [74] solved the reconstruction problem using matrix inversion, where the forward model of scattered acoustic pressure was linearised resulting in the linear system of equations resolving the unknown profile of a rough surface. The use of an iterative approach such as machine learning is an appealing alternative to linearisation and as such is one of the central motivations of the present work.

As opposed to deterministic model-based inversion approaches, machine learning methods in wave scattering problems allow more flexibility. Machine learning and its applications in various fields of acoustics was discussed in detail by Bianco *et al.* [52]. It has been shown that a combination of random forest and neural networks results in a robust method enabling reconstruction of geometrical features against noise [92]. This was achieved by first classifying training shapes with a random forest and then inverting the far-field scattered signal using neural networks to obtain geometrical features of different scattering objects.

Fan *et al.* [88] successfully applied deep learning methodologies utilising the Helmholtz equation in the recovery of the shape and placement of multiple scatterers in two different settings, including a seismic imaging setting where the source and receivers were above the scatterers and receivers were in a linear array. The scatterers were placed randomly and formed from a number of shapes such as triangles, squares or ellipses. It was shown that for a large number of receivers and sources, the locations and orientations of the scatterers were successfully recovered with various amounts of noise in the dataset, while the recovered boundaries of the scatterers became blurred as the noise level increased.

Successful use of machine learning methodologies in acoustics was also demonstrated when identifying parameters such as the porosity and tortuosity of a porous

material with an acoustic signal perturbed by noise [166]. It was shown that "acceptable accuracy with wide variety of noise levels" [166] can be achieved in recovering material properties.

Other works that recovered the parameters of surfaces instead of the full surface include: recovering parameters of a sum of sine waves forming a rough surface [89], recovering coefficients of a parametric curve of an obstacle [90], and using a convolutional neural network to recover the root-mean-squared height and correlation length from a Gaussian rough surface through synthetic aperture radar [91]. The flexibility of data-driven approaches as compared to classical model inversion, in the presence of noise, stands as a central motivation of the present work.

The Kirchhoff Approximation is still an active part of reconstruction efforts as in [167], other methods have risen in inverse scattering especially in the near-field, such as recovering the far-field pattern given the near-field measurements [168] and obtaining the scattering coefficient from near-field measurements [169].

The choice to use phaseless data as input was driven mainly by the characteristics of the random forest approach, which cannot handle coupled complex data. In Dolcetti et al.[74] phase uncertainty was found to have a stronger impact than amplitude uncertainty on the accuracy of the surface reconstruction, and imperfect wrapping of the phase was found to cause a multi-modal distribution of the reconstruction error, especially at large roughness amplitudes (relative to the acoustic wavelength).

This work studies the feasibility of a machine learning approach to characterise a parametric rough rigid surface. Phaseless acoustical data were chosen due to the relatively simple amplitude only calibration technique compared to phase calibration, as well as to avoid the easily corruptible nature of phase measurements which are sensitive to uncertainties, such as uncertainties in position. Scattered phaseless acoustical pressure defined by a single frequency source excitation will be synthetically generated through an application of the Kirchhoff approximation. Specifically, the estimation of the wavelength, amplitude, and offset of a sinusoidal acoustically-rigid scattering surface is considered by means of a random forest algorithm trained on synthetic noisy data and tested on synthetic and experimental data.

The paper is organised in the following way: Section 4.3 presents the random forest model used for the estimation of the surface parameters. Section 4.4 contains relevant information regarding the methodology including the selection of the forward model as the Kirchhoff approximation, the incorporation of noise, the way in which data was split into training and testing sets, the experimental setup, and

the convergence of random forest as the number of trees increase. Section 4.5 contains the relevant results and evaluation of the performance of the testing set and experimental data set including a comparison between the method proposed in this paper and the Short Array method [67] and model performance in recovering unseen parameters. Section 4.6 contains the conclusions of the paper.

4.3 Random forest algorithm

The purpose of machine learning algorithms in this work is to allow the estimation of a parameter set that uniquely defines the shape of a sinusoidal surface using the modulus of the scattered acoustic pressure measured at a finite number of locations. Defining $\psi_s(\mathbf{R})$ as the acoustic pressure field at a point $\mathbf{R}$ produced by a source with co-ordinates (x_1, y_1), scattered by a sinusoidal rigid surface with profile

$$\zeta(x) = \zeta_1 \cos\left[\frac{2\pi}{\zeta_2}(x + \zeta_3)\right], \tag{4.1}$$

where the parameters ζ_i, $i = 1, 2, 3$ indicate the amplitude, wavelength, and offset of the sinusoidal surface, respectively. The signal was recorded at a set of M microphones with co-ordinates of the j-th microphone given by $\mathbf{R}^{(j)} = (x_2^{(j)}, y_2^{(j)})$, $j = 1, \ldots, M$, the aim is to estimate at least one of the parameters ζ_i, given $|\psi_s(\mathbf{R})|$. The general setup of sound scattering by a rough surface in Oxy plane is presented in Figure 4.1 where the source and receivers are located in the acoustic far-field above the surface.

The choice to reconstruct the parameter set instead of the surface shape at each location (as was done in, e.g., [67]) was made in order to limit the complexity of the problem and to develop a method applicable for surfaces of higher complexity, while still allowing a relatively compact parametric representation based on Fourier series, as are typical for example of water waves in some applications [170, 124].

Among the large number of existing machine learning approaches, here it was decided to employ a random forests approach for the recovery of the parameters of the surface. This is due to the simplicity of the model, the structure of a random forest is very strictly defined, giving less options to the user in its creation. This is different to a neural network approach, where the architecture needs to be carefully considered. It was also decided that not being able to extrapolate to parameters outside the range given by the training data would be a benefit for the problem investigated in this paper, to ensure the Kirchhoff condition is maintained. Random forests also benefit from not needing any input features to be scaled or

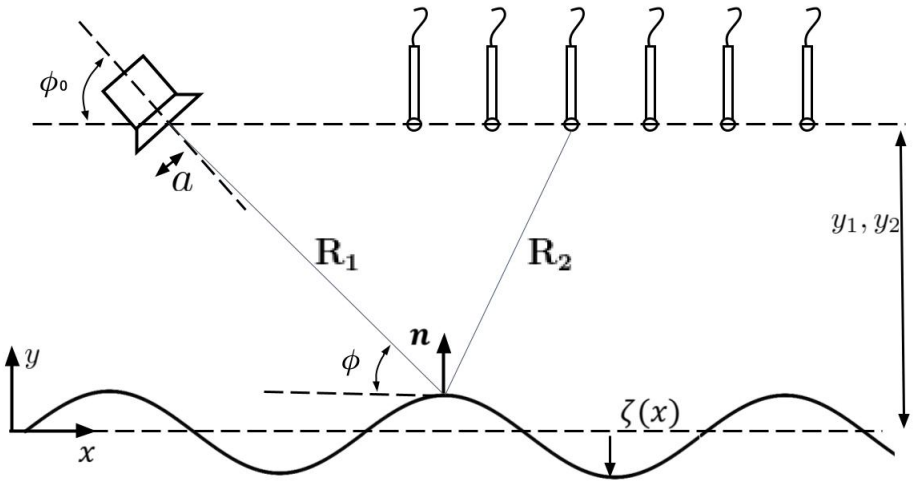

Figure 4.1: The geometry of the problem where the rough surface is defined by a function $\zeta(x)$ from equation (4.1). Surface is not to scale.

standardised while also being able to measure feature importance through the use of Gini importance, although this can be biased when "input variables vary in their scale of measurement of their number of categories". [171] Although, this is not investigated in this paper.

Random forests are a classification and regression model where the model predictions are formed from an average of multiple decision trees. A decision tree is a supervised machine learning model in which the resulting model is a tree-like structure, where queries on the data define the branches and predictions define the leaves. As the values of parameters in this study are real numbers, regression random forests are used. The composition of decision trees are discussed significantly by Breiman *et al.* [153]. However, a brief derivation based from Hastie *et al.* [154] is included in this paper.

4.3.1 Decision tree

Due to random forests being formed from many decision trees, it is important to have an understanding on how decision trees partition data to make predictions. Suppose a dataset $D = (\mathbf{\Omega}, \mathbf{Z})$, where $\mathbf{\Omega} = (\omega_{lj}) \in \mathbb{R}^{N_D \times M}$ and $\mathbf{Z} = (\zeta_{lj}) \in \mathbb{R}^{N_D \times N}$, are the matrices of input and output values, respectively with M the number of receivers and N the number of outputs to recover, and N_D denotes the number of samples in a dataset, with $l = 1..N_D$. Next, it is necessary to define a splitting

criterion (j,S) where j is a column in $\mathbf{\Omega}$ and S is some value defined on an interval $[\min(\mathbf{\Omega}), \max(\mathbf{\Omega})]$. It is noted that throughout the paper indices j, i and l are reserved for the columns in the input dataset (referred to as features and associated with the receiver location in the receiver array), for the columns in the output dataset (referred to as surface parameters) and for the rows in input/output datasets (referred to as samples) respectively.

Then, a binary partition of D forms two datasets $D_1(j,S)$ and $D_2(j,S)$ via the following form,

$$D_1(j,S) = \left\{(\mathbf{\Omega}, \mathbf{Z}) | \omega_{lj} \leq S,\, l = 1..N_D,\, j = 1..M\right\}, \tag{4.2}$$

$$D_2(j,S) = D \setminus D_1(j,S). \tag{4.3}$$

Where $\setminus$ is the set minus operator. To find the best splitting criteria in the case of $\mathbf{Z}$ having one output (i.e. $i = 1$), one must minimise the following equation [154], modified with weights:

$$\min_{(j,S)} \left[\frac{N_{D_1}}{N_D} \sum_{D_1} (\zeta_l - \bar{\zeta}_{D_1})^2 + \frac{N_{D_2}}{N_D} \sum_{D_2} (\zeta_l - \bar{\zeta}_{D_2})^2 \right], \tag{4.4}$$

where $\bar{\zeta}_D$ is an average of all outputs for a dataset. This process is then repeated recursively on D_1 and D_2 until the nodes are "pure", i.e. $\sum_{\omega_{lj} \in D_{\text{leaf}}} (\zeta_l - \bar{\zeta}_{D_{\text{leaf}}})^2 = 0$ for some partition D_{leaf}, or another stopping criterion is reached. The final partitions are called leaves and are where the predictions are measured from. The decision tree's prediction at a leaf node will be the mean of all the outputs in that leaf node. In reality, for regression implementations a value of zero will never be obtained so other stopping criteria to make a leaf must be considered, such as the sum of squared errors becoming lower than a threshold or defining a minimal amount of elements (no less than 2) required to be in a sub-dataset.

Essentially, decision trees recursively split a dataset into grouped subsets via equations (4.2) and (4.3) until the tree is fully formed. Common algorithms to generate the decision trees include the Iterative Dichotomiser (ID) algorithm [155], and the Classification and Regression Trees algorithm (CART) [153]. This paper uses a modified version of the CART algorithm contained in the Python package scikit-learn [50].

Due to the nature of the decision tree algorithm, decision trees tend to overfit the given training data. This can be improved with methods such as cost complexity pruning [154]. Another method to improve performance is through the application

of random forests [47, 156] where the overfitting issue is tackled through incorporating randomness. In this approach, a “forest" is made from many decision trees where each decision tree is individually trained on a random subset of the dataset, and the overall random forest prediction is an average of all the decision trees in the forest. Comparisons of the performance over decision trees have been studied previously, i.e. [156] where in classification, random forests yielded an improved performance in 17 out of 20 datasets tested for the same amount of attributes over decision trees. Random forests have also been used in regression problems, such as in [172] where random forests were compared against support vector machines and a partial least squares (PLS) method to identify heavy metal content in soil from hyperspectral modelling. Zhou *et al.* found that both support vector machines and random forests were “significantly better than that of PLS”[172], and random forests had an improved performance over support vector machines.

Classification often performs well in recovering from a discrete set of labels. For example, the amplitudes could be binned to [0.0-0.0005, 0.0005-0.001, 0.001-0.0015....] and the same can be adopted for the wavelength and offset. However, in order to increase the resolution of the predictions, the number of bins have to increase. Therefore, by tending the number of labels to infinity, regression appears to be the reasonable approach for the present work.

The random forests in this work were created using the Python library scikit-learn. [50]

4.4 Estimation of the surface parameters

As is very common with machine learning, large datasets must be produced to be applied in the training of the models in order to obtain useful results. For this paper, a dataset of the scattered wavefield is generated for the rigid surface given by Eq. (4.1) using the Kirchhoff approximation following [66]. This data was then used for the training of the random forest by using the scattered phase-removed acoustic pressure $|\psi_s(\mathbf{R})|$ as inputs to the random forest ($\mathbf{\Omega}$), and surface parameters as the output ($\mathbf{Z}$), effectively simulating an inverse problem. Finally, the trained learner was applied to two sets of test data (one synthetic and one experimental), to evaluate its performance.

4.4.1 Generation of synthetic data

The Kirchhoff approximation was chosen due to its explicit form, obtained through the approximation of a scattered signal via an assumption based on reflections from a tangent plane. This makes it suitable for the calculation of large amounts of data, which is required for training and testing the random forests, while being fast to compute (approximately 0.01 seconds for 34 receiver Kirchhoff simulations on an AMD Ryzen 9 3900X CPU with 32 GB RAM). The suitability of this approximation for the conditions analysed in this paper was presented in Krynkin *et al.* [67, 68].

Let the rough surface be defined by a function $\zeta(x)$ as shown in Equation (4.1) which satisfies the following condition [36]:

$$\sin(\phi) > \frac{1}{(kh)^{1/3}}, \tag{4.5}$$

where h is the radius of curvature of the surface, k is the acoustic wavenumber and ϕ is the incident angle of the acoustic wave. With the condition of Equation (4.5) satisfied, it is possible to use the Kirchhoff approximation to model reflections of an acoustic wave from a rough surface using a tangent plane approach. In 2D, for a source with a given directivity pattern, the scattered acoustic pressure ψ_s can be expressed in the following equation [68]:

$$\psi_s(\mathbf{R}) = \frac{1}{2k\pi \mathrm{i}} \int_{-\infty}^{\infty} \frac{A(x,0)}{\sqrt{R_1 R_2}} \mathrm{e}^{\mathrm{i}k(R_1+R_2)}(q_y - q_x\gamma)\mathrm{d}x, \tag{4.6}$$

where, as shown in Figure 4.1, the values R_1 and R_2 are the Euclidean distance from the source at (x_1, y_1) and receiver at (x_2, y_2) to a given point $(x, \zeta(x))$ on the surface, respectively:

$$R_1 = \sqrt{(x_1 - x)^2 + (y_1 - \zeta(x))^2}, \tag{4.7}$$

$$R_2 = \sqrt{(x_2 - x)^2 + (y_2 - \zeta(x))^2}. \tag{4.8}$$

In Equation (4.6), $\mathbf{R} = (x_2, y_2)$, $\gamma = \mathrm{d}\zeta(x)/\mathrm{d}x$; q_x and q_y are the x and y components of $\mathbf{q} = -k\nabla_S(R_1 + R_2)$ with the gradient $\nabla_S = (\partial/\partial x, \partial/\partial y)$. The directivity term $A(\mathbf{r})$ is defined in this work as the far-field radiation from a baffled piston, which is given by [24],

$$A(\mathbf{r}) = \frac{2J_1(ka\sin(\phi(\mathbf{r}) - (-\phi_0 + \pi/2)))}{ka\sin(\phi(\mathbf{r}) - (-\phi_0 + \pi/2))}, \tag{4.9}$$

where a is the aperture, J_1 is the Bessel function of the first kind with $n = 1$, ϕ_0 is the angle of inclination of the source main axis to the Ox-axis, and $\phi(\mathbf{r})$ is the angle

between the vector produced from the location of the source and the point $\mathbf{r}$ with the Oy-axis.

Following the application of the Kirchhoff approximation to simulate the scattered field, the phase is removed from Equation 4.6 through the application of modulus:

$$p(\mathbf{R}) = |\psi_s(\mathbf{R})|. \tag{4.10}$$

Taking into account the receiver locations in an array of M receivers, phase-removed acoustic pressure used in the random forest algorithm is given by the following matrix,

$$\mathbf{p} = \{p_l\left(\mathbf{R}^{(j)}\right) | \, j = 1..M, l = 1..N\}, \tag{4.11}$$

where the rows of the matrix are formed from p_l (an ensemble containing the absolute array pressure for a given ζ_l), and $\mathbf{R}^{(j)}$ form the columns (receiver locations defined with respect to the origin of the Oxy plane). For brevity, the dependence on $\mathbf{R}^{(j)}$ will be omitted, resulting in $p_{lj} = p_l\left(\mathbf{R}^{(j)}\right)$, and if operations are row-wise only the j superscript will be omitted resulting in $\mathbf{p}_l$.

4.4.2 Noise

The Kirchhoff approximation model is deterministic, therefore one set of model parameters maps to a given sound pressure field. However, in practical applications, noise is present in measured data. It is proposed to modify the solution of the Kirchhoff approximation via additive noise, calculated as:

$$\tilde{\mathbf{p}}_l = \mathbf{p}_l + \epsilon_l, \tag{4.12}$$

where $\epsilon_{lj} \in \epsilon_l, \epsilon_{lj} \sim \mathcal{N}(0, \sigma)$ is drawn from a normal distribution independently for each receiver. For additive noise, the standard deviation, σ, was selected to be percentages chosen for investigation (0.1%, 1%, 5%, 7%, 8%, 9%, 10%, 12%, 15%, 17%, 20%, 25%, 30%. This relates to an approximate signal-to-noise ratio of 29.7dB, 19.7dB, 12.7dB, 11.2dB, 10.6dB, 10.1dB, 9.7dB, 8.9dB, 7.9dB, 7.3dB, 6.7dB, 5.7dB, 4.9dB respectively) multiplied by $\bar{p}_l$ - the average of the receiver's pressure magnitude taken across all receivers for the given surface in absence of the noise. The acoustic pressure for each receiver is then normalised by the maximum value for the Kirchhoff approximation scattered from the flat surface so that it can be used in the random forest algorithm.

Number of recovered parameters	Amplitude bounds	Wavelength bounds	Offset bounds	Number of samples
1 parameter	-0.01m,0.01m	N/A	N/A	30
2 parameters	-0.01m,0.01m	0.035m,0.15m	N/A	30
3 parameters	-0.01m,0.01m	0.035m,0.15m	-0.02m,0.02m	30

Table 4.1: Bounds for each parameter in the data generation stage as well as the number of samples generated within those bounds.

4.4.3 Synthetic training and testing datasets

A large number of datasets that correspond to different realisations of the parameters ζ_i, $i = 1..3$ were prepared using equations (4.6) and (4.12). For these calculations, the source and receiver locations were chosen in accordance with the existing experimental data [74] that was later used for validation in this paper. The source location was at $(x_1, y_1) = (-0.20, 0.22)$ m. The angle ϕ_0 of the source main axis to the Ox axis was 60 degrees. The receivers were located at a height of approximately $y_2 = 0.28$ m in the y-axis and 34 receivers were distributed evenly with x_2 taking values from -0.13 m to 0.53 m in the x-axis, leading to an average distance between the receivers of 0.02 m. The data was generated numerically through the use of the Kirchhoff approximation, the integration was done numerically through the application of Simpson's rule [173] over the integration range of $x \in [-3, 3]$ m, which was vectorised to improve the speed of data generation.

Multiple datasets were formed for one-parameter, two-parameter, and three-parameter surfaces defined in equation (4.1) in order to investigate the performance of the algorithms as the number of unknowns increased. The values for each parameter were generated with uniform spacing from a lower bound to an upper bound, the choices for parameter values and resolution is shown in Table 4.1.

As well as the surface generation, multiple datasets were generated with different proportions of noise to the absolute acoustic pressure, with σ varied between $0.001\bar{p}_l$ and $0.3\bar{p}_l$ as described above. Noise was added by cloning a pair of pressures and surface parameters 20 times and independently adding noise to every receiver, yielding datasets with the following sizes for one-, two- and three-parameter datasets: 630, 18900, 567000.

The models were trained using the training set and then evaluated on the testing set to provide an indication of the model's performance on unseen data. The same approach described above was applied in order to generate both the training set and the synthetic testing set. The two subsets were split randomly, with a proportion of

70% training set and 30% testing set, such that the intersection of the training and testing set would yield the empty set.

4.4.4 Experimental testing dataset

Experimental data used in this paper for validation purposes was collected with 34 $1/4''$ microphones (G.R.A.S. 40PH) and with a loudspeaker (Visaton G 25 FFL), arranged with the same geometry described in section 4.4.3. A sinusoidal surface (with amplitude $\zeta_1 = 0.0015$ m and wavelength $\zeta_2 = 0.05$ m) illustrated in Figure 4.2 was machined from an aluminium block with a length of 0.55 m in the x-direction, and a width of 0.35 m.

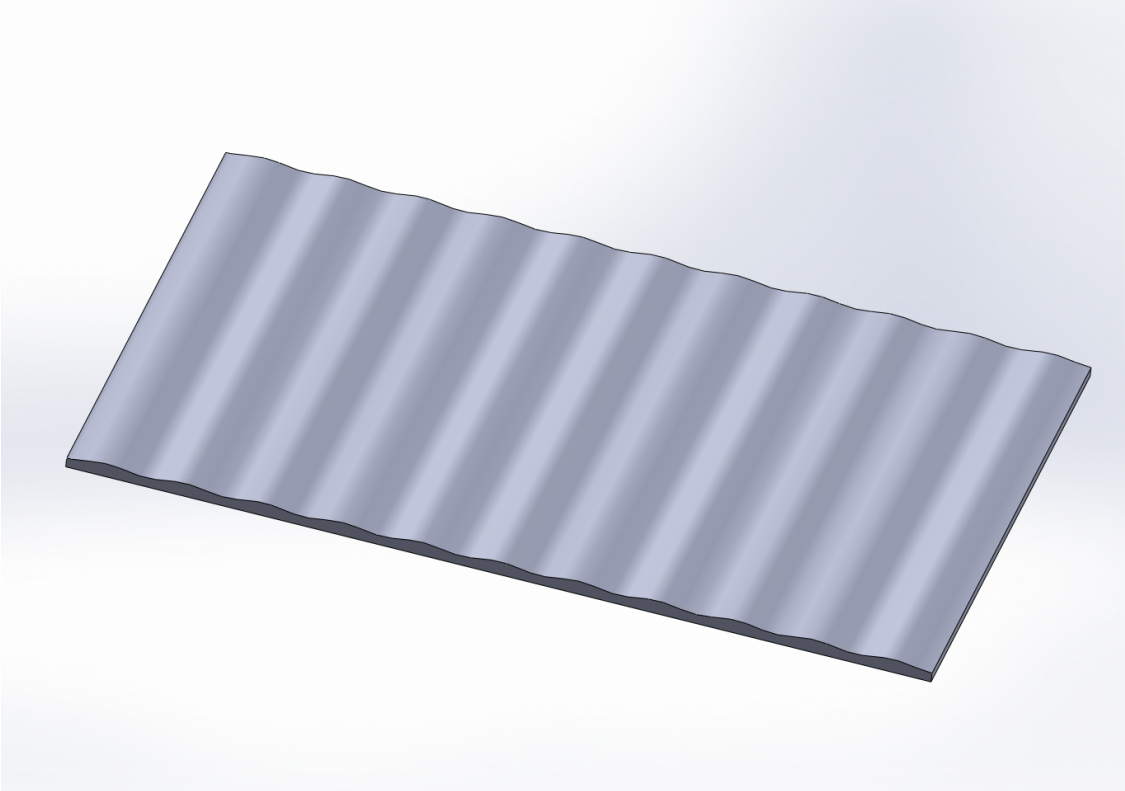

Figure 4.2: 3D rendering of the surface used in the acquisition of the experimental sample. (colour online)

A signal was produced at 14 kHz and recorded simultaneously at all microphones, with a sampling rate of 102.4 kHz. The amplitude at each microphone was calculated by a Fourier transform applied to 0.02 s long segments of the signal, and then averaged over 2000 segments using a Hann window. The data was calibrated in situ by comparing measurements of the sound field reflected by a flat surface

with the corresponding prediction calculated numerically, following the procedure outlined in Dolcetti *et al.*[74].

Even after calibration, the pressure field scattered by the sinusoidal surface differed from the one predicted with the Kirchhoff approximation model, due to the uncertainties in the measurements, especially at the microphones further away from the source. This difference could be seen as an equivalent random noise with σ given by:

$$\sigma = \frac{\sqrt{\sum_{j=1}^{M} \left[\psi_{ref}(\boldsymbol{R}^{(j)}) - p(\boldsymbol{R}^{(j)})\right]^2 / M}}{\bar{p}(\boldsymbol{R})}, \tag{4.13}$$

where p is the Kirchhoff approximation given in equation (4.6), with $\zeta(x) = 0.0015\sin(2\pi x/0.05)$ and $|\psi_{ref}|$ is the experimental data. σ was found to be 0.195 that quantifies the deviations observed in Figure 4.3.

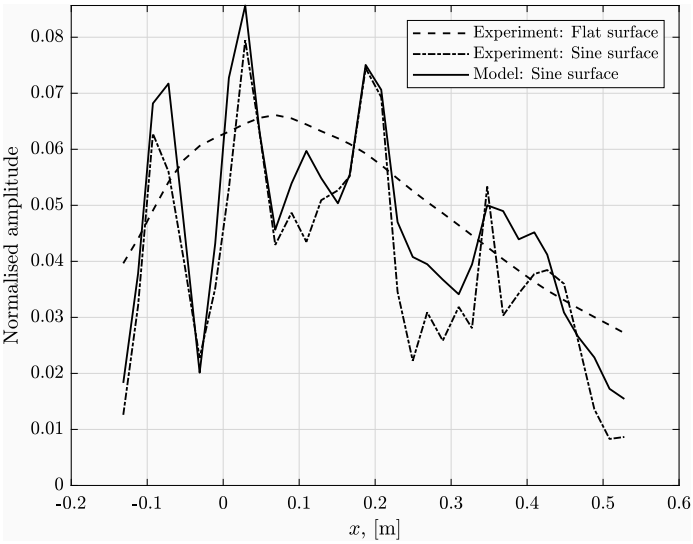

Figure 4.3: Overlay of the Kirchhoff approximation solution in comparison to the experimental example which is calibrated for 14 kHz.

4.4.5 Performance evaluation

In this section, the choices of metrics used to estimate the accuracy of the inversion algorithm are briefly defined. For evaluation against the synthetic testing set, the coefficient of determination ($\mathscr{R}^2$) is used in the following form [174];

$$\mathscr{R}^2(i) = 1 - \sum_{l=1}^{N} \frac{[\zeta_{li} - f(\mathbf{p}_l)_i]^2}{(\zeta_{li} - \bar{\zeta}_i)^2}, \tag{4.14}$$

where $\mathbf{p}_l = |\psi_s(\mathbf{R}^{(j)})|$, $j = 1..M$ are the inputs for a given surface with $\mathbf{Z}_l$ parameters, N is the number of samples, $\bar{\zeta}_i$ is the mean of the i-th output, and ζ_{li} are outputs at the l-th row for the i-th value from $\mathbf{Z}_l$ set of parameters and f is the estimator, which is the random forest explained in Section 4.3. Therefore, $f(\mathbf{p}_l)_i$ is the prediction of the i-th value from the Random Forest given $\mathbf{p}_l$. For the two- and three-parameter estimation, the $\mathscr{R}^2$ score is calculated for each parameter and then averaged.

To evaluate the accuracy of the model predictions when predicting the surface given exclusively from the experimental data, the absolute error (AE) was also used, given by;

$$E_i = |f(\mathbf{p})_i - \zeta_i|, \; i = 1..3. \tag{4.15}$$

As there is only a single surface measurement available from the experimental data, $N = 1$ and there is no averaging in equation (4.15) compared to that in equation (4.14).

When plotting the results, the value of E_i is also normalised by the corresponding surface parameter, except for the offset, which is normalised by the wavelength.

It is noted that in the two- and three-parameter recovery, the AE of each output parameter was considered. This allows for an investigation into the change in parameter prediction as the number of parameters increases, while not allowing the overall AE to be dominated by the highest scale - the wavelength.

4.4.6 Convergence

A key hyperparameter of consideration is the number of decision trees used in the construction of the random forest. There are instances where an increase in the number of trees in a random forest only increases computational cost without much improvement in performance. [175] It was shown that both the errors in classification and regression forests are monotonically decreasing functions with respect to the number of trees. [176] These results also highlight that the most performance improvement was seen from random forests built from 10 trees to 250 trees.

Convergence testing has been performed for random forests generated with 1% and 15% added noise for three-parameter recovery. Three-parameter recovery was chosen due to the size of the dataset as well as the complexity of recovering three parameters. The change of the coefficient of determination as the number of trees increases is presented in Figure 4.4. In the case of 1% noise shown in Figure 4.4, the increase in the coefficient of determination slows significantly after 5 trees in the random forest algorithm. For the case of 15% added noise, the coefficient of

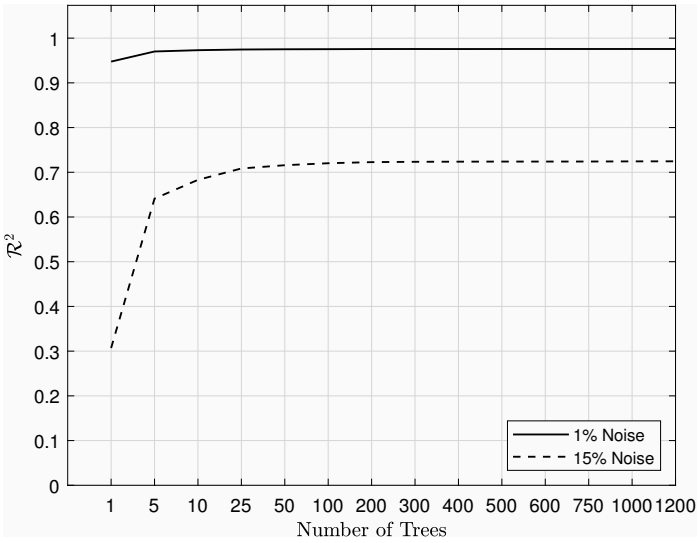

Figure 4.4: Convergence of $\mathscr{R}^2$ when number of trees increase for 1% and 15% added noise

determination increases rapidly for random forests created from 1 tree to 50 trees as shown in Figure 4.4, which signifies a better performance of the algorithm in predicting the testing set. The coefficient of determination demonstrated in Figure 4.4 decreases in gradient rather significantly for the random forests as the number of trees pass 200, with a relative percentage increase in coefficient of determination of 0.18%. When the number of trees reach 750, the increase in the number of trees has a smaller effect on the coefficient of determination, while also significantly affecting computational time. In this study, with the hardware described in Section 4.4.1, the computational time for the random forests with 750 trees increased to 53.67 times that of the random forest with 1 tree. Increasing the number of trees to 1200 results in a further increase of computational time to 81.7 times. Therefore, the approach used in this paper was to generate random forests consisting of 700 trees, which is substantially inside the convergence factor to ensure convergence for all datasets while not having a significantly negative effect in terms of computation time.

4.5 Results

This section is formed from four subsections. Firstly, the coefficient of determination is considered when evaluating model performance using the testing subset of the synthetic data. Following this, a comparison between the random forests approach against the short array method [67] is showcased. Then, a study on the

performance of random forests when evaluating parameters unseen by the model in training is showcased. Finally, the AE between model predictions and the surface used in the experimental sample is considered. For the AE when considering the two and three-parameter surfaces, the AE is presented such that the AE per parameter is separated.

4.5.1 Testing on synthetic data

Testing was done initially based on synthetic data, for a large number of surface realisations, and for various amounts of noise and numbers of receivers, where the first N receivers were considered. For one-parameter estimations, the surface wavelength and offset are assumed to be known, while the amplitude parameter ζ_1 is estimated. In this case, the coefficient of determination was found to be close to 1 for noise levels below 17%, except for 9% noise for random forests generated with 10 receivers where $\mathscr{R}^2 \approx 0.888$, then dropping to slightly below 0.9 at 30% noise, as shown in Figure 4.5. It is noted that for 10 receivers at 17% noise $\mathscr{R}^2 \approx 0.861$. The decrease of coefficient of determination for the data generated by 10 receivers at 9% and 17% noise is interesting due to the drop in value of $\mathscr{R}^2$. This behaviour was deemed to be an outlier from the specific shuffle of training and testing sets. Randomly reshuffling the training and testing sets 1000 times for the 9% and 17% noise cases gave average coefficients of determination of 0.986 and 0.959, with standard deviations of 0.014 and 0.026, respectively.

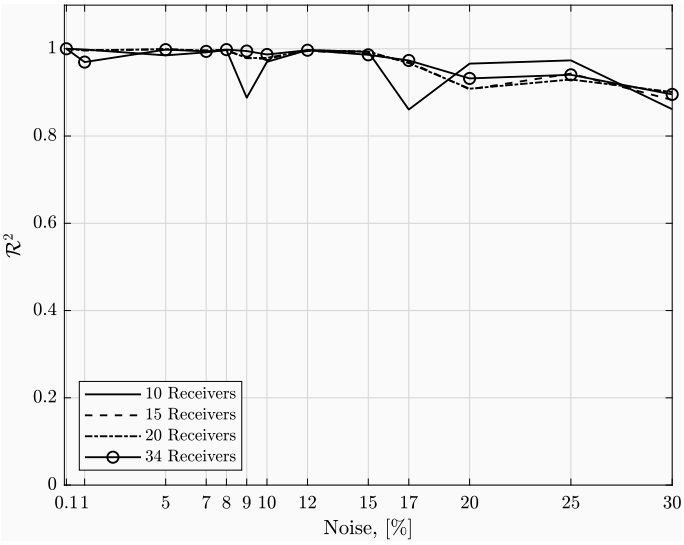

Figure 4.5: Coefficient of determination for the estimation of the surface amplitude, ζ_1, at varying noise levels and considering different number of receivers.

When the surface amplitude ζ_1 and surface wavelength ζ_2 are estimated, the coefficient of determination lowers throughout all the noise percentages, as well as showing a smoother decay of $\mathscr{R}^2$ value with the noise level. For random forests generated with 15, 20 and 34 receivers, the minimal value of the coefficient of determination is above 0.7 at the dataset with 30% noise as shown in Figure 4.6. For the random forest based on 10 receivers, the $\mathscr{R}^2$ is much worse than with higher numbers of receivers, dropping to approximately 0.5 at 30% noise.

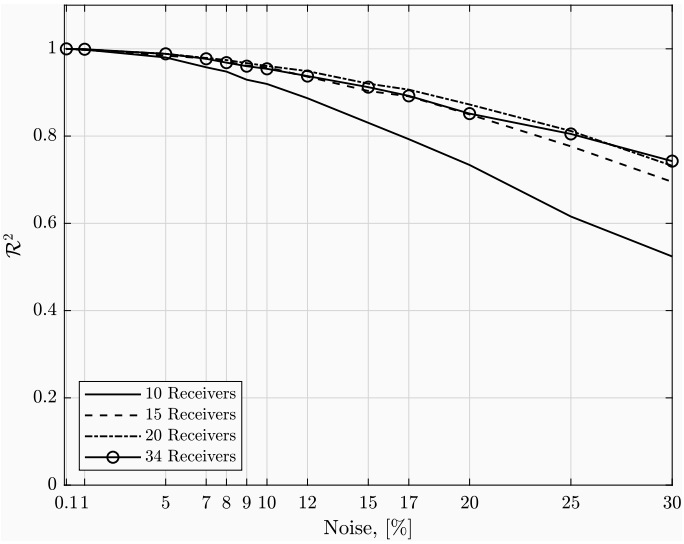

Figure 4.6: Coefficient of determination for the estimation of the surface amplitude, ζ_1 and the surface wavelength, ζ_2 at varying noise levels and considering different number of receivers.

When all three surface parameters (amplitude ζ_1, wavelength ζ_2, and offset ζ_3) are estimated, the coefficient of determination decreases faster compared to the one and two parameter problems. This is highlighted at random forests generated with 10 receivers, where the lowest value $\mathscr{R}^2$ is approximately 0.3 at 30% noise compared to approximately 0.5 and 0.9 in one- and two-parameters, respectively.

A key feature to note is that the coefficient of determination changes only slightly for random forests generated with different receiver combinations when the amount of receivers is greater than 10 as shown in figures 4.5, 4.6 and 4.7. This highlights that favourable model performance using machine learning to aid the inversion process can be obtained with fewer receivers. Having favourable performance with fewer receivers makes it possible to set up cost-efficient and practical applications.

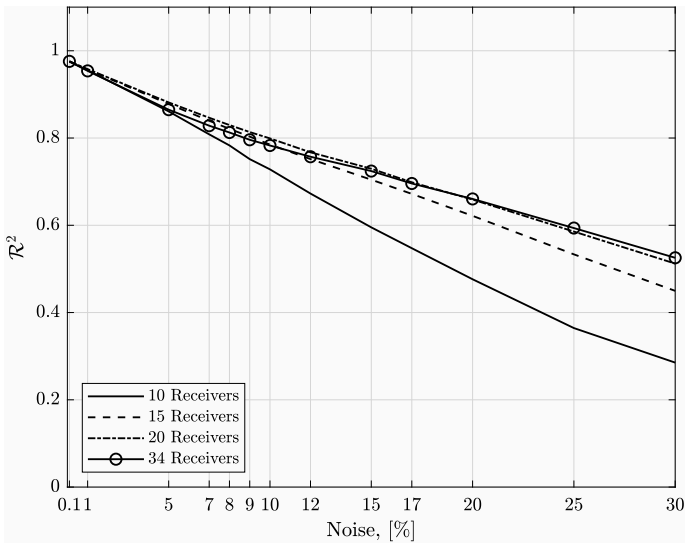

Figure 4.7: Coefficient of determination for the estimation of the surface amplitude, ζ_1, the surface wavelength, ζ_2 and the offset ζ_3 at varying noise levels and considering different number of receivers.

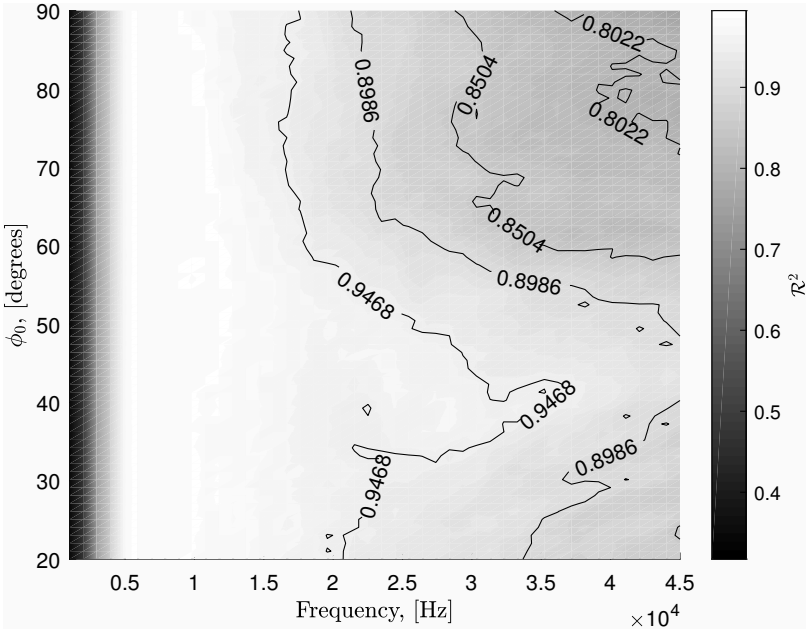

Figure 4.8: Contour plot of the coefficient of determination of a testing set for the two-parameter recovery for varying angle of incidence ϕ_0 (see equation (4.9)) and frequency.

4.5.2 Investigation of change of angle and frequency

In order to judge performance in different setup conditions, and to verify the choice of angle and frequency used in the experiment, varying source angles ϕ_0 and source excitation frequencies were tested. The source angles were varied from 20 degrees to 90 degrees, with 70 equally-spaced samples. The source excitation frequencies varied from 1000Hz to 45000Hz with 45 equally-spaced samples. In order to reduce computation time, two-parameter datasets were created. The offset of the sinusoidal surface was fixed to 0. Datasets were created in the same way as described in Section 4.4.3 where noise was not added to the datasets. Figure 4.8 showcases the results of the coefficient of determination for the resulting testing sets. In the results, the method does not perform well below 5000Hz for all angles tested. This is concluded to be due to the scale of the acoustic wavelength being much larger than the amplitude and wavelength of the surface, causing the scattered absolute acoustic pressure to have no substantially-different features. Between 5000Hz and 15000Hz, the coefficient of determination is at near maximum for all angles tested. As the frequency increases past 15000Hz, an ideal angle region is found between 30 and 60 degrees.

4.5.3 Comparison with Short Array method

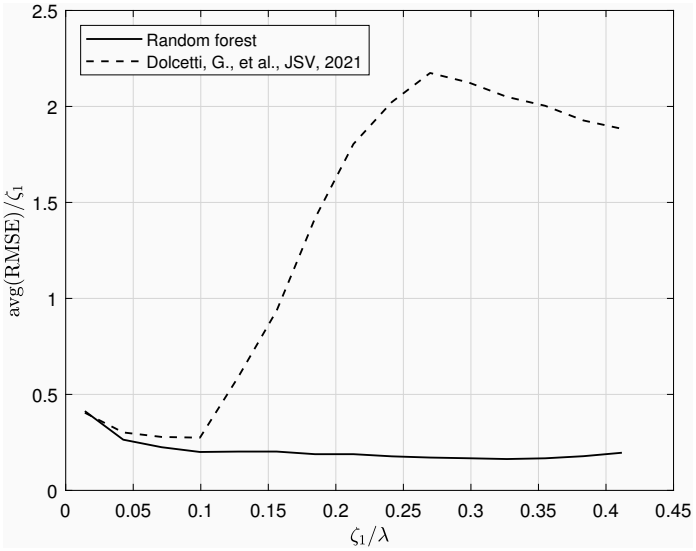

Figure 4.9: Comparison between the approach offered in the paper against the SA0 approach: averaged root mean square difference between target and reconstructed surfaces normalised by the surface amplitude ζ_1, plotted against the surface amplitude normalised by the acoustic wavelength, ζ_1/λ.

A comparison between the method proposed in this paper and the so-called short array method [67] in the unbiased version proposed by Dolcetti et al. [74], hereafter called SA0 method, is discussed in this section. The comparison was made between the three-parameter random forest generated with 5% noise and the SA0 model. Both models had the same initial conditions on setup and were evaluated with 141750 samples taken from the testing set. In order to match the parameter-based recovery from the random forest to the surface based recovery from the SA0 model, a set of surfaces was reconstructed from the parameters provided by the random forest by populating the values into equation (4.1) in the range $x \in [-0.11, 0.17]$, which is the specular range of the source and the receiver array. The two methods were applied to the same set of synthetic pressure data, and compared in terms of the spatial root-mean-square difference between the target and reconstructed surfaces averaged over all surfaces with the same amplitude and normalised by the surface true amplitude parameter. The results can be seen in Figure 4.9. The deviation in methods appear to increase rapidly when $\zeta_1/\lambda > 0.1$ where the SA0 method begins to increase in error significantly. This is mainly because of the loss of validity for the linearisation of the Kirchhoff integral, which is the basis of the SA0 method, whereas the random forest approach uses the Kirchhoff approximation directly without linearisation. A direct comparison to the previous methods can be made by analysing Figure 13c in Dolcetti *et al.* [74]. Calculating the root-mean-squared error factored by the acoustic wavelength for the surface recovered from Table 4.2 within the specular points of the receivers and the microphones (following Dolcetti *et al.* [74]) yields a value of 0.0165, 0.027 and 0.169 for one-, two- and three parameters respectively. This outperforms the SA0 method in recovering the experimental sample and is comparable to reconstruction using multiple frequencies, while also being close to the reconstruction based on synthetic data without noise. The exception is the two-parameter recovery, which performs approximately the same as the SA0 method. Although this is one sample, the results, highlighted from both synthetic recovery as shown in figure 4.9 and experimental recovery earlier in this paragraph, showcase improved performance with the method proposed in this paper, especially as the amplitude increases.

4.5.4 Evaluating surfaces not seen by the model in training

In order to highlight the generality of using a random forest based approach, predictions on surfaces that would have never been seen in the training and testing sets in

the previous section were evaluated. Two-parameter recovery was chosen to highlight the generalisation. Surface parameters were chosen by doubling the number of samples shown in Table 4.1 and removing samples that correspond to the training and testing set used to train the random forest. This leads to 841 surfaces to be predicted. In order to investigate generalisation further, noise was added to modify the receiver pressure at the unseen model parameters, where the percentage chosen to modify the pressure was different compared to that seen by the random forest during training. The random forest was trained on acoustic pressure linked to the two-parameter dataset with 5% added noise, and evaluated on a dataset generated with 7% noise. In these data, the coefficient of determination given by equation (4.14) when training on the surface amplitude and surface wavelength is 0.6 and 0.84, respectively. Figures 4.10 (a) and (b), and 4.11 highlight the results of the recovered two surface parameters.

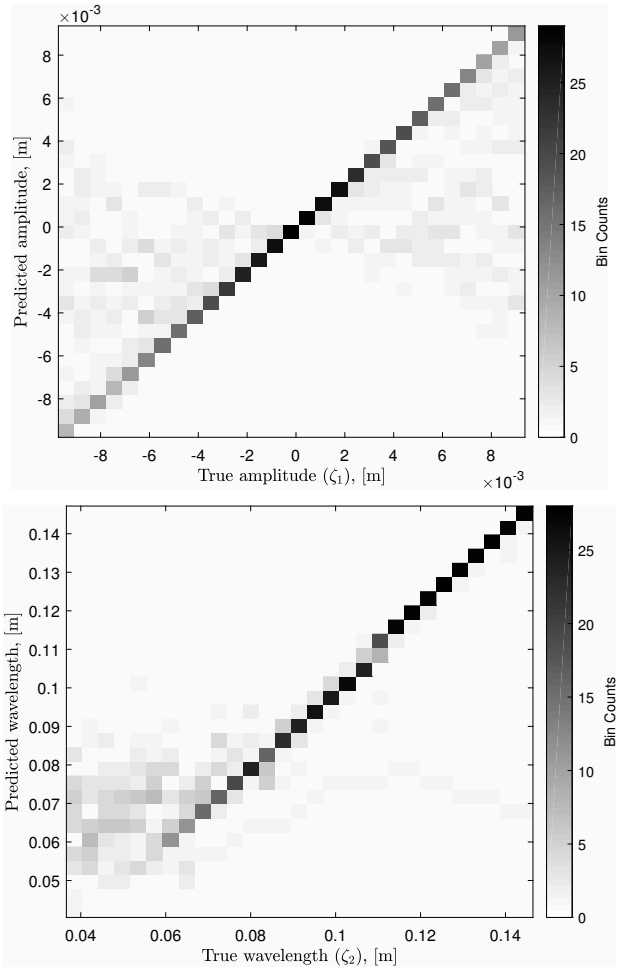

Figure 4.10: The predicted values versus true unseen parameters: (a) surface amplitude ζ_1 and (b) surface wavelength ζ_2.

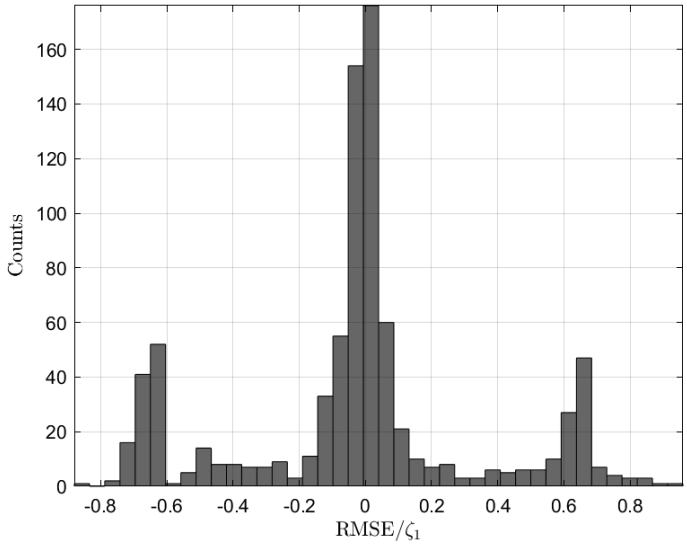

Figure 4.11: Histogram of the RMSE, measuring the difference between the true surfaces produced with the unseen parameters and the reconstructed surfaces produced using the random forest predictions of the unseen parameters, normalised by the true parameter's amplitude.

There is a clear trend in Figures 4.10 (a) and (b) along the identity line, where true and predicted values are equal for both the amplitude and the wavelength. This can be seen from the density shown in the figures. The amplitude component has a spread of predictions that widen in proportion to the surface elevation height. The reconstruction of the wavelength begins to deteriorate for values starting below $\zeta_2 = 0.08$ m. It appears that the performance decreases when recovering surfaces with high amplitude and low wavelength, which corresponds to a higher Kirchhoff parameter.

Figure 4.11, representing the distribution of RMSE (described in subsection 4.5.3) defined along the specular region by the difference between the true surfaces and the surfaces reconstructed with the random forest predictions, demonstrates that the majority (approximately 74%) of the reconstructed surfaces predicted with the random forest algorithm fall within $\pm 0.41\zeta_1$, which is the standard deviation of the RMSE deviation.

4.5.5 Testing on experimental data

The coefficient of determination was used as a metric to measure model performance with a synthetic testing subset of the synthetic data when discussing the

results in Section 4.5.1. In this section, predictions were obtained and compared against the experimental sample given in Section 4.4.3. Using the experimental phase-removed acoustic pressure as an input to the random forests, the prediction was then compared with the true surface parameters from the experiment using AE given in equation (4.15). The value of AE was then normalised by the actual surface parameters and expressed as a percentage point, converting it to a relative error.

Figure 4.12 highlights the relative error from one parameter's prediction of the surface amplitude ζ_1 based on experimental data. For the random forest generated with the full set of 34 receivers, the maximal AE divided by the actual surface amplitude rises from below 26% to 50% as the noise increases from 0.1% to 9%. As the noise level increases above 9%, the relative error decreases under 50% reaching its minimum 5% at 12% noise. This behaviour is closely matched to the random forest generated by 20 receivers. For the random forest generated with 15 receivers, there is a large spike of relative error for noise values under 7% noise, then the error for these random forests match the error curve of the random forests generated with 20 and 34 receivers. For random forests generated with 10 receivers, the relative error tends to stay with the other error curves except for noise levels of 10% where there is a spike in relative error of approximately 300%

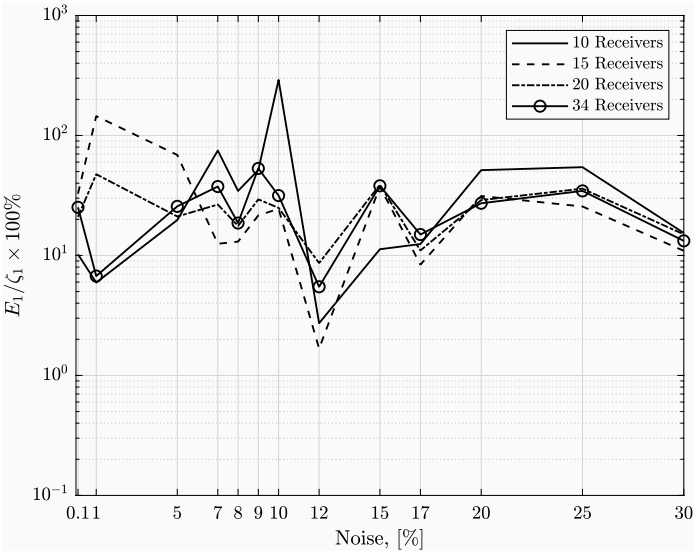

Figure 4.12: The change of relative error values for the random forests generated with different numbers of receivers and noise for one parameter surface recovery of the experimental sample.

Figure 4.13 (a) and (b) contain the relative errors of the amplitudes and wave-

lengths, respectively, for the two-parameter recovery. The random forests generated with 10 and 15 receivers have relatively high errors in comparison to 20 and 34 receivers. The wavelength and amplitude relative error for random forests generated with 20 and 34 receivers are close to the actual wavelength and amplitude values of the surface, staying mostly under 20% of the AE factored by the actual amplitude and under 25% of the AE factored by the actual wavelength. There are exceptions at 9 and 10% noise for random forest generated with 34 receivers and 12% for random forests generated with 20 receivers. For over 20% noise, the random forests generated with 34 receivers also exceed 25% relative error. There is a clear separation for the random forests generated with 10 and 15 receivers in comparison to 20 and 34 receivers in amplitude and wavelength, with the smaller number of receivers producing errors that are a factor of 10 larger for the wavelength component.

Figure 4.14 contains the relative error of all three parameters. For the full set of receivers, the relative error of the recovered surface amplitude decreases from 200% to settle at approximately 50% for random forests generated with 7 or more percent noise - except for 15 and 17 percent noise, where the relative error is found within 3-5% range. Interestingly, the random forest generated with 20 receivers has a lower error curve than the random forest generated with the full set of receivers. This could be due to an increased fit to the Kirchhoff approximation solution with the experimental results, as shown in Figure 4.3. For the wavelength parameter, every choice of the amount of receivers except for 34 receivers yielded a relative error greater than 10%. The offset AE, divided by the actual wavelength, stayed below 10% for every receiver combination and noise level. The random forest generated with 34 receivers kept the lowest AE value compared to the random forests generated with fewer receivers throughout.

The major problem with the three-parameter model is the prediction of the amplitude, where the relative error is high even for the full set of receivers. For the random forest generated with 34 receivers, the relative error was less than 10% at only 15% and 17% noise levels and then over 50% at all other noise levels. Although this error is in the sub-millimeter scale, the consistent underestimation can make the prediction invalid. It is noted that this underestimation could be due to the difference in scale between the parameters, with the wavelength of the surface being significantly larger than the amplitude. It is important to note that 15% and 17% noise is close to the estimated deviation between the measurements and the predictions by the Kirchhoff approximation model calculated in Section 4.4.4 esti-

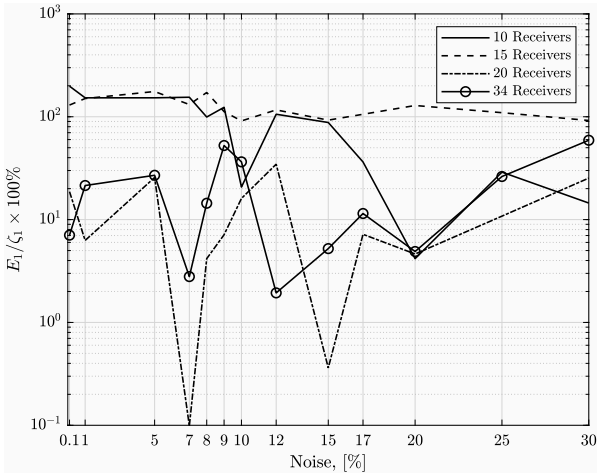

(a)

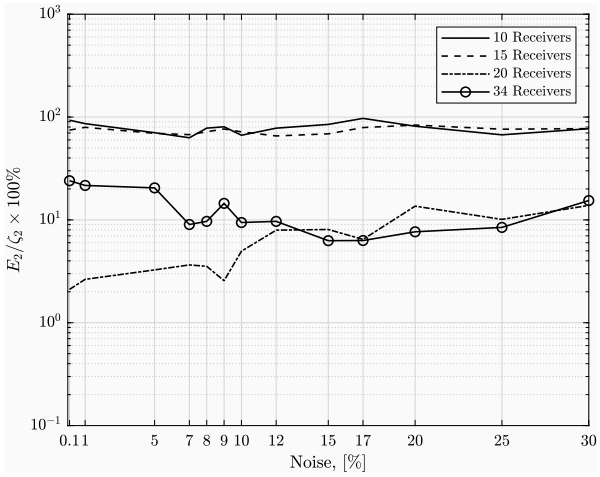

(b)

Figure 4.13: The change of relative error values for the random forests generated with different numbers of receivers and noise for two parameter surface recovery of the experimental sample, separated by parameter: (a) amplitude, (b) wavelength.

Number of recovered parameters	Amplitude	Wavelength	Offset	$\mathscr{R}^2$
Actual parameter	0.0015m	0.05m	0m	N/A
1 parameter	0.00207m	N/A	N/A	0.986
2 parameters	0.00158m	0.0531m	N/A	0.912
3 parameters	0.00142m	0.0516m	- 0.00194m	0.724

Table 4.2: Results from parameter recovery for surface prediction using 15% noise random forest.

mated with the equation (4.13), which could explain the improved performance of the inversion at these noise levels.

Figure 4.15 and Table 4.2 highlights the model's prediction of the surface given the experimental acoustical pressure in comparison to the actual surface shape at datasets with 15% noise and with 34 receivers. 15% noise was selected due to the improved performance in the two and three parameter models and similarity to the expected error from the Kirchhoff approximation model to the experimental data sample. The x-limits of the plots ranging from -0.15 m to 0.15 m are defined by the width of the main lobe in the source directivity pattern given by equation (4.9). The dominating component of difference to the experimental sample is the wavelength due to the scale differences in amplitude and wavelength as shown in Table 4.2.

4.6 Conclusion

While training and testing the random forest regression algorithm, it was observed that for one-parameter datasets, the coefficient of determination is highly favourable, staying significantly above 0.8 over the range of added noise. For the random forests generated with the two-parameter datasets, all receiver subsets except for 10 receivers slowly decay from 1 to just under 0.8. When random forests are trained with the three-parameter datasets, the coefficient of determination is observed to be above 0.7 for added noise levels between 0.1% and 15%, except for the random forest generated with 10 receivers. With 10 receivers, the coefficient of determination decreases significantly for noise levels above 10%.

The relative error has been used as a metric to evaluate model performance when predicting the surface parameters from experimental data. It has been noted

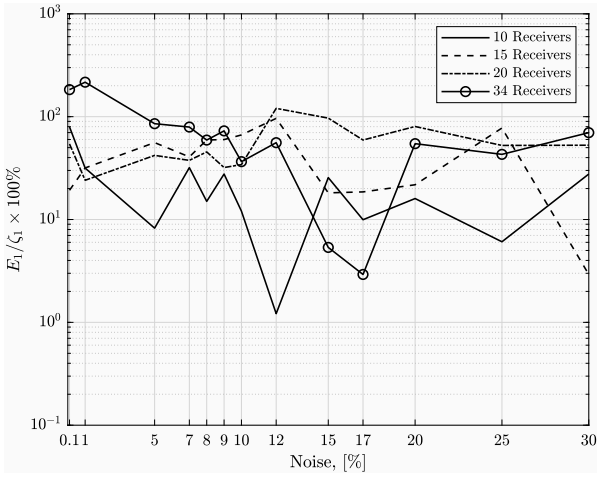

(a)

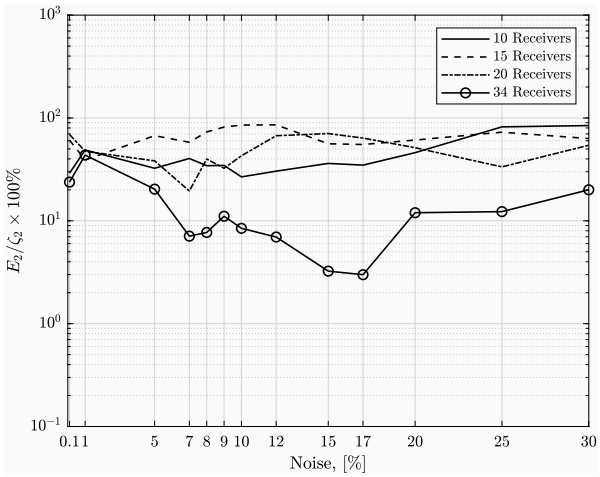

(b)

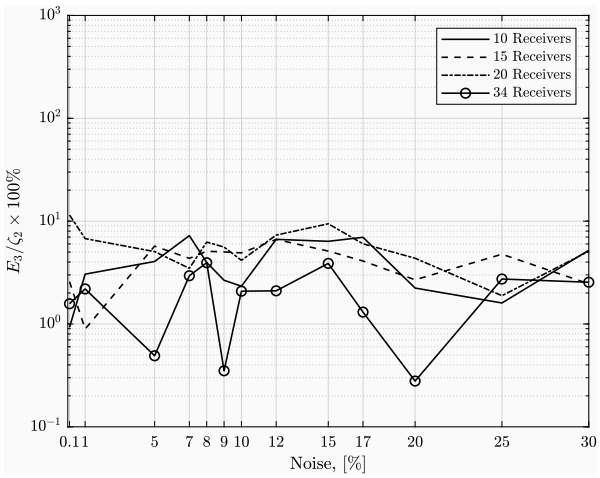

(c)

Figure 4.14: The change of relative error values for the random forests generated with different numbers of receivers and noise for three parameter surface recovery of the experimental sample, separated by parameter: (a) amplitude , (b) wavelength and (c) offset.

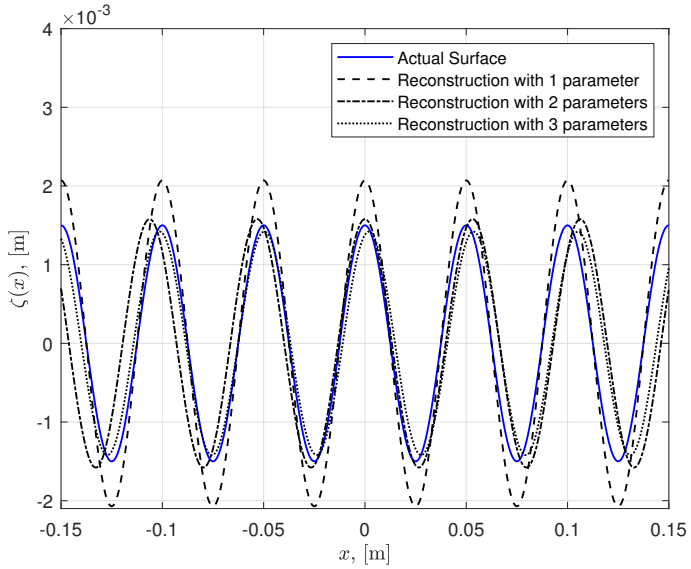

Figure 4.15: Surface prediction for 15% noise random forest generated with 34 receivers (colour online).

that the relative error varies significantly between 0 and 100% depending on the added noise and amount of receivers used in the recovery of parameters. In the three-parameter recovery, the lowest relative error values for 34 receivers have been consistently observed when noise levels are at 15% and 17%. It has been noted that these noise levels are comparable with the estimated discrepancy between the analytical solution used to generate synthetic data and the experimental results.

The results in this paper have shown that the method works well for a simple sinusoidal surface and as such stands as an initial proof of concept that can be generalised to complex surfaces; for example, through Fourier series decomposition. Another extension to the results of this paper would be to incorporate a measure of confidence in the model's predictions, such as Bayesian Inference, which could also benefit from flexibility and could provide complimentary insights.

4.7 Acknowledgments

The authors would like to acknowledge the support of the UK Engineering and Physical Sciences Research Council (EPSRC) via the Knowledge Exchange Support Fund. M.-D. Johnson would like to acknowledge the support of the University of Sheffield through their PhD studentship award. G. Dolcetti is funded by the UK EPSRC Grant EP/R022275/1. M. Alkmim is funded by the Marie Sklodowska Curie program through the H2020 ETN PBNv2 project (GA 721615). The authors are

grateful to reviewers for constructive and valuable comments. The authors would also like to thank Yue Li at Siemens Digital Industries Software, Leuven, for valuable input on addressing the reviewers' comments.

Chapter 5

Data-driven reconstruction of rough surfaces from acoustic scattering

Reference

Johnson, M. D., Krynkin, A., Dolcetti, G., Alkmim, M., Cuenca, J., De Ryck, L., and Li, Y. (2023, February). Data-driven reconstruction of rough surfaces from acoustic scattering. In INTER-NOISE and NOISE-CON Congress and Conference Proceedings (Vol. 265, No. 1, pp. 6188-6198). Institute of Noise Control Engineering.

Author Contributions

- Johnson, M.D., - Problem formulation,. writing, model development, data analysis, editing, structure.
- Krynkin, A. - editing.
- Dolcetti, G. - editing.
- Alkmim, M. - editing.
- Cuenca, J. - editing.
- De Ryck, L. - editing.
- Li, Y. - editing.

Summary

Prior to formulating the results that were used in the previous section, an appropriate model needed to be found, known as model selection. The method of model selection was to first find a region of frequency from the experimental sample calibration data, that behaved as expected to the Kirchhoff approximation, and then use that frequency in the data generation. Then random forests, k-nearest neighbors, linear regression, support vector machines, and artificial neural networks were tested. It was found that the Random Forests performed the best and was consistent in their prediction, so this was the model used in Section 4.

However, there were a few limitations with the approach. Firstly, only a single (or a few) frequencies can be selected, this potentially can be an issue due to the human choice of frequency and due to changes in the environment, the frequency chosen could be dominated by noise. There was an over-reliance on having a high quality calibration dataset in order to extract the frequencies that are sufficient for Random Forest reconstruction. A further limitation of this single frequency approach was that the prediction given was only a single sample, there was not a measure of uncertainty from a point sample. A clear way to avoid this is to generate a cluster of predictions over many frequencies.

The paper presented in this chapter tackles these issues. The acoustic source for the experiment was white noise, which gives information from 10,000Hz to 51,150Hz in 50Hz bins. Model selection was thus run again on each of the 50Hz bins in this range to avoid the issues arising from only looking at a single frequency. The models were selected in this paper to be linear regression, random forests, and k-nearest neighbours.

The mean-squared error of the Kirchhoff approximation against the experimental data collected in the experiments were shown, the coefficients of determination for the models were also shown, where linear regression performs substantially worse than K-Nearest Neighbors and Random Forests. This is entirely expected, as the problem is non-linear.

The key figures are the scatter plots and the histograms of the predictions of each model. Taking a holistic approach using the whole frequency range, the K-Nearest Neighbours approach is clearly more favourable. This is due to the distinct single prediction (minus some outliers) that can be observed in the range from 10,000Hz to 30,000Hz. This causes a very large peak to be found in the histograms. Outside this region, the predictions become random, which can be attributed to the

limitations of the to the Kirchhoff Approximation model as well as the decreasing acoustic wavelength.

Following this, the main method used in further Chapters, the Adaptive Metropolis scheme, was introduced. This allowed for the ability to get a full posterior distribution over the parameters. In this case, the adaptive metropolis scheme is a single frequency based approach that was tested with the three parameter experimental data used in Chapter 4.

5.1 Abstract

This work investigates the use of data-driven approaches for reconstructing rough surfaces from scattered sound. The proposed methods stands as alternatives to matrix inversion, which requires a linearisation of the dependence on the surface parameters. Here, a large dataset was formed from scattered acoustic field, estimated through the Kirchhoff Approximation. Limiting this work to the reconstruction of a static surface, K-Nearest Neighbors, Random Forests and a stochastic approach are compared to recover a parameterisation of surfaces using the scattered acoustical pressure as input. The models are then validated against a laboratory experiment alongside methods highlighted in Dolcetti et. al., JSV, 2021. The models are tested at a frequency that best fits the lab uncertainties, then tested on a broad frequency range. This scheme provides relatively accurate results in comparison to the approaches tested. Estimation errors as well as robustness in the presence of noise are discussed.

5.2 Introduction

Machine Learning has been a highly active section of research in recent years, proving more than capable in many fields, including acoustics. Bianco *et al.* [52] highlighted some key areas in acoustics where Machine Learning has been used. Namely, source localisation, bioacoustics and reverberation. However, as the number of Machine Learning solutions increase, questions are rising about the reproducibility of results [177, 178, 179].

Typically, when evaluating the performance of a model or method in inverse scattering, there are some base cases which are tested. For example, Fan *et al.* [88] successfully applied deep learning methodologies utilising the Helmholtz equation in the recovery of the shape and placement of multiple scatterers in two different

settings, including a seismic imaging setting where the source and receivers were above the scatterers and receivers were in a linear array. The scatterers were placed randomly and formed from a number of shapes such as triangles, squares or ellipses. These results were then verified against positions and shapes that were known. As well as in Johnson *et al.* [1] where the surface was created in laboratory, and those measurements were used to predict the shape of the surface relatively accurately for different noise levels [1] (Figure 5.1). However, although these results are accurate, it is only known to be accurate because of the setup used for validation.

The aim of this work is to investigate a further method of knowing if the model's prediction is correct. This is done by leveraging the potential benefits that a broadband frequency source can bring, more typical regression models (Linear regression, K-nearest neighbours, and random forests) are trained on every frequency in a broadband frequency range to estimate consistency in prediction, in order to give some confidence in prediction. Following this, the Metropolis Markov Chain Monte Carlo (MCMC) algorithm is shown on a single frequency case, yielding more information than merely a single point prediction.

The layout of this paper is as follows: Section 2 holds information about the experiment as well as the properties of the surface tested, section 3 presents the Kirchhoff Approximation, which is used to generate data for the models, as well as a discussion on the data processing. Section 4 showcases results and discussions for the models at a broadband frequency range. Section 5 introduces the Metropolis algorithm, as well as results and discussions. Section 6 contains the conclusions.

5.3 Experiment Setup

For these calculations, the source and receiver locations were chosen in accordance with the existing experimental data [74] which was used for validation in this paper. The source location was at $(x_1, y_1) = (-0.20, 0.22)$ m. The angle ϕ_0 of the source main axis to the Ox axis was 60 degrees. The receivers were located at a height of approximately $y_2 = 0.28$ m in the y-axis and 34 receivers were distributed evenly with x_2 taking values from -0.13 m to 0.53 m in the x-axis, leading to an average distance between the receivers of 0.02 m.

The real-world data used was collected with 34 1/4″ microphones (G.R.A.S. 40PH) and a loudspeaker (Visaton G 25 FFL), arranged with the same geometry discussed. A sinusoidal surface (with amplitude $\zeta_1 = 0.0015$ m and wavelength $\zeta_2 = 0.05$ m) was machined from an aluminium block.

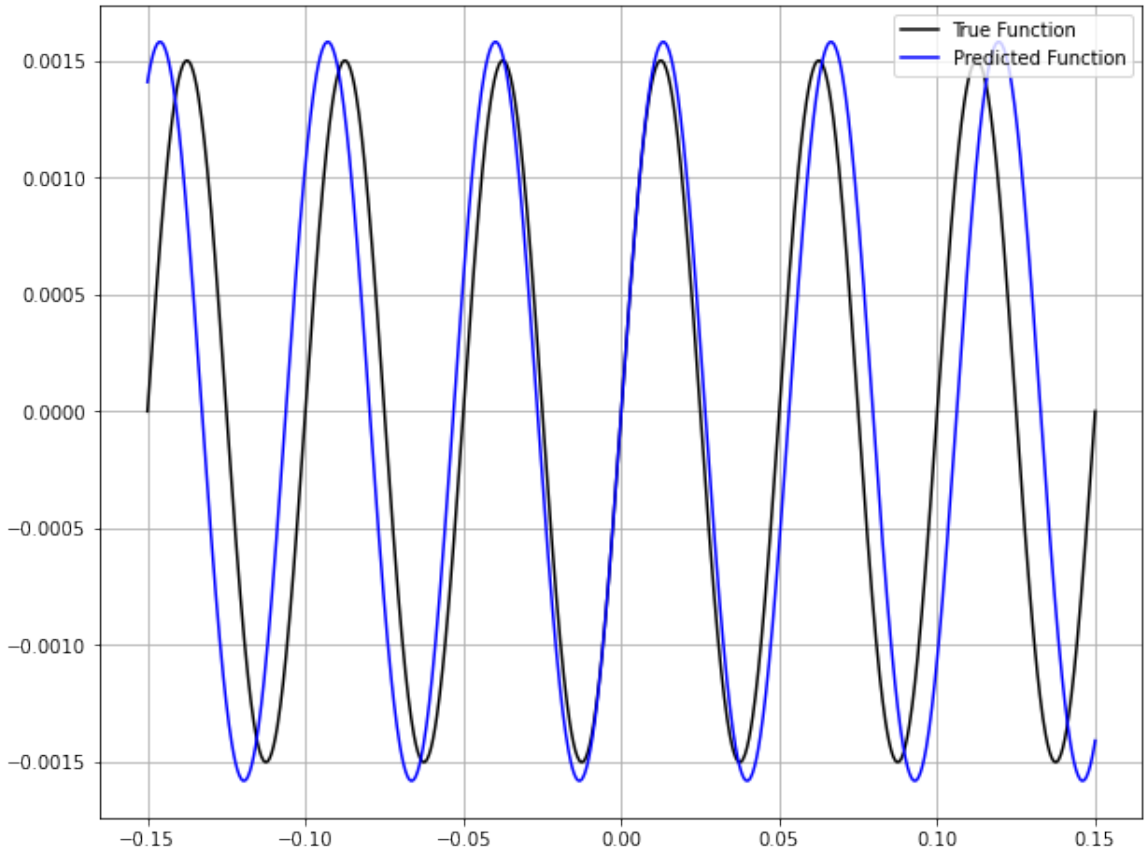

Figure 5.1: Surface reconstruction using a random forest approach, trained with 15% noise included, as highlighted in [1].

A signal was produced from the source and recorded simultaneously at all microphones, with a sampling rate of 102.4 kHz. The amplitude at each microphone was calculated by a Fourier transform applied to 0.02 s segments, and averaged over 2000 segments using Hann windowing. This yields information beginning at 10,000Hz and ending at 51,150Hz. The data was calibrated by comparing measurements of the acoustic field reflected by a flat surface with the corresponding Kirchhoff approximation, following the procedure outlined in Dolcetti *et al.*[74]. The residual difference between the measured pressure field after calibration and the one predicted by the Kirchhoff approximation is shown in Figure 5.3.

5.4 Data Generation through the Kirchhoff Approximation

Defining $\psi_s(\mathbf{R})$ as the acoustic pressure field at a point $\mathbf{R}$ produced by a source with co-ordinates (x_1, y_1), scattered by a sinusoidal rigid surface with profile

$$\zeta(x) = \zeta_1 \cos\left[\frac{2\pi}{\zeta_2}(x + \zeta_3)\right], \tag{5.1}$$

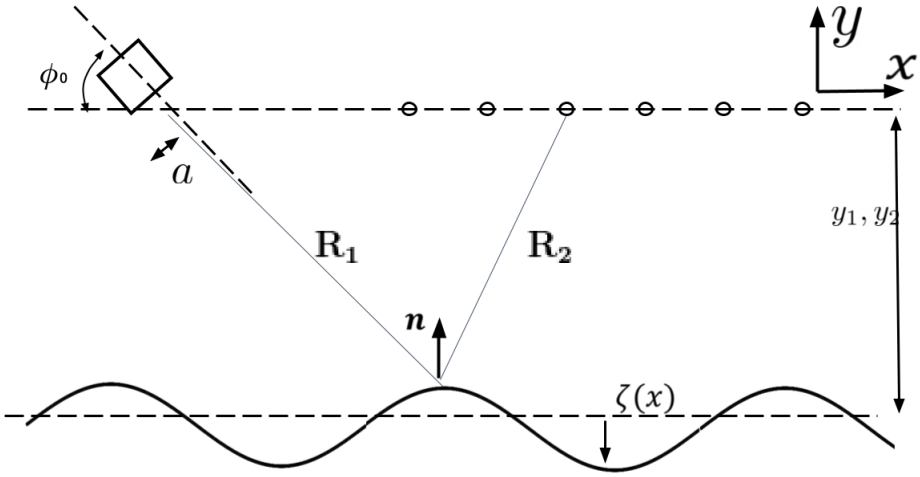

Figure 5.2: The geometry of the problem where the rough surface is defined by a function $\zeta(x)$ from equation (5.1). Surface is not to scale.

The Kirchhoff approximation is assumed to be valid if the following condition is satisfied [36]:

$$\sin(\phi) > \frac{1}{(kh)^{1/3}}, \tag{5.2}$$

where h is the local radius of curvature of the surface, k is the acoustic wavenumber and ϕ is the angle of incidence of the acoustic wave. The validity of this approximation for the conditions investigated in this work was demonstrated in Krynkin *et al.* [67, 68]. The Kirchhoff approximation is suitable for the calculation of large amounts of data, which is required for machine learning problems, while being fast to compute. With this approximation, the scattered 2D acoustic pressure ψ_s is calculated as[68]:

$$\psi_s(\mathbf{R}) = \frac{1}{2k\pi \mathrm{i}} \int_{-\infty}^{\infty} \frac{A(x,0)}{\sqrt{R_1 R_2}} \mathrm{e}^{\mathrm{i}k(R_1+R_2)}(q_y - q_x\gamma)\mathrm{d}x, \tag{5.3}$$

where, as shown in Figure 6.1, the values R_1 and R_2 are the Euclidean distance from the source at (x_1, y_1) and receiver at (x_2, y_2) to a given point $(x, \zeta(x))$ on the surface, respectively:

$$R_1 = \sqrt{(x_1 - x)^2 + (y_1 - \zeta(x))^2}, \tag{5.4}$$

$$R_2 = \sqrt{(x_2 - x)^2 + (y_2 - \zeta(x))^2}. \tag{5.5}$$

$\mathbf{R} = (x_2, y_2)$, $\gamma = \mathrm{d}\zeta(x)/\mathrm{d}x$; q_x and q_y are the x and y components of $\mathbf{q} = -k\nabla_S(R_1 + R_2)$ with the gradient $\nabla_S = (\partial/\partial x, \partial/\partial y)$. The directivity term $A(\mathbf{r})$, the far-field radiation from a baffled piston is given by [24]:

$$A(\mathbf{r}) = \frac{2J_1(ka\sin(\phi(\mathbf{r}) - (-\phi_0 + \pi/2)))}{ka\sin(\phi(\mathbf{r}) - (-\phi_0 + \pi/2))}, \tag{5.6}$$

where a is the aperture, J_1 is the Bessel function of the first kind, ϕ_0 is the angle of inclination of the source main axis to the Ox-axis, and $\phi(\mathbf{r})$ is the angle between the vector produced from the location of the source and the point $\mathbf{r}$ with the Oy-axis.

The phase is then removed from the application of the Kirchhoff approximation to simulate the scattered field by applying the modulus:

$$p(\mathbf{R}) = |\psi_s(\mathbf{R})|. \tag{5.7}$$

Taking into account the receiver locations in an array of M receivers, phase-removed acoustic pressure used in the random forest algorithm is given by the following matrix,

$$\mathbf{p} = \{p_l\left(\mathbf{R}^{(j)}\right) | \, j = 1..M, l = 1..N\}, \tag{5.8}$$

where the rows of the matrix are formed from p_l (an ensemble containing the absolute array pressure for a given ζ_l), and $\mathbf{R}^{(j)}$ form the columns (receiver locations defined with respect to the origin of the Oxy plane).

Further to this, noise can be added to the signal through row-wise operations on 5.8:

$$\tilde{\mathbf{p}}_l = \mathbf{p}_l + \epsilon_l, \tag{5.9}$$

where $\epsilon_{lj} \in \epsilon_l, \epsilon_{lj} \sim \mathcal{N}(0, \sigma)$ is drawn from a normal distribution independently for each receiver.

5.5 Recovering model confidence using a broadband frequency

A way of attempting to recover a measure of confidence in machine learning predictions that are not inherently stochastic is to use a broadband acoustic signal. Therefore, for each frequency one can generate a dataset using that frequency in the Kirchhoff approximation, then train a model on each frequency. Table 5.1 presents the frequencies used, as well as the sampling used for data generation. For brevity, the datasets did not have any noise present in the training, and ζ_3 was fixed to be 0. For each of the 824 frequencies tested, the mean-squared error of the Kirchhoff approximation against the data observed in the laboratory are shown in Figure 5.3. A comparison was made between random forests, k-nearest neighbours, and linear regression, implemented through scikit-learn [50]. The metric to measure model performance was chosen to be the coefficient of determination ($\mathscr{R}^2$) and is presented in figure 5.4. In order to evaluate the potential confidence factor of this method, a scatter plot as well as histograms of the recovered parameters for linear regression, random forests, and k-nearest neighbours are presented in Figures 5.5 and 5.6. The random forests were trained using 300 trees in the forest, and the k-nearest neighbours were trained with scikit-learn's default hyperparameters.

From figure 5.4, it is clear that linear regression is not suited to multiple parameter recovery as expected. For random forest and k-nearest neighbours, the coefficient of determination decreases as the frequency increases. This could be due to the removal of phase information, with stronger impact at higher frequencies. The k-nearest neighbours slightly outperforms the random forests, where the largest deviation is approximately at 35,000Hz.

Figure 5.5 presents the predictions for the model as scatter points compared to the true parameter values from the experiment. For linear regression (Figure 5.5a), the estimated amplitude parameter and wavelength parameter are much larger than the actual values, the predictions are consistently bad for all frequencies. For the random forest parameter (Figure 5.5b), the amplitude seems to mostly be underestimated, and the wavelength parameter seems to deviate from the actual value following the mean-squared error of the predictions presented earlier in Figure 5.3. K-nearest neighbours (Figure 5.5c) appears to be the only model presented in this work that consistently predicts the correct parameters, with only a few outliers up until near 30,000Hz.

	Minimum	Maximum	Num. of samples	Increment
Frequency	10,000Hz	51,150Hz	824	50Hz
Amplitude	-0.01m	0.01m	90	0.0002m
Wavelength	0.035m	0.15m	90	0.0012m

Table 5.1: Bounds for each parameter in the data generation stage as well as the number of samples generated within those bounds, for each frequency tested.

This is reflected in Figure 5.6, where only the k-nearest neighbour's histogram has an extremely large mode at the true parameter value. For the data used in this paper, the k-nearest neighbours could be used with a broadband acoustic signal to get some measure of confidence in prediction.

5.6 Recovering model confidence through single frequency excitation using a metropolis scheme

Instead of training models on each frequency in order to get a measure of confidence, one can also leverage existing stochastic methods on a single-frequency case. Namely, the Metropolis algorithm.

As ϵ is drawn from a probability distribution, equation 6.9 can be interpreted as:

$$P(\theta|\tilde{\mathbf{p}}_l) \sim P(\tilde{\mathbf{p}}_l|\theta)P(\theta) \tag{5.10}$$

The left-hand side is referred to as the posterior distribution and allows for distributions to be taken over parameters, $P(\tilde{\mathbf{p}}_l|\theta)$ is called the likelihood function, and $P(\theta)$ is called the prior distribution and allows for prior belief on the distribution of parameters. Now that the posterior distribution is found, the main concern is how to sample from this posterior distribution. The Metropolis algorithm will be used for this, the Metropolis-Hastings algorithm is described in Algorithm 2.

Note that to get the Metropolis algorithm from Algorithm 2 requires a symmetric proposal distribution $Q(\theta_n \mid \theta') = Q(\theta' \mid \theta_n)$. The choice of the proposal distribution was an selected from the Adaptive Metropolis (AM) algorithm [164] with a targeted acceptance rate of 0.2. The prior distribution was assumed to be independent for each parameter. The amplitude component of the prior was defined to be uniform with a lower bound at 0 and an upper bound at $y_s - 3\lambda$ the near-end of

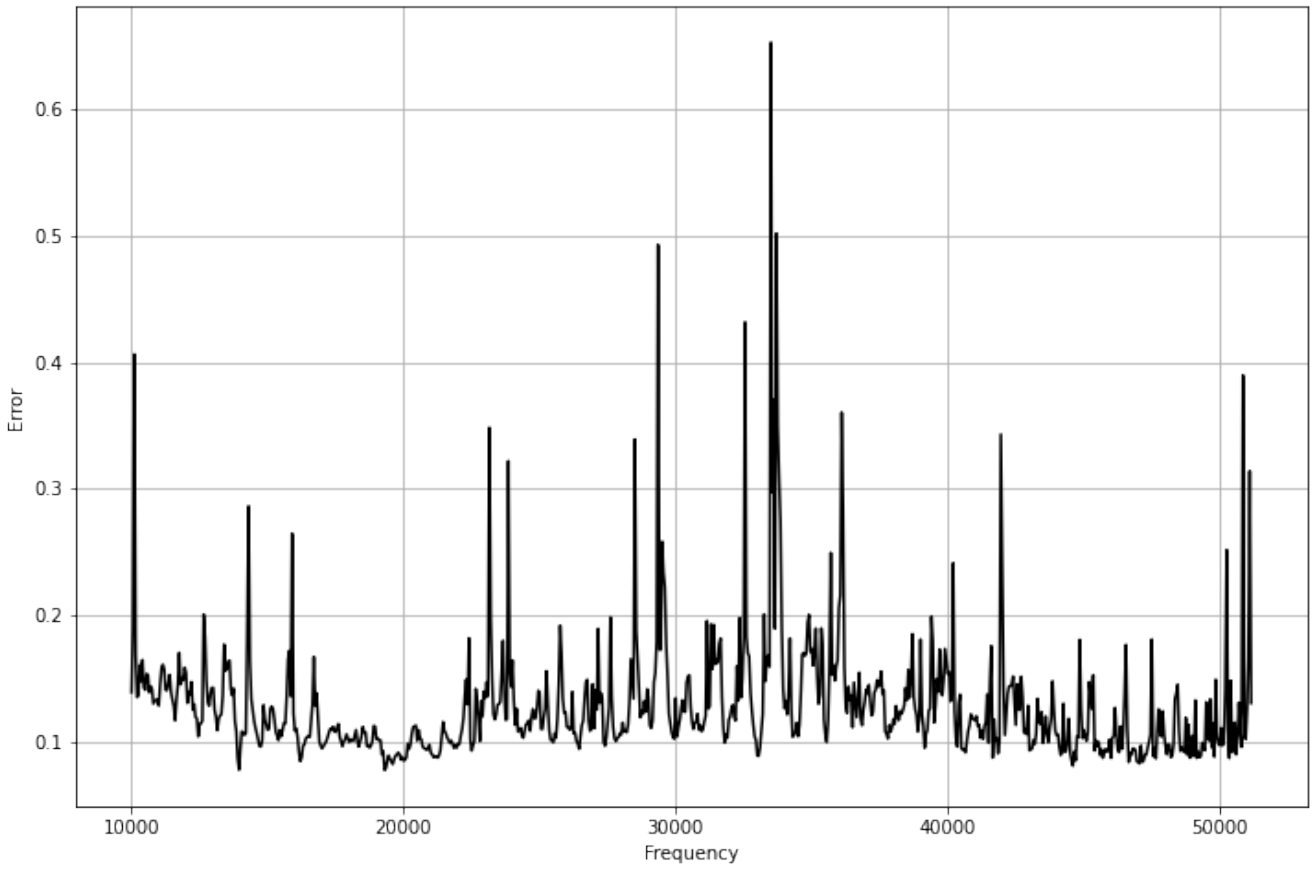

Figure 5.3: Mean-squared error of the Kirchhoff approximation against the data collected in real-world experiments.

the far-field for the acoustic source height. The wavelength was also uniform, with a lower bound of 0.08 and an upper bound of 0.4. The offset was also uniform, with a lower bound of zero and an upper bound of the wavelength. If the proposal distribution proposed a sample outside the Kirchhoff criteria, the prior was set to 0. As ϵ is drawn from a Normal distribution, the likelihood function was defined to be a multivariate normal:

$$P(\tilde{\mathbf{p}}_l|\theta) = \frac{\exp\left[-0.5(\psi_s(\mathbf{R}) - \tilde{\mathbf{p}}_l)^T \Sigma^{-1} (\psi_s(\mathbf{R}) - \tilde{\mathbf{p}}_l)\right]}{\sqrt{(2\pi)^{34}|\Sigma|}} \tag{5.11}$$

Where Σ - the covariance matrix, is a 34x34 identity matrix with ϵ on the diagonal. For the model, ϵ was taken to be 10% of the mean value from the real-data sample

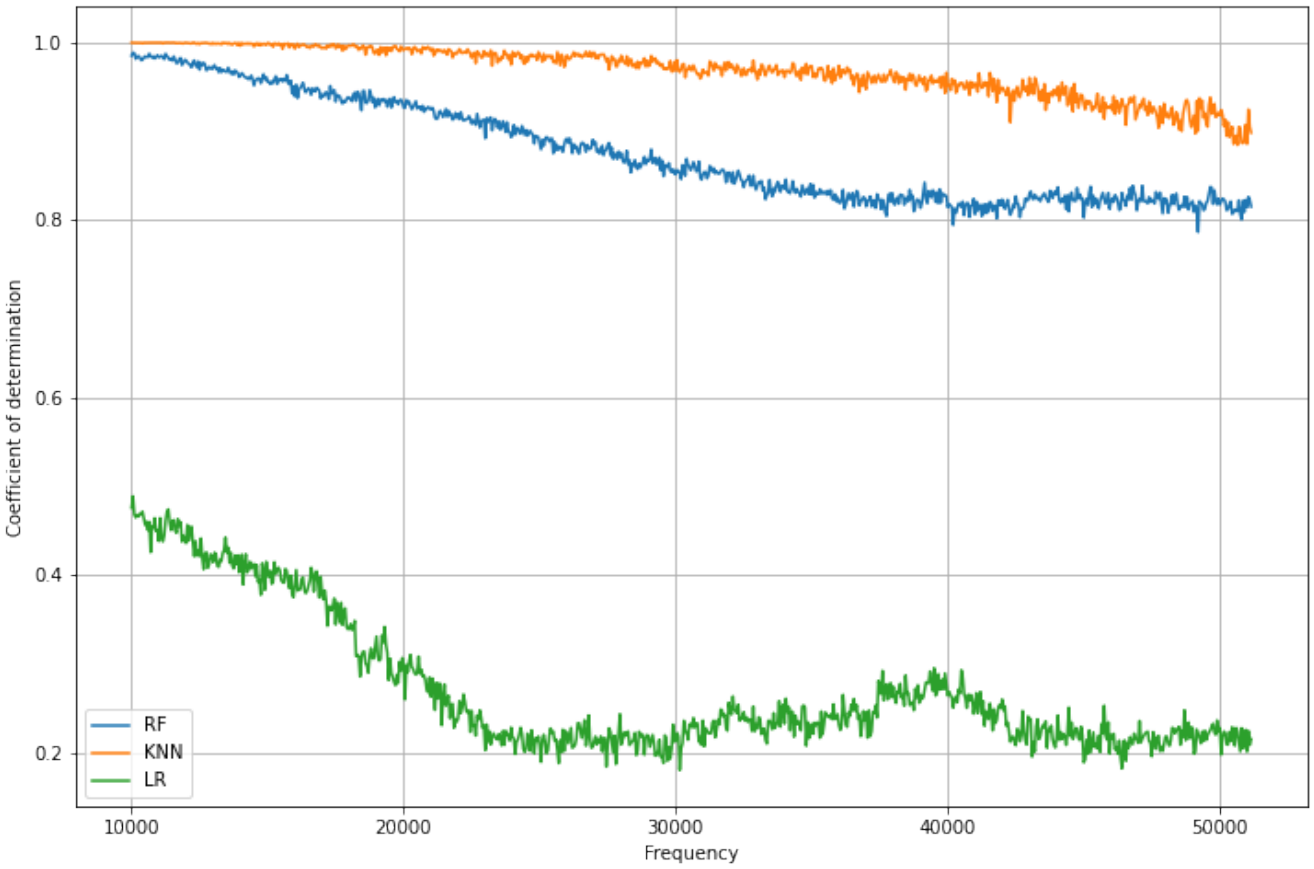

Figure 5.4: Coefficient of determination scores for random forests, k-nearest neighbours and linear regression (higher is better).

at 14,000Hz. As the Metropolis algorithm has been applied to one frequency, the offset parameter is also inferred. Figures 5.7 and 5.8 plot the resulting traces and corner plot of the obtained distribution over the three parameters for 14,000Hz source excitation, with 62,000 iterations to the algorithm.

Figure 5.7 highlights the accepted samples from the Metropolis algorithm, after a burn-in period of 5,000 samples, which is represented in grey with a vertical line indicating the cut-off point. The burn-in period is used to avoid any skew in distributions, as the accepted samples tend to the target distribution. The traces appear to be consistent, and do not jump between two discontinuous heights. Figure 5.8 present the resulting histograms of the density of each parameter on the

Algorithm 2 Metropolis-Hastings Algorithm [180]

Initialise θ_0
for $n = 0, \ldots, N-1$ **do**
  Sample $u \sim U(0,1)$
  Sample $\theta' \sim Q(\theta' \mid \theta_n)$
  if $u \leq \alpha(\theta_n, \theta') = \min\left(1, \frac{P(\theta'|\vec{\mathbf{p}}_l)Q(\theta_n|\theta')}{P(\theta_n|\vec{\mathbf{p}}_l)Q(\theta'|\theta_n)}\right)$ **then**
    $\theta_{n+1} = \theta'$ ▷ Accept sample.
  else
    $\theta_{n+1} = \theta_n$ ▷ Reject sample.
  end if
end for

diagonal, and the joint density between two parameters. The resulting densities are very clear single modal, almost Gaussian, distributions. The wavelength has a mode exactly at the true wavelength parameter, and the amplitude's mode is over-estimated by a millimetre. Interestingly, although the phase is 0, the offset's mode is at the wavelength parameter, which relates to a phase of 2π. So although the offset is unexpected, as the surface is periodic the distribution is expected. The resulting distributions seem to provide more easily interpretable information than the broadband frequency investigation highlighted earlier.

5.7 Conclusions

To conclude, utilising a broadband acoustic source could be used in order to find some metric of confidence in the model's predictions. In this case, the peak mode given from the K-NN constant prediction at the true parameter values could be leveraged in order to have a more informed prediction for real-time predictions. However, this leveraging does not produce “clean" Gaussian-like behaviour, such as what was observed using the Metropolis scheme. If true stochastic information is needed, then the Metropolis scheme is highly recommended over the broadband signal. However, due to the time taken for the Metropolis scheme to run (approximately 1 hour), this would not be able to yield real-time predictions. It is also important to note that there have been some limitations in creating the datasets for this paper, the most important of which are: not including noise inside the data, which limits generalisation, and a limited number of samples, which allows for a more dense domain knowledge for the model. It is also important to note that this method, which fits a dataset on every frequency, will be affected by the curse

of dimensionality [181] where the data required for higher dimensional surface recovery will require much more data to be able to give any reasonable predictions.

5.8 Acknowledgements

The authors are grateful to Dr. Timo Lähivaara at the University of Eastern Finland for valuable guidance on the statistical sampling procedure.

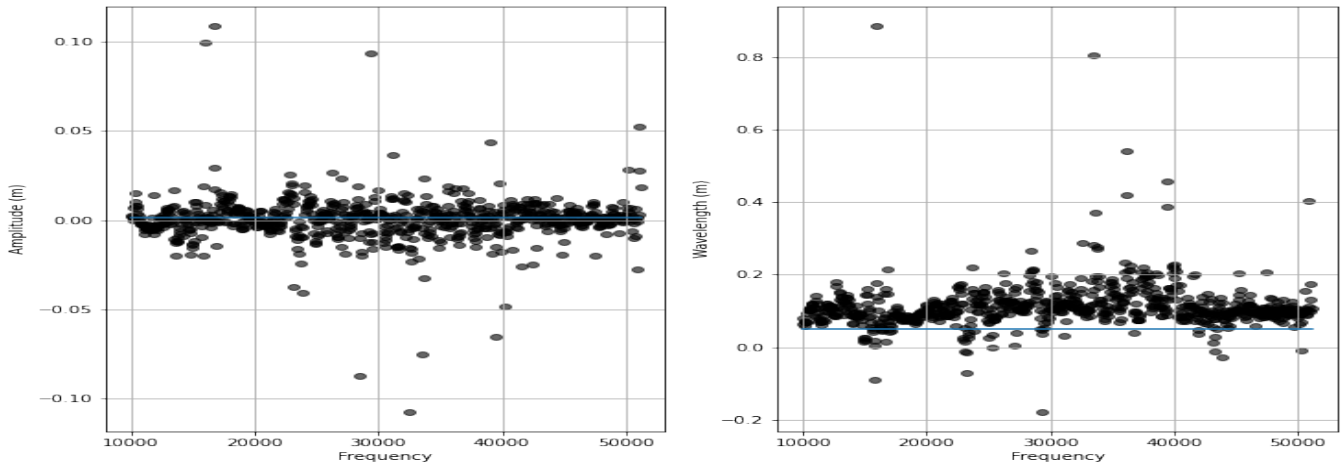

(a)

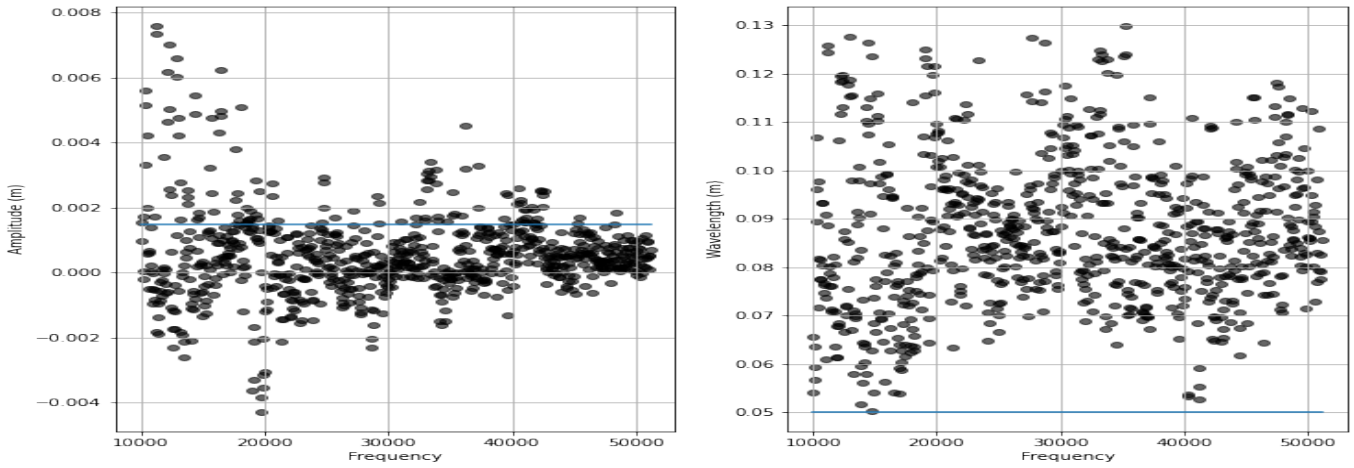

(b)

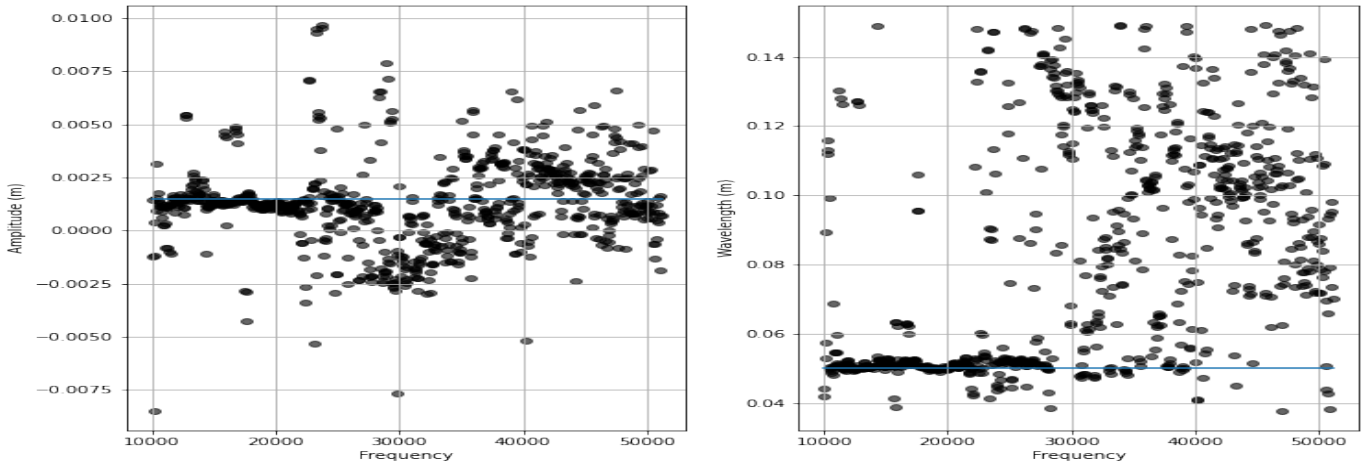

(c)

Figure 5.5: Scatter plots for the parameter recovery at all frequencies for (a) linear regression, (b) random forests, and (c) k-nearest neighbors. The blue horizontal line indicates the true parameter values from the experiment.

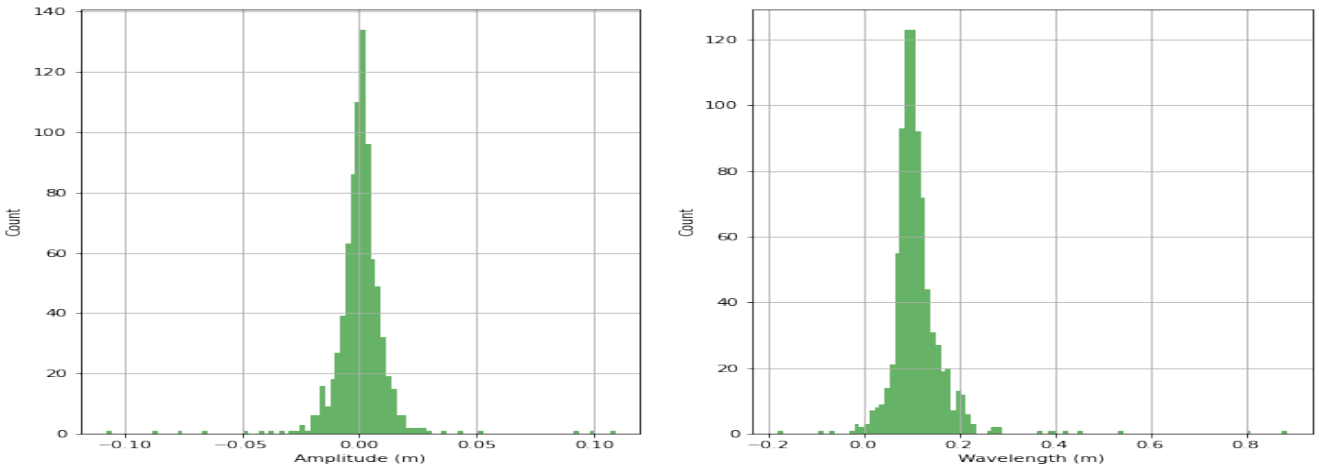

(a)

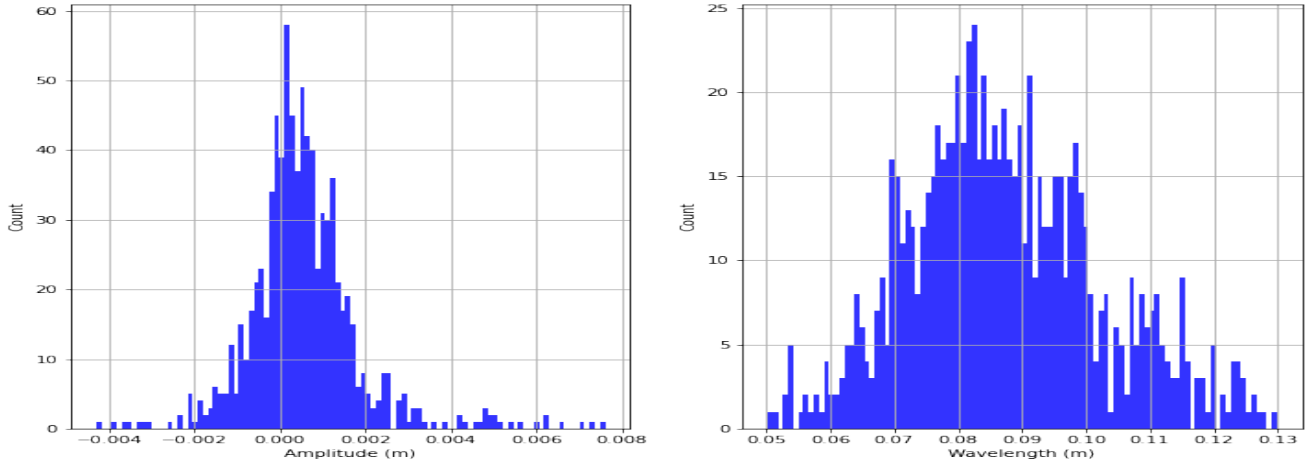

(b)

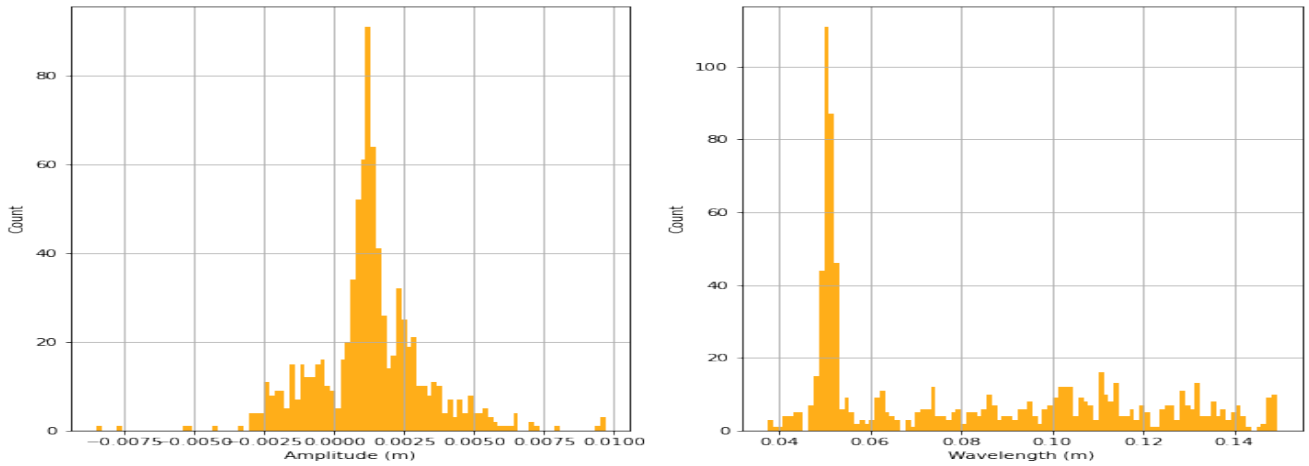

(c)

Figure 5.6: Histograms for the parameter recovery at all frequencies for (a) linear regression, (b) random forests, and (c) k-nearest neighbors.

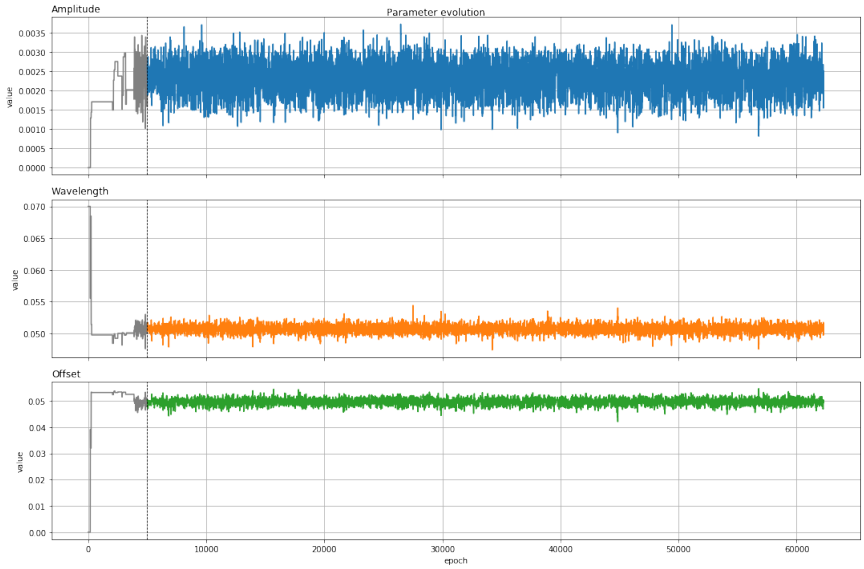

Figure 5.7: Traces of the resultant Metropolis-Hastings scheme for the amplitude, wavelength, and offset. Including the cutoff for the burn-in period.

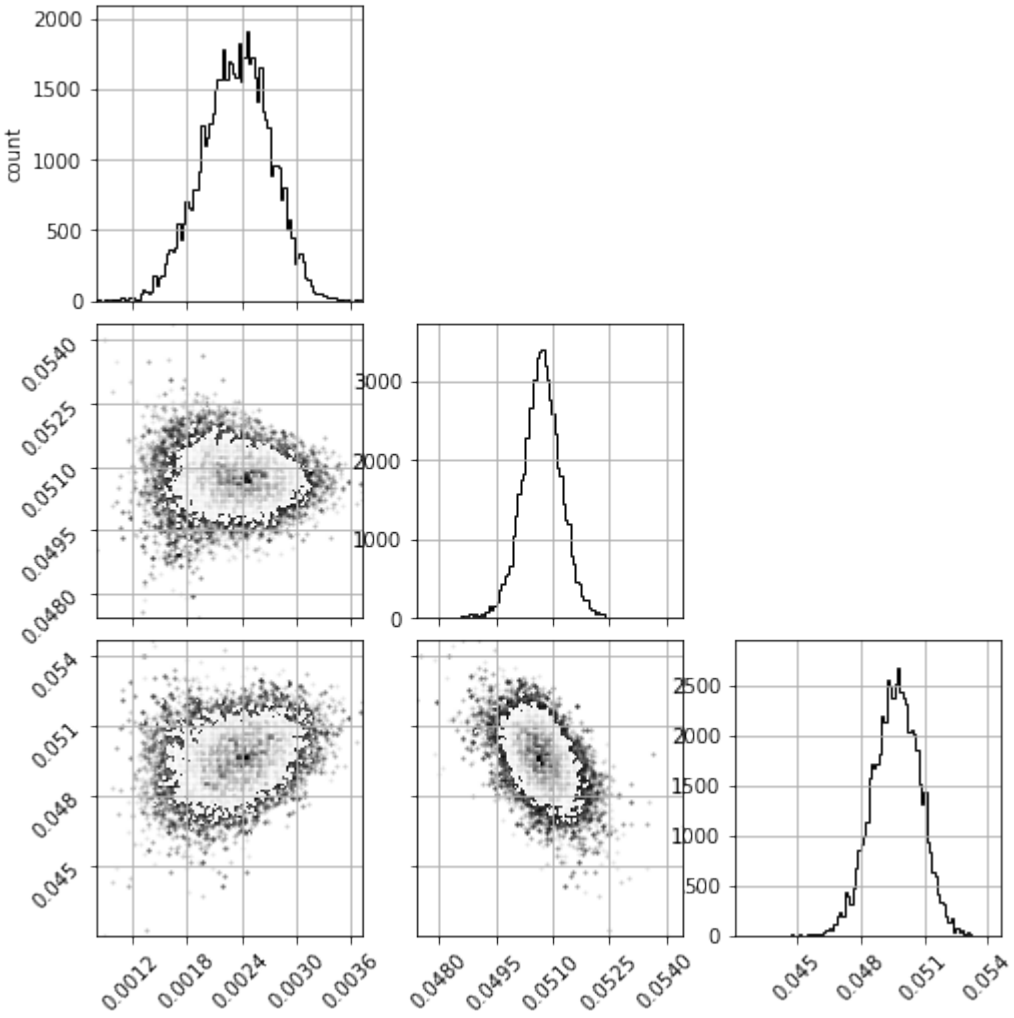

Figure 5.8: Corner plot of the Metropolis-Hastings scheme for the amplitude, wavelength, and offset.

Chapter 6

Bayesian reconstruction of surface shape from phaseless scattered acoustic data

Reference

Johnson, M. D., Cuenca, J., Lahivaara, T., Krynkin, A., Dolcetti, G., Alkmim, M., and De Ryck, L. Bayesian reconstruction of surface shape from phaseless scattered acoustic data.

Author Contributions

- Johnson, M.D., - Problem formulation, writing, model development, data analysis, editing, structure.
- Cuenca, J. - editing, technical advice.
- Lahivaara, T. - editing, technical advice.
- Krynkin, A. - editing, figure editing.
- Dolcetti, G. - editing, data collection, writing with respect to the data collection subsection
- Alkmim, M. - editing, data collection.
- de Ryck, L. - editing, data collection.

Summary

A key problem with the results in Chapter 4 is the lack of ability to gain a measure of confidence, or error, for a single sample. This was answered with a holistic approach to the broadband nature of the source excitation in Section 5, where data can be created for each frequency bin, then a model can be trained on each frequency and thus N predictions can be made (where N is the number of distinct frequencies in the frequency range). In the paper presented in this section, the problem is rephrased such that it can be considered from a Bayesian viewpoint. This allows the posterior distribution of the parameters to be extracted; in this instance the adaptive metropolis scheme was used. The application of this was the main outcome from this section.

This section also investigates higher order problems, where the rough surface can be approximated by 20 rather than 1 cosine. Alongside the three-parameter dataset and experimental data, another experimental dataset was collected. This dataset was a rough surface which could be approximated as a sum of twenty cosine waves. The problem is reduced to finding the amplitudes and phases of each term in the sum by assuming that the wavelengths are known. This is a safe assumption because the surface was broken down by a Fourier series, so the wavelength component is known.

The Kirchhoff Approximation was extended into the Bayesian framework, and the appropriate prior distribution, and likelihood function was defined. The prior distribution was modified such that the Kirchhoff condition of the acoustic wavenumber being much larger than the radius of curvature was included. This is powerful because assumptions in the model approximation, and the physics, can be encoded in the prior. For three-parameter estimation, this can be found analytically, and this is included in this section. For 40 parameters, this is found numerically.

The three-parameter experimental data was used in the Adaptive Metropolis scheme and was compared to the Random Forest approach from chapter 4. There are further visualisations of how the phaseless acoustic pressure changes with respect to the trace. The forty-parameter recovery was also showcased for the whole printed surface of 60 cm. There is a clear thinning of the credible interval and better agreement to the truth in the region of high insonification. The spatial dependence on the credible interval gives good information on the region of validity as well as the regions not to be trusted.

6.1 Abstract

The recovery of the properties or geometry of a rough surface from scattered sound is of interest in a wide range of applications, including medicine, water engineering or structural health monitoring. Existing approaches to reconstruct the roughness profile of a scattering surface based on sound or electromagnetic wave scattering have no intrinsic way of predicting the uncertainty of the reconstruction. In an attempt to recover this uncertainty, a Bayesian framework, and more explicitly an Adaptive Metropolis scheme, is used in the present work to infer the properties of a rough surface, parameterised as a superposition of sinusoidal components. The Kirchhoff Approximation is used in the present work as the underlying model of wave scattering, and is constrained by the assumption of surface smoothness. This implies a validity region in the parameter space which is incorporated in the Bayesian formulation, making the resulting method more physics informed than data-based approaches. For a three-parameter sinusoidal surface and a rough surface with a random roughness profile, the experiments were conducted to collect scattered acoustic pressure data. The models were then tested on the experimental data. The recovery highlights regions where the method is confident, and could be used as a method to identify uncertainty.

6.2 Introduction

Non-intrusive acoustic inversion to recover the elevation or other properties of rough surfaces is of great interest and an active research field [182, 183, 184, 185], especially in the setting of river monitoring, where intruding the flow could change the properties significantly. A numerical method based on the boundary integral equations and Kirchhoff Approximation to reconstruct the shape of a scattering surface was outlined in [67, 68]. This approach was found to be highly sensitive to uncertainties, partly because of the strong dependence on the phase of the scattered signal [74]. The errors in the inversion results were associated with the underdetermined and ill-posed nature of the problem [74]. The range of applicability in reconstructing a surface is also limited by the validity of a partial linearisation of the scattering problem, which is required in order to make the numerical inversion feasible. The method was expanded to a multiple frequency approach [74], and a machine learning approach utilising random forests [186]. However, although the

performance of these methods have been promising, the statistical measure of the uncertainty is an open question.

The Kirchhoff Approximation is still an active part of reconstruction efforts, as in [167]. Other methods have risen in inverse scattering, especially in the near-field, such as recovering the scattering coefficients [168] [169].

Bianco *et al.* [52] presented machine learning in the context of acoustics, with key examples such as source localisation. Similarly, Andrieu *et al.* [98] introduced Markov-Chain Monte-Carlo (MCMC) methods, providing key theoretical understanding and algorithms for many methods, including Metropolis-Hastings and Sequential Monte-Carlo.

Bayesian methods have recently gained popularity in the field of acoustics, with applications such as recovering parameters from the seafloor using acoustic backscattering [99], estimation of rough surface elevation using a Bayesian compressive sensing [100], and for acoustic holography [101] [102]. Li *et al.* [103] applied a Metropolis-Hastings (MH) MCMC scheme in order to reconstruct the locations and intensities of acoustic sources from near-field and far-field data. The numerical results using Metropolis-Hastings for one of the examples analysed by Li *et al.* are “close to the exact ones" [103], and improvement is shown in other examples.

Application of a Bayesian approach for acoustic scattering with phaseless data was proposed by Yang *et al.* [104, 105]. In Yang *et al.* [104], the location and shape of a sound-soft scatterer were reconstructed. The approach was tested on shapes such as kites, disks, and line cracks with favourable results, noting that the number of parameters being recovered from the MCMC algorithm was no larger than 6. In Yang *et al.* [105], the method was extended to use a Gibbs sampling method in order to recover more parameters, with phaseless data and a point source excitation. Palafox *et al.* [106] also used a Bayesian formulation in order to reconstruct the shape of a kite, through a reduction of the problem by a Fourier-based representation using a t-walk [107]. The effective dimension method was presented where, given a parametric representation of the solution of the inverse problem, the normalising constant can be approximated. Bayesian methods have also been applied in inverse problems in other fields, such as for seismic waveform inversion [108], and automatic motion analysis in tagged magnetic resonance imaging scans [109][110]

Application of the adaptive Metropolis-Hastings scheme in relation to acoustical inverse problems can be seen in Niskanen *et al.* [111], where the Johnson–Champoux–Allard–Lafarge model was used in conjunction with a Metropolis-

Hastings in order to recover the model parameters of a homogeneous rigid frame porous media. The joint probability densities verified that the least-squares solution was close to the Maximum a posteriori estimation from the MCMC method. Konarski *et al.* [187] used a similar method, to recover properties from aluminium foams.

This work re-frames the Kirchhoff Approximation into a Bayesian viewpoint, allowing for well-developed sampling schemes such as the Adaptive Metropolis [164] algorithm to be used to infer the uncertainties of the recovery. Further, the rough surface is parameterised into a sum of sinusoidal functions, thus potentially reducing the number of parameters to recover, as well as allowing the use of the validity criterion of the Kirchhoff Approximation as a constraint. A three-parameter sinusoidal surface presented in [1] is used for verification, as well as a random Gaussian elevation profile used in [74]. The latter is parameterised from a specific Fourier decomposition, where the unknowns of the problem are the amplitude and phase values of a number of sinusoidal components over a fixed wavelength range.

The paper is organised in the following way: Section 6.3 presents the parameterisation method of rough surfaces and the theory for the Kirchhoff Approximation. Section 6.4 proposes a formulation within the Bayesian framework, the Metropolis-Hastings algorithm, and the approximation for the prior with three-parameter surfaces. Section 6.5 presents the information on the acoustic experiment setup for the three-parameter and the recovery of a 40-parameter rough surface. Section 6.6 presents the results for the recovery of the three-parameter surface, and random 40-parameter rough surface with a flat surface as an initial condition. This is followed by discussions on efficiency of the inversion algorithm. Section 6.7 concludes the report.

6.3 Forward model of acoustic scattering

The goal of the work is to recover the shape of a rough surface from scattered acoustic pressure. In order to reduce the number of parameters needed to infer and approximate the shape of the surface of interest, this work investigates surfaces whose shape can be described as a superposition of harmonic components. Defining N harmonics of the surface through parameters $\theta = \{\theta_j | \, j = 1, \ldots, 3N\}$ a surface profile can be expressed as:

$$\zeta(x, \theta) = \sum_{i=0}^{(N-1)} \theta_{3i+1} \cos\left(\frac{2\pi x}{\theta_{3i+2}} + \theta_{3i+3}\right) \tag{6.1}$$

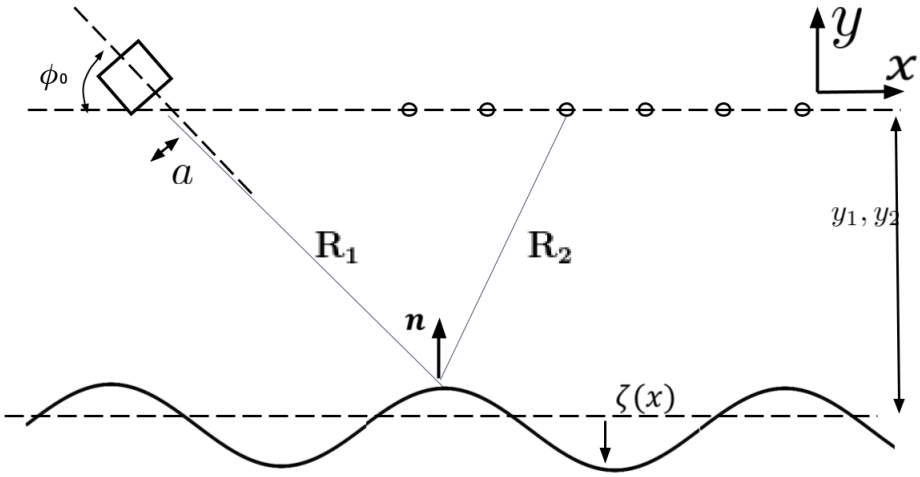

Figure 6.1: The geometry of the problem where the rough surface is defined by a function $\zeta(x)$ from Equation (6.1). Surface is not to scale.

The acoustic signal was recorded at a set of M microphones with coordinates given by $\mathbf{R}^{(j)} = \{(x_2^{(j)}, y_2^{(j)}) | \, j = 1, \ldots, M\}$.

The Kirchhoff Approximation (KA) was chosen due to its ability to represent the scattered acoustic field in an explicit form, obtained with the assumption based on reflections from a tangent plane. This closed form enables fast calculations, as opposed to the full boundary integral equation solution, for instance. The suitability of this approximation for the conditions analysed in this paper was presented in Krynkin *et al.* [67, 68]. The problem is stated in two-dimensional Oxy semi-infinite domain, assuming a uniform solution in the out-of-plane direction and time harmonic dependence $\exp(-\mathrm{i}\omega t)$.

The domain is bounded by the rough surface $\zeta(x, \theta)$ defined with Equation (6.1). The surface $\zeta(x, \theta)$ satisfies the Kirchhoff Approximation condition given by [36]

$$\sin(\phi) > \frac{1}{(kh)^{1/3}}, \tag{6.2}$$

where h is the radius of curvature of the surface, k is the acoustic wavenumber, and ϕ is the angle of incidence of the acoustic wave. Assuming separation of variables, with the condition (6.2) satisfied and for a source with a given directivity pattern at a given point on the surface $A(x, y)$, the scattered acoustic pressure ψ_s can be expressed in the following Equation [68]:

$$\psi_s(\mathbf{R}, \theta) = \frac{1}{2k\pi\mathrm{i}} \int_{-\infty}^{\infty} \frac{A(x, y)}{\sqrt{R_1 R_2}} \exp\left(\mathrm{i}k(R_1 + R_2)\right)(q_y - q_x\gamma)\,\mathrm{d}x, \tag{6.3}$$

where, as shown in Figure 6.1, the values R_1 and R_2 are the Euclidean distances from the source at (x_1, y_1) and receiver at (x_2, y_2) to a given point $(x, \zeta(x,\theta))$ on the surface, respectively:

$$R_1 = \sqrt{(x_1 - x)^2 + (y_1 - \zeta(x,\theta))^2}, \tag{6.4}$$

$$R_2 = \sqrt{(x_2 - x)^2 + (y_2 - \zeta(x,\theta))^2}. \tag{6.5}$$

In Equation (6.3), $\mathbf{R} = (x_2, y_2)$, $\gamma = \mathrm{d}\zeta(x,\theta)/\mathrm{d}x$; q_x and q_y are the x and y components of $\mathbf{q} = -k\nabla_S(R_1 + R_2)$ with the gradient defined by the nabla operator in 2D, $\nabla_S = (\partial/\partial x, \partial/\partial y)$. The directivity term $A(x,y)$ is defined in this work as the far-field radiation from a baffled piston, which is given by [24],

$$A(x,y) = \frac{2J_1(ka\cos(\phi(x,y) + \phi_0))}{ka\cos(\phi(x,y) + \phi_0)}, \tag{6.6}$$

where a is the aperture, $J_1(\cdot)$ is the Bessel function of the first kind, ϕ_0 is the angle of inclination of the source main axis to the Ox-axis, and $\phi(x,y)$ is the angle between the vector defined by the location of the source and the point (x,y) with the Oy-axis.

Following the application of the Kirchhoff Approximation to simulate the scattered field, the phase is removed from Equation (6.3) through the application of the modulus:

$$p(\mathbf{R},\theta) = |\psi_s(\mathbf{R},\theta)|. \tag{6.7}$$

Taking into account the receiver locations in an array of M receivers, phase-removed acoustic pressure is given by the following matrix,

$$\mathbf{p}(\theta) = \{p\left(\mathbf{R}^{(j)},\theta\right) | \, j = 1,\ldots,M\}, \tag{6.8}$$

where the matrix is formed from p (an ensemble containing the absolute array pressure for a given surface profile ζ), where $\mathbf{R}^{(j)}$ form the columns (receiver locations defined with respect to the origin of the Oxy plane).

The Kirchhoff Approximation model is deterministic, therefore one set of surface parameters maps to a given sound pressure field. However, in practical applications, noise is present in measured data. It is proposed to modify the solution of the Kirchhoff Approximation via additive noise, calculated as:

$$\tilde{\mathbf{p}}(\theta) = \mathbf{p}(\theta) + \epsilon, \tag{6.9}$$

where $\epsilon = \epsilon_j | \, j = 1,\ldots,M, \quad \text{with} \quad \epsilon_j \sim \mathcal{N}(0,\sigma)$ is drawn from a normal distribution independently for each receiver with mean 0 and standard deviation σ.

6.4 Inverse problem

6.4.1 Bayesian Framework

The observation model in Equation (6.9) is here considered in the Bayesian framework. As ϵ is drawn from a probability distribution, Equation (6.9) motivates:

$$\mathscr{P}(\theta|\tilde{\mathbf{p}}) \propto \mathscr{P}(\tilde{\mathbf{p}}|\theta)\mathscr{P}(\theta). \tag{6.10}$$

The left-hand side is referred to as the posterior distribution and allows for distributions to be taken over parameters θ, $\mathscr{P}(\tilde{\mathbf{p}}|\theta)$ is called the likelihood function which is the probability of the observed acoustic pressure given the model parameters, and $\mathscr{P}(\theta)$ is called the prior distribution and encompasses prior belief on the distribution of parameters. In the present paper, the prior distribution is defined from the Kirchhoff Approximation condition, as detailed further below.

With the Gaussian noise in the observation model (6.9), the likelihood $\mathscr{P}(\tilde{\mathbf{p}}|\theta)$ can be written as:

$$\mathscr{P}(\tilde{\mathbf{p}}|\theta) = f_{MN}(\tilde{\mathbf{p}}, \theta, \Sigma) \tag{6.11}$$

with

$$f_{MN}(\tilde{p}, \theta, \Sigma) = \frac{\exp\left\{-[\tilde{p} - \mathbf{p}(\theta)]^T \Sigma^{-1} [\tilde{p} - \mathbf{p}(\theta)]/2\right\}}{\sqrt{(2\pi)^k |\Sigma|}}, \tag{6.12}$$

where f_{MN} is a multivariate Gaussian probability density function and Σ is a covariance matrix representing the error ϵ added to each receiver. In the present work, the observed acoustic pressure is assumed uncorrelated across receivers and therefore the covariance matrix is assumed to be diagonal.

6.4.2 Posterior sampling algorithm

The algorithm used for this work is the Metropolis-Hastings (MH) algorithm, where the proposal distribution is obtained adaptively to target a specific acceptance rate [112], [164] which helps navigate the proposal widths when the number of dimensions is high. The proposal distribution determines the probability of moving the samples in the trace, and the construction is given in Haario [164]. A key piece of literature in understanding various MCMC methods, including the method used in this work, is given in [188]. As an initial state the surface is considered flat, both in the three-parameter and 40-parameter problems. For every iteration, a uniform random number is generated in order to randomly accept or reject the sample. The

next sample is drawn from the proposal distribution. The posterior is then calculated for the current sample, as well as the proposed sample, and the ratio is calculated. If the posterior of the proposed sample is greater than the posterior of the previous sample, then the value is greater than 1, guaranteeing that the proposed sample is accepted. If the ratio is greater than zero and less than 1, then the uniformly generated number is used to add the Monte-Carlo element. Typically, the collection of accepted and rejected samples is referred to as the trace, and the trace tends to settle to the required behaviour. Removing that transitional period at the start of the trace is referred to as removing the "burn-in" period. The reader can find a more detailed description of the Metropolis-Hastings algorithm in [189].

6.4.3 An approximation for three-parameter recovery

For three-parameter recovery, the Kirchhoff condition (6.2) only depends on the surface amplitude θ_1, the surface wavelength θ_2, and the acoustic wavelength from the source excitation λ. For the range of parameters that this paper is dealing with, the bounds of surface wavelength for satisfying the Kirchhoff condition for a given source excitation frequency at a given acoustic wavenumber, surface amplitude, and angle of incidence can be approximated with the following expression [Appendix A]:

$$\theta_2 > \sqrt{\frac{(2\pi)^2}{k\sin^3(\phi)}|\theta_1|} = \beta. \tag{6.13}$$

The surface amplitudes θ_1 is further restricted by constraining the maximum amplitude to be $y_s - 3\lambda$ as an empirical bound for the acoustic far field. Assuming a maximum allowed wavelength value $\theta_{2,\max}$ say, this gives a clear closed region of satisfied parameters in amplitude-wavelength space, allowing for a change in the prior (assuming uniform prior):

$$\mathscr{P}(\theta) = f(\theta_1, \theta_2)U(0, 2\pi), \tag{6.14}$$

where (θ_1, θ_2) is the conditional uniform distribution of θ_1 and θ_2 over the domain of satisfied parameters given by Equation (6.15).

$$f(\theta_1, \theta_2) = \begin{cases} \left[\displaystyle\int_{-(y_s-3\lambda)}^{y_s-3\lambda} \int_{\beta}^{\theta_{2,\max}} 1 \, \mathrm{d}\theta_2 \, \mathrm{d}\theta_1 \right]^{-1} & \text{if } |\theta_1| \leq y_s - 3\lambda,\ \beta \leq \theta_2 \leq \theta_{2,\max} \\ 0 & \text{otherwise.} \end{cases} \tag{6.15}$$

U is the uniform distribution for the phase between 0 and 2π. Therefore, for the three-parameter case, the prior can be evaluated analytically. For higher dimensional cases, the Kirchhoff condition needs to be evaluated numerically, for every step in the MCMC scheme. In the case of the 40 parameter recovery for this research, the prior on the amplitude and phase parameters are drawn from a uniform distribution, with exception when the Kirchhoff criterium fails. In the case when the Kirchhoff condition fails, the prior is set to zero.

It should also be noted that to measure the accuracy of the recovered surface parameters, two types of mean surfaces are used in this paper. For the first type, the mean surface (referred to as $\zeta(x,\overline{\theta})$) is found by substituting mean $\bar{\theta}$ of surface parameter samples θ obtained from traces of Metropolis-Hastings scheme into Equation (6.1). The second type of the mean surface (referred to as $\overline{\zeta(x,\theta)}$) is found by taking the mean of all surfaces recovered from traces of Metropolis-Hastings scheme with Equation (6.1).

6.5 Data collection

In order to validate the surface reconstruction methodology, scattered acoustic pressure was recorded by a set of 34 1/4″ microphones (G.R.A.S. 40PH) above two acoustically rigid surfaces with known profiles seen in [74]. One surface profile was milled on the upper face of an aluminium block with horizontal dimensions 0.55×0.35 m^2. The profile was sinusoidal along the longer dimension, with a wavelength of 50 mm and a peak-to-peak amplitude of 3 mm, and was constant along the shorter dimension. The second profile was milled onto a block of medium-density fiberboard (MDF) with dimensions of 0.6×0.4 m^2. This profile was generated via Fourier synthesis[190] as a sum of cosines as in Equation (6.16):

$$\zeta_{\exp}(x) = \sum_{i=0}^{N/2} \sqrt{2\Psi(K_i)}\mathcal{N}(0,1)\cos\left(K_i x - \mathcal{U}(0,2\pi)\right), \tag{6.16}$$

where $\mathcal{N}(0,1)$ indicates a sample from a normal distribution, and $\mathcal{U}(0,2\pi)$ a sample from a uniform distribution in the interval $[0,2\pi]$. $\Psi(K_i)$ represents the surface power spectrum as a function of the wavenumber $K_i = i2\pi/L$. The amplitude spectrum varied like a power function of the wavenumber, $\Psi(K_i) \propto K_i^{-\alpha}$, which is representative of natural surfaces such as the water surface or the bed surface of rivers or of the oceans[124, 191, 192, 193]. Here, the surface had $\alpha = 5$, in agreement with experimental observations of the water surface of open-channel flows[18].

To ensure the integrability of the spectrum, a saturation range at low wavenumbers $K_i < 2\pi/0.05$ rad m^{-1} was introduced following Stewart *et al.* (2019),[193] i.e., $\Psi(K_i < 2\pi/0.05) = \Psi(2\pi/0.05)$. The spectrum had a small-scale cutoff at $K_i > 2\pi/0.01$ rad m^{-1}. The standard deviation of the random surface was equal to 1 mm and satisfied the Kirchhoff condition.

A signal was produced at 14 kHz with a loudspeaker (Visaton G 25 FFL), arranged with the same geometry described in Johnson *et al.* [1], and recorded simultaneously at all microphones, with a sampling frequency of 102.4 kHz. The signal amplitude at each microphone was calculated by a Fourier transform applied to 0.02 s long segments of the signal using a Hann window, and then averaged over 2000 segments. The data was calibrated in situ by comparing measurements of the sound field reflected by a flat surface with the corresponding prediction calculated numerically, following the procedure outlined in Dolcetti *et al.*[74].

6.6 Results

6.6.1 Three-parameter recovery

For the three-parameter surface, the Adaptive Metropolis scheme was used, running for 100,000 samples. The burn-in period was set at 10,000 samples, and the covariance matrix was updated every 20 samples. $\sigma = 0.15$ was measured as noise standard deviation. Due to the covariance matrix and the adaptive scheme, the width of the proposal distribution was adapted to allow a 20% acceptance rate.

Figure 6.2 presents a corner plot generated with the method outlined in Foreman-Mackey[194]. The leading diagonal presents a histogram representing the density for each parameter, with the vertical lines representing the 68% credible interval. The scatter plots represent the 2D marginal probability distributions. The wavelength parameter is highly accurate, with approximately 0.1% error from the true wavelength at the mean of the distribution. The amplitude is overestimated by 0.5 mm, and the spread is high.

Figure 6.3 presents the comparison between the surface obtained from the conditional mean of each parameter in the trace, the mean of all the surfaces generated from the distribution of parameters, and the 68% credible interval. For the case of the surfaces generated from the mean of each parameter in the trace (dashed line in Figure 6.3), the mean amplitude is overestimated, and the wavelength - in the region of the most insonified area - matches favourably. Outside this region, the

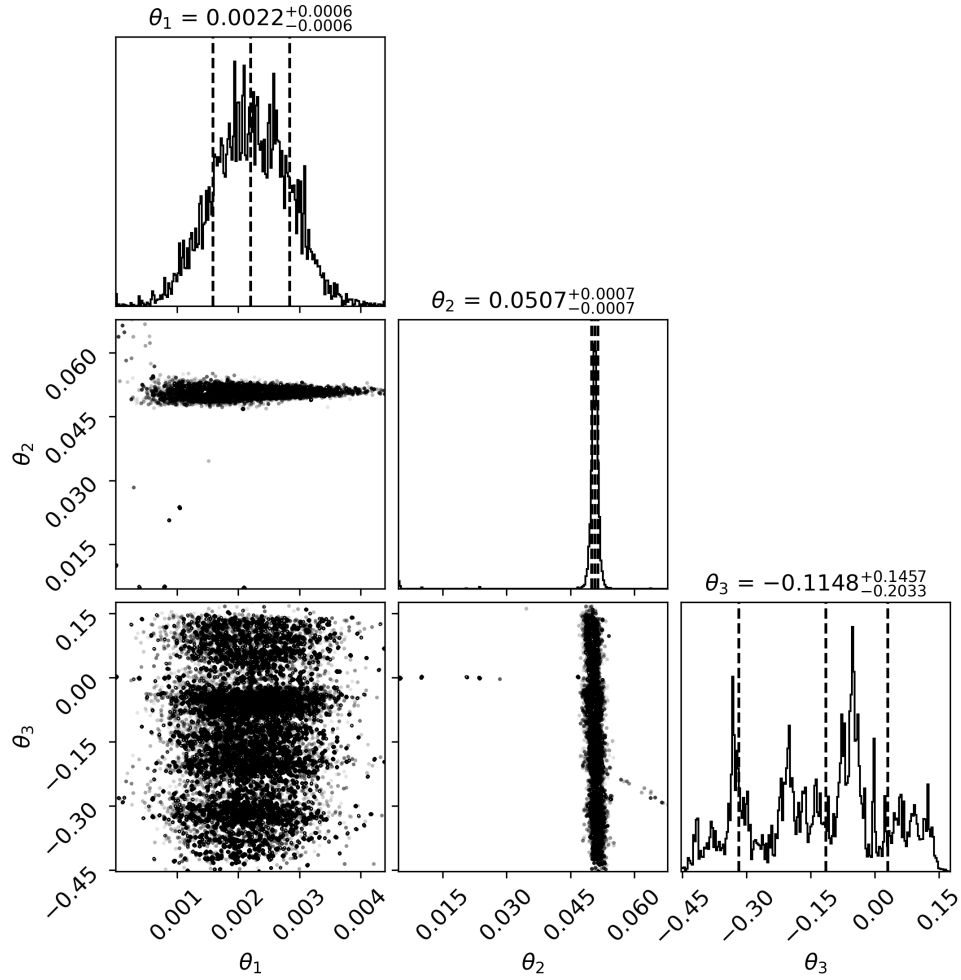

Figure 6.2: Corner plot of the distribution of the traces for the amplitude, wavelength, and phase. The subtitles contain the mean and the 68% credible interval bounds.

accuracy due to the wavelength begins to decrease. This behaviour is replicated in the credible interval, where the shaded region widens further away from the region of high energy.

For the case of the mean from the collection of surfaces generated by the parameters in the distribution, the amplitude decreases as the x coordinate increases, this is due to the variation in wavelength as x increases.

Figure 6.4 presents the acoustic pressure from 1000 random samples from the trace. Investigating the pressure, the peaks in the absolute pressure are well mapped, as the random samples from the trace converge to the peaks. The regions where the absolute pressure does not change much, such as in regions between receivers 10 and 15, contain more uncertainty, which can be seen from the widening of the

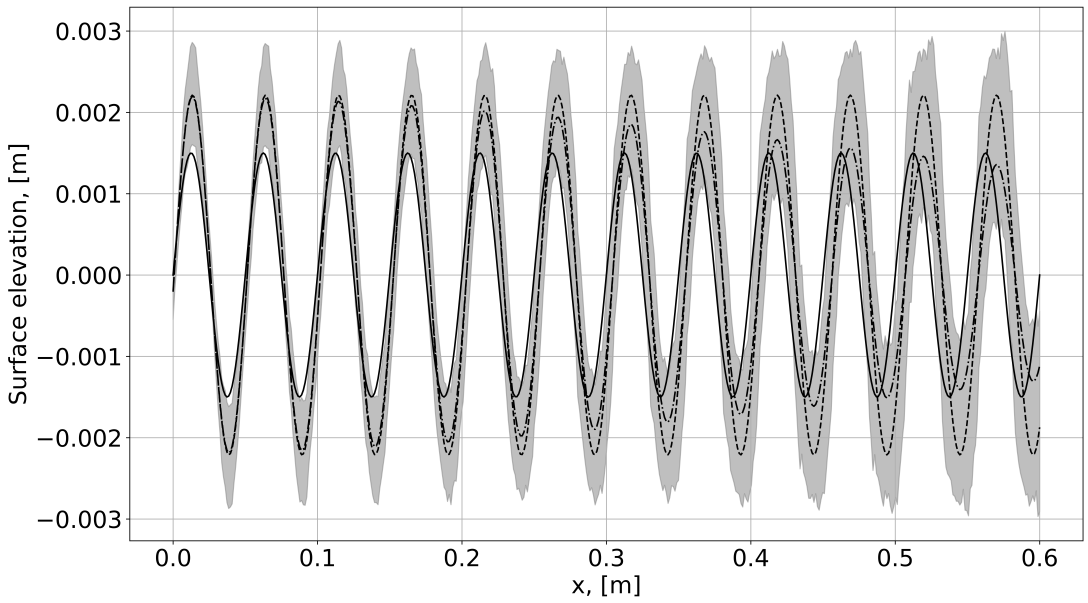

Figure 6.3: Surface elevation of the three-parameter surface. True geometry (solid line); surface $\zeta(x, \overline{\theta})$ generated from the conditional mean of MCMC parameter samples (dashed line); mean of all surfaces $\overline{\zeta(x, \theta)}$ obtained from MCMC parameter samples (dash-dotted line); 68% credible interval (shaded region).

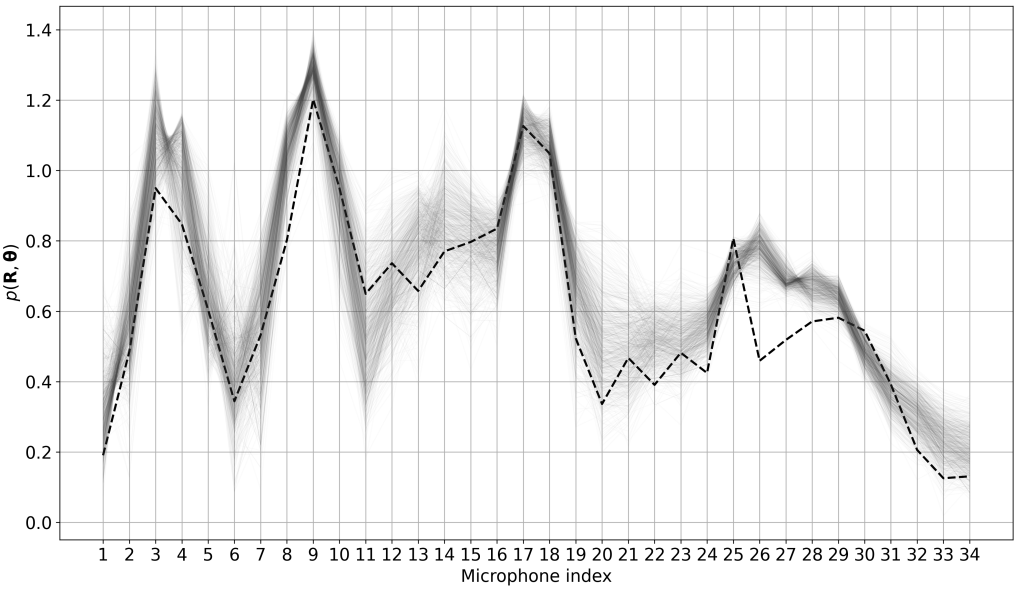

Figure 6.4: 1000 random samples of the trace (shaded region), plotted against the real data (dashed line) for the three-parameter surface recovery

traces. The traces appear to be certain on the results at the tail end of the receivers, but do not match the experimental pressure at receivers 25-28. Investigating the trace values without considering the experimental true pressure, it can be seen the proposed receiver configuration causes significant uncertainty. This could indicate that a change in the receiver configuration is needed.

In order to benchmark the performance of this method for the 3 parameter recovery, the results from Johnson *et al.* [1] are used for comparison. With a random forest recovery trained on the three parameters with 15% additive Gaussian white noise, the results for the amplitude, wavelength and offset are $0.00142, 0.0516, -0.00194$[1]. The offset for the proposed method at the mean is approximately -0.00093, the offset and wavelength have improved with the method proposed in this paper. The mean amplitude has performed worse than the amplitude presented in Johnson *et al.* Nevertheless, the uncertainty bounds contain the result from the random forest. The further knowledge to be gained from the uncertainty bounds over the parameters is useful in showing which parameter causes the most uncertainty, the amplitude θ_1.

6.6.2 40-parameter recovery

To further test the adaptive Metropolis scheme, the scattering of the acoustic signal was studied over the surface referred to as second surface profile in Section 6.5. For the computation and the prediction of the parameters, the rough surface of the second profile was approximated as a further truncation from Equation (6.1) rank ordered by the largest wavelength to the smallest wavelength to reduce the number of parameters to recover, while still capturing the original rough surface. This means, for the MCMC, the wavelengths were given (see Appendix B). In order to select a viable truncation, the relative root-mean-square error (RRMSE) of the truncated surface against the true surface normalised by the standard deviation of the true surface, as well as the RRMSE of Kirchhoff Approximation obtained with the truncated surface against KA solution based on the true surface normalised by the standard deviation of the KA for the true surface were used to evaluate the differences in comparison to the second surface profile. The results are shown in Figure 6.5. It is observed that the KA error exceeds 10% and increases rapidly at truncations below 20 terms. Therefore, a truncation of 20 terms was selected, which corresponded to recovering 40 parameters. The resulting approximations of the surface and the Kirchhoff Approximation are shown in Figure 6.6. The corresponding parameters are contained in Table 6.1 that can be found in Appendix 6.8.2.

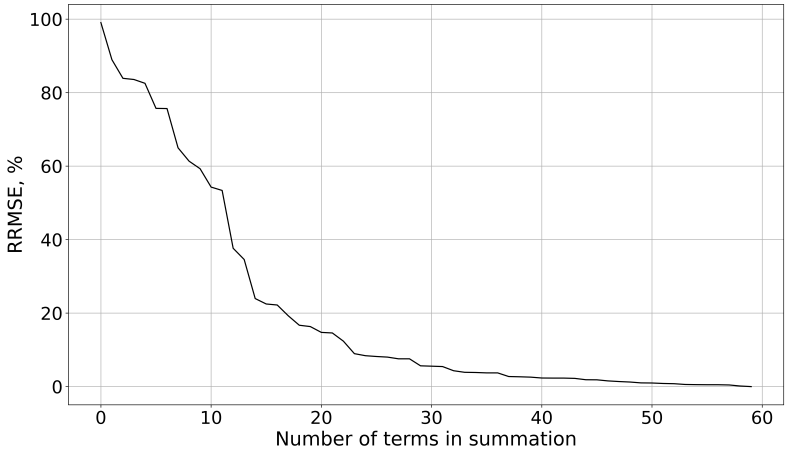

(a)

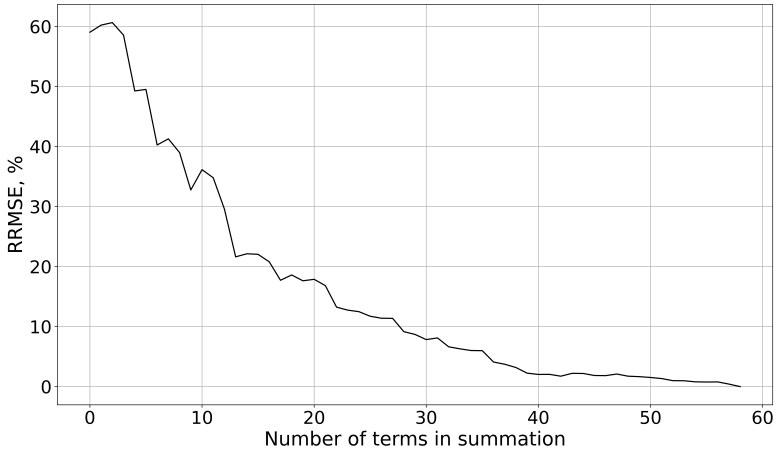

(b)

Figure 6.5: Relative root mean square error (RRMSE) of the surface and the acoustic pressure, respectively. (a) RRMSE of the true surface against a truncated version of the surface, and (b) the resulting RRMSE in the Kirchhoff Approximation.

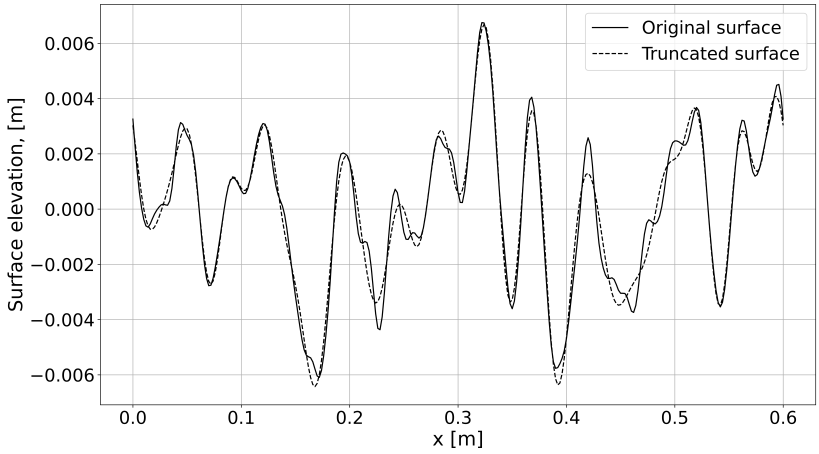

(a)

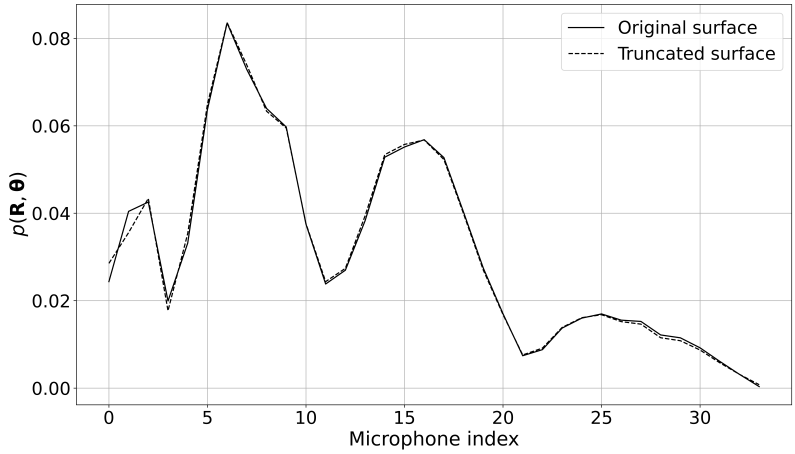

(b)

Figure 6.6: Comparison of the second rough surface profile against the truncated sum of 20 sinusoidal waves for (a) the surface elevation and (b) the corresponding Kirchhoff Approximation

For the 40-parameter case, the adaptive metropolis sampling scheme was used to generate 500,000 samples. The burn-in period was set at 50,000 samples, and the covariance matrix was updated every 50 samples. The acceptance rate was reduced to 10%. The phase parameter in the MCMC was not allowed to increase past 2π, and this was achieved by restricting the value back to the region $[0, 2\pi]$. This causes instantaneous jumps in the trace for the phase parameters. This is accounted for in the angular mean metric as shown in Appendix 6.8.3 which is used throughout this work. This restriction does not break ergodicity, or the Markov Chain definition.

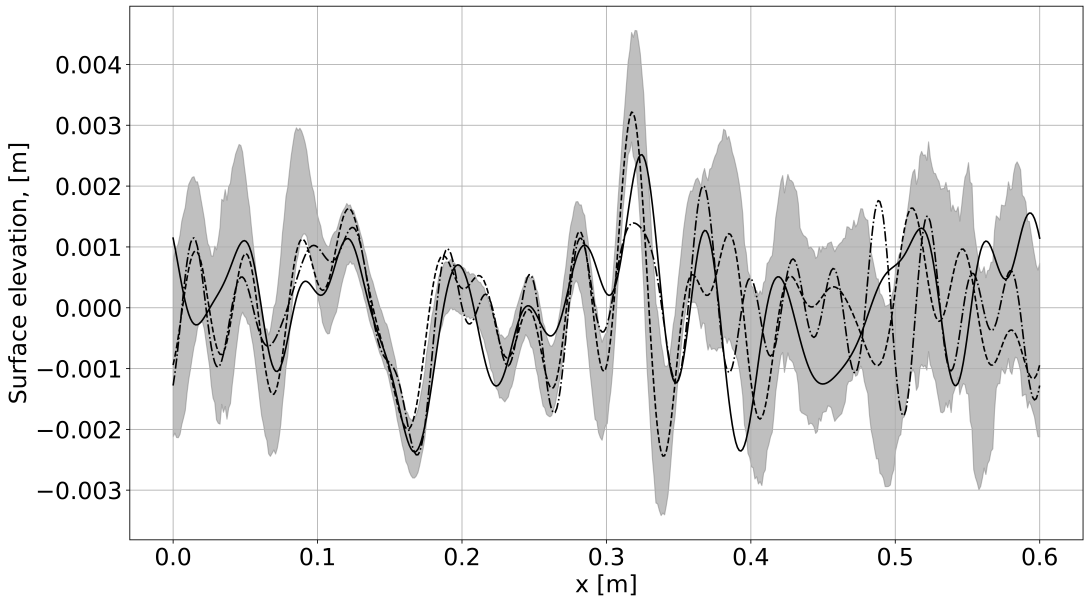

Figure 6.7: Surface elevation of the 40 parameter surface. True geometry (solid line); surface $\zeta(x, \overline{\theta})$ generated from the conditional mean of MCMC parameter samples (dashed line); mean of all surfaces $\overline{\zeta(x, \theta)}$ obtained from MCMC parameter samples (dash-dotted line); 68% credible interval (shaded region).

Due to the substantially increased number of parameters, a corner plot similar to that in Figure 6.2 is not shown here. The MH scheme was initialised with a flat surface. Figure 6.7 presents the results for the flat surface initial condition with a 68% credible interval obtained via the highest posterior density interval. It can be observed that the mean function closely matches the exact solution from the experiments in the region $x \in [0.05, 0.25]$ then begins to deviate from the mean surface outside that region. The uncertainty from the model is shown in the grey

filled region and represents the solution traces from 68% credible interval. It can be observed that the width of the 68% credible interval decreases in the specular region of the directional source with directivity pattern defined by Equation (6.6). This observation is consistent with the results obtained for 3 parameter surface (see Figure 6.3) and conclusions made for the surface reconstruction interval in Dolcetti *et al.* [74]. The credible interval also highlights that in the areas outside the specular region, the model becomes uncertain. This is expected as the information in the scattered signal is dominated from the high insonification region.

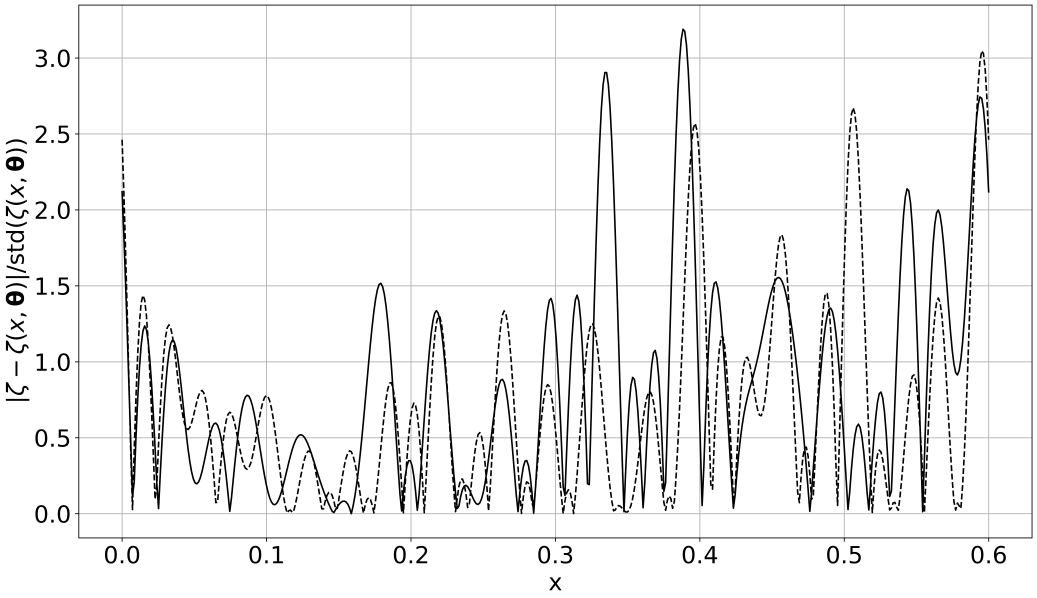

Figure 6.8: The absolute error for the surface $\zeta(x, \overline{\theta})$ of the mean of each parameter in the posterior (solid line), and the mean of the resulting surfaces $\overline{\zeta(x, \theta)}$ (dashed line), against the true surface factored by the standard deviation of the true surface.

Figure 6.8 highlights the absolute error for both the mean surface predictions (defined as ζ in the label for the vertical axis of the graph) compared against the true surface $\zeta(x, \theta)$. In the region of high insonification, the mean of the surfaces $\overline{\zeta(x, \theta)}$ outperforms the surface generated by the mean of the parameters $\zeta(x, \overline{\theta})$. In the region of good recovery [0.1,0.3], the error for both mean surfaces varies between 0 and approximately 1.5 standard deviations off the true surface.

Figures 6.9 and 6.10 presents histograms of surface harmonics amplitudes from the traces of MCMC parameter samples, and elevation of the corresponding surfaces

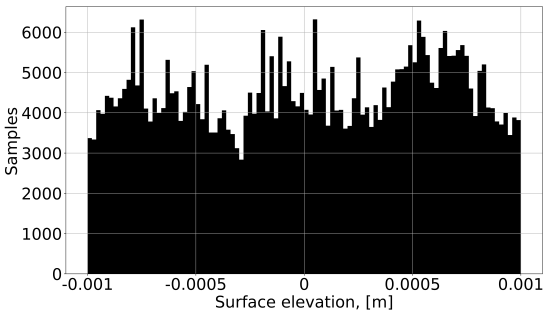

(a)

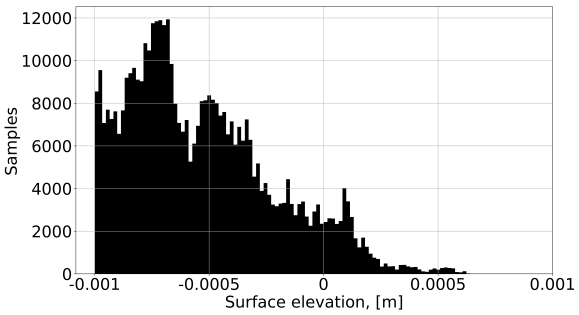

(b)

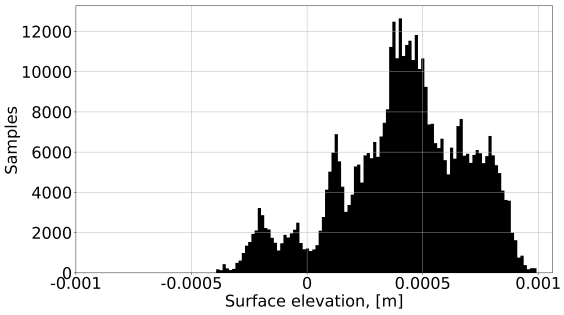

(c)

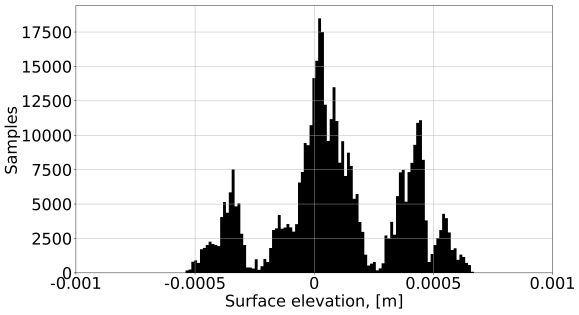

(d)

Figure 6.9: Histograms of the traces (excluding the burn-in period) of the amplitude parameters defined by Equation (6.1) for (a) the first amplitude term, (b) the 7th amplitude term, (c) the 9th amplitude term, and (d) the 14th amplitude term.

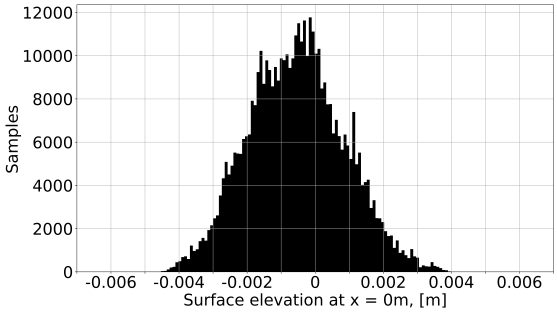

(a)

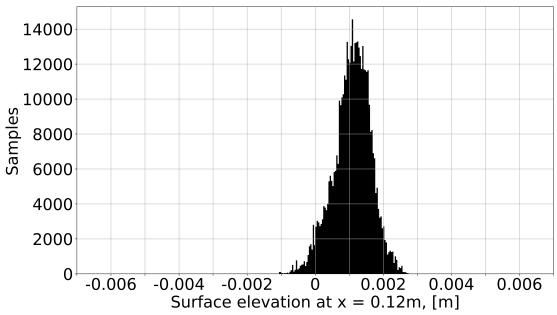

(b)

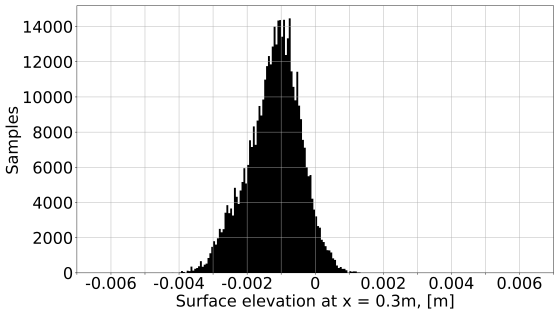

(c)

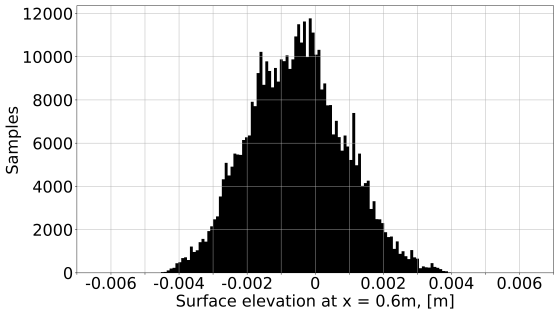

(d)

Figure 6.10: Histograms of the surface elevation from the collection of surfaces generated from the MCMC traces (excluding the burn-in period) for (a) $x = 0.0$ m, (b) $x = 0.12$ m, (c) $x = 0.30$ m, and (d) $x = 0.6$ m.

taken at a discrete set of points (the two end points, as well as $x = 0.12$ and $x = 0.3$), respectively. Due to the large amount of parameters and surface resolution, a subset was taken for visualisation. The histograms from the surface elevations result in a Gaussian shape compared to those for the amplitude parameters. This can be attributed to the 2π rollover of the phase implemented in the MH scheme for 40 parameter surface. It is also noted that the distribution of the amplitude parameters becomes uniform as the wavelength increases, which highlights almost equivalent contribution of the large surface scales within the given range of the parameters to the scattered acoustic wave.

6.7 Conclusion

The purpose of the paper was to reconstruct a rough surface from acoustic scattering and to obtain a measure of the uncertainty, highlightd in Figures 6.10, 6.7. The methodology can be used on its own, or as a means to extend deterministic methods, such as previous work by the authors using random forests [1]. In this paper, the Metropolis-Hastings algorithm was used in order to treat the set of parameters that form a parameterisation of the surface elevation function as a posterior distribution, this posterior distribution can then be queried to get a credible interval, as a measure of uncertainty. The model was tested on two surfaces, a single harmonic surface parameterised with 3 parameters, and a rough surface composed of the multiple harmonics dependent on 40 parameters (amplitudes and phases) and where the wavelengths were fixed. Laboratory measurements were taken to acquire the scattered field. The prior was decided to be uniform, and the Kirchhoff criterion was inserted into the prior to inform the model of the physics. The results for the mean surface acquired from the mean of each parameter were highlighted as a model prediction. The mean surface generated for both the three and the forty parameter surfaces were acceptable, particularly in the region of high insonification. The credible intervals highlighted the region where the model is more certain. This interval is also consistent with the underlying physics, as the scattered field will be most affected by the surface roughness in the region of high insonification The errors in the predictions were metricised through the application of the absolute error factored by the true surface standard deviation, and this was tested with the two potential mean functions that can be recovered from using a parameterisation of the surface. It was observed that the mean function produced by taking the mean at each x value for the complete set of surfaces generated with the distribution of

parameters outperformed the method of taking the mean for each parameter, then generating one surface, over the entire region. The results showcase the promising aspect of including the credible interval, especially for higher dimensional surfaces - in which methods such as random forests would require significantly more data. Further extensions to this work include varying the wavelength - in this work, the wavelengths were fixed due to the assumption that surfaces were following the Fourier decomposition. However, these fixed wavelengths could have been a distribution themselves, although more research would be needed for this. Also, the application of a more accurate optimiser or a comparison of different optimisers would be an extension of an initial surface condition, allowing for a shrinking or extending of the credible region. Finally, as the dimensions increase due to the surface, methods such as Hamiltonian Monte-Carlo may provide more favourable results.

6.8 Appendix

6.8.1 Derivation of the three-parameter recovery inequality

Starting from Equation (6.2), as k and h are non-negative, the following is true:

$$\frac{1}{h^{\frac{1}{3}}} < k^{\frac{1}{3}} \sin\phi. \tag{6.17}$$

Recalling the definition of the radius of curvature[195], then:

$$\frac{1}{h^{\frac{1}{3}}} = \left(\frac{\left| \frac{\partial^2 \zeta}{\partial x^2} \right|}{\left(1 + \left(\frac{\partial \zeta}{\partial x}\right)^2\right)^{\frac{3}{2}}} \right)^{\frac{1}{3}}, \tag{6.18}$$

To verify if the inequality (6.17) is satisfied, finding the maximum of the Equation (6.18) is required. Therefore, the denominator in the right hand side of Equation (6.18) needs to be minimised. Using the definition of the surface elevation function for 3 parameters given by Equation (6.1) for $N = 1$, the minimum of the denominator of Equation (6.18) is achieved at

$$\frac{\partial \zeta}{\partial x} = -\frac{2\pi\theta_1}{\theta_2} \sin\left(\frac{2\pi x}{\theta_2}\right) = 0. \tag{6.19}$$

Where $\theta_3 = 0$ as the phase does not raise or lower the upper and lower bounds, just shifts the value. The condition for the minimum is obtained as

$$x = \frac{\theta_2 n}{2}, \quad n \in \mathbb{Z}. \tag{6.20}$$

Then this implies:

$$\frac{\partial^2 \zeta}{\partial x^2} = -(-1)^n \frac{(2\pi)^2 \theta_1}{\theta_2^2}, \quad n \in \mathbb{Z}. \tag{6.21}$$

It is noted that condition (6.19) also guarantees maximum value of the numerator in Equation (6.18).

Using Equations (6.19)-(6.21) the criterion of the Kirchhoff Approximation (6.17) can be rewritten as

$$\left(\left| -(-1)^n \frac{(2\pi)^2 \theta_1}{\theta_2^2} \right| \right)^{\frac{1}{3}} < (k)^{\frac{1}{3}} \sin(\phi). \tag{6.22}$$

Using Equation (6.22), the lower bound of parameter θ_2 can be expressed in terms of another parameter θ_1 as

$$\theta_2 > \sqrt{\frac{(2\pi)^2 |\theta_1|}{k \sin^3(\phi)}} \tag{6.23}$$

6.8.2 Table of parameters

Table 6.1: Parameters that define the truncated surface representing the overall surface.

Amplitude [m]	Wavelength [m]	Phase	Amplitude [m]	Wavelength [m]	Phase
-1.86e-04	0.6	3.42	3.37e-04	0.055	1.70
6.11e-04	0.3	6.21	-1.44e-04	0.05	0.29
4.22e-04	0.2	2.82	-5.33e-04	0.046	2.62
9.95e-05	0.15	5.82	-2.11e-04	0.043	5.19
1.83e-04	0.12	0.90	3.52e-04	0.04	5.54
4.62e-04	0.1	5.64	1.17e-04	0.038	0.87
-3.93e-05	0.089	5.35	-4.99e-05	0.035	5.33
5.50e-04	0.075	2.081	1.56e-04	0.033	1.79
-3.03e-04	0.067	4.86	1.36e-04	0.032	1.66
2.22e-04	0.06	4.98	4.88e-05	0.03	1.059

6.8.3 Phase averaging

In the calculation of the surface generated from the mean of the parameters, there is a potential issue with the phase. Averaging the amplitude is fine, and the arithmetic mean will yield a sensible result. But due to the poles at $\pm\pi$, other averaging methods have to be considered. The angular mean is used for the parameters which relate to the phase information of the surface, and is calculated by:

$$\bar{\theta} = \tan^{-1}\left(\frac{\sum_i \sin(\theta_i)}{\sum_i \cos(\theta_i)}\right). \tag{6.24}$$

This calculation takes into account the poles at $\pm\pi$ and should yield an expected average value.

6.9 Acknowledgments

This work was partially supported by the UK EPSRC Grant EP/R022275/1 and Knowledge Exchange Support Fund provided by the UK Engineering and Physical Sciences Research Council (EPSRC).The authors would like to acknowledge the support of the Academy of Finland (the Finnish Center of Excellence of Inverse Modeling and Imaging), and the Academy of Finland project 321761. M.-D. Johnson would like to acknowledge the support of the University of Sheffield through

their PhD studentship award.For the purpose of open access, the authors have applied a ‘Creative Commons Attribution (CC BY) licence to any Author Accepted Manuscript version arising.

Chapter 7

Recovering the free surface frequency-wavenumber spectra of shallow turbulent open channel flows using Digital Image Correlation (DIC)

Reference

Johnson, M. D., Muraro, F., Tait, S., Dolcetti, G., and Krynkin, A. Recovering the free surface frequency-wavenumber spectra of shallow turbulent open channel flows using Digital Image Correlation (DIC).

Author Contributions

- Johnson, M.D., - Problem formulation, writing (Theory, Results, Conclusion), model development, data processing, data analysis, editing, structure.
- Muraro, F. - Data collection, data processing, writing (Experiment setup)
- Tait, S. - writing (Introduction), editing, technical advice.
- Dolcetti, G. - editing.
- Krynkin, A. - editing.

Summary

The work presented in Chapters 4, 5, and 6 are concerned with the (acoustic) reconstruction of static rough surfaces. The work in this and the following Chapters

investigates if parameters can be recovered from a moving surface. In this chapter, videos were taken of the free-surface of the water, and analysed. This Chapter is concerned with the reconstruction of the frequency-wavenumber spectrum using a Digital Image Correlation (DIC). The DIC approach used tracers in the water of a flume to then estimate the free surface elevation. The extent of data loss was prohibitive to successful analysis of the data through other approaches. A visual inspection of the videos showed that the main cause of the issue was the traces being sucked down into the flow, such that they are below the free surface and not detected by the camera. This could be seen from the fact that the missing data points follow the flow structure. Because the missing data points follow the flow, in a way that is characteristic to the underlying dispersion relation, the frequency-wavenumber spectrum is recovered with reasonable accuracy without needing to handle the missing data. This means that the frequency-wavenumber spectrum is much more forgiving for an inconsistent seeding regime.

The frequency-wavenumber spectra was used as the analysis method. This is a relatively new approach for shallow turbulent flow, and the results reveal a set of dispersion curves that represent the average flow. Ten different flow conditions as well as one extra flow condition with a different slope was presented, alongside the proportion of missing data as well as the ratio of stream-wise length by the depth. Throughout all conditions, there is good agreement to the Advection dispersion curve approximated by [18] as well as the gravity capillary dispersion curve introduced by [151] [2] [126] especially at the lower flow conditions.

As the flow conditions increase, information in the negative wavenumber domain (for the $K_y = 0$ slices) is lost in favour of the dominating behaviour of the rotation due to the increase in streamwise velocity. This paper finds that the DIC is an appropriate tool for investigating the frequency-wavenumber spectrum.

7.1 Introduction

Recent studies have indicated that free-surface deformations of turbulent flows in channels might be caused by a variety of physical phenomena found in laterally and depth-sheared flows. A consensus on the main mechanisms behind the generation of the free-surface wave patterns has yet to be reached [127]. [196] and [197] suggested that the interaction between the water surface and the underlying turbulence driven structures are expected to produce a wide variety of water surface patterns (e.g. vortex dimples, scars, and boils). Surface waves might also

be generated by resonance phenomena which selectively amplify specific periodic waves such as gravity-capillary waves as supported by [126], or can originate due to an interaction with the channel bed [18]. Turbulence-forced surface patterns and gravity-capillary waves are believed to be representative of different processes, but measuring and understanding the behaviour of both are necessary for the interpretation of the mutual interaction between the flow and the free surface. The combination of these different wave types can produce a complex, moving three-dimensional (3D) surface wave pattern that can be difficult to visually interpret and measure.

A separation between the two types of surface deformations can be obtained spectrally by means of a Fourier transform in space and in time of collected elevation data, e.g., the frequency-wavenumber spectrum [125, 18]. Often it is difficult to separate out these two processes given the typical quality and resolution of water surface measurements. Turbulence-forced surface deformations travel approximately at the surface flow velocity and gravity-capillary waves propagate relative to the flow at their own speed, which depends on their wavelength, and they travel in all directions. This difference in velocity results in a different dispersion relationship, that can be identified in the frequency-wavenumber spectra.

However, the estimation of frequency-wavenumber spectra requires a simultaneous characterisation of the water surface dynamics in space and in time, which can be hard to achieve with the required accuracy and resolution for many practical situations. This requirement justifies the need for water surface measurement techniques which are able to accurately characterise the 3D form and dynamics of such water interfaces sufficiently to enable accurate frequency-wavenumber spectra to be obtained.

[125] and [18] determined the frequency-wavenumber spectra of the water surface elevation along the streamwise and lateral direction separately, using a scanning laser beam and an array of conductance wave gauges, respectively. 1D spectra are difficult to interpret, since the contributions of all waves with the same projection of the wavenumber vector along the measurement direction collapse onto a single point regardless of their actual wavenumber modulus. This is a strong limitation for the characterisation of the surface patterns of turbulent shallow flows, because of the marked three-dimensionality of the surface patterns and because of the lack of symmetry caused by the advection by the flow in the streamwise direction[18]. [198] managed to estimate the frequency wavenumber spectra in three dimensions using a wavelet spectral method [199] applied to a group of wave

gauges arranged in the streamwise and lateral directions. However, the resulting spectra had a limited resolution. [200] employed a synthetic Schlieren method to reconstruct the evolution of the surface shape in time and calculated its frequency-wavenumber spectrum. However, their flow conditions were not representative of typical shallow turbulent flows due to a relatively small flow velocity to gravity wave velocity, and their surface measurement method is not easily applicable to practical channel flows over a rough bed.

[201] combined a decomposition of the simulated surface deformation patterns based on the frequency-wavenumber spectrum with a proper orthogonal decomposition of the simulated turbulent flow field, to highlight the complex interactions between turbulence and the free surface for a flow behind a backward-facing step simulated via large eddy simulation, thereby demonstrating the potential for rigorous surface decomposition to provide an improved fundamental understanding of turbulent flow behaviour. It is therefore of great importance to identify a suitable experimental technique that is able to provide similar high-resolution 3D data resolved in space and in time, while minimizing the disturbance to the flow and without impairing the characterization of the velocity field below the water surface.

In general, non-contact water surface measurement techniques can be based on optical, acoustic or radio approaches. Acoustic techniques have already been used to locally reconstruct a dynamic air-water interface or to derive areal wave patterns properties such as mean roughness height, frequency-wavenumber spectra and surface velocity [202, 198]. For similar purposes, [203] and [10] used radio waves, while [204] and [205] made use of optical methods.

Each method has comparative advantages and disadvantages. For example, acoustic and radio techniques require a careful calibration when reconstructing a surface, whilst the calibration of optical methods are more robust and less prone to uncertainty. On the other hand, for acoustic and radio methods the free surface represents a very good reflecting surface due to the higher impedance of water than air [183]. The same advantage, however, does not apply for optical techniques as the identification of the transparent water free surface can be affected by the presence in the images of underlying bed topography. To prevent this interference, optical methods require specific illumination and/or cameras positioning or opaque water.

The use of optical technologies to measure the shape of the surfaces is well established. Descriptions and characteristics of these methods can be found in the reviews by [206] and [207]. Among the numerous optical techniques, Digital Image Correlation (DIC) [208] is one of the most popular. This is because DIC can

accurately measure and robustly reconstruct a surface and can operate with flexibility [209, 207]. The complete theory behind image correlation is presented in [210].

A technique to measure the dynamics of the water surface of a turbulent open-channel flow employing a DIC system in combination with small buoyant surface tracers is presented here. The aim of the study was to assess whether DIC could be used to recover sufficiently high quality information on a dynamic air-water interface to ensure that the different types of surface wave could be separated and identified. This would allow the in-depth study of the underlying physical processes in free-surface turbulent flows over man-made and natural channels. The study used DIC data from a series of controlled laboratory flume experiments combined with analytical models to test whether a DIC based measurement system could be usefully deployed in the field.

7.2 Experiment setup

Two series of steady, uniform flow depth experiments employing different beds arrangements were performed in a tilting, recirculating glass-walled flume. The flume has a working length of 15 m and a width of 0.503 m. The inlet tank is designed to minimise any transitory effects produced by the re-circulation pump by using a porous filter, while the outlet has an adjustable tailgate to ensure uniform flow conditions in the working length of the flume.

The flume bed was covered from the inlet to a location 4.80 m downstream with well sorted river gravel with a nominal size of 25 mm to encourage the development of a stable turbulent boundary layer. The remaining length of the flume bed contained a layered bed arrangement of plastic spheres and sand to simulate a stable bed with a geometrically well described surface (spheres), but which had an inherent porosity variation (sand) as found in natural gravel river beds (Fig. 7.1). In this study, the 24.7 mm diameter spheres were organised in two different surface packing arrangements, termed A and B (Fig. 7.2). Pattern A was a hexagonally-packed arrangement having peak to peak planes oriented along the spanwise direction, whilst B arrangement was again a hexagonally-packed arrangement but having peak to peak planes aligned along the streamwise flow direction (i.e. packing B was statistically similar to packing A but was rotated by 90°). These arrangements provided stable surface configurations with the same bed elevation distribution but a different surface orientation in relation to the main direction of

the flow. Narrow grain size distribution sand (99% of its mass distributed between 600 and 850 μm) was used to fill the gaps between spheres in order to produce a vertical porosity profile from the top to the base of the spheres that resembles natural river gravel deposits. These beds were placed in the flume which was then tilted to have a slope of 1/500. Before each series of tests, the discharge was progressively increased up to 25 l/s and held steady for 12 hours. At this flow rate, the boundary shear stress was enough to remove all the excess of sand, revealing the bed texture created by the packed spheres. This process of water-working also allowed the consolidation of the sand and the creation of a complex but stable bed structure for the subsequent tests. At the end of this procedure, the bed resulted in hemispheres emerging from a permeable sand layer, resembling a fluvial gravel bed developed under armouring conditions.

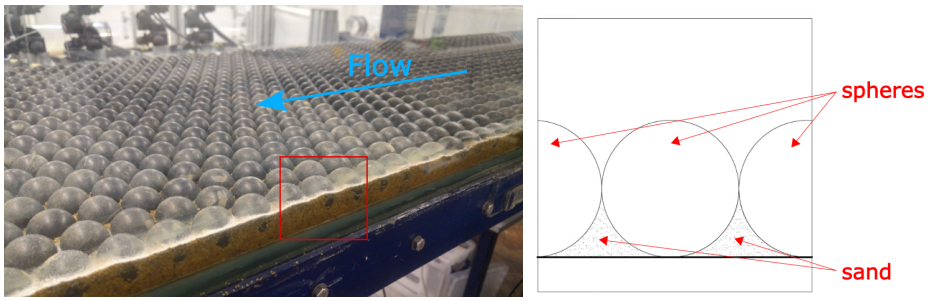

(a) (b)

Figure 7.1: a) Composite bed made of spheres embedded in sand. b) Sketch for the composite bed.

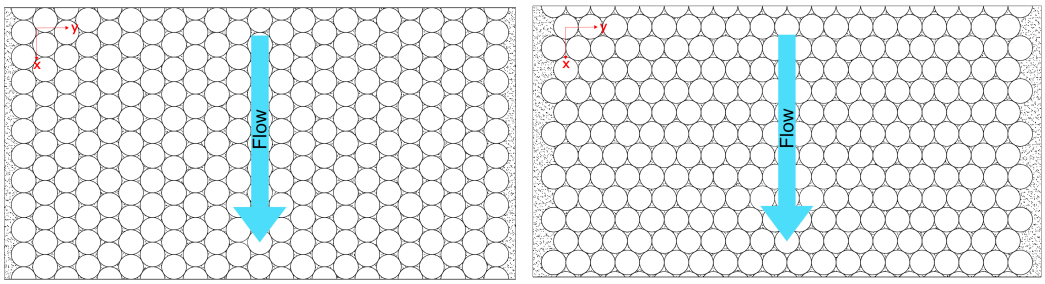

(a) (b)

Figure 7.2: a) Arrangement A: hexagonally-pack with planes aligned with the streamwise direction. b) Arrangement B: hexagonally-pack with planes aligned with the spanwise direction.

Two series of experiments were conducted with steady, uniform flow conditions over two beds with different sphere arrangements. The hydraulic characteristics of

Test	Q (l/s)	$\bar{U}_B$ (m/s)	$\bar{U}_S$ (m/s)	d (mm)	*Re*	*Fr*	*AR*
FC1A	1.4	0.14	0.18	19.8	2800	0.32	25.4
FC2A	3.3	0.2	0.26	33.1	6500	0.35	15.2
FC3A	10.5	0.33	0.43	64.1	20700	0.41	7.8
FC4A	15.7	0.38	0.47	81.6	30900	0.43	6.2
FC5A	21.1	0.43	0.53	97.5	41500	0.44	5.2
FC1B	1.93	0.19	0.23	20.7	4100	0.41	24.3
FC2B	3.53	0.23	0.31	30.7	7700	0.42	16.4
FC3B	10.84	0.35	0.45	61.5	24200	0.45	8.2
FC4B	15.85	0.41	0.51	76.7	34700	0.47	6.6
FC5B	21.56	0.47	0.58	91.9	47400	0.49	5.5

Table 7.1: Characteristics of the flow conditions tested. Q is discharge; $\bar{U}_B$ is Time- and Depth-averaged Velocity; $\bar{U}_S$ is Average Surface Velocity; d is Water Depth; *Re* is Reynolds Number, with Re $= \bar{U}_B d/\nu$ where ν is the kinematic viscosity of water (m^2s^{-1}); *Fr* is Froude Number, with Fr $= \bar{U}_B/(gd)^{0.5}$ where g is gravitational acceleration,; *AR* is Aspect Ratio

each flow condition are reported in Table 7.1. The controlling parameters of each experiment were determined based on the measured depth and time-averaged velocity, $\bar{U}_B$, and on the time-averaged surface velocity, $\bar{U}_S$. Considering the threshold value of the minimum phase velocity for gravity-capillary waves in still water, c = 0.23 m/s, it was decided to have a flow condition with both $\bar{U}_B$ and $\bar{U}_S$ below 0.23 m/s, one flow condition where $\bar{U}_B$ was below and $\bar{U}_S$ was above the threshold value and three flow conditions with both velocities above the minimum phase velocity for each bed configuration. The experimental hydraulic conditions were designed to evaluate the free-surface behaviour and the different wave generation mechanisms and the change they may experience for progressively higher free-surface velocities. It was expected that for these flow conditions that a mixture of turbulent forced surface deformations and advecting gravity-capillary waves would be observed [127]. The flow conditions had aspect ratios (ratio between width of the flume and flow depth) between 5.2 and 25.4, and relative submergence values (ratio between flow depth and diameter of the spheres) between 1.5 and 10.5. These values were described by [211] and [212] as typical within natural gravel bed rivers.

The water surface behaviour was investigated using a Digital Image Correlation (DIC) system positioned at the location 9.4 m (4.6 m downstream from the beginning of the test bed, corresponding to 232 to 59 times the experimental water depths). This system was formed by two Imager MX 4M cameras (2048x2048 pixel, 5.5 μm size pixel) mounting Tamron M112FM16 lenses (16 mm focal length,

F/2.0). The cameras were placed side by side along the flume centreline 0.40 m above the bed and a distance 0.70 m from each other (7.3). During the different tests the cameras' position was fixed, but because of the different flow conditions the free surface to cameras distance ranged between 462 and 516 mm, causing the Field of View (FOV) to range in size from a rectangle of side 325mm to 363 mm, and the cameras spatial resolution to vary between 0.16 and 0.18 mm/pixel. The angle between the cameras changed as well, varying from 40.8° to 47.3° respect with the horizontal plane. The lens aperture was set at f/16 to produce a depth of field as wide as possible and so have as much as possible of the FOV in focus. Illumination was provided by two blue LEDs arrays shining from above for a total illuminated area of 350x250 mm^2 (streamwise and spanwise). The LED arrays were positioned 0.6 m above the bed without obstructing the cameras' view. The cameras were secured onto a stiff mounting bar that was isolated from the flume to ensure that any vibrations within the flume did not impact on the DIC measurements. The mounting bar was set to be parallel to the flume bed.

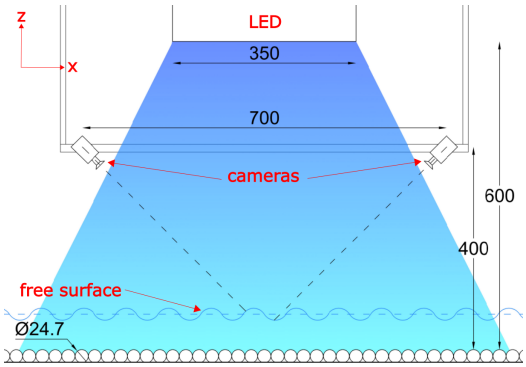

Figure 7.3: Cameras and illumination setup. The cameras were positioned directly above the water surface on the sides of the illumination. (colour online)

To allow the reconstruction of the instantaneous free-surface profile using the DIC system, cenospheres (POS-IBW 300 produced by Possehl Erzkontor GmbH) were used as small floating tracers to identify the water surface in the DIC system images. Cenospheres are ceramic hollow spheres which float due to their low density (ρ_{cs} = 700 kg/m3). They also present different off-white shades of colour that create a light speckle patterns on the free surface, allowing the surface reconstruction algorithm within the DIC system to quantify the surface deformation. Compared to other buoyant surface tracer candidates, like hollow glass spheres or silver-coated hollow glass spheres, cenospheres do not produce any electrostatic

interactions, therefore surfactants are not needed to prevent coalescing and lumping. Cenospheres are hydrophilic and do not stick to the interface. Tracers failing to do so would impact on the surface tension [213]. The cenospheres were first sieved to isolate the fraction with particle diameters below 300 μm. This value was chosen as for larger diameters the Stokes number, St, becomes greater than 0.1. The Stokes number, defined as the ratio between the particle and fluid characteristic time scales, is used to verify the capability of a particle to follow the flow without disturbing it [214]. [215] suggested tracers having $St < 0.1$ are able to correctly describe the flow with an accuracy error below 1%. The sieved material was characterised by a range of diameters between 90 and 280 μm, resulting in Stokes numbers between 0.08 and 0.1.

All the experiments were carried out following the same procedure. Before starting a test a calibration plate was placed at the expected streamwise and vertical position of the air-water interface and the cameras were adjusted to aim at the same location. A calibration image data set for the DIC cameras was obtained by taking 40 in-focus images of the calibration plate at different heights and inclinations. The discharge was slowly increased to the desired value and the flume outlet gate was adjusted to ensure the establishment of uniform flow conditions. Sixty minutes after the discharge and gate position were set, images were collected at a frequency of 100 Hz in 300 second long acquisitions. DIC data sets consisted of time series containing 30000 images. To produce the free-surface coating necessary for the DIC algorithm to work, cenospheres were introduced concurrently in different ways. Surface skimmers were positioned inside the flume storage tank to allow the recirculation of the spheres already present in the flume system. Peristaltic pumps were also used to introduce a highly-concentrated mixture of water and cenospheres just below the free surface at the inlet tank position. Finally, dry cenospheres were manually sprinkled from above in correspondence of the transition between gravel and composite bed (i.e. 4.80 m from the inlet). Uniformly coating the free surface was more challenging for progressively higher flow rates and depths because as a consequence of stronger secondary flows and of larger and more frequent coherent structures causing the renewal of the free surface. Nonetheless, a sufficiently high level of surface coating was achieved (especially at low flow rates), allowing the DIC algorithm to accurately reconstruct sufficient of the free-surface shape for later analysis (Fig. 7.4). Once the images were acquired, uniform flow conditions were verified again by taking water depth measurements along the flume with a spacing of 30 cm and confirming the water slope was the same as the bed slope. As a last

step, small buoyant tracers were released at position 4.80 m and the time required for them to travel between two distinct sections was measured for 20 times. This allowed an estimate for the average free-surface velocity to be obtained.

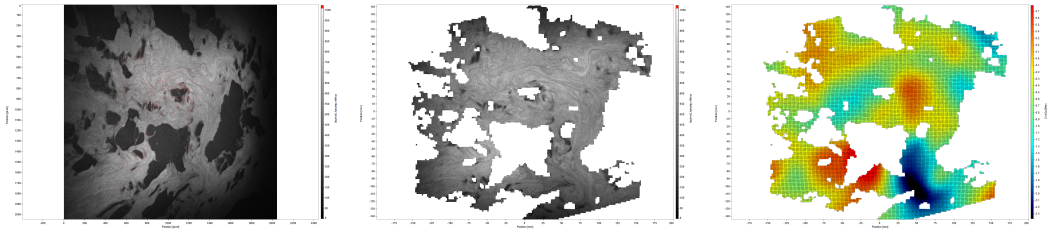

(a) (b) (c)

Figure 7.4: Processing sequence for a frame extracted from flow condition FC5J. a) Raw camera image b) Orthorectified free surface. c) Reconstructed free-surface height field.

To obtain the instantaneous shape of the free surface the raw images were firstly processed using the Strain toolbox provided with DaVis by LaVision [216, 217]. The images were subdivided in 21 pixel-wide facets and the step size (displacement of the interrogation window) was set to 13 pixels, resulting in a spatial resolution varying between 1.5 and 2.2 mm according to the water depth. Facet and step sizes were chosen as these values were reckoned to be optimal between spatial accuracy and uniqueness of the speckle pattern created by the floating tracers. The reconstructed instantaneous surface height, however, presented deviations from the mean water level. This occurred as the calibration plate was not perfectly aligned with the water surface at the time of the calibration. To compensate this anomaly, the time series for the reconstructed height at each location were time-averaged over the entire duration. The resulting time-averaged height field, representing the trend inherited from the plate misalignment during the calibration procedure, was later subtracted from the corresponding instantaneous height field to obtain the surface fluctuations around the mean water level set now to 0 mm. Five 60 second long time-averages of surface elevation were also obtained, allowing independent comparisons of each 60 second long segment to demonstrate the stationarity of the water height statistics. No differences were noticed between the independent segments.

7.3 Analysis of Water Surface Level Measurements

The water surface shape of turbulent open-channel flows is the product of a number of processes that act at a range of scales so that a description using simple non-dimensional parameters is not possible [127]. The identification of the different patterns (turbulence-forced and freely propagating gravity-capillary waves) on the surface of turbulent open-channel flows is achieved by means of the frequency-wavenumber spectrum. This method decomposes the elevation at any location into frequency $\omega = 2\pi f$, and wavenumber $\mathbf{k}$ via a Fourier transform of the surface elevation $\zeta(x, y, t)$ in space (x, y) and in time t. The quantity ω/k, where $k = |\mathbf{k}|$, is the wave speed.

Turbulence-forced surface fluctuations are expected to move along the direction of the flow at a speed comparable to that of the turbulent disturbance that originates them [126] If the mean surface velocity $\bar{U}_S$ of the flow is faster than pattern deformations, the fluctuations in time at a fixed point is primarily due to advection yielding the following approximate dispersion relation for turbulence-forced fluctuations [2]:

$$\Omega_A(\mathbf{k}, \bar{\mathbf{U}}_\mathbf{S}) \approx \mathbf{k}\bar{\mathbf{U}}_\mathbf{S}. \tag{7.1}$$

The dispersion curve for gravity capillary waves is:

$$\Omega_{GW}(\mathbf{k}, \bar{\mathbf{U}}_\mathbf{S}) \approx \Omega_A(\mathbf{k}, \bar{\mathbf{U}}_\mathbf{S}) \pm \sqrt{(g + \frac{\gamma}{\rho}k^2)k\tanh(kd)} \tag{7.2}$$

where γ is the surface tension of water and air, ρ is the density of water, and d is the water depth.

A further dispersion curve due to gravity capillary waves can also be used [151, 126, 2]:

$$\Omega_i(\mathbf{k}, d) = k\sqrt{gd\frac{1+B}{B}\frac{\tanh(kd)}{kd}} \tag{7.3}$$

$$\Omega_{GW}(\mathbf{k}, d) = (1-\beta)\Omega_A + \sqrt{(\beta\Omega_A)^2 + \Omega_i^2} \tag{7.4}$$

where:

$$B = \frac{\rho g}{k^2\gamma} \tag{7.5}$$

is the Bond number and:

$$\beta = \frac{m}{2}\tanh(kd). \tag{7.6}$$

In this work, m is set to 0.34 as in [2]. In Equation 7.4, only the positive square root is taken due to the lack of information in that region for the lower wave regimes.

7.3.1 Feature extraction method

This analysis yields a dispersion relation for turbulence induced (forced waves) and dispersion relations to describe different gravity waves. These relations can therefore describe the complex combination of different wave types on the free surface of any turbulent flow.

The frequency-wavenumber spectrum was obtained in three dimensions in order to identify the wave types from the spatial elevation data that were recovered for each flow condition using the DIC system. The underlying assumption is that the free-surface elevation can be analysed via Fourier Analysis, and this analysis adheres to the dispersion relations. If these assumptions hold, it is possible using the frequency-wavenumber spectrum to recover the different dispersion relations [218, 219, 220]. Essentially, because this representation yields a function of $\mathbf{k}$ and Ω. In the continuous case, defining the DIC surface elevation recovery as a function in space and time $\zeta(x, y, t)$ say, the frequency-wavenumber spectrum can be found by the Discrete Fourier transform:

$$\hat{\zeta}(k_i, k_j, \omega_k) = \sum_{m=0}^{N_x-1} \sum_{n=0}^{N_y-1} \sum_{p=0}^{N_t-1} \zeta(x_m, y_n, t_p) \exp\left(-i\left(\frac{2\pi}{N_x} k_i n + \frac{2\pi}{N_y} k_j m + \frac{2\pi}{N_t} \omega_j p\right)\right) \quad (7.7)$$

Where N_x, N_y, N_t are the number of samples in the x, y, and time dimension respectively. The power spectrum of the frequency-wavenumber spectrum was calculated for every ten seconds (1000 frames) of DIC surface elevation data, and then the results averaged at every location by the number of ten second segments (found by rounding down the number of samples in time to the thousandth). This average power spectrum was analysed.

The Nyquist limits $L_\omega, L_{k_x}, L_{k_y}$, the resolution $S_\omega, S_{k_x}, S_{k_y}$ for ω, k_x, k_y, and the spectra size is presented in Table 7.2. No window was used in the DFT analysis.

As the DIC scheme yields an estimation of the surface elevation, the frequency-wavenumber spectrum should be applicable, as was observed in [18] for wave probes. As the DIC recovers surface elevation from the observation of tracers that are on the surface, the overall recovered elevation is dictated by the density and behaviour of the tracers. As the flow advects the tracers, the spatial density is not uniform and there are regions in the flow where the number of tracers is close to

Test	L_ω (rad/s)	L_{k_x} (rad/m)	L_{k_y} (rad/m)	S_ω (rad/s)	S_{k_x} (rad/m)	S_{k_y} (rad/m)	Shape
FC1A	314.16	1948.4	1948.4	0.02	19.0	18.5	(205 211 29999)
FC2A	314.16	1903.4	1903.4	0.021	19.7	18.0	(193 211 29999)
FC3A	314.16	1931.1	1931.1	0.022	21.7	17.5	(178 221 28089)
FC4A	314.16	1948.4	1948.4	0.021	22.7	17.9	(172 218 29999)
FC5A	314.16	2084.3	2084.3	0.025	21.1	17.4	(198 240 25483)
FC1B	314.16	1760.1	1760.1	0.021	17.5	16.1	(201 218 29999)
FC2B	314.16	1558.8	1558.8	0.023	19.1	14.8	(163 211 26770)
FC3B	314.16	1708.3	1708.3	0.021	19.9	15.3	(172 224 29999)
FC4B	314.16	1742.6	1742.6	0.021	20.7	15.0	(168 232 29999)
FC5B	314.16	1739.8	1739.8	0.021	21.7	15.7	(160 222 29999)

Table 7.2: Spatial information of the flow conditions tested. N_ω is the Nyquist limit from angular frequency; N_{k_x} is the Nyquist limit for k_x; N_{k_y} is the Nyquist limit for k_y; S_ω is the resolution in angular frequency; S_{k_x} is the resolution in k_x; S_{k_y} is the resolution in k_y; *Shape* is the resulting frequency-wavenumber shape.

zero. At these locations, the DIC scheme does not successfully recover elevation information. Figure7.5 demonstrates the proportion of pixels that are successfully recovered at each frame of the resulting video. This data was smoothed through the use of a Gaussian kernel density estimation (KDE) method. These values are normalised based on the maximum value of the distribution for all measurements. It can be observed that the spread of the KDE histograms increase as the flow rates increase from FC1 to FC5. The proportion of pixels with spatial information for the Bed B measurements has an intermediate value of around 0.5 for flow condition FC1, whereas the proportion of pixels with spatial information for the Bed A measurements decrease from FC1 to FC5. It is important to note that there is a left shift to the data, which is from the zero padding outside of the region of recovery as shown in Figure 7.4. However, the spread is dictated by "holes" that advect with the flow, these holes are not interpolated before the application of the DFT and are set to 0. However, if this non-complete DIC data can reconstruct robust frequency-wavenumber plots, in the streamwise and lateral directions, with sufficient fidelity to separate the different wave types then this 3D surface elevation data can be used to investigate the nature of the free surface of turbulent flows.

7.4 Results

Once the DIC system has completed the measurements the elevations are processed, the 3D averaged power spectrum was found for each time series. This gives a full spatial spectra for values of the wavenumbers in the streamwise (x) and lateral (y) direction. For the presentation of the results, two slices which correspond to

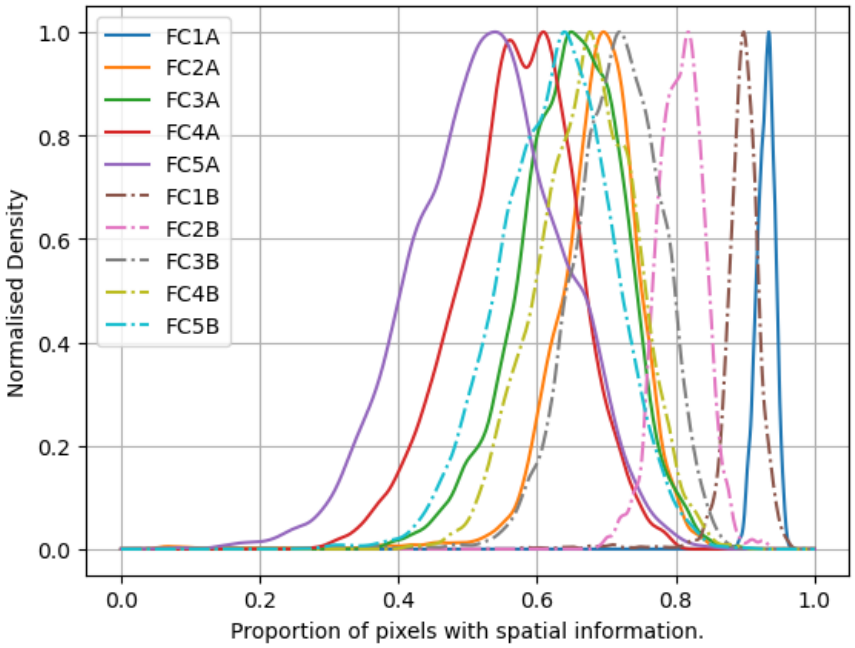

(a)

Figure 7.5: Normalised kernel density estimation of proportion of pixels in the images that contain surface elevation information. For all measurements. The normalisation was done by the division of the maximum value.

$k_x = 0$, and $k_y = 0$, which represent waves in the streamwise and the lateral direction respectively were selected. Theoretical dispersion relations can be obtained for the streamwise direction and the lateral direction from Equations (7.1) (7.2) based on the depth and velocity reported in Table 7.1 (in the lateral direction the velocity is assumed to be 0). The theoretical lines are overlaid to the results presented from the DIC scheme. Due to the missing streamwise velocity information for FC2B in Table 7.1, the figures for this condition are not presented. Figures 7.6 7.7 7.8 7.9 7.10 present the Fourier representation of the DIC recovery for the case where $k_y = 0$ and $k_x = 0$ for all the flow conditions outlined in Table 7.1. In the tests with higher flow velocities and deeper water depths (Fig.7.9 and 7.10), and where a higher proportion of data is missing, the dispersion relations blur more in the negative wavenumber region. This is to be expected, as the proportion of missing data increases more noise appears on $\omega = 0$ line. Throughout all of the flow conditions, the $k_x = 0$ curves fit well to the center of the dispersion curves acquired from the Fourier representation of the DIC results.

For Flow Condition 1A,1B and 2A,2B in Figures. 7.6 7.7, there is good agreement for both the turbulent advection dispersion relation (Eq.(7.1)) and the down-

stream gravity capillary waves (Eq.(7.4)) for the wavenumber larger than 0. There is good agreement for the negative wavenumber until less than -100, then the agreement decreases. This behaviour is replicated for flow condition 2. For Flow Conditions 3 on-wards, the features of the advection and the downstream gravity capillary waves blur together, there is not as clear a separation from the advection and the gravity capillary waves as in flow condition 1 and 2. An issue that has arisen through the analysis of the results is the lack of information for downstream gravity waves, which would not be present in laboratory conditions. Due to this, there is no information in the Fourier representation of the DIC recovery where there is a theoretical line shown in Flow Conditions 3,4, and 5.

For the recovery for the lateral waves, the agreement is good throughout. Although the blur does increase as the flow conditions get higher, the overall shape adheres to the theoretical dispersion curve well especially in cases such as the ones presented in Figure 7.8. Where, in the streamwise direction the gravity dispersion relation has been blurred and dominated by the effect of the turbulence-generated advection. However, the in lateral direction there is still good agreement with the theoretical dispersion curve.

In order to visualise the separation of the dispersion relation with respect to the change of parameters, the dispersion relations for all flow conditions were presented in Figure 7.12. There is a clear separation in the streamwise direction for both the A and B measurements, with emphasis on the negative wavenumber. The behaviour is mimicked in the lateral direction, although the change with respect to depth decays very quickly, with minimal separation in FC4 FC5 for both the A and B measurements. The ability to separate out the gravity-capillary behaviour and the forced behaviour is an extremely powerful benefit of this approach, allowing for further analysis in the structures. This is achieved due to the full three-dimensional spectral reconstruction the DIC method allows for.

7.5 Conclusion

The work in this paper analysed the quality of the frequency-wavenumber analysis of the free-surface of shallow turbulent flows, from data collection using Digital Image Correlation (DIC). The DIC scheme was tested in a laboratory, under various uniform, steady flow conditions. The DIC scheme relies on particles that are placed in the flow that float on the surface, this causes some issues in reconstruction when particles submerge into the flow, via downwelling or other phenomena. As the

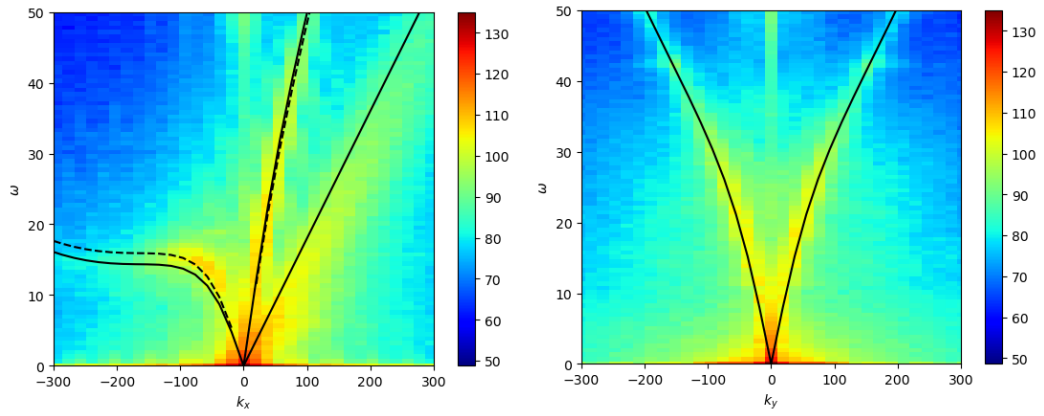

Figure 7.6: Frequency wavenumber spectrum for (a) $K_y = 0$, (b) $K_x = 0$ for flow condition 1(A), (c) $K_y = 0$, and (d) $K_x = 0$ for flow condition 1(B) (solid line relates to Equations 7.1 and 7.2, dotted relates to 7.4, colour online).

missing data follows the same structure as the recovered data, due to the hydraulic conditions, this appears to not hinder analysis much, even as the proportion of missing data reached 60% of the interrogated region. The method used to analyse the behaviour of the reconstructed free-surface elevation profile was the frequency-wavenumber spectrum.

For the A series and the B series of measurements, care was taken to maintain the same experiment setup for a pair of flow conditions (i.e. FC1A and FC1B). This can be seen with the matching of the discharge given in Table 7.1. This allows for an investigation on the effect of the different bed layouts to the streamwise velocity and the depth. Overall, the B series of measurements has a higher surface velocity, depth, and Froude number, in comparison to the A series of measurements. Care should be taken in comparing FC1A and FC1B, where the change in discharge is

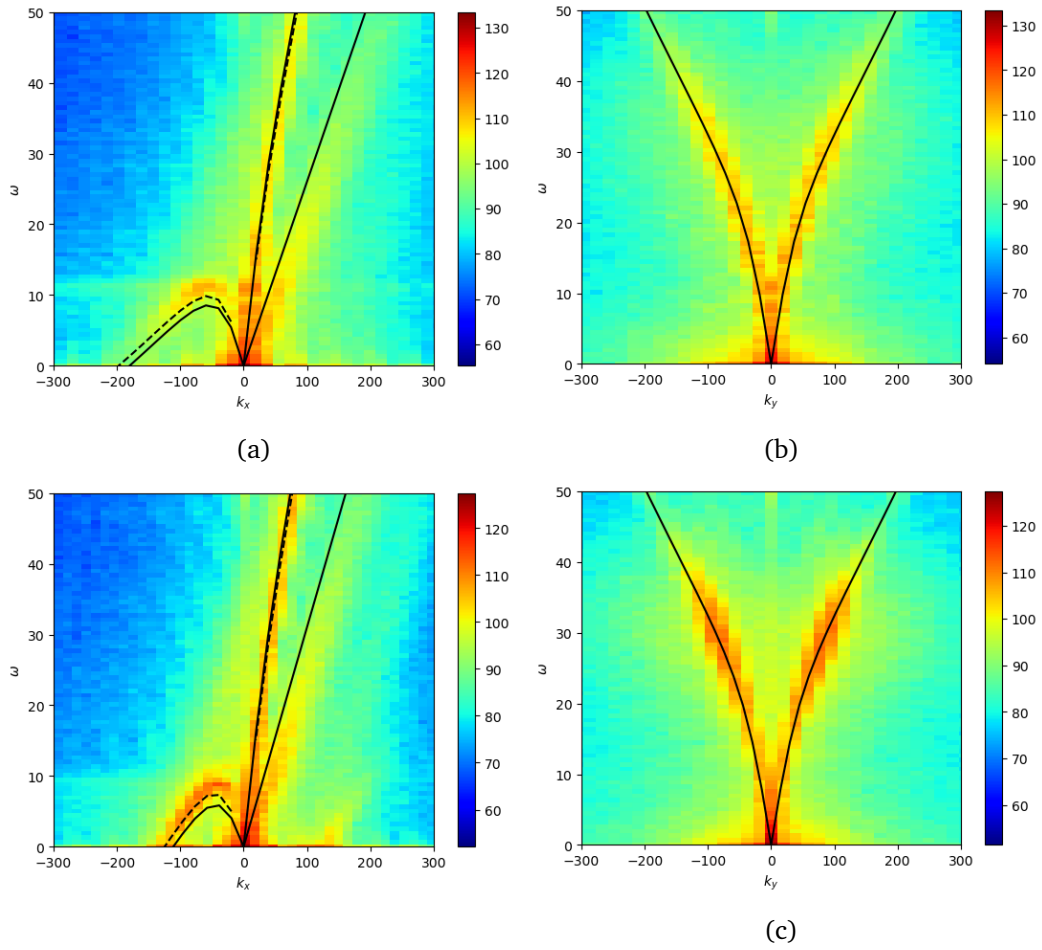

Figure 7.7: Frequency wavenumber spectrum for (a) $K_y = 0$, (b) $K_x = 0$ for flow condition 2(A).(solid line relates to Equations 7.1 and 7.2, dotted relates to 7.4, colour online).

high. These effects are represented in the frequency-wavenumber plots, and the theoretical dispersion relations fit well.

The results presented in this work relate to the matching of the experimental frequency-wavenumber spectrum and the theoretical dispersion relations. Good matching, and separation, indicates that the reconstruction from the DIC scheme has good agreement to theoretical relations, as well as being predictable. The results show that gravity capillary waves are present in Flow conditions 1 and 2 for both the A and B measurements, and this information is captured in the dispersion relation. As the flow rate increase, the gravity capillary waves appear to change substantially, and seem to be following the trend of the velocity dominated advection dispersion curve. Throughout all flow conditions, the lateral frequency-wavenumber plot shows excellent agreement to the expected dispersion relation,

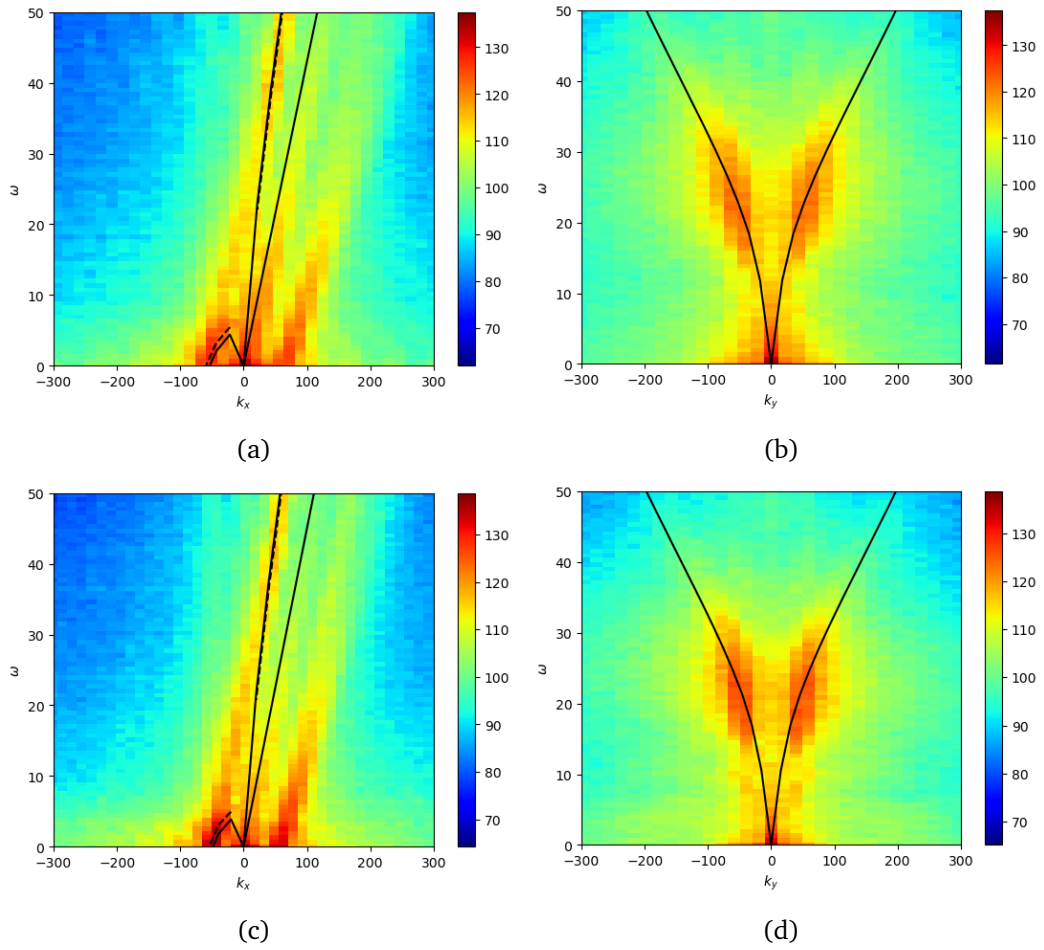

Figure 7.8: Frequency wavenumber spectrum for (a) $K_y = 0$, (b) $K_x = 0$ for flow condition 3(A), (c) $K_y = 0$, and (d) $K_x = 0$ for flow condition 3(B) (solid line relates to Equations 7.1 and 7.2, dotted relates to 7.4, colour online).

and the streamwise frequency-wavenumber plot shows great agreement to the expected dispersion relation. This validates the approach for non-intrusive DIC-based systems to analyse the free-surface of shallow turbulent flow, even with the issue of data sparsity.

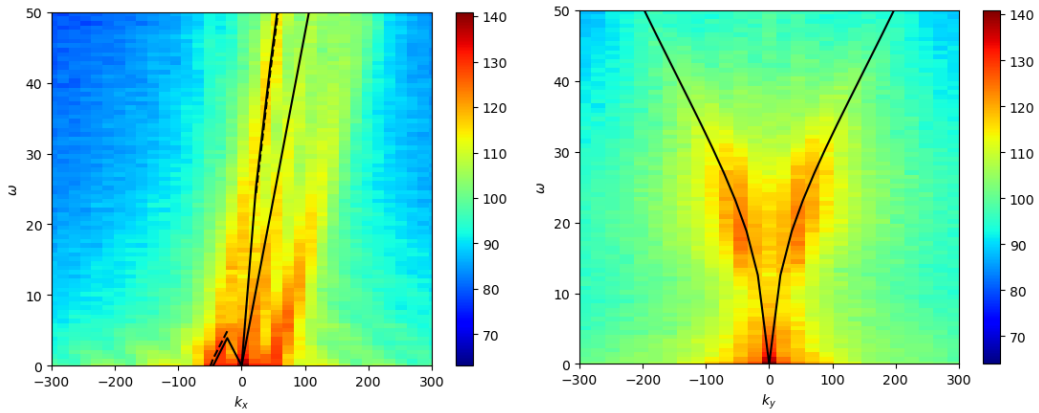

Figure 7.9: Frequency wavenumber spectrum for (a) $K_y = 0$, (b) $K_x = 0$ for flow condition 4(A), (c) $K_y = 0$, and (d) $K_x = 0$ for flow condition 4(B) (solid line relates to Equations 7.1 and 7.2, dotted relates to 7.4, colour online).

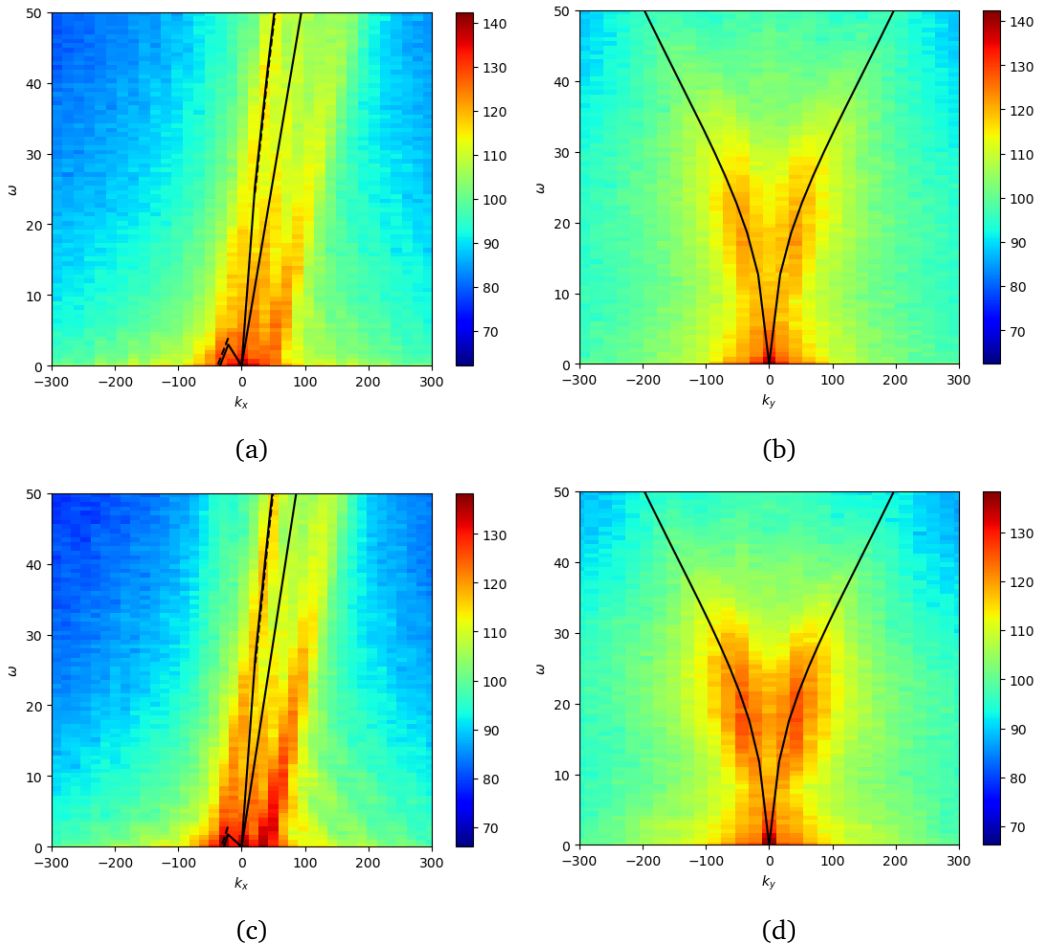

Figure 7.10: Frequency wavenumber spectrum for (a) $K_y = 0$, (b) $K_x = 0$ for flow condition 5(A), (c) $K_y = 0$, and (d) $K_x = 0$ for flow condition 5(B) (solid line relates to Equations 7.1 and 7.2, dotted relates to 7.4, colour online).

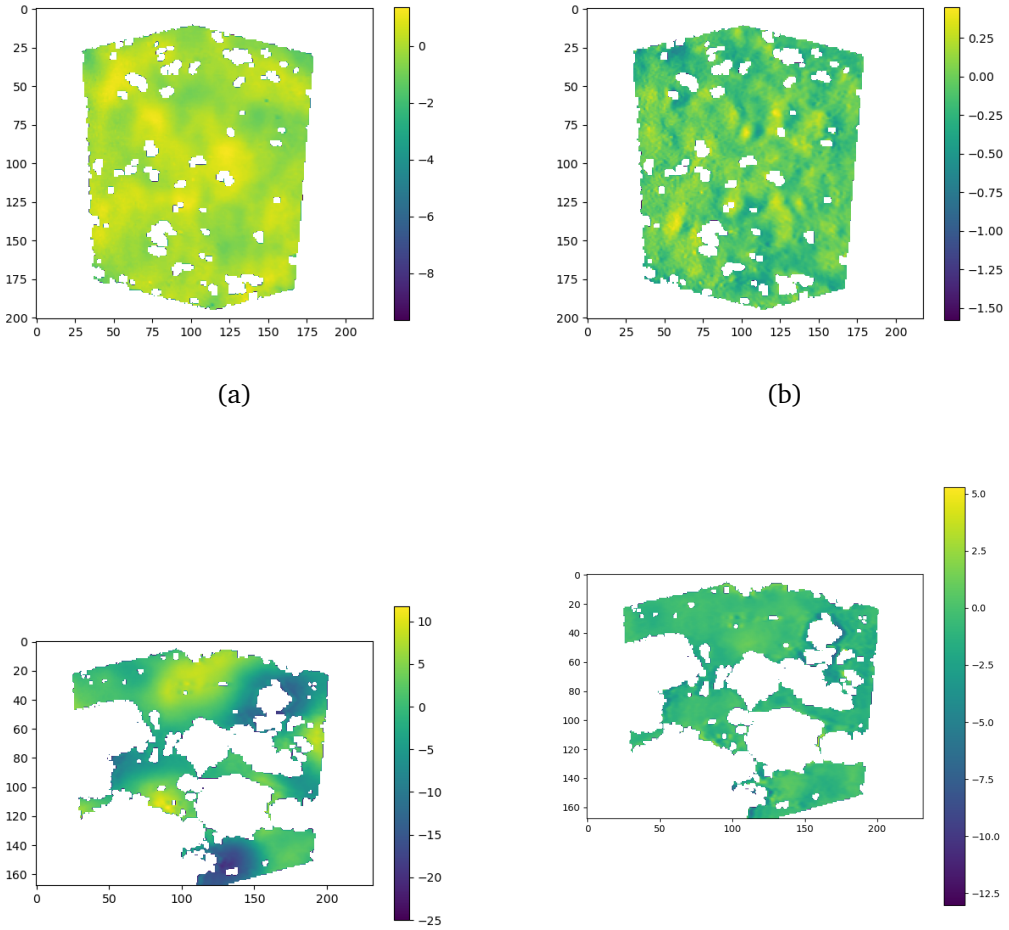

(a) (b)

(c) (d)

Figure 7.11: Extraction of the forced waves and the gravity-capillary waves using a mask centered at the forced dispersion relation. In (a) The gravity-capillary waves for FC1B, (b) contains the forced waves for FC1B. In (c) and (d) FC5B gravity-capillary waves, and forced waves are presented, respectively. The image corresponds to 5.21 seconds in the data.

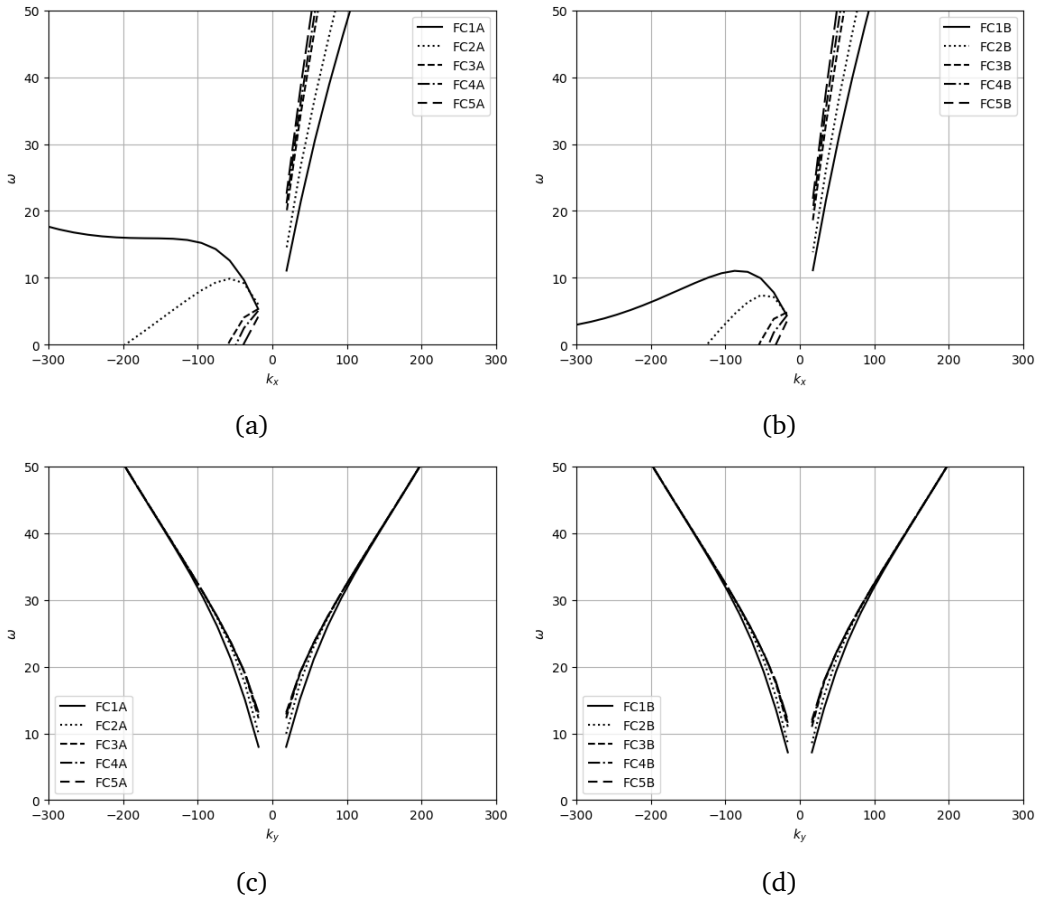

Figure 7.12: Comparison of the theoretical dispersion relation lines grouped by the A set of measurements, and the B set of measurements. In (a) the streamwise dispersion relations are shown for the A measurements, (b) contains the lateral dispersion relations for the A measurements. In (c) and (d) the B measurement's streamwise and lateral relations are presented, respectively.

Chapter 8

Using Metropolis-Hastings to estimate parameters of shallow turbulent flow from the free-surface elevation, a study

Reference

Johnson, M. D., Muraro, F., Tait, S., Dolcetti, G., and Krynkin, A. Using Metropolis-Hastings to estimate parameters of shallow turbulent flow from the free-surface elevation.

Author Contributions

- Johnson, M.D., - Problem formulation, writing, model development, data analysis, editing, structure.
- Muraro, F. - editing, data collection,
- Tait, S. - editing, technical advice.
- Dolcetti, G. - editing, data collection.
- Krynkin, A. - editing.

Summary

For the reasons already given in chapters 4-6, it is desirable to extract the parameters of the moving surface from the frequency wavenumber spectrum generated

using the technique given in the chapter 7. The practical application of this for a moving surface is to extract the depth and velocity of a river from its free-surface. The following Chapter attempts to do this. Due to the noisy nature of the frequency-wavenumber plots, as well as the fact that there is inherent spatial dependence in x and y, the model used for inversion needs to take advantage of these conditions. Because of these factors, random forests, K-nearest neighbours and other models were omitted in favour of the iterative MCMC approach, which in the likelihood function can get a metric of spatial dependence.

This Chapter aims to find the posterior distribution of the streamwise velocity, the lateral velocity, and depth given a set of two frequency-wavenumber slices corresponding to $k_x = 0, k_y = 0$. The Adaptive Metropolis scheme was tested on this, due to the relatively low dimensionality of the parameter space and the input space. If more slices were used (increasing the dimension of the input space) then Hamiltonian Monte Carlo would be more appropriate, as it has a greater ability to handle higher dimensional spaces.

The model was tested on two sets of experimental data. The first set of experimental data was the DIC data used previously in Chapter 7, the second set of data was collected at the River Sheaf in Sheffield. This data was provided open access from the paper [2].

The underlying methodology of this approach is first to assume that the dispersion curves can be approximated in analytic form. Therefore, artificial images can be produced by setting the value 1 to a pixel corresponding to the correct k_x, ω, k_y, ω bin. Once done, the theoretical image can be compared with the normalised experimental data in order to evaluate the likelihood. The further assumption is then made that once normalised, the maximal value at each frequency must correspond with the signal of the underlying flow dispersion, otherwise the MCMC method is fitting to noise.

Through both the DIC and the CCTV images from the River Sheaf, the mean velocity is recovered well. Investigating the credible interval overlaid on the frequency-wavenumber plot, the spread of the velocities in the data is also well recovered. This posterior distribution could then give further information regarding the spread of velocities present in the videos, which is an upgrade to the typical average approach one gets when using a frequency-wavenumber optimiser. This is a significant improvement in generating results from a frequency-wavenumber based approach.

The main problem with this approach is the recovery of the depth. The depth is not recovered well. This could be due to a multitude of factors. Changing the

mean flow velocity rotates the dispersion curves due to the Doppler effect, and thus causes a large amount of noise in the depth component. The depth is also much less sensitive than the velocity, causing minimal overall change in the dispersion relation compared to the velocity.

This work paves the way for a Bayesian reconstruction of the flow velocity, without the need for tracers. Further work is needed to be able to recover the depth, but initial results are promising.

8.1 Abstract

Estimating parameters in river monitoring non-intrusively has been a major area of research, especially with respect to gaining velocity information. Two key methods currently used for this are Particle Image Velocimetry (PIV) and Fourier based methods. Although PIV methods are superior with their spatial resolution, there is a strict requirement on movable tracers in the flow. Fourier methods have the benefit of probing the underlying dispersion relation, and do not need tracers. However, they can only capture the spatial and temporal average. This work aims to extract further information than the average one typically gets from Fourier based methods. In order to capture the spread of information that is present in the underlying frequency-wavenumber relation, this work aims to use an Adaptive Metropolis algorithm to obtain posterior distributions of predicted flow velocities and depths such that more information about the flow can be obtained as opposed to a single point estimate.

8.2 Introduction

Non-intrusive evaluation of the behaviour of flow that can be observed in river flow is of great importance. Floods are one of the leading causes of naturally occurring damage to property in the UK. For example, the estimated cost over the winter of 2015/2016 for property and business affected by storm Desmond was “likely to be >£1.3 billion" [5], and in November 2019 estimated insurance payouts to homes and business that were effected by flooded “would reach £110 million" [6]. Due to this the prediction and prevention of floods is an area of active research [7] [8] [9]. Much of this research is the development of non-intrusive evaluation of the river flow, typically to target the discharge which takes the velocity of the flow and the depth of the flow into account. It should be noted that any technique should

be evaluated not only on its accuracy but also the ease of its implementation and cost given that surveying a wise area is key to building a network of information to prevent damage.

A key issue when monitoring some rivers is where they are shallow and turbulent. If intrusive measurement systems are in place, the local depth and the velocity could reduce the reliability of the results that can be observed. A key non-intrusive evaluation method that is prominent in this field is Particle Image Velocimetry (PIV). PIV methods rely on “tracers" that are present through the video recording of the region. These tracers may be naturally occurring or may be introduced into the flow, the restriction on this is that the chosen tracers need follow appropriately the movement of the flow, and the interrogation area needs to be sufficiently covered in order to drive the high spatial resolution that PIV benefits from. Many review papers have been released since its inception in 1984 [132] such as [133] [134] and most relevantly [135]. PIV has proven to be a powerful method for obtaining velocity field measurements over a large region. This has lent itself to measuring the velocities at the free surface of rivers. For example [136] collates several different examples where this has been used for rivers, such as the Katsura river.

A defining feature PIV is the reliance on tracers in the flow that are either naturally present in the flow, or are artificially introduced into the flow in such a way as to not significantly change the flow, the motion of these is used to find the velocity field. This poses a significant issue, especially when attempting to scale this up. There are two options: one is being completely passive, having cameras in a vast amount of locations and only capturing data in the event of natural tracers appearing, thus reducing the region of interrogation in space and time or automatically add seeder to the flow. Or the motion of flow can be looked at directly, two of these approaches are optical flow (some examples of using this for free-surface measurements are [137], [138], [139], [140]), or Fourier analysis. This work will focus on the latter.

The specific method of Fourier analysis that will be considered is that of the frequency-wavenumber spectrum. Using spectral analysis for ocean waves has been studied extensively, and has been explained clearly in [17], it has been extended to the study of shallow turbulent flows using wave probes in [18] and [127]. The key point of these papers was to investigate how the free-surface’s dispersion relation changed with rough beds, which cause a large factor in shallow flows where boundary conditions have more of an effect [2]. The culmination of this was a non-invasive approach in [2] where an approximation of the dispersion relation due to

advection was linked with the dispersion relation due to gravity capillary waves. Good agreement was found experimentally with these relations, then an optimizer was fit to be able to estimate the discharge and the depth. An issue that arises when considering an optimizer on Fourier transformed data is that only a single value for velocity and depth can be recovered. These values represent the spatial and temporal average of the system. However, as it is not true that the velocity and the depth are constant in space and time, this work aims to extend the prediction by using a Bayesian framework. This is done by first treating the frequency-wavenumber spectrum as an image, and these images are formed from the theoretical dispersion relations. The images are compared through the use of the MCMC methods, which have shown promise in gathering information from dispersion relations in the seismic domain [142]. The MCMC generates a posterior distribution of the depth and the velocity, which should captures the noise in the data from measurement noise and also the spread of velocities in the timeline of measurement.

This work is presented as follows: Section 2 contains relevant summaries of the theory of dispersion relations, investigates the sensitivity of the dispersion relations to their parameters, explains how the frequency-wavenumber plots were obtained and outlines the theory for the Adaptive Metropolis scheme. Section 3 outlines the setup of the two experiments that provide the data used in the analysis. Section 4 contains the results, and section 5 the conclusions.

8.3 Theory

The key structure that one obtains from a frequency-wavenumber spectrum is a measure of the underlying dispersion relation. This section introduces three dispersion relations that well approximate the shallow turbulent flow. If the mean speed of the flow is faster than pattern deformations, the fluctuations in time at a fixed point is primarily due to advection yielding an approximate dispersion relation[2]:

$$\Omega_A(\mathbf{k}, \mathbf{U_0}) \approx \mathbf{kU_0} \tag{8.1}$$

Where $\mathbb{U}$ is the velocity in the streamwise and lateral direction. The dispersion relation due to gravity capillary waves can also be approximated as[151] [2] [126]

$$\Omega_{GW}(\mathbf{k}, d, \mathbf{U_0}) = (1-\beta)\Omega_A \pm \sqrt{(\beta\Omega_A)^2 + \Omega_i^2} \tag{8.2}$$

$$\Omega_i(\mathbf{k}, d) = k\sqrt{gd\frac{1+B}{B}\frac{\tanh kd}{kd}} \tag{8.3}$$

Where

$$B = \frac{\rho g}{k^2\gamma} \tag{8.4}$$

Is the Bond number, and

$$\beta = \frac{m}{2}\tanh kd. \tag{8.5}$$

In this work, m, the velocity gradient, is set to 0.34, $g \approx 9.81$ is acceleration due to gravity, γ is the surface tension between water and air, ρ is the density of water, and d is the depth.

The dispersion relations are mainly affected by the depth averaged flow velocity $\mathbf{U_0}$ and the depth of the flow. However, the dispersion relation is substantially more sensitive to the velocity in comparison to the depth[2], usually only being able to visibly see a change at $k \in [-60, 60]$, as

$$\frac{\partial \Omega_{GW}}{\partial U_0} = k(1 - 0.17\tanh(kd)) + \frac{0.0289k^2U_0\tanh(kd)^2}{\sqrt{\left(\frac{\gamma k^3(1+\frac{g\rho}{\gamma k^2})\tanh(kd)}{\rho} + 0.0289k^2u^2\tanh(kd)^2\right)}} \tag{8.6}$$

$$\frac{\partial \Omega_{GW}}{\partial d} = \frac{k^2}{\cosh(kd)^2}\left(-0.17U_0 + \frac{0.5\gamma k^2 + 0.5g\rho + 0.0289k\rho U_0^2\tanh(kd)}{\rho\sqrt{\frac{k\tanh(kd)(\gamma k^2 + g\rho + 0.0289k\rho U_0^2\tanh(kd))}{\rho}}}\right) \tag{8.7}$$

Sensitivity analysis of the parameters are presented in Figures 8.1 and 8.2, which show the change in Equations (8.6) and (8.7) (here the ± is reduced to the plus case) respectively. As can be seen in the figures, the change with respect to depth happens only in a small region below 0.5m and this change cannot be observed easily at wavelengths when the depth increases. The scale difference between the values presented in the sensitivity to the velocity in comparison to the sensitivity due to the depth also highlights a potential issue, as the velocity is much higher than the depth.

The underlying assumption driving this work is that the observed free-surface elevation is behaving similarly to what is expected from the dispersion relations. That is to say, taking the Fourier transform in both spatial directions and the temporal

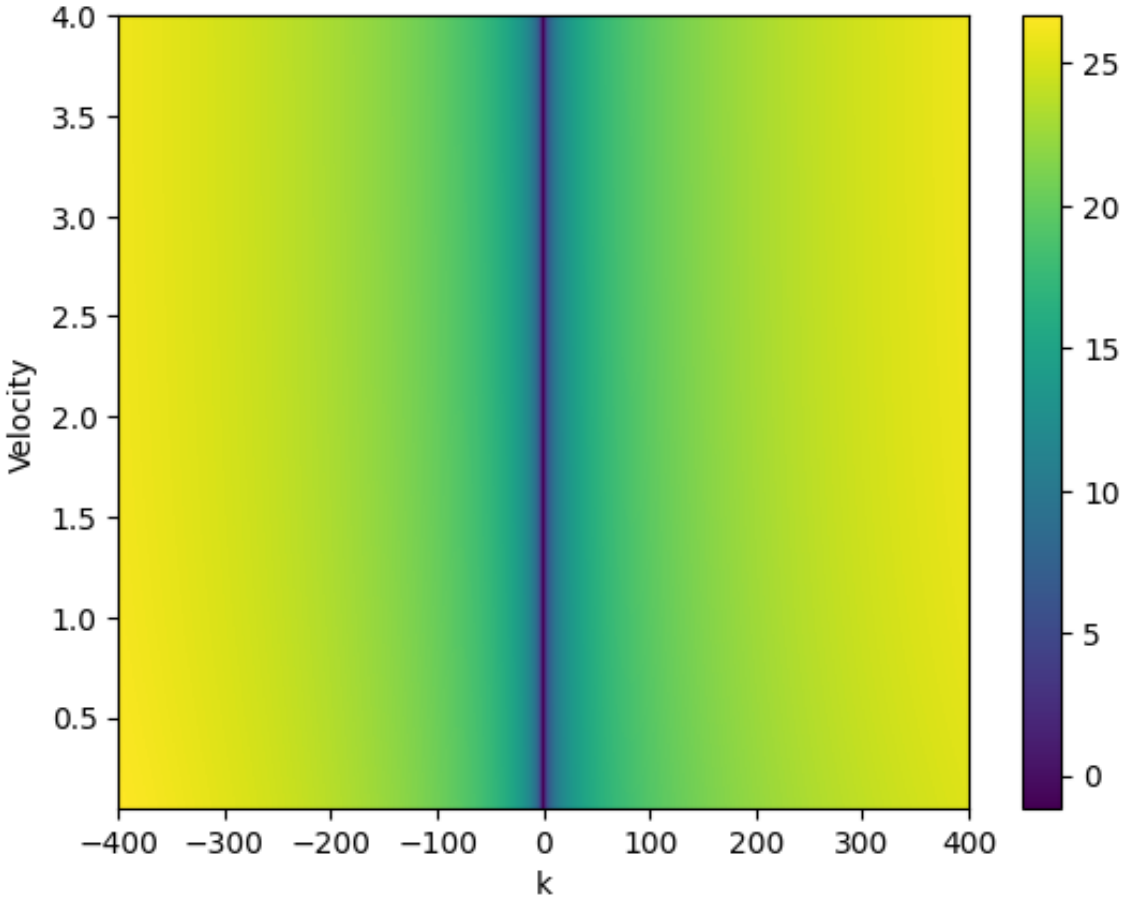

Figure 8.1: Heatmap presenting the $10\log_{10}$ sensitivity of the gravity-capillary dispersion relation with respect to the velocity as the velocity varies from 0m/s to 4m/s and wavenumber between -400 and 400. The depth was fixed at 0.3.

direction (to obtain a frequency-wavenumber spectrum) should yield information that can be related back to the dispersion relations.

In the case of this work, the resulting frequency-wavenumber spectrum is treated like a pattern in an image. Suppose ζ represents an image of size $N_x \times N_y \times N_t$, where $\mathbf{x} = [x_0, ..., x_{N_x-1}]$, $\mathbf{x} = [y_0, ..., y_{N_y-1}]$ $\mathbf{x} = [t_0, ..., t_{N_t-1}]$, and $\zeta(x_i, y_j, t_k)$ represents the pixel intensity at a specific location and time. Then, the Discrete Fourier Transform (DFT) is applied as such:

$$\hat{\zeta}(k_i, k_j, \omega_k) = \sum_{m=0}^{N_x-1} \sum_{n=0}^{N_y-1} \sum_{p=0}^{N_t-1} \zeta(x_m, y_n, t_p) \exp\left(-i\left(\frac{2\pi}{N_x} k_i n + \frac{2\pi}{N_y} k_j m + \frac{2\pi}{N_t} \omega_j p\right)\right) \quad (8.8)$$

This was implemented in the data analysis and model through numpy's fftn function. Figure 8.3 highlights what the resulting frequency-wavenumber plot looks

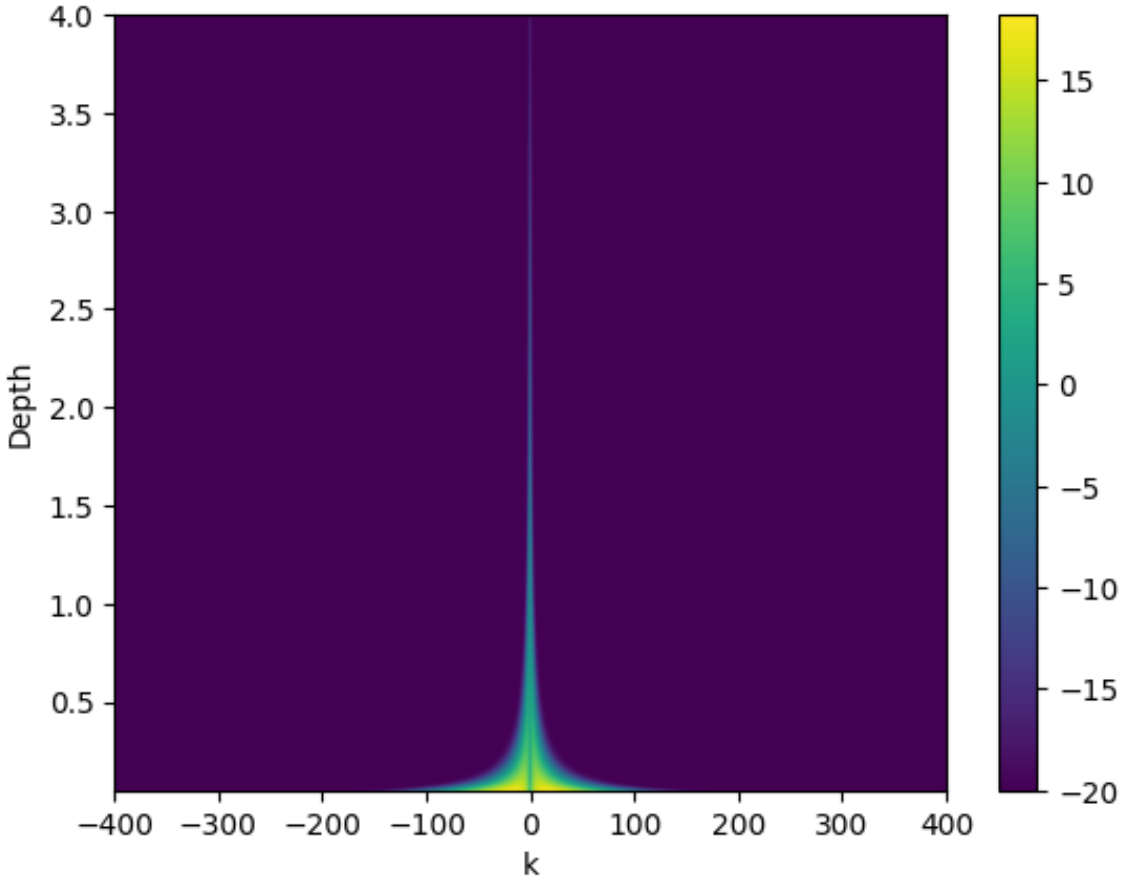

Figure 8.2: Heatmap presenting the $10\log_{10}$ sensitivity of the gravity-capillary dispersion relation with respect to the depth as the depth varies from 0m to 4m and wavenumber between -400 and 400. The velocity was fixed at 0.1.

like, for $k_y = 0$. The results were obtained by producing a dynamic surface that strictly obeyed the above dispersion relations. Three distinct lines are present in the figure, and these align to the theoretical dispersion relations for the velocity and depth which were presented in Equations 8.2 8.1.

Similar to the behaviour that can be seen in Figure 8.3 this work considers only the slices of frequency-wavenumber when $k_x = k_y = 0$. This allows for treating the two slices as “images", where each pixel in the image corresponds to a particular (frequency, wavenumber) bin. Images can be produced from the theoretical dispersion relations, for a specific velocity U_0 and depth d, given in Equations (8.1) and (8.2) by the given relation.

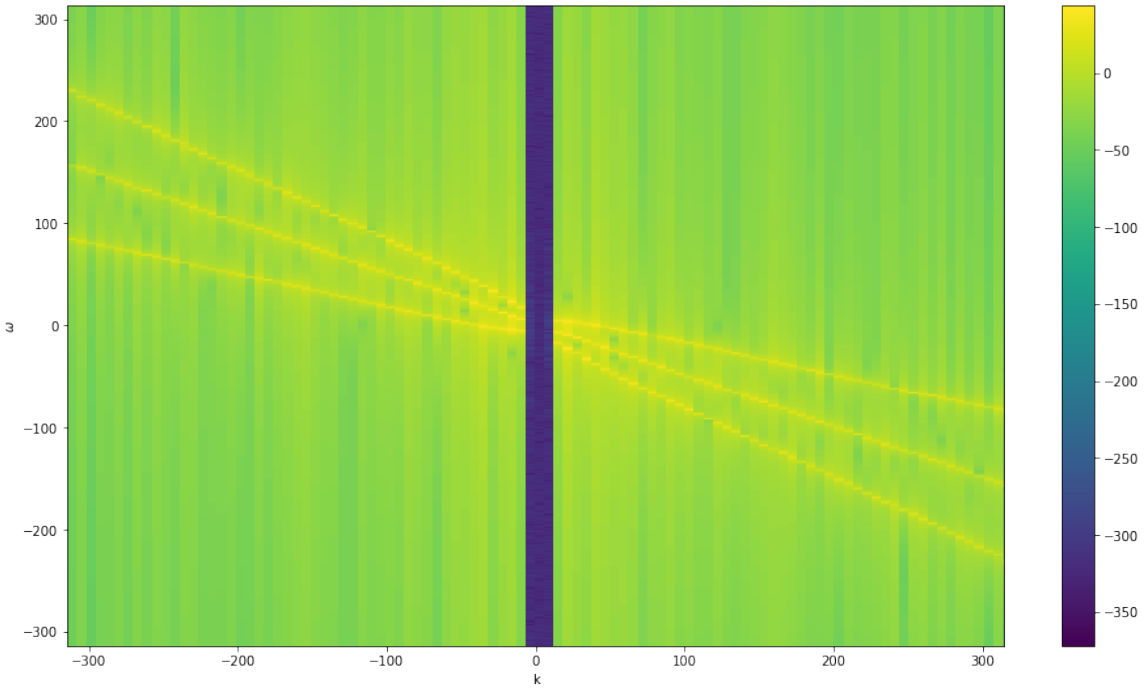

Figure 8.3: Absolute value $10\log_{10}$ frequency-wavenumber spectrum from a surface generated using the dispersion relations given in Equations 8.18.2, for: depth = 0.4m, streamwise velocity = 0.5m/s, temporal sample rate = 200Hz, spatial sample rate = 10001/m.

$$I(\omega_i, k_j, U_0, d) = \begin{cases} 1 & abs(\omega_i - k_j U_0) \leq \epsilon \\ 1 & abs\left(\omega_i - \left((1-\beta)\Omega_A \pm \sqrt{(\beta\Omega_A)^2 + \Omega_i^2}\right)\right) \leq \epsilon \\ 0 & \text{else} \end{cases} \tag{8.9}$$

With this, a theoretical image can be produced that is 1 when the current pixel relating to ω_i, k_j is close to the theoretical dispersion relation and is 0 otherwise. Once a theoretical image is produced, errors can be calculated.

8.3.1 Metropolis-Hastings

Figure 8.3 presented an idealised representation of the frequency-wavenumber spectra. No representative noise sources were added. This causes three very clear lines in this figure. In reality, this will not be observed due to noise such as unstable lighting, objects interfering with the video (e.g. a duck swimming through the frame), and other miscellaneous camera issues. Due to the noise sources, it was decided that a model under the Bayesian framework would be more representative

of the underlying data. The Metropolis-Hastings algorithm was selected for this due to the relatively low dimension of the parameter space. In order to introduce the Metropolis-Hastings algorithm, define $\mathbf{D}$ to be a given dataset, and θ to be a set of parameters to infer. In this case, streamwise velocity, depth, and lateral velocity. By Bayes' theorem:

$$\mathscr{P}(\theta|\tilde{\mathbf{D}}) \propto \mathscr{P}(\tilde{\mathbf{D}}|\theta)\mathscr{P}(\theta). \tag{8.10}$$

Where $\mathscr{P}(\theta)$ is the Prior distribution, which contains information about existing beliefs about the physics of the system and acts as a starting point for the algorithm. In this work, this is defined as

$$\mathscr{P}(\theta) = f_{HN}(\theta_1, 0, 1.1) f_{HN}(\theta_2, 0.0005, 0.2) f_{HN}(\theta_3, 0, 0.01) \tag{8.11}$$

Where f_{HN} denotes the Half Normal distribution, where the first argument is a parameter that is estimated through the MCMC scheme. The second argument is the location where the step discontinuity occurs, and the third argument is the standard deviation.

$\mathscr{P}(\theta|\tilde{\mathbf{D}})$ is the Posterior distribution, which yields probability distributions for each parameter of interest. In the case of this work, the posterior distribution is used to infer the distributions of the streamwise velocity, the depth, and the lateral velocity.

The likelihood function is $\mathscr{P}(\tilde{\mathbf{D}}|\theta)$ which is a term which evaluates how likely the data was produced from the selected parameters. In this work, Gaussian likelihood was selected and is defined as

$$\mathscr{P}(\tilde{\mathbf{D}}|\theta) = f_{MN}(\tilde{\mathbf{D}}, \theta, \Sigma) \tag{8.12}$$

with

$$f_{MN}(\tilde{\mathbf{D}}, \theta, \Sigma) = \frac{\exp\left\{-\alpha^T \Sigma^{-1} \alpha/2\right\}}{\sqrt{(2\pi)^k |\Sigma|}}, \tag{8.13}$$

$$\boldsymbol{\alpha} = [\tilde{\mathbf{D}_x} - \boldsymbol{I(\omega, k, \theta_0, \theta_1)} + \tilde{\mathbf{D}_y} - \boldsymbol{I(\omega, k, \theta_2, \theta_1))}] \tag{8.14}$$

Where Σ is a covariance matrix representing the estimated error in the data. The likelihood function aims to compare the real data and the theoretical result. The relationship between the parameters θ and the flow parameters are $[\theta_0, \theta_1, \theta_2] =$

$[U_x, d, U_y]$. The Metropolis-Hastings algorithm acts on two slices of the frequency-wavenumber representation, one for $k_x = 0$ and the other for $k_y = 0$. These two theoretical images are then compared to the slices of the real data which corresponds to $k_x = 0, k_y = 0$ through the use of f_{MN}. If the model perfectly fits the data, this value will be maximal. The required values are defined so the Metropolis-Hastings algorithm can be applied as in Algorithm 3. The proposal step was altered adaptively through the application of an updated covariance matrix as in [164] and is known as Adaptive Metropolis (AM).

The workflow used throughout this work is as follows. First, extract each frame of a video as separate images then, using the Fast Fourier Transform, construct the full frequency-wavenumber spectra. These spectra contain all values of k_x and k_y, so the slices relating to $k_x = 0$ and $k_y = 0$ need to be extracted. Following this, a normalisation scheme was applied. For each frequency, the maximum value of k_x (or k_y) was found, the whole range was then divided by this maximum. The reason for this normalisation scheme was that the signal in the presence of noise should be maximal at - or close to - the theoretical value, and normalising to 1 causes the difference with Equation 8.9 to be 0 and thus the likelihood function is maximised.

Algorithm 3 Metropolis-Hastings Algorithm

Initialise θ_0
for $n = 0, \ldots, N-1$ **do**
  Sample $u \sim U(0,1)$
  Sample $\theta' \sim q(\theta' \mid \theta_n)$
  if $u \leq \alpha(\theta_n, \theta') = \min\left(1, \frac{\tilde{p}(\theta')q(\theta_n|\theta')}{\tilde{p}(\theta_n)q(\theta'|\theta_n)}\right)$ **then**
    $\theta_{n+1} = \theta'$ ▷ Accept sample.
  else
    $\theta_{n+1} = \theta_n$ ▷ Reject sample.
  end if
end for

8.4 Data collection

In order to evaluate the viability of using the Metropolis-Hastings approach to reconstruct the posterior probability distribution of the streamwise velocity, depth and lateral velocity, the method was used to infer these values from two distinct data collection schemes. The first scheme was Digital Image Correlation (DIC) acquired

elevation profile of the free-surface, in laboratory conditions. DIC benefits from reconstructing true elevation based on tracers in the flow.

The next collection scheme is from the field, as opposed to the laboratory. This collection scheme was from the river Sheaf, through the analysis of Closed-Circuit Television (CCTV). A CCTV camera was placed such that the free-surface of the river can be viewed. Although the elevation isn't directly recovered, the change in intensity of the pixels should exhibit the same motion as what would be expected from the frequency-wavenumber spectrum. The data collected from the river Sheaf has more potential issues than the DIC recovery, due to uncontrollable lighting conditions, as well as interference in the motion of the pixels due to wildlife or debris. Some specifics of the measurements are presented below.

8.4.1 DIC measurements

Ten experiments were conducted with steady, uniform flow conditions over two different bed arrangements. The surface behaviour was investigated using a Digital Image Correlation system positioned 4.4 m downstream from the beginning of a given bed. The DIC system was comprised of two Imager MX 4M cameras (2048x2048 pixel, 5.5 μm size pixel) with Tamron M112FM16 lenses (16 mm focal length, F/2.0). The cameras were placed 0.40 m above the bed and spaced 0.70 m apart. Because of the different flow conditions, the field of view varied between a square of side 325 to 363 mm, and the camera's spatial resolution varied between 0.16 and 0.18 mm/pixel. The angle between the cameras varied from 40.8° to 47.3° with respect to the horizontal plane. Two blue LEDs illuminated a total area of 350x250 mm^2, and were positioned 0.20 m above the cameras in elevation.

The tracers used in order to reconstruct the free-surface profile were cenospheres (POS-IBW 300 by Possehl Erzkontor). These were used to identify the location of the water surface. These tracers are designed to have low density ρ_{cs} = 700 kg/m3 such that they float on the water surface. They also produce a light colour on the free-surface, allowing the DIC to reconstruct the free-surface elevation.

The streamwise velocity and depths for all the experiments are located in Table 8.1, where the lateral velocity was taken to be 0, and thus not taken into account in this table. This table also contains some of the results from the MCMC, discussed further in Section 4.

8.4.2 River Sheaf

Field measurements were taken at the River Sheaf, in Sheffield. This was selected to allow direct comparison with [2] which also used measurements from this site to test an optimiser based approach to estimate the discharge and depth. The site was originally selected because of nearby gauging stations where the interrogation area was situated 25 m upstream of a river gauging station operated by the UK Environment Agency. The channel width was approximately 9.25 m. Dolcetti provides more contextual information regarding the selection process of this river, as well as the methods to recover depth in [2]. Orthorectified images for 17 different flow conditions were provided in [2] and all that was required was a further rotation of 45 degrees before processing into the frequency-wavenumber representation. The streamwise velocity was recovered from the discharge estimations given in [2], the depth information, and the bed width. Table 8.2 provides the wave gauge information on the streamwise velocity and depth, as well as the reconstruction effort from Dolcetti [2] followed by the reconstruction efforts in this work, as well as the corresponding errors.

8.5 Results

The algorithm was run for all flow conditions with 100,000 epochs. The first 10,000 of these was classified as the burn in period and thus was removed from the analysis. For both experiments the following figures and metrics are used to visualise the results of the analysis and evaluate its performance. First, a frequency-wavenumber plot of the data is shown, with overlaid lines that relate to the model prediction found from the mode of the parameters and the $\pm\sigma$ interval, found from a highest density interval (HDI). Following this, the smoothed plots, generated with a Gaussian kernel density estimation, of the distribution of streamwise velocity and depth are shown, as well as distributions of the streamwise velocity along the mode of the depth and the distribution of the depth along the mode of the streamwise velocity. Following this, the density plot of the streamwise velocity and the depth is produced, overlaid with black lines indicating the mode solution the location of the crossing point is thus the mode prediction.

8.5.1 DIC recovery

Figures 8.4, 8.5,8.6,8.7, 8.8, and the top half of Table 8.1 relate to the results from the Adaptive Metropolis scheme for the F series of measurements. Here, the F series of measurements relate to flow conditions that were measured in laboratory conditions in February 2022.

Figure 8.4 presents the frequency-wavenumber spectra from the data, overlaid with the mode prediction from the MCMC, overlaid with the 68% credible interval. Investigating the resulting overlays in Figure 8.4 it can be observed that the mode prediction and the 68% credible region capture the signal in the image well, this indicates that the Adaptive Metropolis traces have found the signal in the image.

In order to further understand the posterior distribution, Figures 8.5,8.6,8.7 are presented. This shows a Gaussian Kernel Density estimation of the results from the MCMC scheme. Investigating the mode predictions of the streamwise velocity, the errors are at worst -12%. The key outlier to this is FC2 where the streamwise velocity is 33.6%, this is identified as an outlier where the model has swapped from predicting the turbulence curve to the gravity capillary curve, causing a very distinct bi-modality in Figures 8.5,8.6,8.7. Looking at the first mode, the value is much closer to the full value. As long as the separation of the modes are distinct, then it should be easy to extract the true value (which will be the slower one) in these cases. Looking at the distributions of the streamwise velocity specifically in Figure 7.5 it can be observed that velocities tend to have a nice peak and tend to be Gaussian like, but tend to skew slightly to the right at the higher flow conditions. The errors with respect to the depth reconstruction are much higher, peaking at -63.1% for FC5. This can be observed in the distributions with respect to depth in Figures 8.5,8.6,8.7 with a consistently wide spread, indicating a lack of sensitivity to the depth for the F measurements.

The 2D densities from the streamwise velocity and the depths were produced in Figure 8.8, which visualises the spread over both dimensions. Investigating the densities shown in Figure 8.8 it can be observed that the location of the ground truth is always close to a region of high density.

Figures 8.9, 8.10,8.11,8.12, 8.13, and the bottom half of Table 8.1 relate to the results from the Adaptive Metropolis scheme for the J series of measurements, similar behaviour can be observed in comparison to the F series of measurements, within 20% error of the streamwise velocity. The depth is marginally improved, but still not entirely consistent with the ground truth. The same behaviour can be

$Test$	$\bar{U}_S$ (m/s)	D (mm)	$\bar{U}_{estS}$ (m/s)	D_{est} (mm)	Err_U	Err_D
FC1A	0.18	19.8	0.16	28	−11%	41.4%
FC2A	0.26	33.1	0.35	38	33.6%	14%
FC3A	0.43	64.1	0.38	75	−11.6%	17%
FC4A	0.47	81.6	0.45	45	−4.26%	−44.9%
FC5A	0.53	97.5	0.51	36	−3.78%	−63.1%
FC1B	0.23	20.7	0.22	30	−4.35%	−45.0%
FC2B	0.31	30.7	0.29	42	−6.45%	36.8%
FC3B	0.45	61.5	0.40	40	−11.1%	−35.0%
FC4B	0.51	76.7	0.44	56	−13.7%	−27.0%
FC5B	0.58	91.9	0.54	36	−6.9%	60.8%

Table 8.1: Table representing the different experiments from the DIC collection scheme. The first column represents names of the experiments. The second column represents the streamwise velocity. The information regarding the depth is in the third column, the fourth column represents the recovered mode streamwise velocity from the MCMC scheme, the fifth column represents the recovered mode depth from the MCMC scheme. The final two columns showcase the percentage error difference between the two.

observed in the smoothed results from the traces in Figures 8.10,8.11,8.12 as well as the densities presented in Figure 8.13.

8.5.2 CCTV recovery - River Sheaf

The full table of results from the Adaptive Metropolis (AM) scheme from the parameter recovery from the CCTV data is provided in Table 8.2. This table contains a comparison between the wave gauge measurements, as well as the predictions from the optimiser scheme in Dolcetti *et al* [2]. For visualisation of the results, a subset of the full dataset was selected that represents an even spacing of data to ensure that most flow regimes were covered without selection bias. Table 8.2 shows good self consistency in the velocity predictions, in comparison to the optimiser provided in [2], with an average absolute error in the velocity of approximately 4%. These results therefore are a further extension to the optimizer results in [2], because the resulting velocities recovered in the MCMC scheme form a full posterior distribution that can be used to gauge uncertainty in the prediction. For the depth however, the model fails at recovering the true depth through all flow conditions.

Investigating the frequency-wavenumber plots overlaid with the Adaptive Metropolis results (Figure 8.14) the significantly increased amount of noise in the form of blurring should be noted. Mostly this is due to the fact that clearly the flow is not

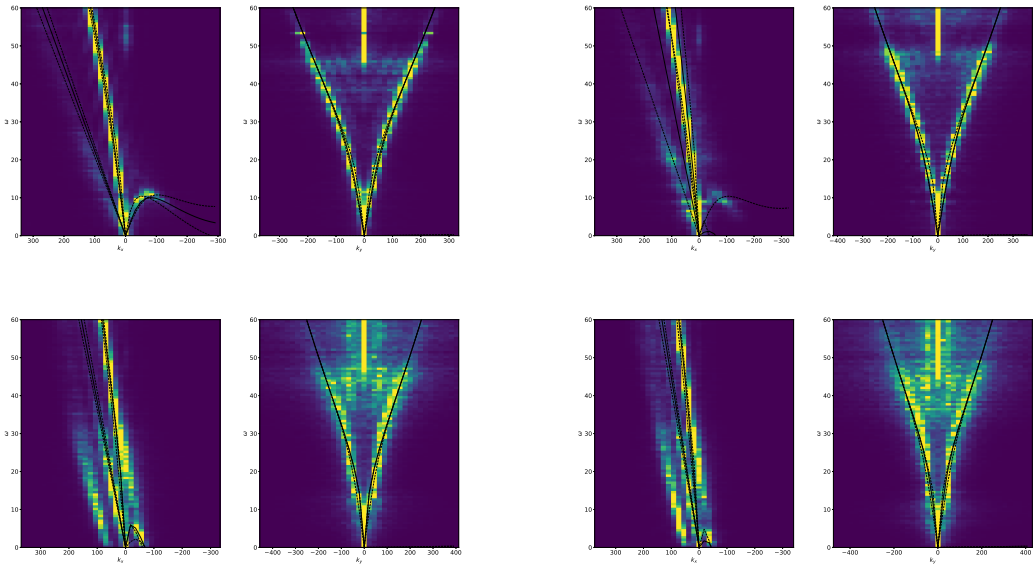

Figure 8.4: Frequency-wavenumber plot of the F series of measurements from the DIC collection scheme, with the overlaid mode prediction, as well as the prediction from the upper and lower bound of the 68 percent credible interval. For a) FC1 b) FC2 c) FC3 d) FC4

uniform in space and in time. This means that different regions propagate at different velocities at different points in time, which causes a blurring that increases with wavenumber, as velocity rotates the dispersion relation. Also, there is the presence of zero frequency noise in the $\frac{k_y}{2\pi}$ images, presumably due to stationary noise elements present in the image. Clearly, this is a more complicated domain than the DIC recovery scheme. In the presence of these increased challenges, however, the lines created from the results of the Adaptive Metropolis scheme capture the signal in the data well, widening at regions of higher blur. Looking at these plots also gives some insight on a potential reason the depth was not recovered: there is little to no signal in the $\frac{k_y}{2\pi}$ slices close to 0, which is where the sensitivity to depth is most present.

Figure 8.15 presents the 2D density plot for the streamwise velocity and the depth. It can be observed that the velocity mode line is close to the velocity recovered by Dolcetti in [2]. As the flow conditions increase, there is a widening of the velocity in the density plot, indicating more uncertainty present in the data. The depth 120mm onwards covers most of the domain space for the depth, again showcasing the lack of ability to reconstruct depth.

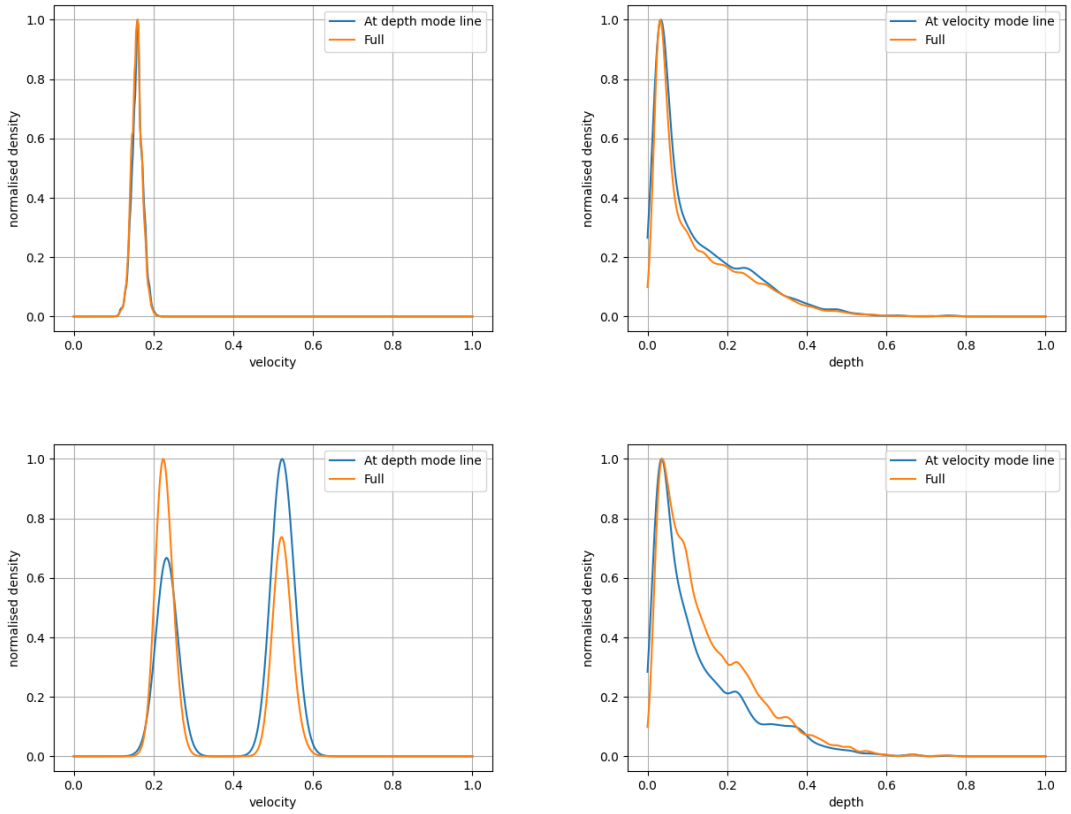

Figure 8.5: Smoothed histograms recovered from the MCMC scheme for the streamwise velocity and depth, as well as the streamwise velocity along the mode of the depth, and the depth along the mode of the streamwise velocity. For FC1A FC2A.

8.6 Conclusion

This work investigated using the theoretical dispersion relations to approximate parameters of the underlying flow through the application of an Adaptive Metropolis-Hastings scheme and the frequency-wavenumber spectrum. Because the dispersion relation is defined from its streamwise and lateral velocity, as well as its depth, an MCMC scheme was used to infer the posterior distribution of these three parameters. As the lateral velocity in all experiments was zero, this was omitted in presentation in favour of analysing the streamwise and lateral velocity. First, the sensitivity of the dispersion relations was analysed, which found that the sensitivity to changes in velocity was much higher throughout all values of frequency and wavenumber while the the sensitivity to depth was relatively small. An AM MCMC was tested on two distinct measurement schemes, both of which gave estimations of the free surface. It was found that the streamwise velocity was recovered well

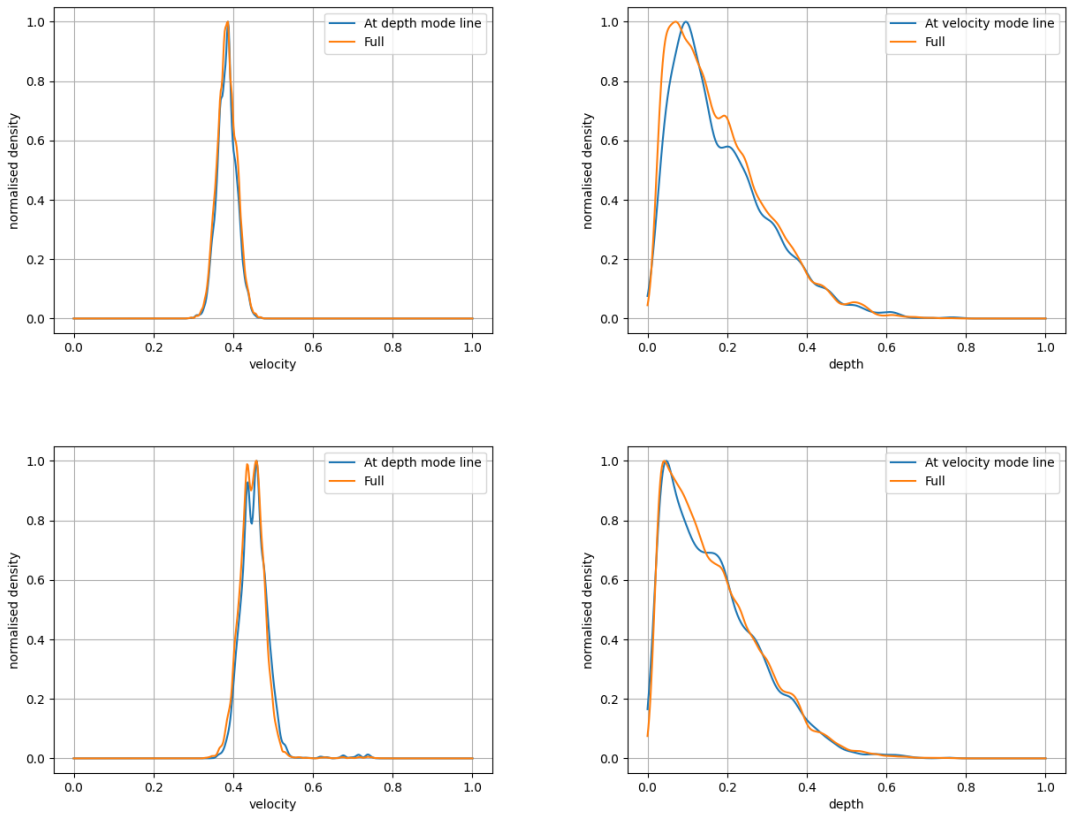

Figure 8.6: Smoothed histograms recovered from the MCMC scheme for the streamwise velocity and depth, as well as the streamwise velocity along the mode of the depth, and the depth along the mode of the streamwise velocity. For FC3A FC4A.

throughout the measurements, forming narrow Gaussian-like distributions in the posterior distribution. The method struggled to recover the depth. In order to make the likelihood function more sensitive to depth changes, such as one that integrates the energy in the image, as opposed to the line fitting approach in this work. The main benefit of the approach presented in this paper is that it successfully recovered the velocity of a moving surface using both DIC and CCTV measurements; an accurate means of recovering the surface velocity using CCTV measurements allows for tracer-free river tracking. This paper has also demonstrated that MCMC methods provide a credible interval for the velocity, this contains information about both the noise sources in the image and the distribution of surface velocities that are present .Future work could exploit this behaviour, and thus get more information about the surface velocimetry than the existing technologies which only provide the average flow velocity. Fully exploiting this ability to extract the distribution of surface velocities from spectra would represent a considerable step forward in using spectra

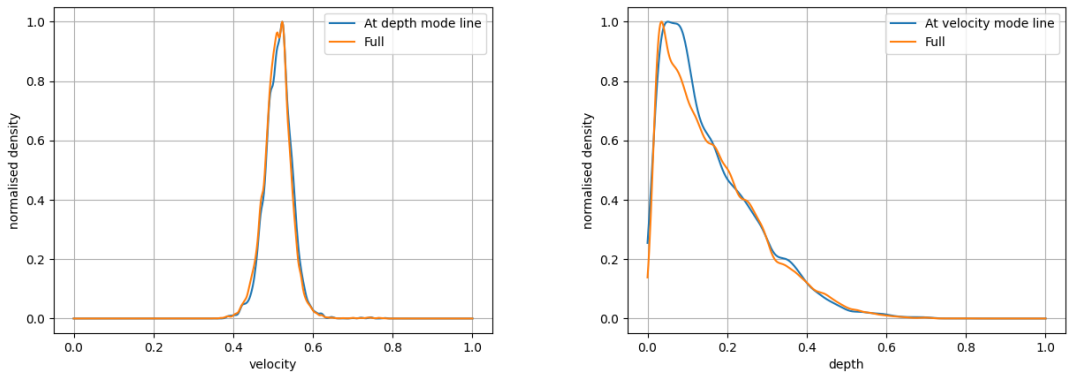

Figure 8.7: Smoothed histograms recovered from the MCMC scheme for the streamwise velocity and depth, as well as the streamwise velocity along the mode of the depth, and the depth along the mode of the streamwise velocity. For FC5A.

for surface velocimetry.

8.7 Acknowledgments

The authors would like to acknowledge the support of the UK Engineering and Physical Sciences Research Council (EPSRC) via the Knowledge Exchange Support Fund. M.-D. Johnson would like to acknowledge the support of the University of Sheffield through their PhD studentship award.

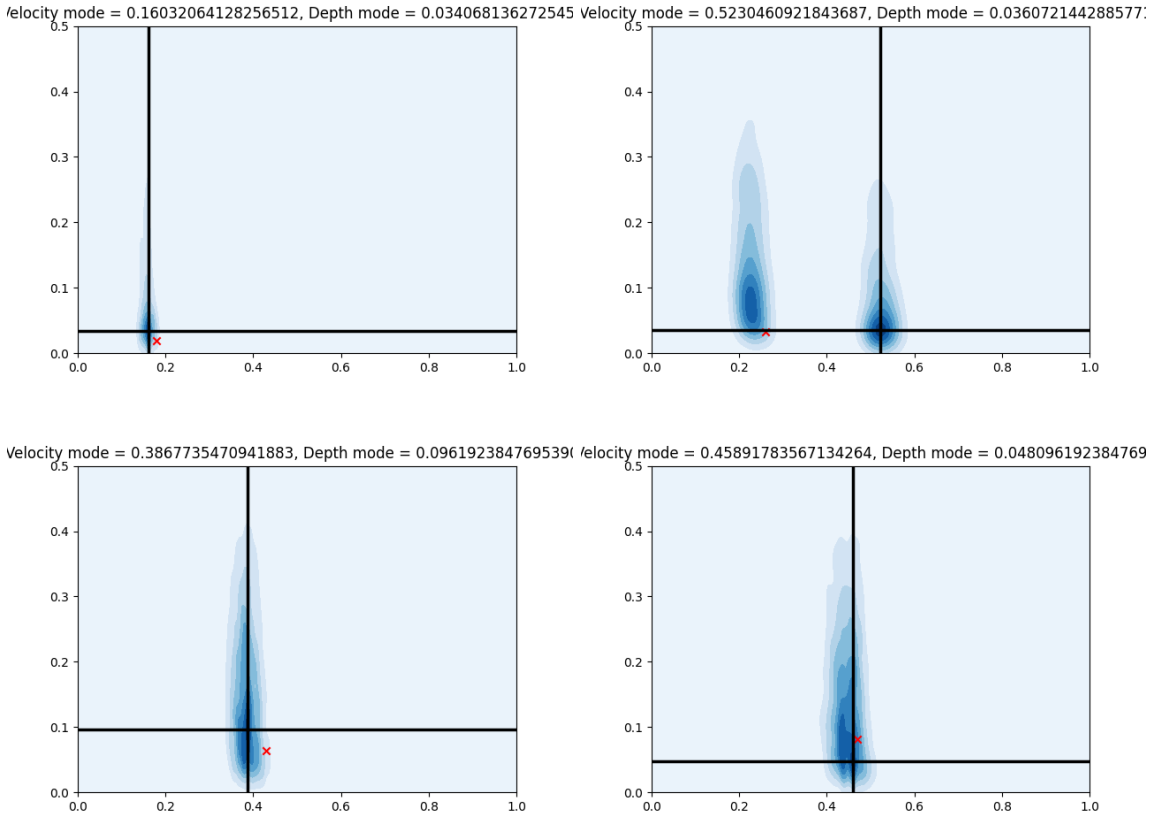

Figure 8.8: 2D densities of the recovered streamwise velocity and depth from the Adaptive Metropolis scheme, overlayed with black lines indicating the mode of the velocity (x axis) and the mode of the depth (y axis). The cross is the ground truth. For the F measurements where a) FC1 b) FC2 c) FC3 d) FC4

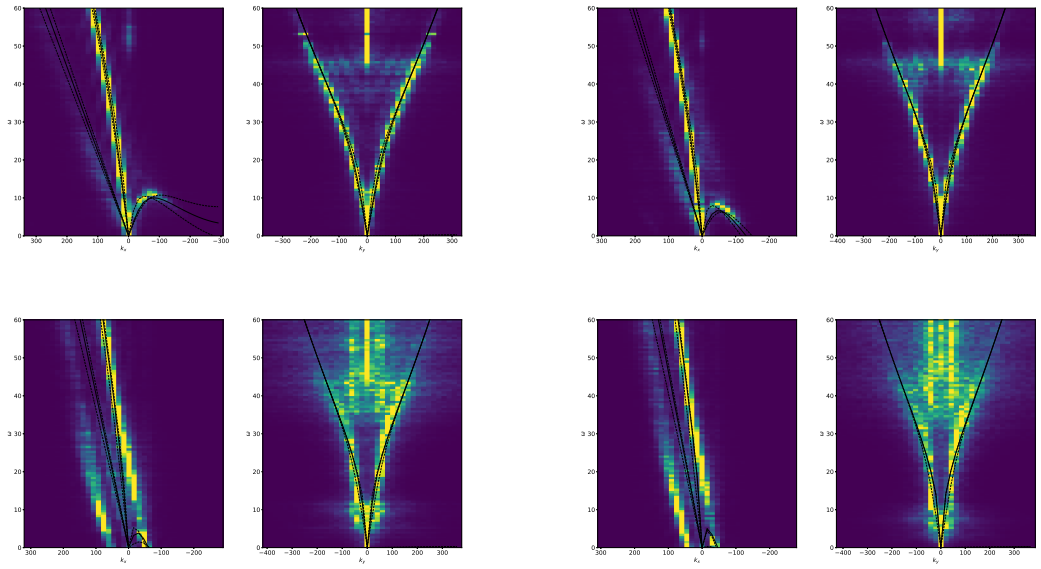

Figure 8.9: Frequency-wavenumber plot of the J series of measurements from the DIC collection scheme, with the overlaid mode prediction, as well as the prediction from the upper and lower bound of the 68 percent credible interval. For a) JFC1 b) JFC2 c) JFC3 d) JFC4

$Test$	$\tilde{U}_S$ (m/s)	D (mm)	$\tilde{U}_{S2}$ (m/s)	D_2 (mm)	$\tilde{U_{est}S}$ (m/s)	D_{est} (mm)	Err_U	Err_D	Err_{US2}	Err_{D2}
FC1	0.540	70	0.335	70	0.334	146.1	−39%	41.4%	−0.30%	−40.9%
FC2	0.539	70	0.335	70	0.310	127.1	33.6%	81.57%	−0.299%	81.57%
FC3	0.543	120	0.623	140	0.625	208.2	15.1%	73.5%	0.321%	48.7%
FC4	0.564	120	0.456	100	0.436	150.0	−22.7%	25.0%	−4.39%	50.0%
FC5	0.590	150	0.547	100	0.491	148.3	−16.78%	−1.133%	−10.23%	48.3%
FC6	0.611	160	0.571	130	0.530	586.3	13.26%	266.4%	−7.18%	351.0%
FC7	0.644	170	0.590	150	0.560	242.8	−13.0%	42.8%	−5.08%	61.87%
FC8	0.630	180	0.630	180	0.605	425.7	−3.97%	136.44%	−3.97%	136.44%
FC9	0.710	220	0.740	230	0.712	151.2	0.28%	−31.27%	−4.80%	−34.26%
FC10	0.734	220	0.721	300	0.704	209.9	−4.09%	−4.60%	−2.40%	−30.03%
FC11	0.80	260	0.844	270	0.811	422.6	1.38%	62.5%	−3.91%	56.52%
FC12	0.891	310	0.994	300	0.945	418.4	6.06%	35.0%	4.93%	39.5%
FC13	0.996	340	1.04	340	1.01	471.9	1.41%	38.8%	−2.89%	38.8%
FC14	1.07	370	1.20	410	1.21	350.0	13.1%	−5.41%	0.833%	−14.63%
FC15	1.185	420	1.49	510	1.520	501.6	28.27%	19.4%	2.01%	−1.65%
FC16	1.370	490	1.524	570	1.497	495.5	9.28%	1.12%	−1.77%	−13.1%
FC17	1.366	490	1.501	510	1.517	531.0	11.1%	8.37%	1.1%	4.12%

Table 8.2: Table representing the different experiments from the river Sheaf CCTV collection scheme. The first column represents names of the experiments. The second and third columns represents the measured streamwise velocity and depth. The fourth and fifth columns represents the recovered streamwise velocity and depth from [2]. The fifth and sixth column report the mode streamwise velocity and depth recovered from the MCMC scheme. The final four columns highlight the percentage difference from the MCMC scheme and the gauge station, and the reconstruction from [2], respectively.

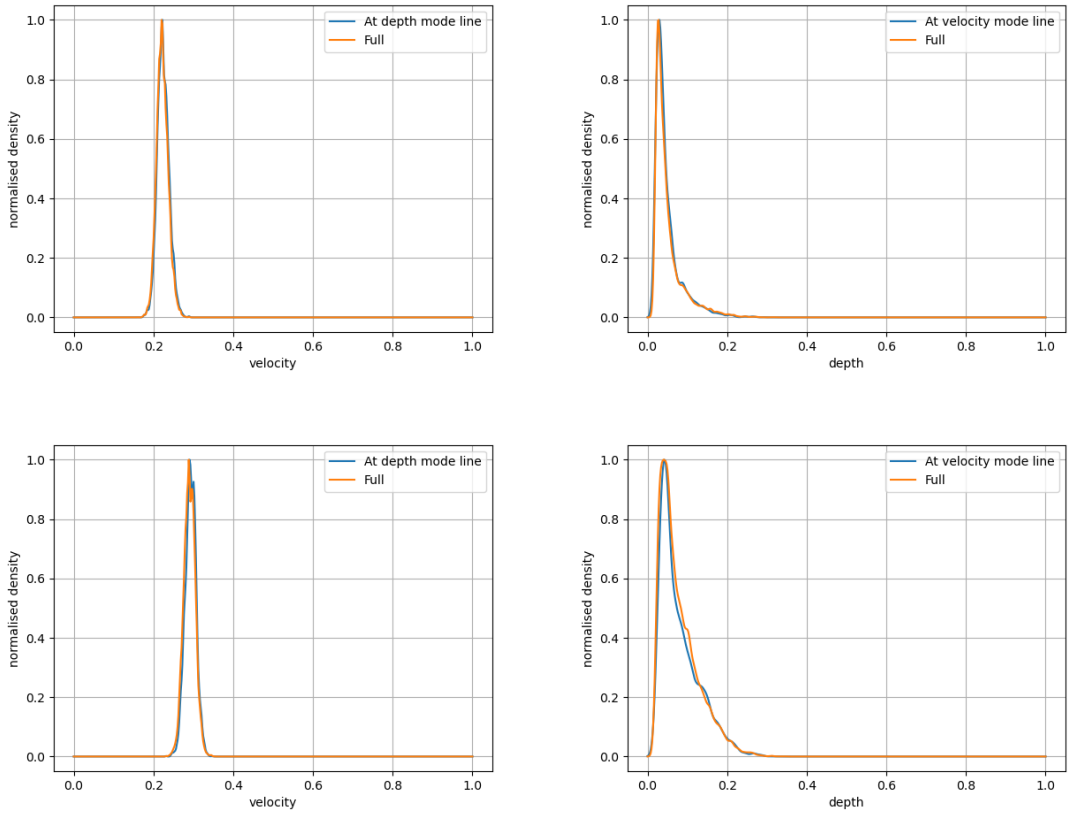

Figure 8.10: Smoothed histograms recovered from the MCMC scheme for the streamwise velocity and depth, as well as the streamwise velocity along the mode of the depth, and the depth along the mode of the streamwise velocity. For FC1B FC2B.

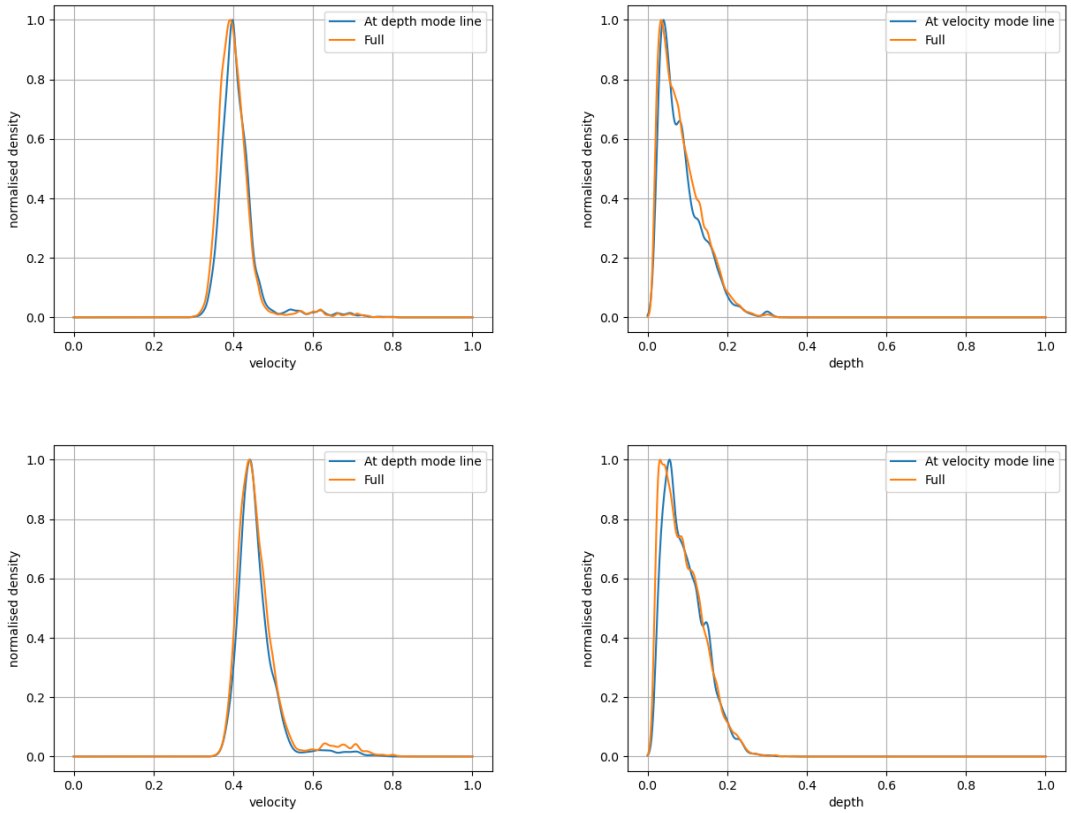

Figure 8.11: Smoothed histograms recovered from the MCMC scheme for the streamwise velocity and depth, as well as the streamwise velocity along the mode of the depth, and the depth along the mode of the streamwise velocity. For FC3B FC4B.

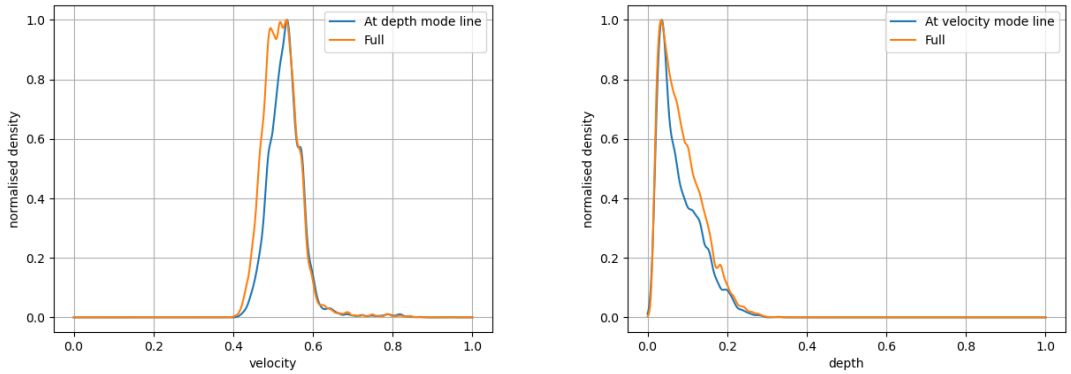

Figure 8.12: Smoothed histograms recovered from the MCMC scheme for the streamwise velocity and depth, as well as the streamwise velocity along the mode of the depth, and the depth along the mode of the streamwise velocity. For FC5B.

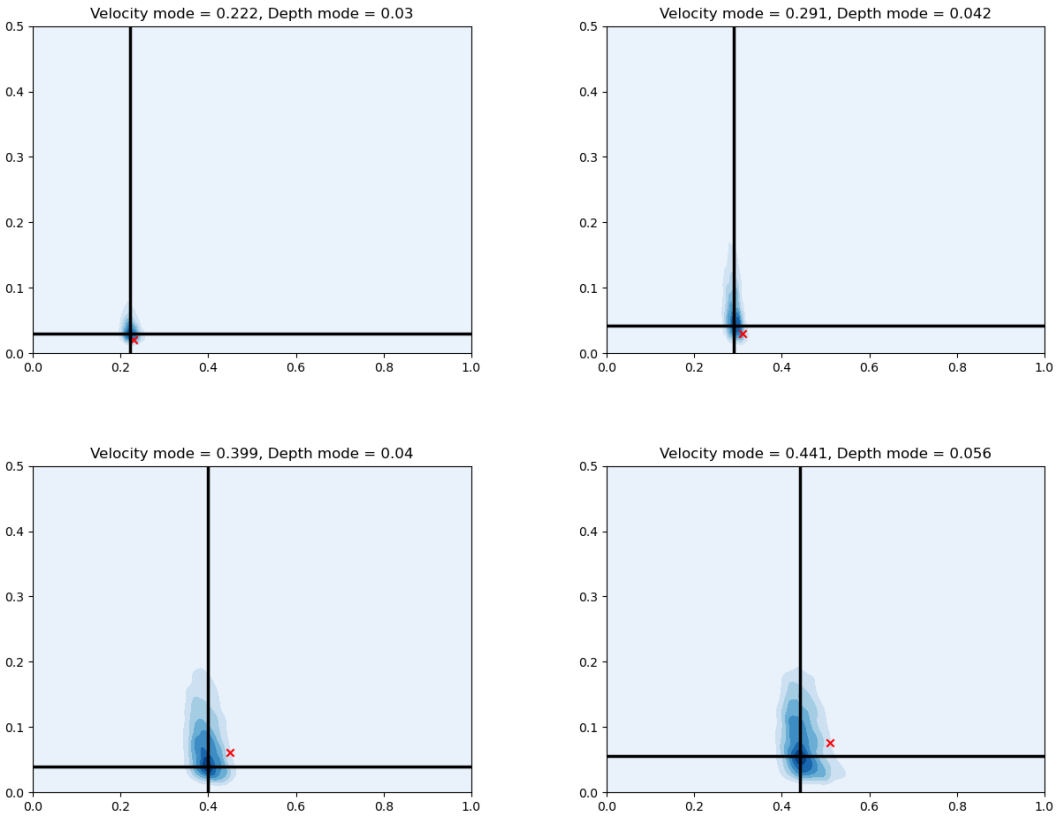

Figure 8.13: 2D densities of the recovered streamwise velocity and depth from the Adaptive Metropolis scheme, overlayed with black lines indicating the mode of the velocity (x axis) and the mode of the depth (y axis). The cross is the ground truth. For the F measurements where a) JFC1 b) JFC2 c) JFC3 d) JFC4

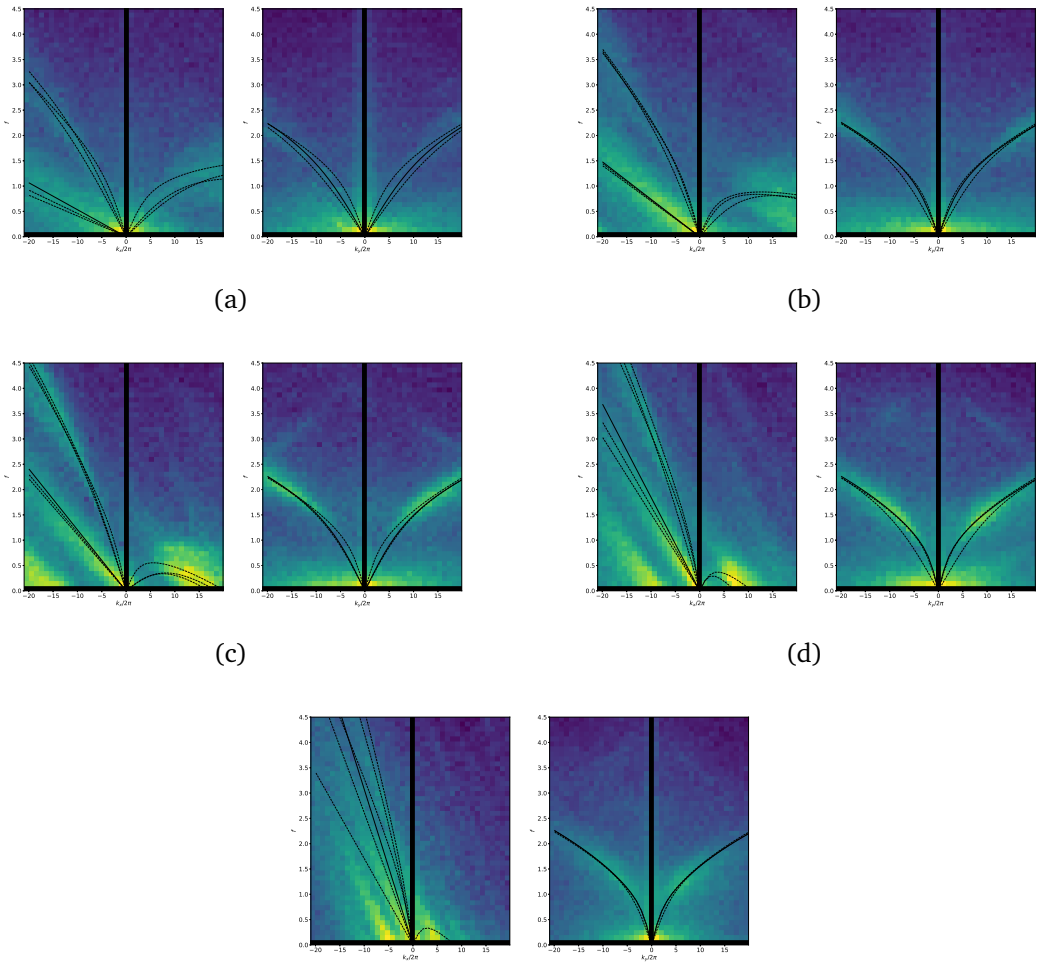

Figure 8.14: Frequency-wavenumber plot from the CCTV collection scheme, with the overlaid mode prediction, as well as the prediction from the upper and lower bound of the 68 percent credible interval. For a) FC1, b) FC5, c) FC9, FC13, and FC17)

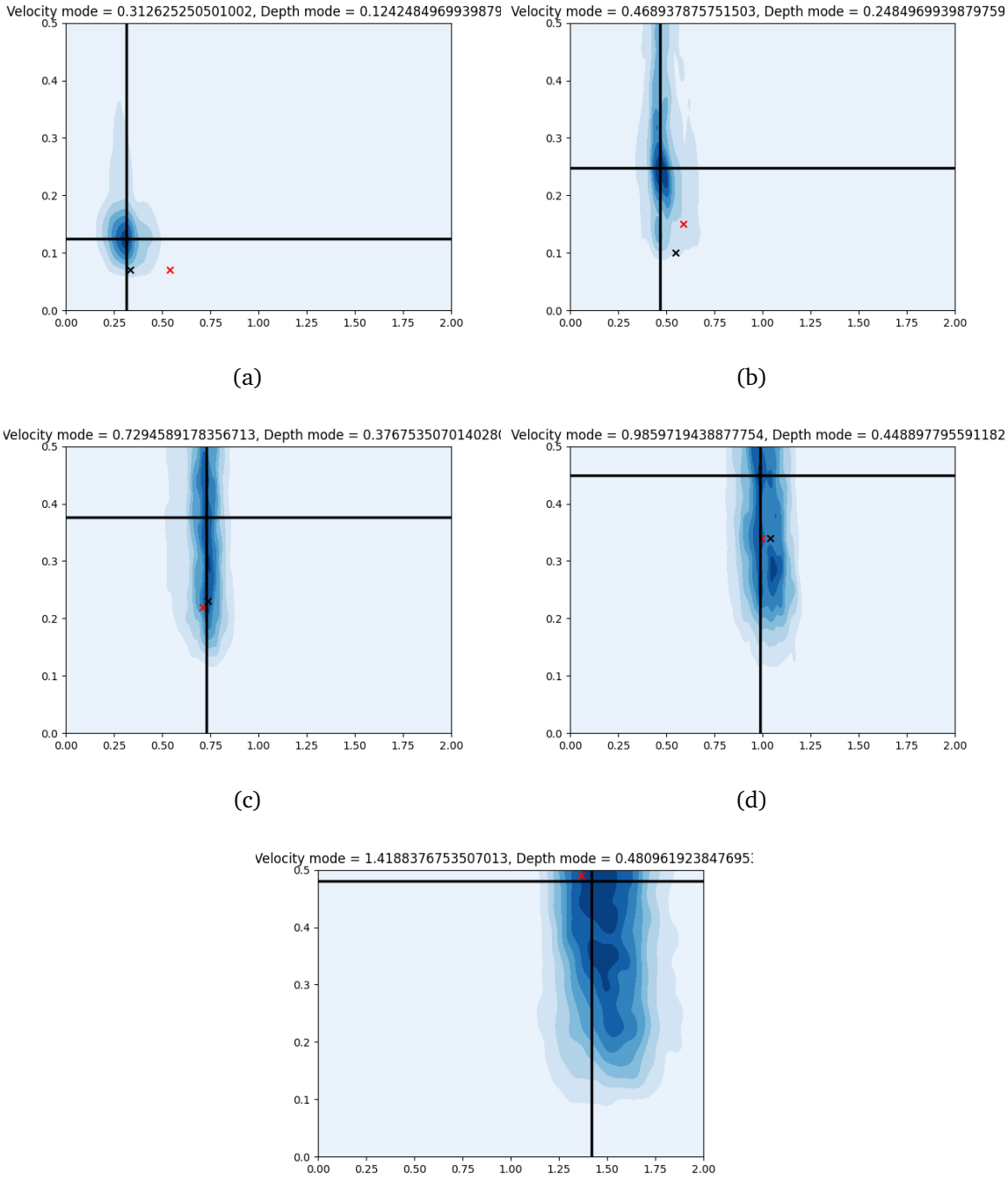

Figure 8.15: 2D densities of the recovered streamwise velocity and depth from the Adaptive Metropolis scheme, overlaid with black lines indicating the mode of the velocity (x axis) and the mode of the depth (y axis). The red cross is the ground truth, the black cross is the prediction from Dolcetti *et al* for a) FC1, b) FC5, c) FC9, d) FC13 and e) FC17

Chapter 9

Conclusions

The main aim of this work was to investigate and build a platform for the application of deterministic and stochastic data-driven / machine learning based approaches for rough surface reconstruction with the aim of inferring characteristics of the dynamic free-surface produced from shallow turbulent flows. The objectives identified as way-points to reaching this goal were introduced in chapter 1, the extent to which they have been achieved is discussed below.

9.1 Research Objectives

- To investigate the validity of data-driven machine learning based approaches for the inverse problem of acoustic scattering from a rough surface, and compare against more standard approaches.

Chapters 4, 5, and 6 answer this objective. In Chapter 4, a random forest based procedure was used to further develop and improve the inversion with comparison to the Short Array method [74]. The random forest was trained on different synthetic realisations of the scattered field from a harmonic surface. The model was trained with varying levels of noise introduced to the data, and was tested and evaluated on different synthetic data with varying noise, and experimental data from laboratory measurements. An extensive comparison between the short array method and the random forest was done by investigating the recovery as the amplitude increases. Investigating Figure 4.9 when the amplitude normalised by the acoustic wavelength is small, the Short Array method and the random forests are comparable. As the amplitude increases, the performance of the Short Array method decays rapidly, whereas the random forest does not have this issue.

Chapter 5 extended this approach to find a more holistic prediction based on the nature of the broadband source. Training a model on synthetic data at every frequency in the broadband signal, a prediction histogram can be produced to form an overall prediction. It is found that over more frequencies, especially when the error from the experiment to the Kirchhoff approximation is larger k-nearest neighbors yields a tight histogram over the frequency-range, at the correct value allowing for confidence in the overall prediction. This removes some of the inherent ambiguity that occurs when using machine learning on truly unseen data.

A clear issue with this approach is the need for the creation of data at every frequency, this becomes computationally more expensive and leads to intractably large data sets as the dimension of the surface increases. Therefore, an iterative scheme was investigated.

Chapter 6 pursued this iterative approach while maintaining the Bayesian perspective with the Adaptive Metropolis scheme. This scheme resulted in the the most informative representation. This not only gave a measure of prediction for three-parameters and forty-parameters, the resulting parameter estimation was a posterior distribution allowing for substantial spatial analysis. This was shown to a great effect when considering the forty-parameter surface, as the region of high insonification (where the prediction was accurate), had a much narrower credible region than the region outside. This meant that it was easy to trust the model spatially. Other models investigated in this thesis would have just returned the surface as a prediction with no information about spatial uncertainty. In general, this objective has been achieved.

- Provide a measure of uncertainty in the reconstruction, allowing for reasonable interpretation for when the model is accurate or not.

Chapters 5, 6, and 8 attempt to answer this objective. Chapter 5 answers this by training on each frequency, where a histogram of predictions can be made. Chapter 6 used the Adaptive Metropolis scheme for the reconstruction of the same surface that was highlighted in Chapter 4, as well as a surface much higher in complexity. Because of the iterative nature of this scheme, no training needs to be made. A clear advantage of this is that the required amount of data to be generated can be less. The downside to this is that for each test, the trace has to be produced, and therefore the runtime at testing is much higher than the approaches shown in Chapter 4 and 5.

The mean prediction of the surface introduced in chapter 4 with the Adaptive Metropolis approach used in chapter 7, was comparable to the random forest prediction, while able to contain the level of spatial uncertainty in the prediction. This yields information regarding the physical setup of the problem. Further away from the region of high insonification the uncertainty is higher, which makes sense as it has a less significant impact on the scattered field. This is extended for the more complicated surface.

- To extend this inversion methodology to reconstruction of a dynamic rough surface, i.e. the free-surface of rivers.

Chapter 7, and 8 tackle this objective. These Chapters were concerned with extracting and analysing the frequency-wavenumber spectrum of Digital Image Correlation (DIC) data in a flume. The DIC method yields elevation, but suffers from holes in the data. Fortunately, these holes propagate with respect to the underlying flow structures, so the frequency-wavenumber based analysis works well. It can be seen that there is good agreement with the theoretical dispersion relations, as well as low noise in the data.

Combining the DIC data with CCTV footage of the River Sheaf, the Adaptive Metropolis scheme was fitted in order to get a posterior distribution for the streamwise and lateral velocity, as well as the depth. The streamwise velocity is well recovered in the DIC scheme. The width of the posterior distribution of velocity estimation is small, indicating confidence in predicted value. As the flow velocities increase, the distribution shifts to the right slightly meaning there is a slight bias in predicting higher velocity. The recovery of the depth suffers throughout. As the CCTV footage is analysed the results in the velocity are consistent with the predictions from the optimizer based approach presented in [2], at worse 10% off from the results here. The results for the method presented in this work, as well as the method presented in [2] deviate sometimes from the wave station's results. Again, throughout the CCTV recovery, the depth was not recovered consistently. The results in this work are a further improvement to the results in [2], for the velocity reconstruction. This is because a posterior distribution of the velocity field is found. This means that the field can be analysed to be able to check for validity in the results. For example, bimodality was found in some of the slow conditions. This is due to the jumping of the advection dispersion line to the gravity capillary, an optimizer using the same model function could have selected the wrong one of these peaks, but as the separation is large, it only requires slight user input to find the

correct peak. The distribution of the peak is in some way measuring the spread of signal in the frequency wavenumber plots. Some of this is due to signal noise, and some of this is due to the simple fact that the flow is not uniform everywhere in space and time. Deviating from the average nature of the frequency-wavenumber spectrum is a clear improvement, and should be studied further.

- Validate against experimental data.

Every main result in Chapters 4, 5, 6, 7, 8 has been based on experimental validation. Although the underlying methods are based on a simulation (for acoustics this was the scattering method of the Kirchhoff Approximation, for the videos this was creating a theoretical frequency-wavenumber plot from synthesising theoretical dispersion curves into an image), the conclusions were formed from the application of the simulation to real-world experiments. In Chapter 4 and 5, a harmonic surface was formed and tested experimentally. In Chapter 6, two surfaces of varying complexity were formed and tested experimentally. In Chapter 7, the model of the dispersion curves was checked against the frequency-wavenumber plots and in Chapter 8, the experiments from Chapter 7 and a data collection scheme in River Sheaf were used to make conclusions on the frequency-wavenumber inversion.

9.2 Future Work

There are many branching areas of research that were made apparent during the course of analysis for this thesis. A brief summary of some of these ideas is presented here. Some have been developed more than others, but all require more work to be considered complete research sections.

9.2.1 Acoustic Doppler

As the surface moves at a given $t \in [0, T]$, the Kirchhoff approximation is used to calculate the given acoustic field via a frozen-surface [221] approach. Following this, the Doppler spectra can be calculated [124]

$$S(\omega) = \frac{1}{T} \left| \int_0^T \psi_s(\mathbf{R}, t) \mathrm{e}^{\mathrm{i}(\omega+\omega_a)t} dt \right|^2 \tag{9.1}$$

Where ω represents the Doppler shift from the acoustic carrier frequency ω_a. The acoustic carrier is introduced as an established 'trick' to reduce the required

sampling rate: whereas usually the sampling rate is determined by Nyquist's formula where the sampling rate must be twice the frequency of interest, the carrier frequency can be removed such that it is the difference between the frequency of interest and the carrier frequency which determines the sampling frequency. The discrete Fourier transform was used to convert discrete measurements from the rough surface realisations into discrete frequency bins.

The frozen-surface based approach forms a powerful combination with the Kirchhoff approximation approach presented as a main method throughout the thesis. This means that (especially with the removal of the carrier frequency, i.e. passband down to baseband) the Doppler spectra can be found very quickly. Figure 9.1 presents an example Doppler spectrum.

The spread and the amplitude of these Doppler spectra contains information on not only the velocity of the flow, but also the depth and the surface slope. The initial investigation was presented at the Surface Velocimetry Workshop in 2022.

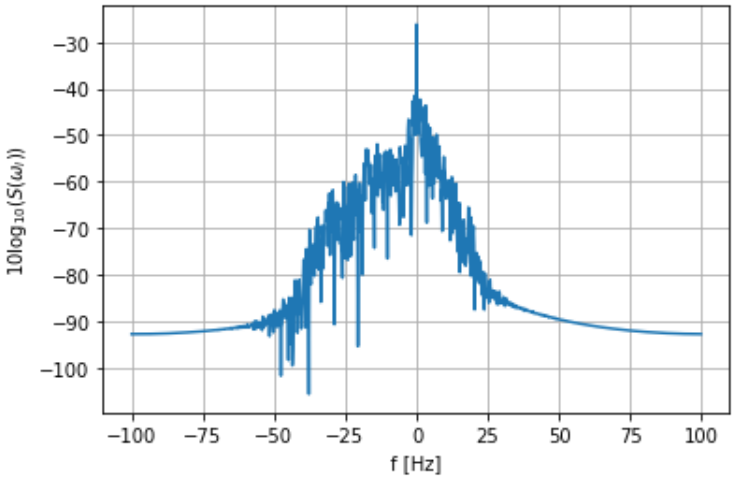

Figure 9.1: Spread of Doppler from a single receiver, obtained from the scattered field with the Kirchhoff Approximation against a randomly rough moving surface.

This could be thought of a forward-scattered based approach to a "radar gun" that has had some success in the monitoring of rivers, as long as incidence angle is taken into account [222]. Further citations on handheld radar guns can be found in [223] [224] [225] [226]. These papers are concerned with estimating the velocity, and not necessarily approximating the depth from the spectrum.

Simulations were created at various frequencies, for a single receiver forward-scattered acoustic pressure from a directed source. The resultant Doppler spectrum was then run through a Random Forest in order to estimate the discharge, depth,

and velocity. It could be seen that at higher frequencies, on the order of 40kHz, there is sensitivity to the depth, as well as sensitivity to the velocity. Figures 9.2, 9.3, 9.4, show initial results from this. Lower than this, at approximately 18kHz, there was only sensitivity to the velocity. This strikes as an interesting avenue to pursue, unfortunately it could not be continued as part of this thesis due to a lack of experimental data.

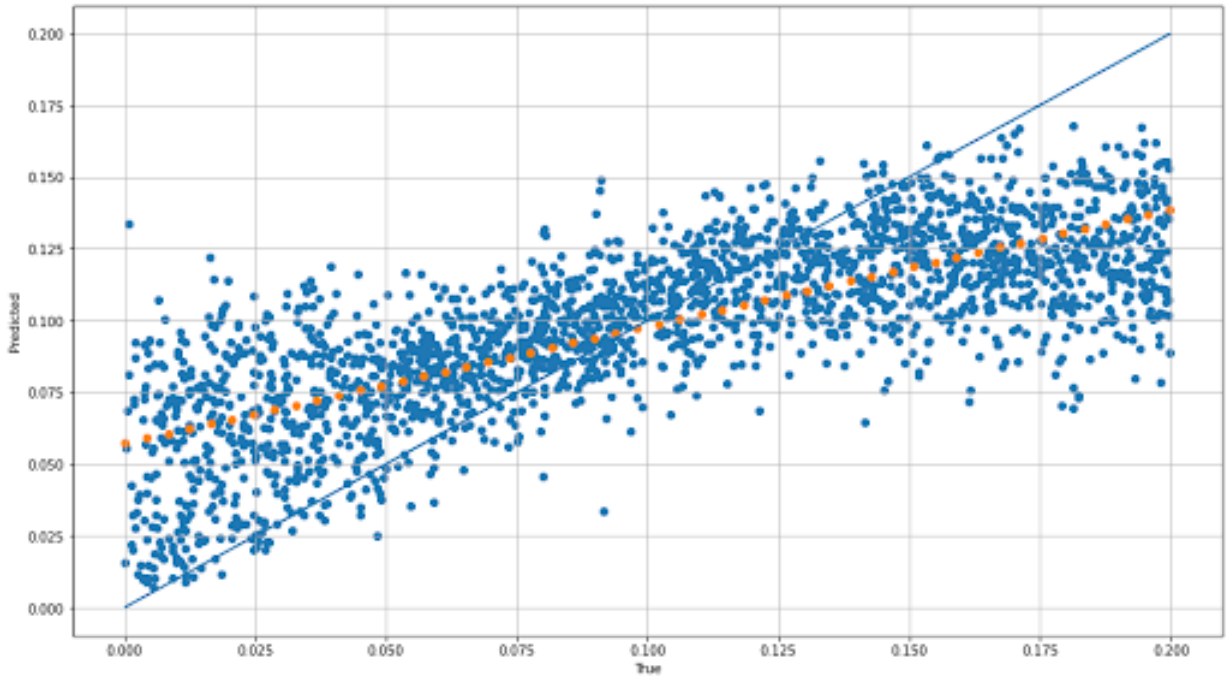

Figure 9.2: Scatter plot showing predictions against true rough surface amplitude from simulated data, 43kHz. The blue line represents perfect predictions against the true values. The orange dotted line represents the line of best fit through the predictions. The label in the horizontal axis is True, and the vertical axis is Predicted.

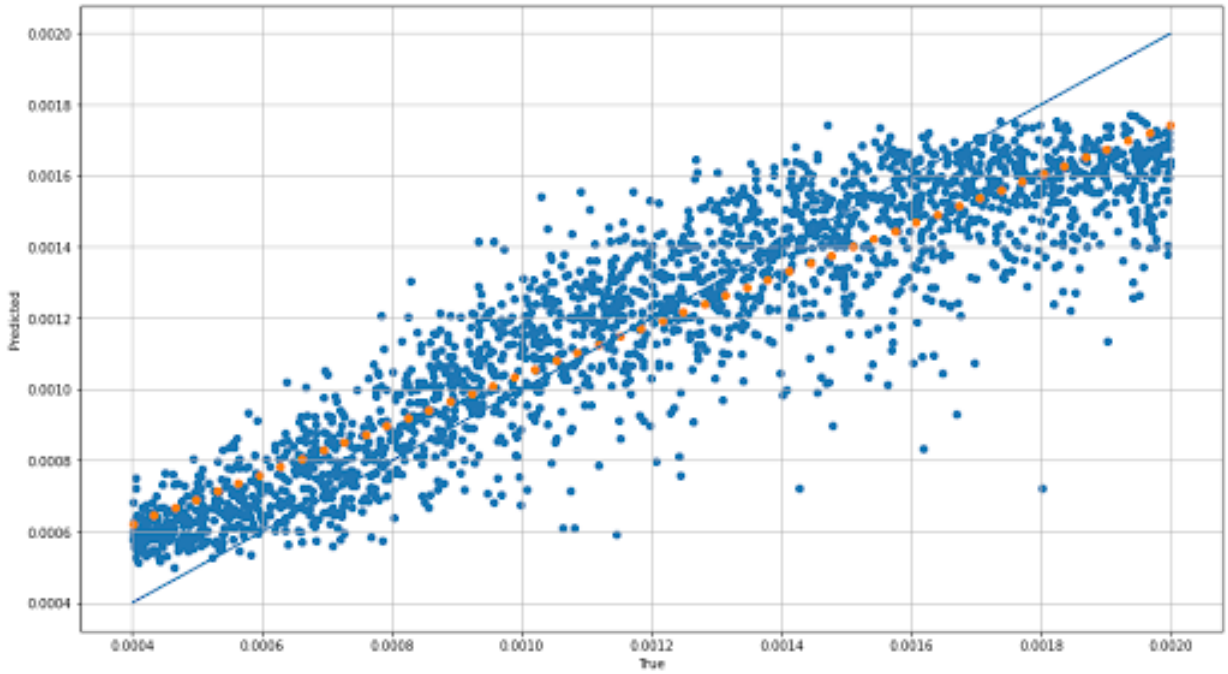

Figure 9.3: Scatter plot showing predictions against true rough surface depth from simulated data, 43kHz. The blue line represents perfect predictions against the true values. The orange dotted line represents the line of best fit through the predictions. The label in the horizontal axis is True, and the vertical axis is Predicted.

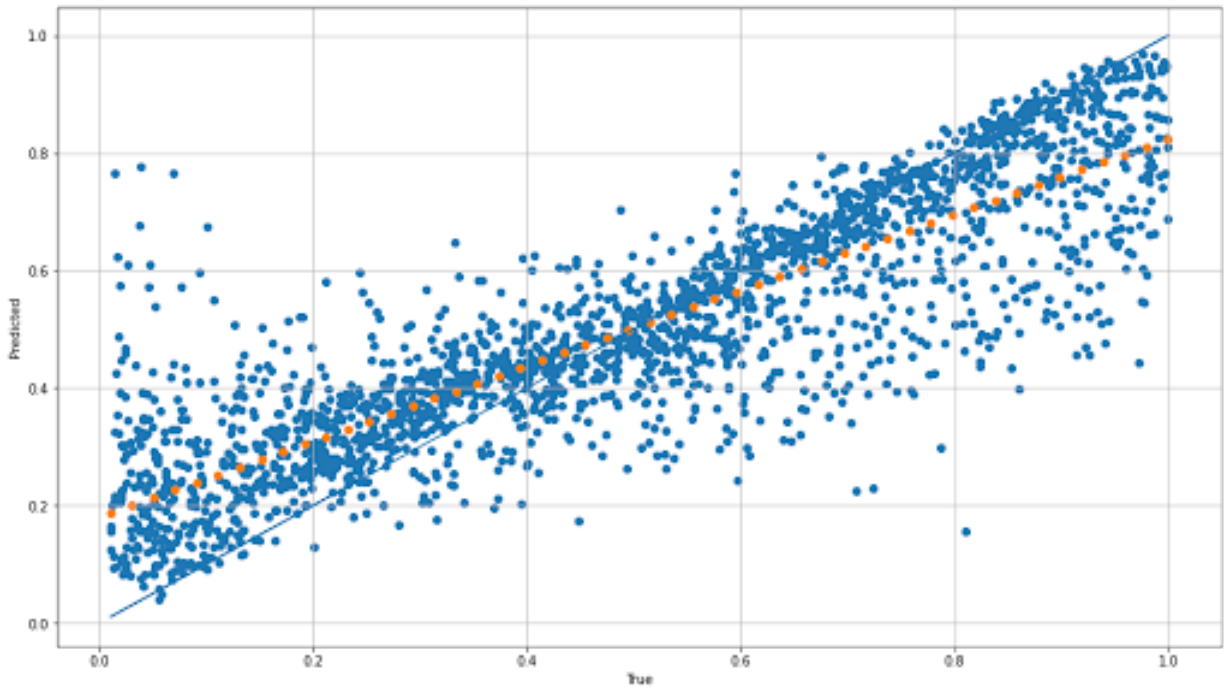

Figure 9.4: Scatter plot showing predictions against true rough surface velocity from simulated data, 43kHz. The blue line represents perfect predictions against the true values. The orange dotted line represents the line of best fit through the predictions. The label in the horizontal axis is True, and the vertical axis is Predicted.

9.2.2 Acoustic frequency-wavenumber spectrum inversion

A further extension to the Doppler approach is to create an array of receivers. For example, a 2D plane of receivers, or various shapes that form a discretised surface. All of these time series, for each receiver, can then be used to form an acoustic frequency-wavenumber spectrum. This can then be analysed in a similar way to the frequency-wavenumber plots generated from CCTV data in chapter 8. Because most of the information, particularly the depth value in the dispersion curves, are in the lower values of acoustic wavenumber and frequency, a camera that drives a high resolution isn't too important. Once this is created, then the inversion methods presented in Chapter 8 could be applied to get posterior distributions of the parameters. Time constraints and the lack of experimental data were two of the main reasons the author did not pursue this endeavour.

9.2.3 Further improvements to the MCMC scheme of videos of the water surface

The method provided in Chapter 8 gives some information on the posterior streamwise/lateral velocity and depth. The largest issue is that although the signal is well represented by the credible region and the streamwise velocity is recovered well, the depth is inconsistent, performing okay in laboratory DIC measurements, but giving poor results in the depth reconstruction when going to the field with the CCTV measurements in river Sheaf. This is due to the noise in the data, the rotation of the frequency-wavenumber representation of the dispersion curves. So, when comparing the theoretical dispersion curve image against the real data in the likelihood function, the depth is not as sensitive. The depth itself is also much less sensitive than the velocity. It is believed that a change in the model used for the likelihood function could yield a significant improvement in the depth predictions. For example, the energy in certain regions could be integrated, which would give a more holistic metric for the image. Further to this, the spatial relationship can be exploited through the use of a Convolutional Neural Network (CNN) while abandoning the stochastic approach.

The posterior of the velocity is much more accurate than that for depth, but still has room for improvement. In the best, noise-free case the posterior distribution of the velocity maps exactly to the spread of velocities present in the image, allowing for a mapping of more than just the average behaviour. This is a large step on from the Fourier analysis. However, if the image is dominated by noise everywhere, then

this does not apply. Investigating the histogram of the posterior velocities for two flow conditions given in chapter 6, FC3A and FC5A presented in Figures 9.5 and 9.6 the mean values of the velocity can be used in the prediction. This can be used to produce Figures 9.7 and 9.9 respectively. Assuming that the observed structure in the frequency-wavenumber plots is the presence of different surface velocities in the image as well as image noise, an assumption can be made that the full-width half-maximum of the resulting posterior distribution of velocity is dominated by signal, not image noise. Therefore, this region can be discretised, and Equation (3.116) can be used to create a random surface such that each discretised component can then be summed up. This results in the aggregate frequency-wavenumber plots shown in Figures 9.8, and 9.10. It can be seen visually that outside a larger blur at zero frequency, the spread of the blurred result roughly follow the results seen in Figures 7.8 7.10. This shows that empirically, there is some information regarding the spread of the data in relation to the spread of velocities. This intuitively makes sense. In a river, the velocity isn't constant in space and in time. Doing a frequency-wavenumber based approach with an optimiser results that only the mean can be found, this method with MCMC yields the mean and a distribution. The reason why this needs some more work in future is because of the slight bias to the right of the histograms. This isn't entirely expected and could be due to the choice of likelihood function. So this approach would benefit from being investigated further.

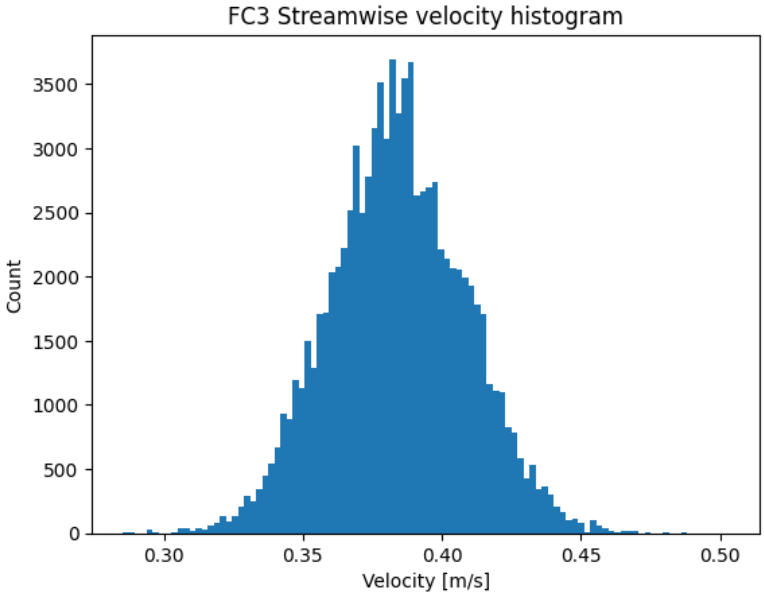

Figure 9.5: Posterior distribution of the velocity from the flow condition FC3A, given in chapter 6.

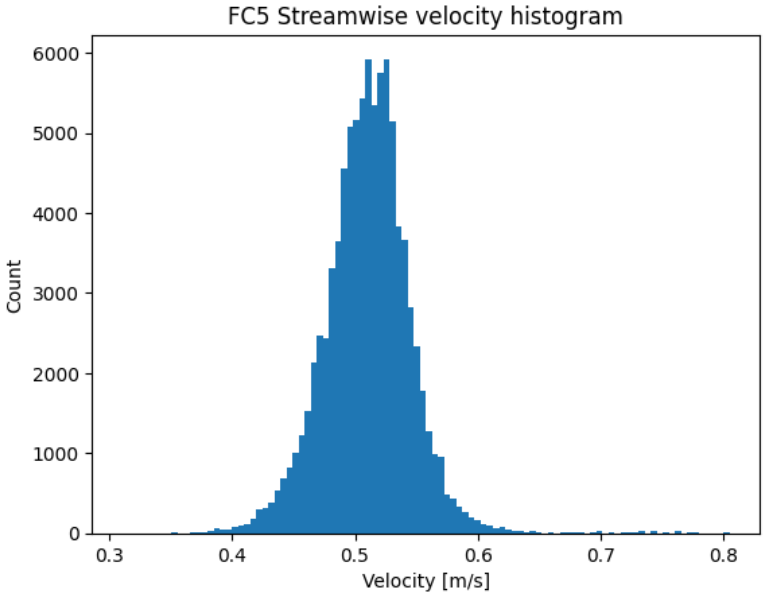

Figure 9.6: Posterior distribution of the velocity from the flow condition FC35, given in chapter 6.

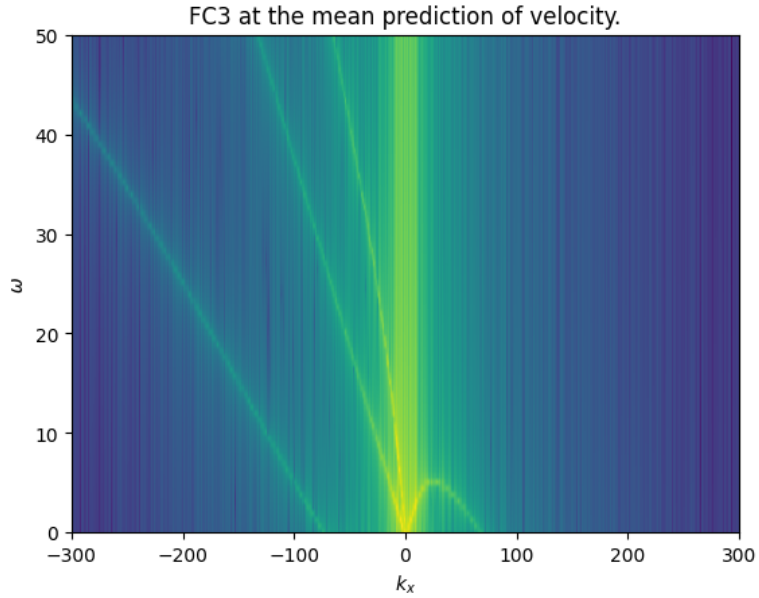

Figure 9.7: Frequency-wavenumber spectra produced from a synthetic random surface that adhered to the mean surface velocity from FC3A.

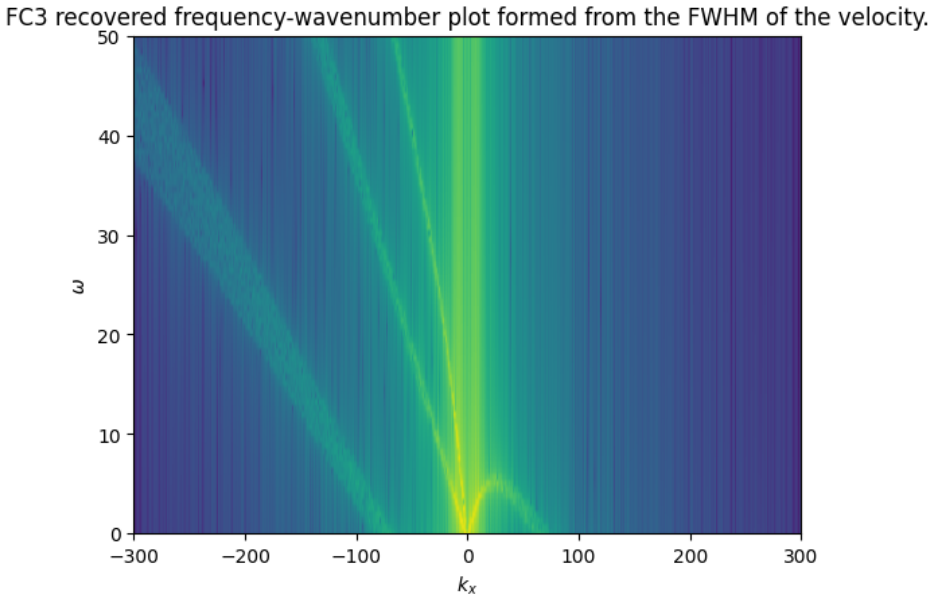

Figure 9.8: Frequency-wavenumber spectra produced from a summation of synthetic random surfaces that adhered to the full width half maximum of the velocity distribution, from FC3A.

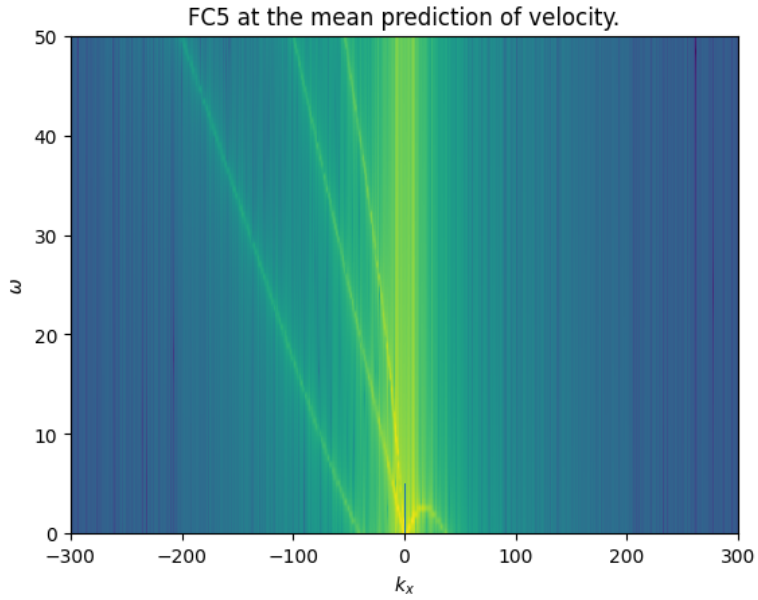

Figure 9.9: Frequency-wavenumber spectra produced from a synthetic random surface that adhered to the mean surface velocity from FC5A.

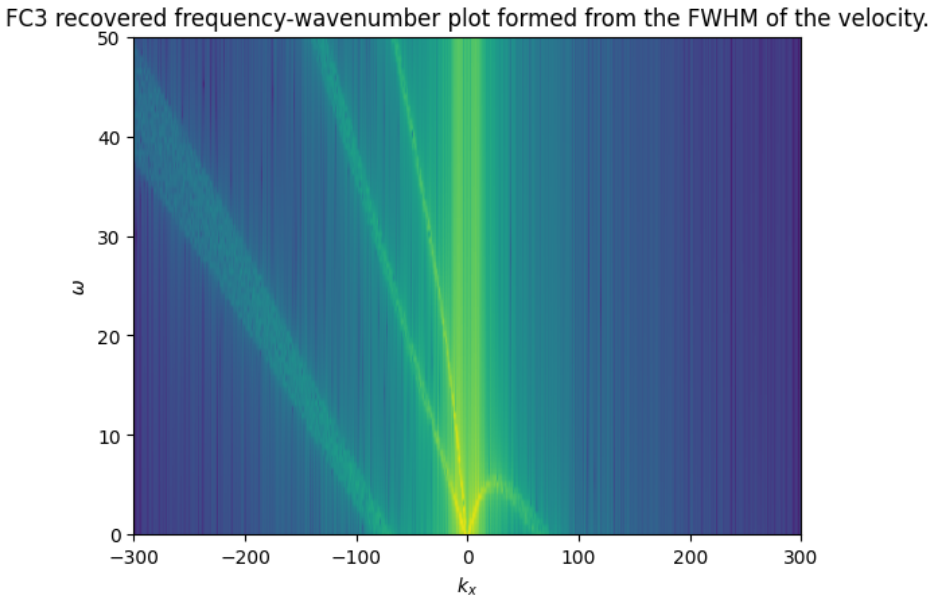

Figure 9.10: Frequency-wavenumber spectra produced from a summation of synthetic random surfaces that adhered to the full width half maximum of the velocity distribution, from FC5A.

9.2.4 MCMC for static surface reconstruction with varying wavelength

An assumption was made in the surface reconstruction in Chapter 6 that the surface wavelengths can be fixed. This is a reasonable assumption due to the choice of taking a sine series decomposition. Making this choice for a given length of surface yields the wavelengths directly. However, it is important to analyse what happens if the wavelengths were allowed to vary. This constitutes future work, but initial analysis is presented here.

Firstly, a randomised rough surface was created with wavelengths the same as in Chapter 6, but amplitudes and phase randomised. Once this was done, the Kirchhoff Approximation was used to simulate acoustic data and noise was added to corrupt the data. The random surface is given in Figure 9.11. Two MCMC instances were run at different frequencies, 19000Hz and 25000Hz. Having a look at how the credible interval changes in Figures 9.12 and 9.13 as opposed to 6.7 it first must be noted that the credible intervals in Figures 9.12 and 9.13 are 95% as opposed to 68%, meaning that there should be an overall widening as the number of standard deviations shown is larger. There is also a distinct change of behaviour in the credible interval. For the varying wavelength, there is a much sharper distinction

between the region that contributes the most energy to a set of receivers to that which contributes least, causing a large blob of grey to appear in the images. Errors around the true surface with the mean of the parameters against the mean of the surfaces were presented in Figures 9.14 and 9.15 and exhibit the same behaviour observed in Figure 6.8 where there is a small region where the errors are good, and this relates to the same region of high ensonification. Zoomed in plots of this region with the true surface, and the predicted mean surfaces, are presented in Figures 9.16 and 9.17. The largest amplitude component in the surface is recovered well, as well as the region before it. In the region after this, the surface and the prediction decay, presumably because that area has a much lesser contribution to the overall field seen by the receivers.

There is more that can be analysed with this approach. One of the more interesting would be to look into how the spread of the credible interval can be used to find optimal probing locations for receivers.

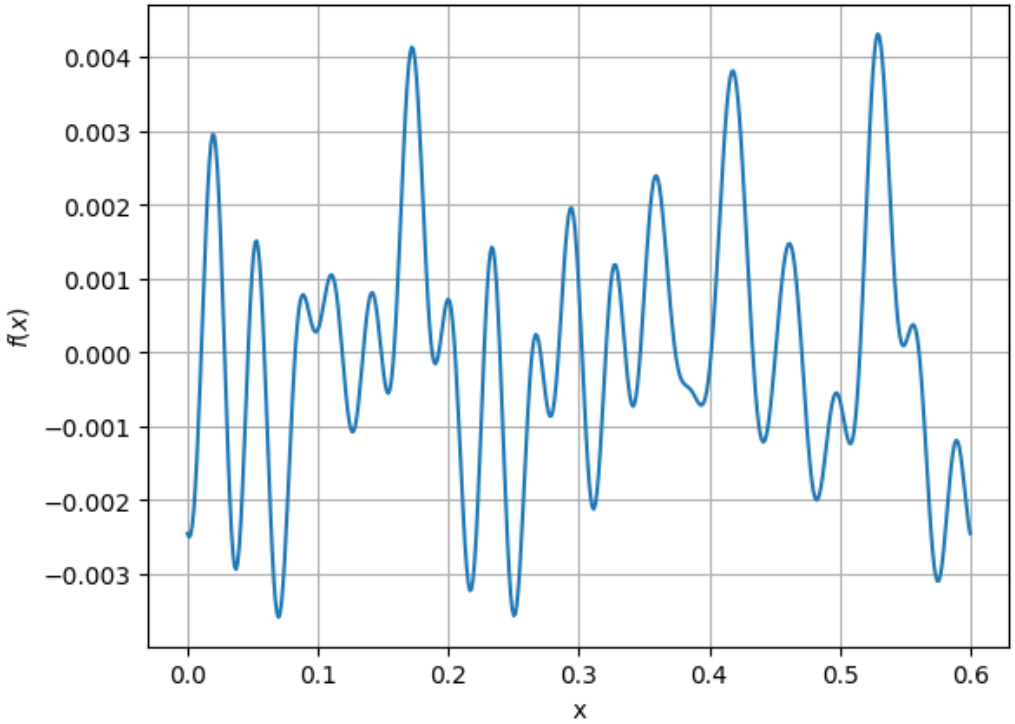

Figure 9.11: Randomised rough surface used in the analysis.

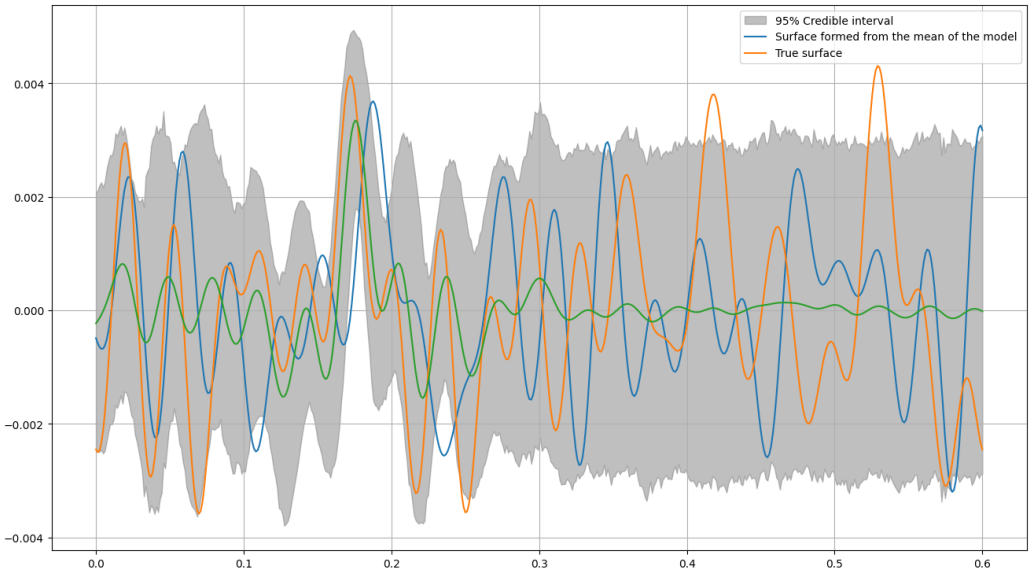

Figure 9.12: 95% credible interval formed from the MCMC algorithm recovering the amplitude, wavelengths, and phases from a random rough surface. 19kHz source excitation.

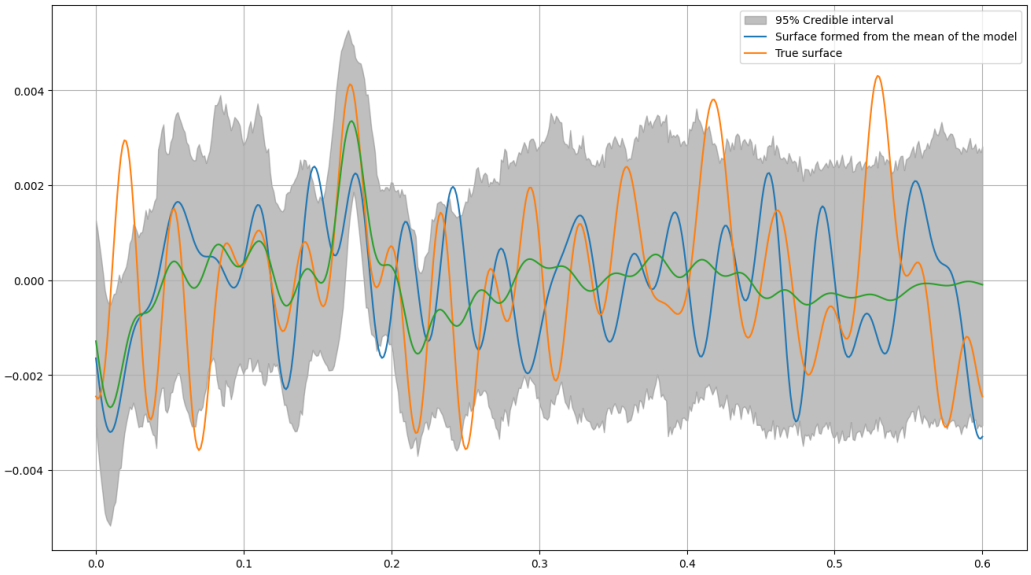

Figure 9.13: 95% credible interval formed from the MCMC algorithm recovering the amplitude, wavelengths, and phases from a random rough surface. 25kHz source excitation.

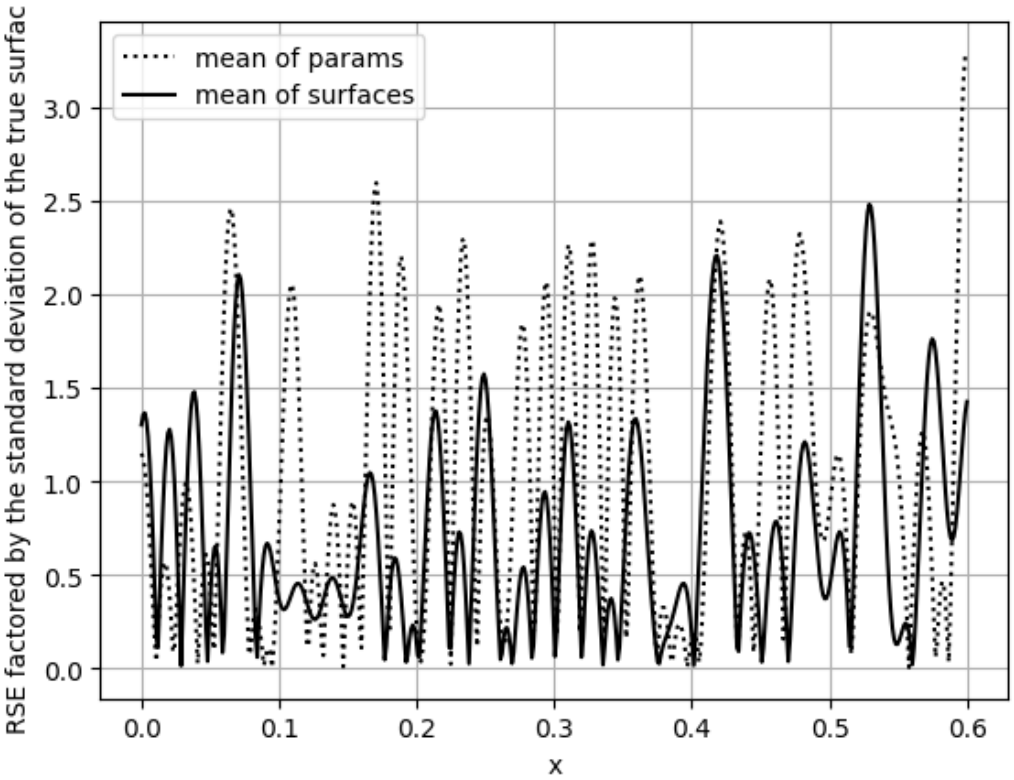

Figure 9.14: Errors of the mean value of the surfaces and the mean value of the parameters against the true surface, recovered from an MCMC algorithm applied to recovering the amplitudes, wavelengths, and phases. 19kHz source excitation.

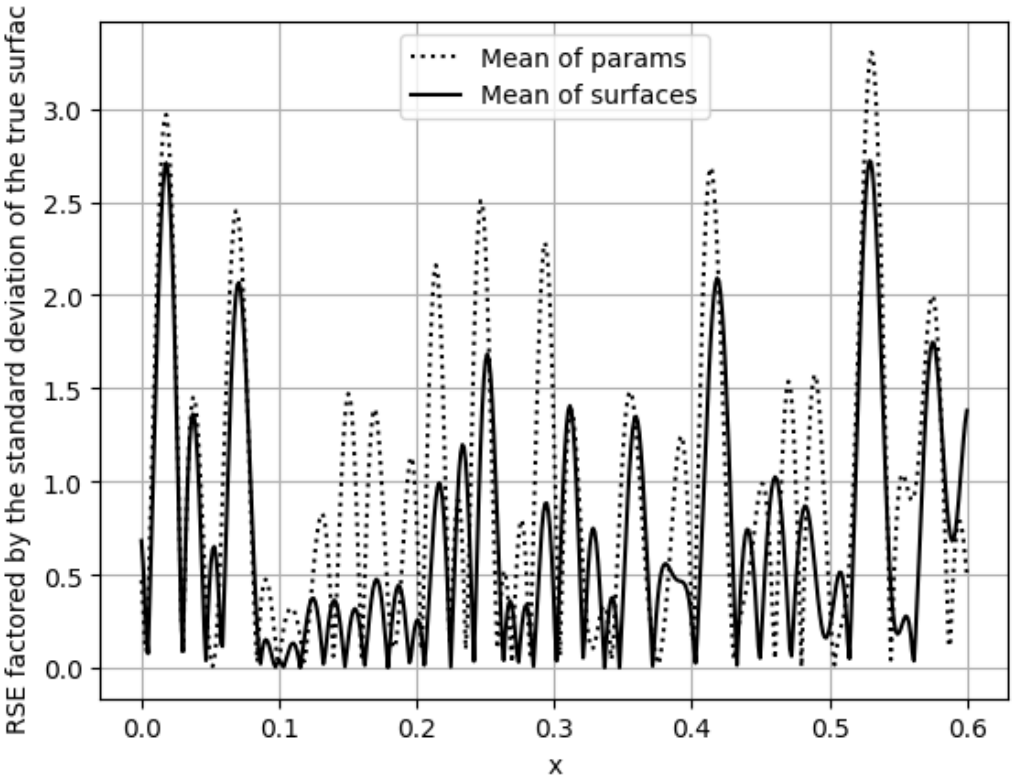

Figure 9.15: Errors of the mean value of the surfaces and the mean value of the parameters against the true surface, recovered from an MCMC algorithm applied to recovering the amplitudes, wavelengths, and phases. 25kHz source excitation.

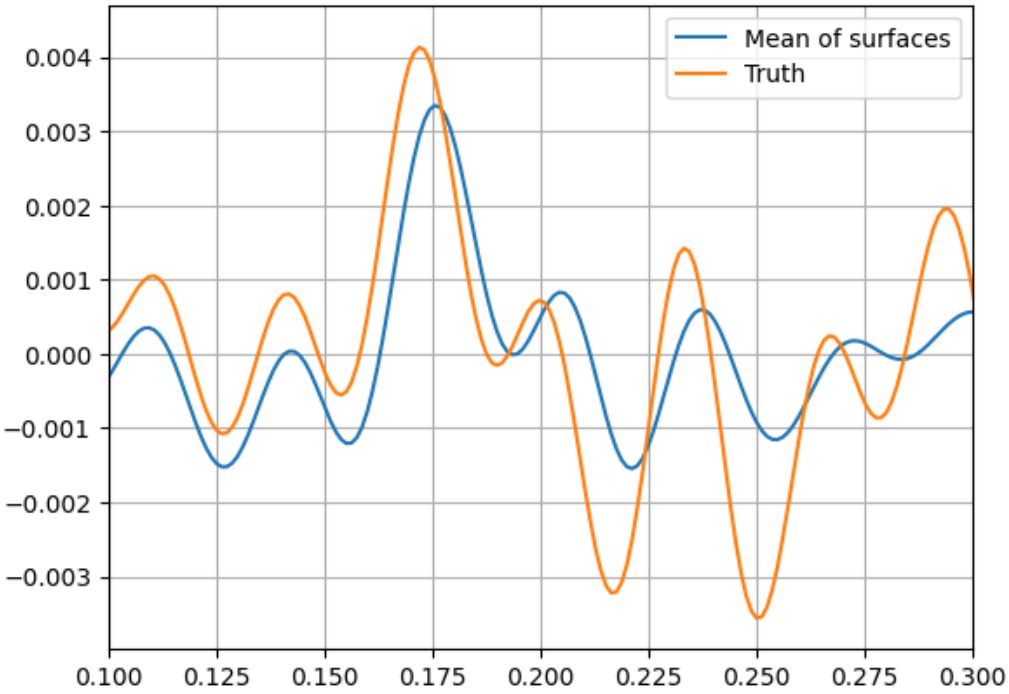

Figure 9.16: Mean value of the surfaces recovered from an MCMC algorithm applied to recovering the amplitudes, wavelengths, and phases. 19kHz source excitation, zoomed in to the region of high insonification.

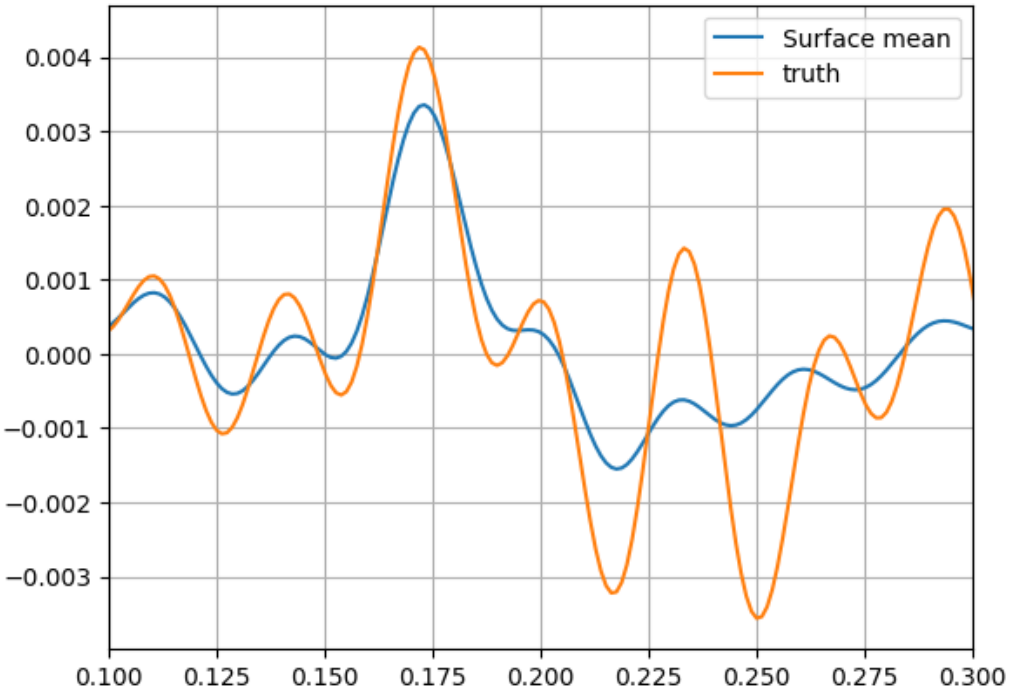

Figure 9.17: Mean value of the surfaces recovered from an MCMC algorithm applied to recovering the amplitudes, wavelengths, and phases. 25kHz source excitation, zoomed in to the region of high insonification.

9.2.5 Bringing back phase information into the reconstruction

Throughout this work, the author considered phaseless information. That is, looking at the absolute value of the pressure only. This was useful as phaseless recovery is used less in literature, and is useful in the real world, where amplitude calibrations are much easier to implement than a full calibration. However, extending the approaches used in this work to include phase information would be an obvious next step for the future.

9.2.6 Concluding Remarks

The work contained in this thesis was concerned with the application of novel non-intrusive methods in order to obtain information from a surface of interest. These surfaces were created as approximations of surface waves that would typically be seen in the context of shallow river flow. It was seen in the static surface case that a parameterisation of the surface could be recovered, as well as spatial uncertainty.

This is a useful in itself, however it would be more broadly applicable if it could be extended to recovering the parameters of dynamic surfaces, such as the free surface of rivers. Unfortunately this could not be investigated thoroughly due to a lack of experimental data - instead proof of concept work was conducted using models. In the case of dynamic surfaces the Doppler effect spreads the information over many frequencies, and simulated data was created to train models as shown in Chapter 9.2.1. It is posed in this section that a model can be trained to extract the overall root-mean-square amplitude, the surface velocity and the depth of the synthetically created dynamic surfaces. This is all the information one could need (aside from the velocity index constant) to obtain an estimate for the discharge and, as such, could be used in river monitoring.

Working with videos collected by CCTV cameras over real rivers was powerful. Because the intensity of the pixels in an image change according to the dispersion relation of the surface that the camera is looking at, the depth and the velocity can be acquired, as well as uncertainty on those parameters. Due to this, a full posterior probability distribution of the discharge can be obtained, which allows for substantial understanding of the river properties including the uncertainties therein and analysis. A significant additional benefit of this approach is that it allows for the separation of features: this transcends the application shown in this thesis and is not limited to just obtaining discharge, it can also be used as a step in further, deeper analysis of the underlying flow structures. As shown in Appendix C, with only

the posterior distribution of the recovered surface velocity, a mask can be applied to the experimental data sample which separates the gravity-capillary waves and the forced turbulence waves into two videos. This clean separation could be used for further analysis of flow structures that are unclear when the two dispersion structures are combined.

Inevitably there are unfinished aspects to this work, however in and of itself it forms a coherent study of the use of machine learning and statistical methods for surface reconstruction with applications to river monitoring. The work has been broken down into three main aims and these have been addressed. The author looks forward to contributing to and witnessing how future research continues to look into the gaps presented.

Appendix A

Derivation of the Reflection Coefficient

Equations 3.63 and 3.64 were introduced as common knowledge. However, the author views that it is worth the time fleshing out. Therefore, this appendix attempts to derive the coefficients by considering plane wave scattering and transmission between two media with two densities and sound speeds.

Figure A.1 showcases a reflected and transmitted plane wave generated from an indicent wave scattering from a tangent plane. The incident wave hits the boundary between the media at angle θ_I which leads to reflected and transmitted plane waves. These propagate at angles θ_R and θ_T. The two media have distinct densities and sound speeds $\rho_1, c_1,\ \rho_2, c_2$. The acoustic plane-waves represented as complex pressure are:

$$P_I(x,y,t) = A_I e^{-i\omega\left(t-\left(\frac{sin(\theta_I)}{c_1}\right)x-\left(\frac{cos(\theta_I)}{c_1}\right)y\right)} \tag{A.1}$$

$$P_R(x,y,t) = A_R e^{-i\omega\left(t-\left(\frac{sin(\theta_R)}{c_1}\right)x+\left(\frac{cos(\theta_R)}{c_1}\right)y\right)} \tag{A.2}$$

$$P_T(x,y,t) = A_T e^{-i\omega\left(t-\left(\frac{sin(\theta_T)}{c_2}\right)x-\left(\frac{cos(\theta_T)}{c_2}\right)y\right)}. \tag{A.3}$$

The equations above are plane waves travelling in a constant direction, this direction is found from the angles presented in Figure A.1. There are two continuity conditions for pressure and velocity on the boundary between the two media:

$$lim_{y\to 0^-}(P_I(x,y,t) + p_R(x,y,t)) = lim_{y\to 0^+} p_T(x,y,t) \tag{A.4}$$

$$lim_{y\to 0^-}(u_{yI}(x,y,t) + u_{yR}(x,y,t)) = lim_{y\to 0^+} u_{yT}(x,y,t). \tag{A.5}$$

Where u_y is is the velocity of the waves in the y-direction and the subscript I, R, T relate to the incident wave, reflected wave, and transmitted wave respectively. The

relationship between pressure and velocity is defined as Equation (3.13):

$$u_y = -\frac{1}{\rho}\int \frac{\partial p}{\partial y} dt. \tag{A.6}$$

Using this relationship one can find values for the velocity of the incident, reflected and transmitted waves:

$$u_{yI}(x,y,t) = \frac{A_I}{\rho_1 c_1} cos(\theta_I) e^{-i\omega\left(t - \frac{xsin(\theta_I)}{c_1} - \frac{ycos(\theta_I)}{c_1}\right)} \tag{A.7}$$

$$u_{yR}(x,y,t) = \frac{A_R}{\rho_1 c_1} cos(\theta_R) e^{-i\omega\left(t - \frac{xsin(\theta_R)}{c_1} + \frac{ycos(\theta_R)}{c_1}\right)} \tag{A.8}$$

$$u_{yT}(x,y,t) = \frac{A_T}{\rho_2 c_2} cos(\theta_T) e^{-i\omega\left(t - \frac{xsin(\theta_T)}{c_1} - \frac{ycos(\theta_T)}{c_1}\right)}. \tag{A.9}$$

Now we know always the angle of incident is the same as angle of reflection i.e. $\theta_I = \theta_R$ by the law of reflection. Considering the continuity of pressure:

$$\lim_{y\to 0^-} \left(p_I(x,y,t) + p_R(x,y,t)\right) = \lim_{y\to 0^+} p_T(x,y,t), \quad \forall x,t \tag{A.10}$$

$$A_I e^{-i\omega\left(t - \left(\frac{sin(\theta_I)}{c_1}\right)x\right)} + A_R e^{-i\omega\left(t - \left(\frac{sin(\theta_R)}{c_1}\right)x\right)} = A_T e^{-i\omega\left(t - \left(\frac{sin(\theta_T)}{c_2}\right)x\right)} \tag{A.11}$$

Which implies, using the law of reflection:

$$\sin(\theta_I) = \sin(\theta_R), \quad \frac{\sin(\theta_I)}{c_1} = \frac{\sin(\theta_T)}{c_2} \tag{A.12}$$

$$\Rightarrow A_I + A_R = A_T. \tag{A.13}$$

Where the second term is the definition of Snell's law [227]. Similarly, substituting into the velocity continuity equation yields

$$\frac{A_I}{\rho_1 c_1} cos(\theta_I) - \frac{A_R}{\rho_1 c_1} cos(\theta_R) = \frac{A_T}{\rho_2 c_2} cos(\theta_T) \tag{A.14}$$

Now this is a system of equations of which can be solved by utilising Equations (A.13) (A.14) Doing this to isolate A_R and A_T respectively yields

$$A_R = \left(\frac{cos(\theta_I) - \frac{\rho_1 c_1}{\rho_2 c_2} cos(\theta_T)}{cos(\theta_I) + \frac{\rho_1 c_1}{\rho_2 c_2} cos(\theta_T)}\right) A_I \tag{A.15}$$

$$A_T = \left(\frac{2cos(\theta_I)}{cos(\theta_I) + \frac{\rho_1 c_1}{\rho_2 c_2} cos(\theta_T)}\right) A_I \tag{A.16}$$

This gives the Reflection and Transmission coefficients

$$\mathscr{V} = \left(\frac{cos(\theta_I) - \frac{\rho_1 c_1}{\rho_2 c_2} cos(\theta_T)}{cos(\theta_I) + \frac{\rho_1 c_1}{\rho_2 c_2} cos(\theta_T)} \right) \tag{A.17}$$

$$\mathscr{T} = \left(\frac{2cos(\theta_I)}{cos(\theta_I) + \frac{\rho_1 c_1}{\rho_2 c_2} cos(\theta_T)} \right) \tag{A.18}$$

Allowing for a redefinition of terms $Z_1 = \rho_1 c_1$, $Z_2 = \rho_2 c_2$ the above equations can be equated as

$$\mathscr{V} = \left(\frac{Z_2 cos(\theta_I) - Z_1 cos(\theta_T)}{Z_2 cos(\theta_I) + Z_1 cos(\theta_T)} \right) \tag{A.19}$$

$$\mathscr{T} = \left(\frac{2Z_2 cos(\theta_I)}{Z_2 cos(\theta_I) + Z_1 cos(\theta_T)} \right) \tag{A.20}$$

Setting $\cos\theta_I and \cos\theta_T$ to be 1, which implies that $\theta_I, \theta_T = 2\pi n, n \in \mathbb{Z}$ the reflection and transmission coefficients look familiar.

$$\mathscr{V} = \left(\frac{Z_2 - Z_1}{Z_2 + Z_1} \right) \tag{A.21}$$

$$\mathscr{T} = \left(\frac{2Z_2}{Z_2 + Z_1} \right) \tag{A.22}$$

For the tangent plane approximation, the transmission coefficient has no particular importance, as the scattered field is the priority. All that is left is to rearrange in order to get the tangent plane method. As the tangent plane method only considers the boundary between the two media i.e. $y = 0$. This leaves:

$$A_R e^{-i\omega\left(t - x\left(\frac{sin(\theta_R)}{c_1}\right)\right)} = V A_I e^{-i\omega\left(t - x\left(\frac{sin(\theta_I)}{c_1}\right)\right)} \tag{A.23}$$

$$\Rightarrow P_R = V P_I, \tag{A.24}$$

using the fact of the law of reflection, the angle of incidence is the same as the angle of reflection. We aim to take the normal derivative, this is equivalent to multiplying Equation (A.23) by $-cos(\theta_I)c_1^{-1}$:

$$-cos(\theta_I)c_1^{-1} A_R e^{-i\omega\left(t - \left(\frac{sin(\theta_R)}{c_1}\right)\right)} = -cos(\theta_I)c_1^{-1} V A_I e^{-i\omega\left(t - \left(\frac{sin(\theta_I)}{c_1}\right)\right)} \tag{A.25}$$

$$\frac{\partial P_R}{\partial n} = -\mathscr{V} \frac{\partial P_I}{\partial n} \tag{A.26}$$

Which yields the relationship between the incident field and the scattered field, assuming reflection from an infinite plane. Note that this was done in the x-y direction

and in 2D. This applies easily in 3D and in any orientation. Orientations are just (in this case) an isomorphism to the case discussed in the appendix, as one can simply restructure the frame of reference to make the orientation the same as the method discussed. 3D is similar, however there's another angle to account for.

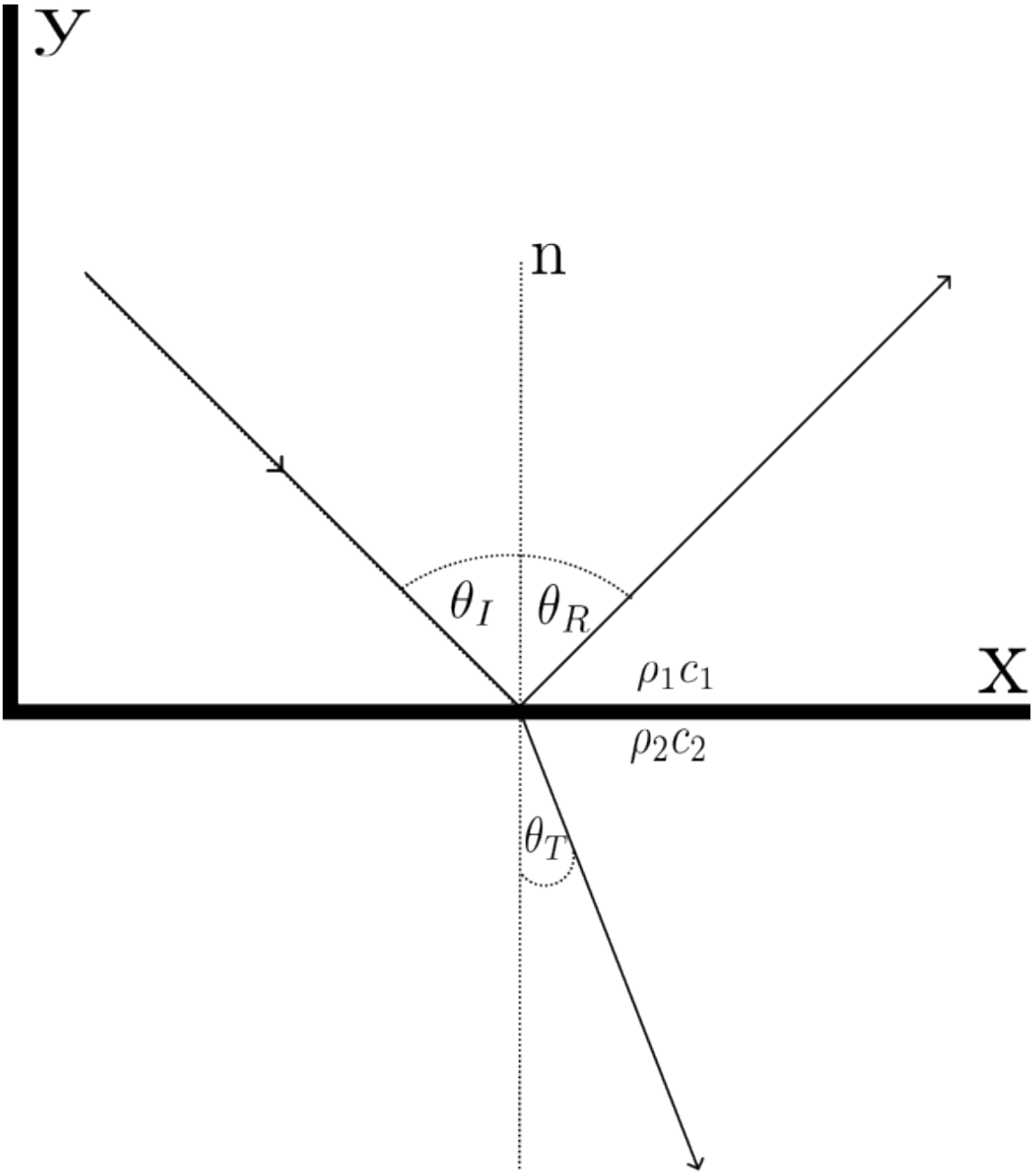

Figure A.1: Graphical representation of the problem. The incident field travels from one media to another. Because of the discontinuity in density ρ and speed of sound c, the incident field forms two new plane waves. The scattered wave propagates in the same media at the same angle as the incident wave, but the y velocity has changed sign. The transmitted wave propagates through the second media and refracts due to the change in density and sound speed.

Appendix B

Rearrangement of $d\mathbf{r}$

In Equation 3.83, a re-arrangement was used in order to remove the normal derivative and replace as values of $\mathbf{q}$ and $\zeta(x,y)$. This Appendix presents the derivation of this. We aim to show

$$(\mathbf{n}\cdot\mathbf{q})\frac{d\mathbf{r}}{n_z} = (q_z - \mathbf{q}\nabla_r\zeta(x,y))d\mathbf{r}. \tag{B.1}$$

We begin by expanding the left hand size, noting that the normal derivative is in the z direction.

$$(\mathbf{n}\cdot\mathbf{q})\frac{d\mathbf{r}}{n_z} = (\mathbf{i_z} - \nabla_r\zeta(x,y))\cdot\mathbf{q})d\mathbf{r}, \tag{B.2}$$

$$= -k(\mathbf{i_z} - \nabla_r\zeta(x,y))\cdot\nabla_S(R_1+R_2))d\mathbf{r}. \tag{B.3}$$

Expanding this as row vectors we have

$$= -k\left(-\frac{\partial\zeta}{\partial x},-\frac{\partial\zeta}{\partial y},1\right)\cdot\left(\frac{\partial(R_1+R_2)}{\partial x},\frac{\partial(R_1+R_2)}{\partial y},\frac{\partial(R_1+R_2)}{\partial z}\right)d\mathbf{r}, \tag{B.4}$$

$$= -k\left(-\frac{\partial\zeta}{\partial x}\frac{\partial(R_1+R_2)}{\partial x} - \frac{\partial\zeta}{\partial y}\frac{\partial(R_1+R_2)}{\partial y} + \frac{\partial(R_1+R_2)}{\partial z}\right)d\mathbf{r}, \tag{B.5}$$

$$= -k\left(-\frac{\partial\zeta}{\partial x}\frac{\partial(R_1+R_2)}{\partial x} - \frac{\partial\zeta}{\partial y}\frac{\partial(R_1+R_2)}{\partial y}\right) + q_z d\mathbf{r}. \tag{B.6}$$

We now have:

$$\nabla_r\zeta(x,y) = \left(\frac{\partial\zeta}{\partial x},\frac{\partial\zeta}{\partial y},0\right)d\mathbf{r} \tag{B.7}$$

We aim to drop the z component, because the z component is 0 everywhere, a projection can be made from 3D down to 2D by noting the subspace formed from

all $(x, y, 0) \in \mathbb{R}^3$ is isomorphic to $\mathbb{R}^2$ with the mapping $(x, y, 0) \to (x, y)$. Therefore, the z component can be dropped leaving

$$(\mathbf{n} \cdot \mathbf{q}) \frac{d\mathbf{r}}{n_z} = (q_z - \mathbf{q} \nabla_r \zeta(x, y)) d\mathbf{r}, \tag{B.8}$$

as required.

Appendix C

Chapter 7 Supplementary Results

One of the final figures presented in Chapter 7 highlight the benefit of being able to split apart the reconstructed surface elevation into the components of just the forced dispersion relation, and the gravity capillary relation. This can only be done because the full three-dimension frequency-wavenumber spectra was recovered. Flow conditions 1 and 5 were showcased in the Chapter, but the author believes that the results are important enough to show every condition recovered from the data.

The figure produced in Chapter 7 contain an extra mask which removed areas where the original video did not have any data. The results in this appendix show the behaviour both with that mask applied, and without.

Further, animations created by ten seconds of footage using this separation for all flow conditions can be at https://github.com/michaeldavidjohnson/Animations.

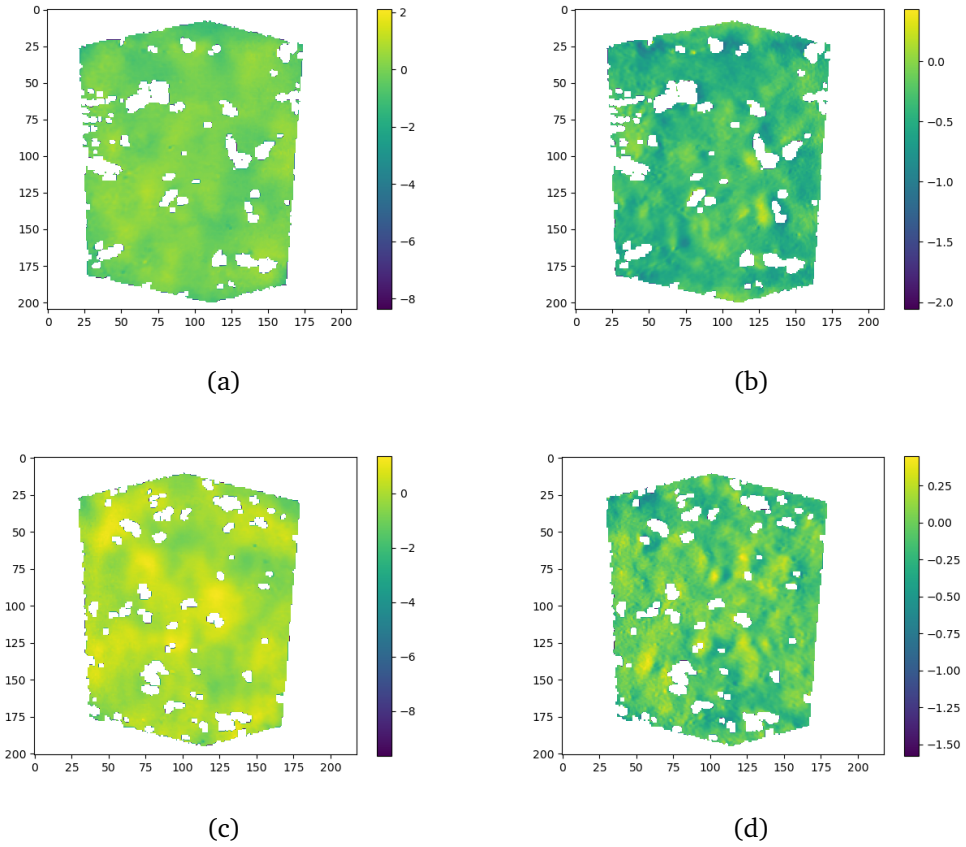

(a) (b)

(c) (d)

Figure C.1: Reconstructed separation from extracting the forced turbulence relation and the gravity-capillary dispersion relation for a) FC1F Gravity-capillary, b) FC1F Turbulence, c) FC1J Gravity-Capillary, d) FC1J Turbulence. Mask applied to remove holes.

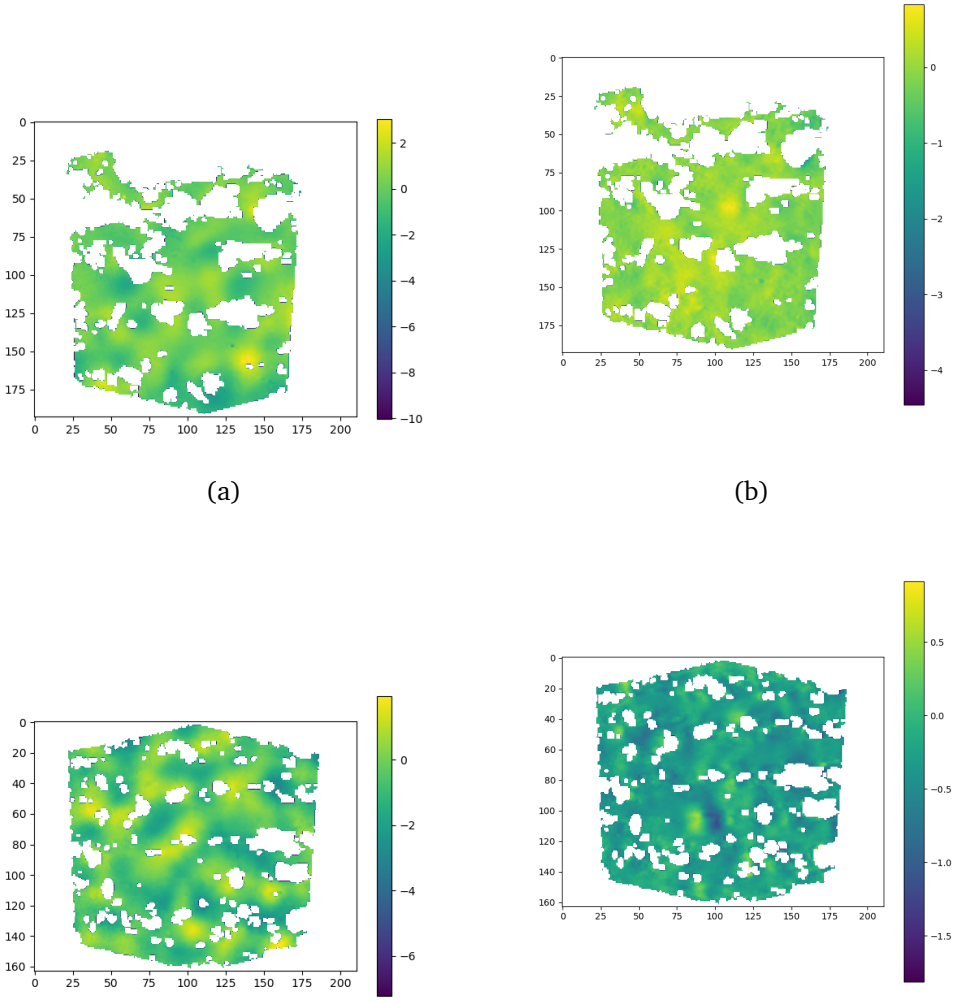

(a) (b)

(c) (d)

Figure C.2: Reconstructed separation from extracting the forced turbulence relation and the gravity-capillary dispersion relation for a) FC2F Gravity-capillary, b) FC2F Turbulence, c) FC2J Gravity-Capillary, d) FC2J Turbulence. Mask applied to remove holes.

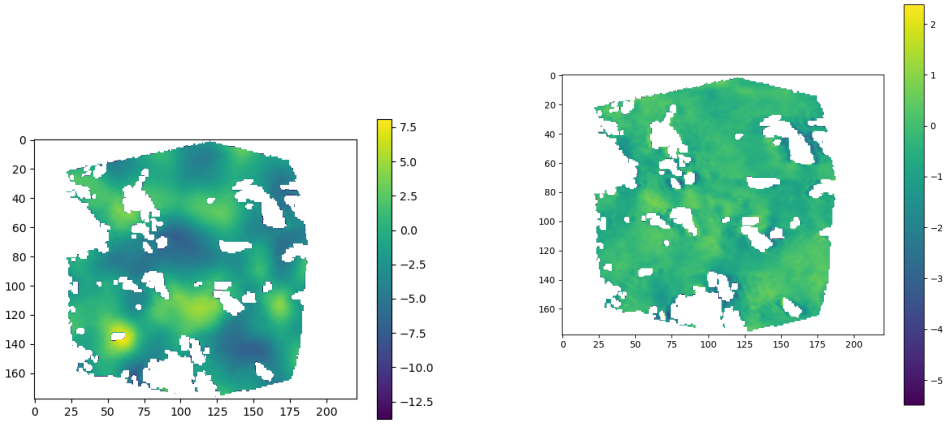

(a) (b)

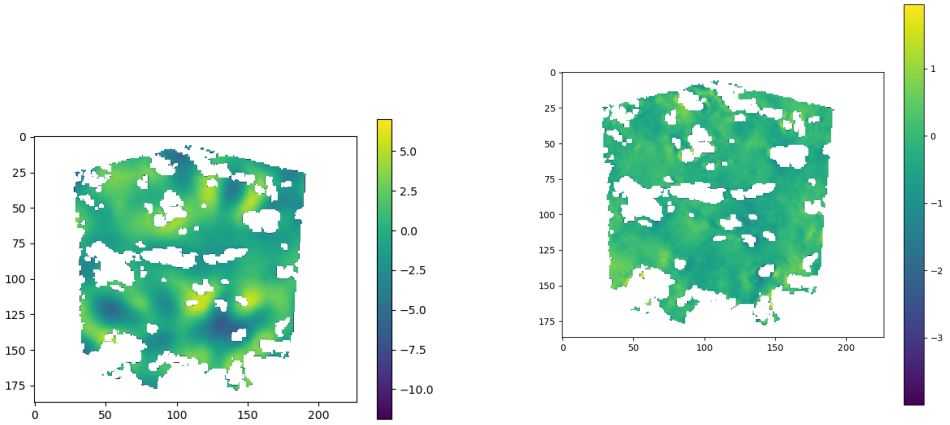

(c) (d)

Figure C.3: Reconstructed separation from extracting the forced turbulence relation and the gravity-capillary dispersion relation for a) FC3F Gravity-capillary, b) FC3F Turbulence, c) FC3J Gravity-Capillary, d) FC3J Turbulence. Mask applied to remove holes.

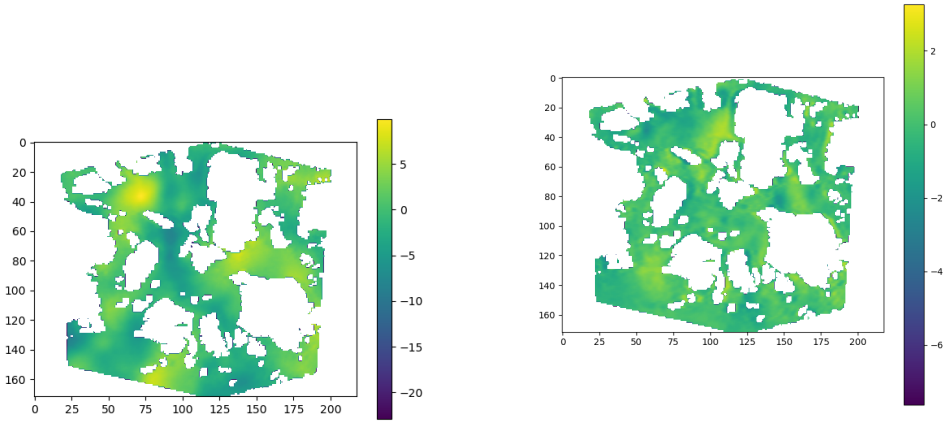

(a) (b)

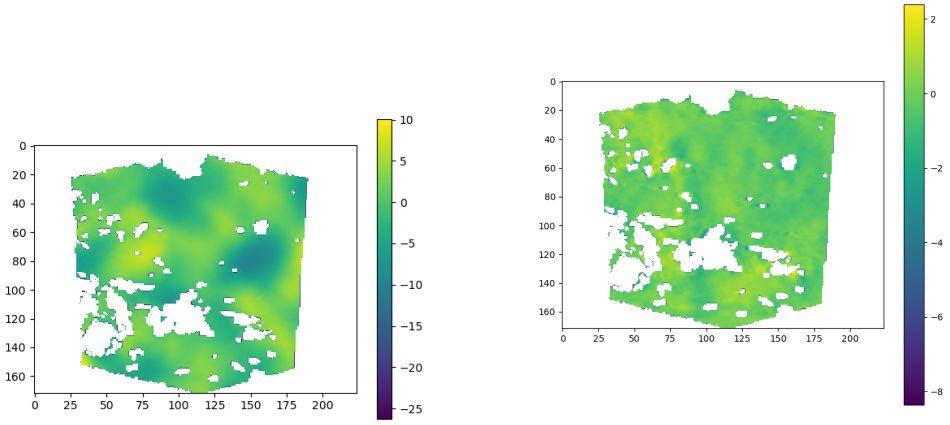

(c) (d)

Figure C.4: Reconstructed separation from extracting the forced turbulence relation and the gravity-capillary dispersion relation for a) FC4F Gravity-capillary, b) FC4F Turbulence, c) FC4J Gravity-Capillary, d) FC4J Turbulence. Mask applied to remove holes.

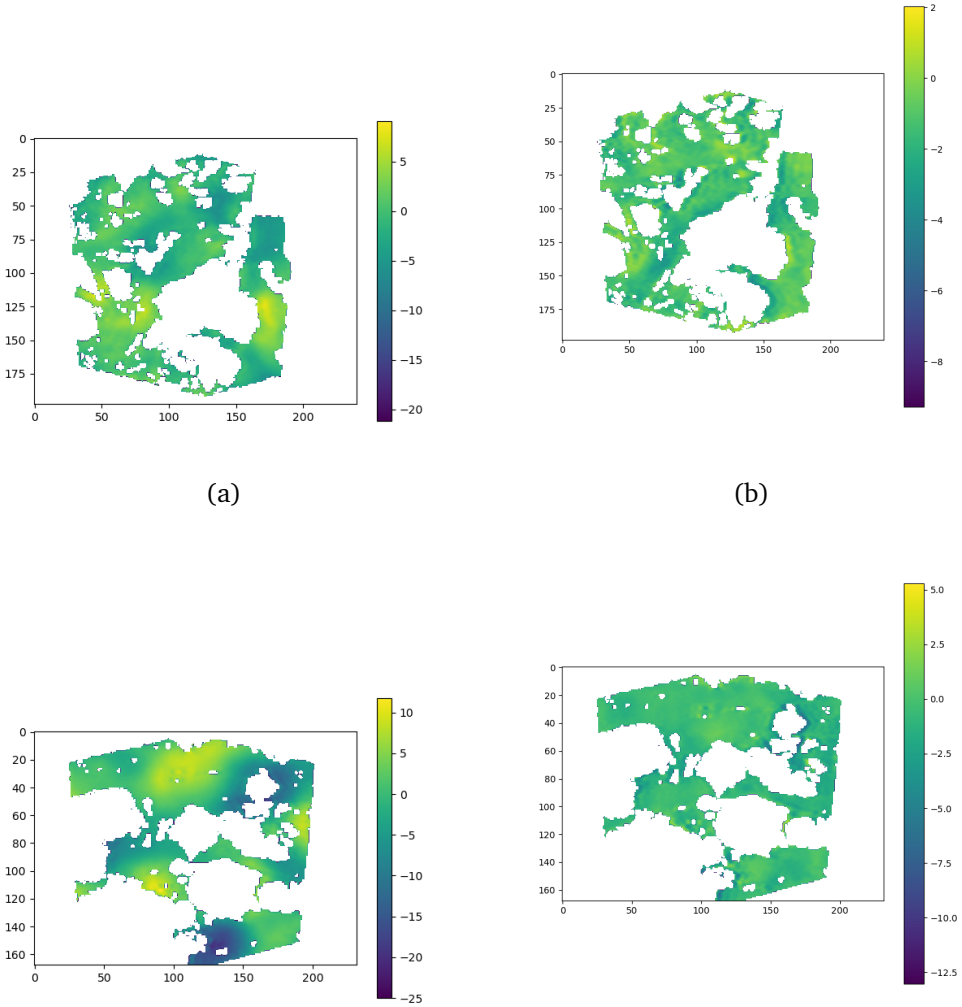

Figure C.5: Reconstructed separation from extracting the forced turbulence relation and the gravity-capillary dispersion relation for a) FC5F Gravity-capillary, b) FC5F Turbulence, c) FC5J Gravity-Capillary, d) FC5J Turbulence. Mask applied to remove holes.

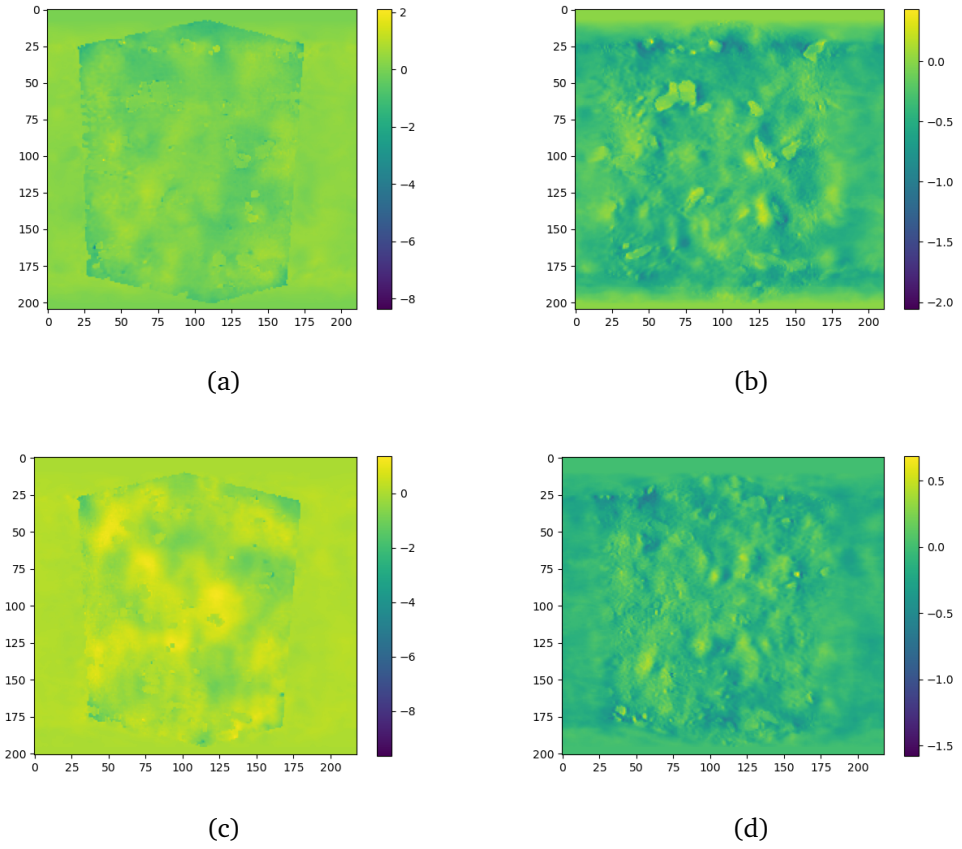

(a) (b)

(c) (d)

Figure C.6: Reconstructed separation from extracting the forced turbulence relation and the gravity-capillary dispersion relation for a) FC1F Gravity-capillary, b) FC1F Turbulence, c) FC1J Gravity-Capillary, d) FC1J Turbulence.

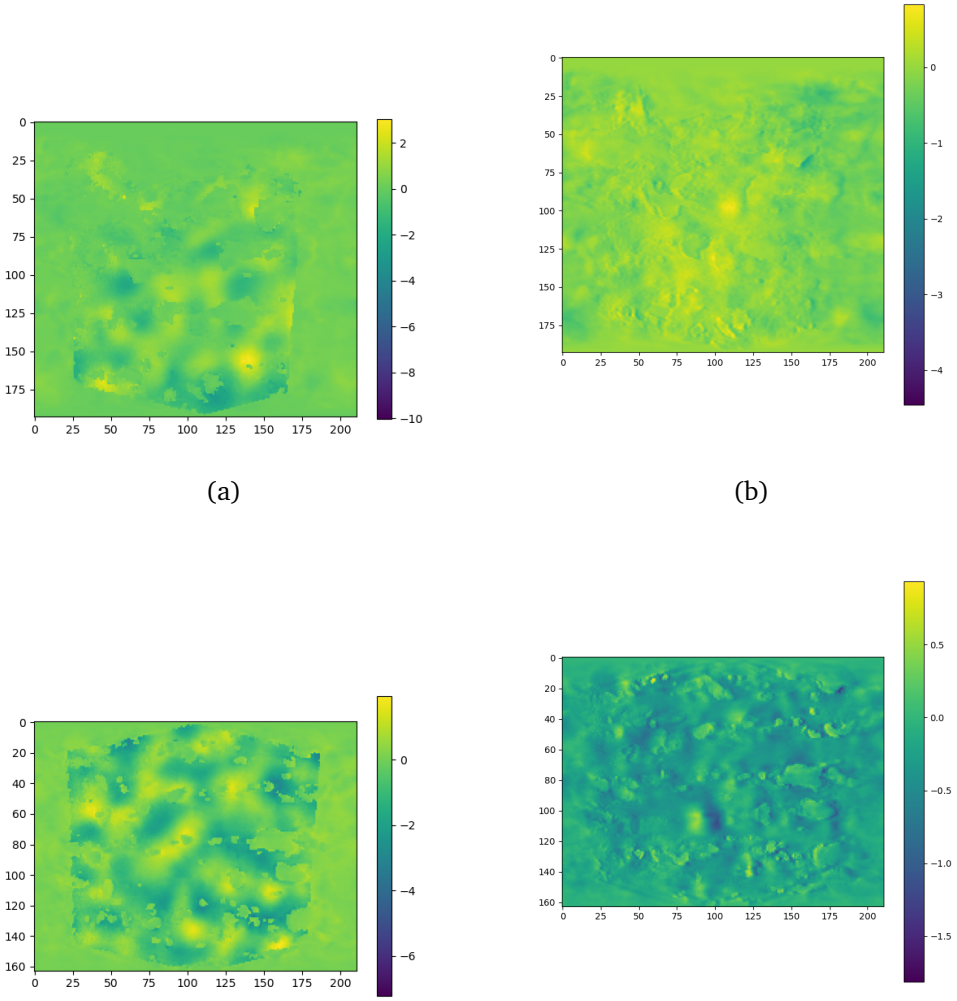

Figure C.7: Reconstructed separation from extracting the forced turbulence relation and the gravity-capillary dispersion relation for a) FC2F Gravity-capillary, b) FC2F Turbulence, c) FC2J Gravity-Capillary, d) FC2J Turbulence.

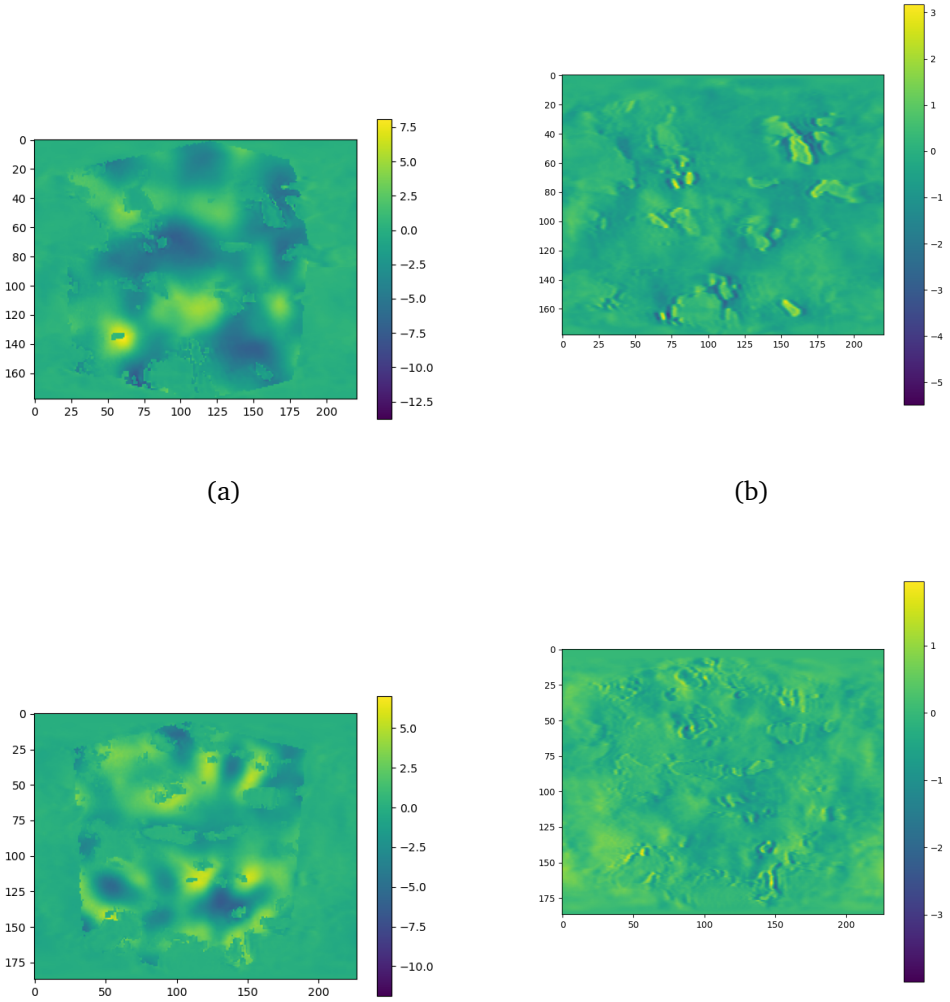

Figure C.8: Reconstructed separation from extracting the forced turbulence relation and the gravity-capillary dispersion relation for a) FC3F Gravity-capillary, b) FC3F Turbulence, c) FC3J Gravity-Capillary, d) FC3J Turbulence.

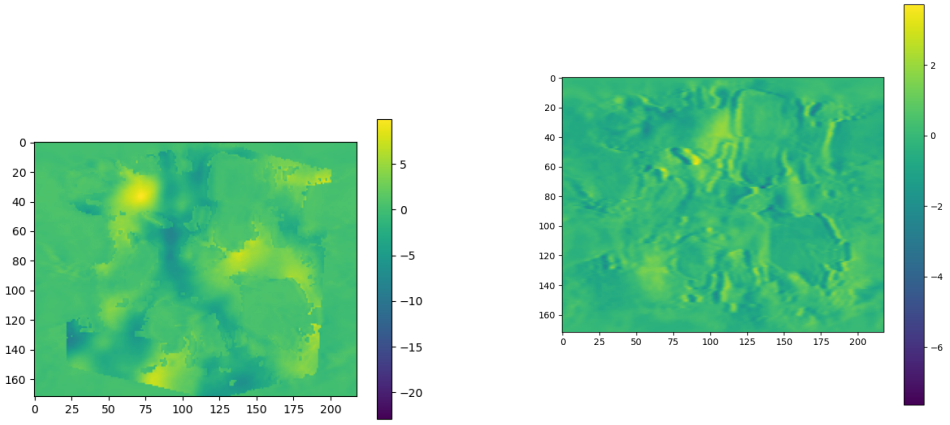

(a) (b)

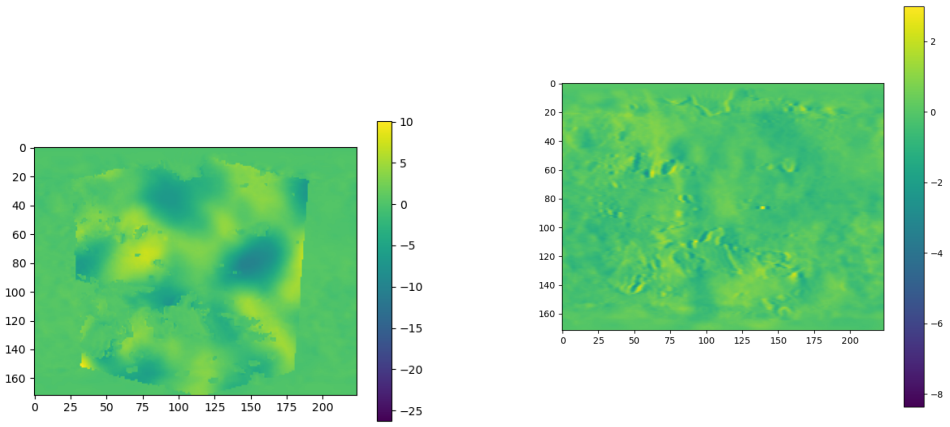

(c) (d)

Figure C.9: Reconstructed separation from extracting the forced turbulence relation and the gravity-capillary dispersion relation for a) FC4F Gravity-capillary, b) FC4F Turbulence, c) FC4J Gravity-Capillary, d) FC4J Turbulence.

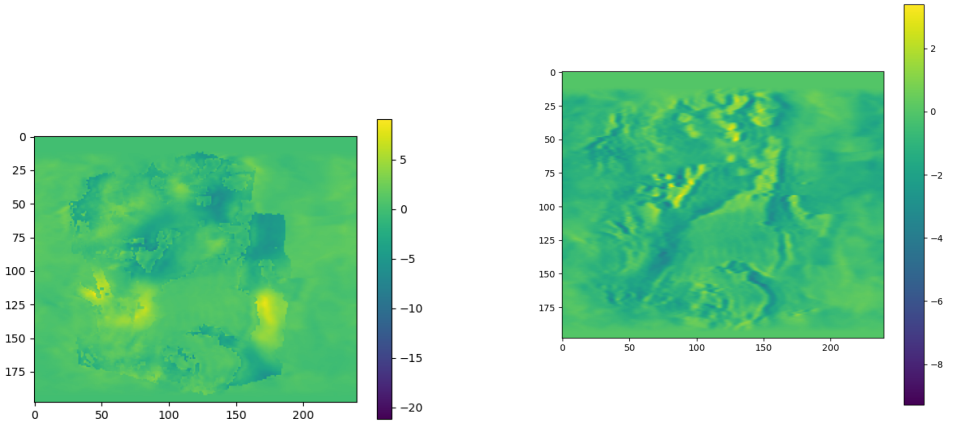

(a) (b)

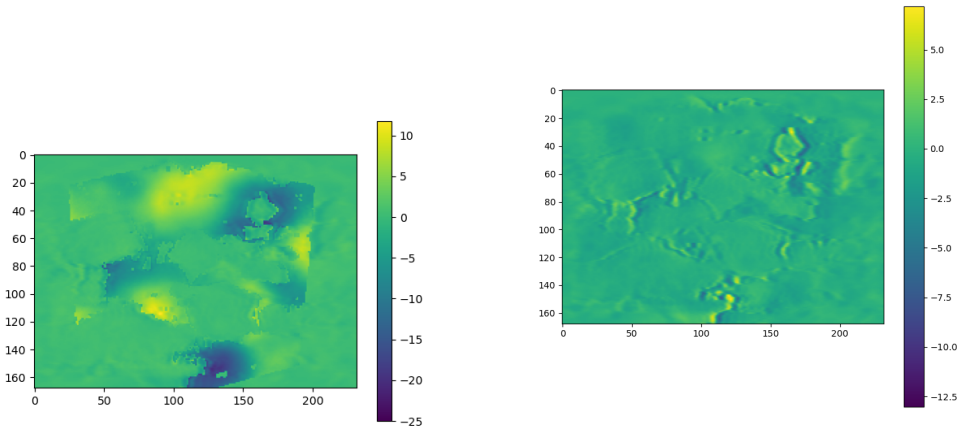

(c) (d)

Figure C.10: Reconstructed separation from extracting the forced turbulence relation and the gravity-capillary dispersion relation for a) FC5F Gravity-capillary, b) FC5F Turbulence, c) FC5J Gravity-Capillary, d) FC5J Turbulence.

Bibliography

[1] M.-D. Johnson, A. Krynkin, G. Dolcetti, M. Alkmim, J. Cuenca, and L. De Ryck, "Surface shape reconstruction from phaseless scattered acoustic data using a random forest algorithm," *The Journal of the Acoustical Society of America*, vol. 152, no. 2, pp. 1045–1057, 2022.

[2] G. Dolcetti, B. Hortobágyi, M. Perks, S. Tait, and N. Dervilis, "Using non-contact measurement of water surface dynamics to estimate river discharge," *Water Resources Research*, p. e2022WR032829, 2022.

[3] D. A. Lavers, R. P. Allan, E. F. Wood, G. Villarini, D. J. Brayshaw, and A. J. Wade, "Winter floods in britain are connected to atmospheric rivers," *Geophysical Research Letters*, vol. 38, no. 23, 2011.

[4] A. Sibley *et al.*, "Analysis of extreme rainfall and flooding in cumbria 18-20 november 2009.," *Weather*, vol. 65, no. 11, pp. 287–292, 2010.

[5] T. Marsh, C. Kirby, K. Muchan, L. Barker, E. Henderson, and J. Hannaford, *The winter floods of 2015/2016 in the UK-a review*. NERC/Centre for Ecology & Hydrology, 2016.

[6] C. Sefton, K. Muchan, S. Parry, B. Matthews, L. Barker, S. Turner, and J. Hannaford, "The 2019/2020 floods in the uk: a hydrological appraisal," *Weather*, vol. 76, no. 12, pp. 378–384, 2021.

[7] C. Huntingford, T. Marsh, A. A. Scaife, E. J. Kendon, J. Hannaford, A. L. Kay, M. Lockwood, C. Prudhomme, N. S. Reynard, S. Parry, *et al.*, "Potential influences on the united kingdom's floods of winter 2013/14," *Nature Climate Change*, vol. 4, no. 9, pp. 769–777, 2014.

[8] J. D. Miller and M. Hutchins, "The impacts of urbanisation and climate change on urban flooding and urban water quality: A review of the evi-

dence concerning the united kingdom," *Journal of Hydrology: Regional Studies*, vol. 12, pp. 345–362, 2017.

[9] R. Rojas, L. Feyen, and P. Watkiss, "Climate change and river floods in the european union: Socio-economic consequences and the costs and benefits of adaptation," *Global Environmental Change*, vol. 23, no. 6, pp. 1737–1751, 2013.

[10] M. Welber, J. Le Coz, J. B. Laronne, G. Zolezzi, D. Zamler, G. Dramais, A. Hauet, and M. Salvaro, "Field assessment of noncontact stream gauging using portable surface velocity radars (svr)," *Water Resources Research*, vol. 52, no. 2, pp. 1108–1126, 2016.

[11] B. J. Peterson, R. M. Holmes, J. W. McClelland, C. J. Vorosmarty, R. B. Lammers, A. I. Shiklomanov, I. A. Shiklomanov, and S. Rahmstorf, "Increasing river discharge to the arctic ocean," *science*, vol. 298, no. 5601, pp. 2171–2173, 2002.

[12] J. D. Milliman and K. L. Farnsworth, *River discharge to the coastal ocean: a global synthesis*. Cambridge University Press, 2013.

[13] M. T. van Vliet, W. H. Franssen, J. R. Yearsley, F. Ludwig, I. Haddeland, D. P. Lettenmaier, and P. Kabat, "Global river discharge and water temperature under climate change," *Global Environmental Change*, vol. 23, no. 2, pp. 450–464, 2013.

[14] J. Costa, R. Cheng, F. Haeni, N. Melcher, K. Spicer, E. Hayes, W. Plant, K. Hayes, C. Teague, and D. Barrick, "Use of radars to monitor stream discharge by noncontact methods," *Water Resources Research*, vol. 42, no. 7, 2006.

[15] R. L. Gordon, "Acoustic measurement of river discharge," *journal of hydraulic Engineering*, vol. 115, no. 7, pp. 925–936, 1989.

[16] M. Raffel, C. E. Willert, F. Scarano, C. J. Kähler, S. T. Wereley, and J. Kompenhans, *Particle image velocimetry: a practical guide*. Springer, 2018.

[17] S. F. Barstow, J.-R. Bidlot, S. Caires, M. A. Donelan, W. M. Drennan, H. Dupuis, H. C. Graber, J. J. Green, O. Gronlie, C. Guérin, *et al.*, *Measuring and analysing the directional spectrum of ocean waves*. COST office, 2005.

[18] G. Dolcetti, K. Horoshenkov, A. Krynkin, and S. Tait, "Frequency-wavenumber spectrum of the free surface of shallow turbulent flows over a rough boundary," *Physics of Fluids*, vol. 28, no. 10, p. 105105, 2016.

[19] S. Chandler-Wilde and S. Langdon, "Boundary element methods for acoustics," *Lecture notes, University of Reading, Department of Mathematics*, 2007.

[20] J. Montalt-Tordera, V. Muthurangu, A. Hauptmann, and J. A. Steeden, "Machine learning in magnetic resonance imaging: image reconstruction," *Physica Medica*, vol. 83, pp. 79–87, 2021.

[21] A. S. Lundervold and A. Lundervold, "An overview of deep learning in medical imaging focusing on mri," *Zeitschrift für Medizinische Physik*, vol. 29, no. 2, pp. 102–127, 2019.

[22] L. Rayleigh, "The theory of sound," *vol. II*, p. 226, 1945.

[23] L. Pierce, *Acoustics*, vol. 3. Springer, 2019.

[24] P. M. Morse and K. U. Ingard, *Theoretical acoustics*. Princeton university press, 1986.

[25] F. B. Jensen, W. A. Kuperman, M. B. Porter, H. Schmidt, and A. Tolstoy, *Computational ocean acoustics*, vol. 2011. Springer, 2011.

[26] H. Kuttruff, *Room acoustics*. Crc Press, 2016.

[27] A. Dell, A. Krynkin, K. Horoshenkov, and G. Sailor, "Low frequency attenuation of acoustic waves in a perforated pipe," *The Journal of the Acoustical Society of America*, vol. 153, no. 3, pp. 1791–1801, 2023.

[28] L. L. Foldy, "The multiple scattering of waves. i. general theory of isotropic scattering by randomly distributed scatterers," *Physical review*, vol. 67, no. 3-4, p. 107, 1945.

[29] J. V. Venås and T. Kvamsdal, "Isogeometric boundary element method for acoustic scattering by a submarine," *Computer Methods in Applied Mechanics and Engineering*, vol. 359, p. 112670, 2020.

[30] C. Farhat, A. Macedo, and M. Lesoinne, "A two-level domain decomposition method for the iterative solution of high frequency exterior helmholtz problems," *Numerische Mathematik*, vol. 85, pp. 283–308, 2000.

[31] C. Testa and L. Greco, "Prediction of submarine scattered noise by the acoustic analogy," *Journal of Sound and Vibration*, vol. 426, pp. 186–218, 2018.

[32] H. H. de Sénarmont, E. Verdet, and L. F. Fresnel, *Oeuvres Complètes D'Augustin Fresnel*. Imprimerie impériale, 1866.

[33] R. L. Haupt and M. Cote, "Snell's law applied to finite surfaces," *IEEE transactions on antennas and propagation*, vol. 41, no. 2, pp. 227–230, 1993.

[34] G. Kirchhoff, "Zur theorie der lichtstrahlen," *Annalen der Physik*, vol. 254, no. 4, pp. 663–695, 1883.

[35] G. Kirchhoff, "On the ray theory of light," 2016.

[36] I. F. F.G. BASS, "Wave scattering from statistically rough surfaces," 1979.

[37] A. Ishimaru, *Wave propagation and scattering in random media*, vol. 2. Academic press New York, 1978.

[38] S. Kirkup, "The boundary element method in acoustics: A survey," *Applied Sciences*, vol. 9, no. 8, p. 1642, 2019.

[39] P. A. Martin, *Multiple scattering: interaction of time-harmonic waves with N obstacles*. No. 107, Cambridge University Press, 2006.

[40] B. Peterson and S. Ström, "Matrix formulation of acoustic scattering from an arbitrary number of scatterers," *The Journal of the Acoustical Society of America*, vol. 56, no. 3, pp. 771–780, 1974.

[41] C. M. Linton and P. A. Martin, "Multiple scattering by multiple spheres: A new proof of the lloyd–berry formula for the effective wavenumber," *SIAM Journal on Applied Mathematics*, vol. 66, no. 5, pp. 1649–1668, 2006.

[42] C. D. Jones and D. R. Jackson, "Small perturbation method of high-frequency bistatic volume scattering from marine sediments," *IEEE journal of oceanic engineering*, vol. 26, no. 1, pp. 84–93, 2001.

[43] B. Smith, "Geometrical shadowing of a random rough surface," *IEEE transactions on antennas and propagation*, vol. 15, no. 5, pp. 668–671, 1967.

[44] H. T. Siegelmann and E. D. Sontag, "On the computational power of neural nets," *Journal of computer and system sciences*, vol. 50, no. 1, pp. 132–150, 1995.

[45] Y. LeCun, Y. Bengio, G. Hinton, *et al.*, "Deep learning. nature, 521 (7553), 436-444," *Google Scholar Google Scholar Cross Ref Cross Ref*, vol. 521, no. 7553, pp. 436–444, 2015.

[46] L. Rokach and O. Maimon, "Decision trees," in *Data mining and knowledge discovery handbook*, pp. 165–192, Springer, 2005.

[47] L. Breiman, "Random forests," *Machine learning*, vol. 45, no. 1, pp. 5–32, 2001.

[48] O. Ibe, *Fundamentals of applied probability and random processes*. Academic Press, 2014.

[49] H. Park, N. Kim, and J. Lee, "Parametric models and non-parametric machine learning models for predicting option prices: Empirical comparison study over kospi 200 index options," *Expert Systems with Applications*, vol. 41, no. 11, pp. 5227–5237, 2014.

[50] F. Pedregosa, G. Varoquaux, A. Gramfort, V. Michel, B. Thirion, O. Grisel, M. Blondel, P. Prettenhofer, R. Weiss, V. Dubourg, *et al.*, "Scikit-learn: Machine learning in python," *the Journal of machine Learning research*, vol. 12, pp. 2825–2830, 2011.

[51] M. Abadi, A. Agarwal, P. Barham, E. Brevdo, Z. Chen, C. Citro, G. S. Corrado, A. Davis, J. Dean, M. Devin, *et al.*, "Tensorflow: Large-scale machine learning on heterogeneous distributed systems," *arXiv preprint arXiv:1603.04467*, 2016.

[52] M. J. Bianco, P. Gerstoft, J. Traer, E. Ozanich, M. A. Roch, S. Gannot, and C.-A. Deledalle, "Machine learning in acoustics: Theory and applications," *The Journal of the Acoustical Society of America*, vol. 146, no. 5, pp. 3590–3628, 2019.

[53] M. Elforjani and S. Shanbr, "Prognosis of bearing acoustic emission signals using supervised machine learning," *IEEE Transactions on industrial electronics*, vol. 65, no. 7, pp. 5864–5871, 2017.

[54] A. K. Das, D. Suthar, and C. K. Leung, "Machine learning based crack mode classification from unlabeled acoustic emission waveform features," *Cement and Concrete Research*, vol. 121, pp. 42–57, 2019.

[55] R. Palaniappan, K. Sundaraj, and S. Sundaraj, "A comparative study of the svm and k-nn machine learning algorithms for the diagnosis of respiratory pathologies using pulmonary acoustic signals," *BMC bioinformatics*, vol. 15, pp. 1–8, 2014.

[56] Y. H. Jung, S. K. Hong, H. S. Wang, J. H. Han, T. X. Pham, H. Park, J. Kim, S. Kang, C. D. Yoo, and K. J. Lee, "Flexible piezoelectric acoustic sensors and machine learning for speech processing," *Advanced Materials*, vol. 32, no. 35, p. 1904020, 2020.

[57] J. A. Gonzalez, L. A. Cheah, A. M. Gomez, P. D. Green, J. M. Gilbert, S. R. Ell, R. K. Moore, and E. Holdsworth, "Direct speech reconstruction from articulatory sensor data by machine learning," *IEEE/ACM Transactions on Audio, Speech, and Language Processing*, vol. 25, no. 12, pp. 2362–2374, 2017.

[58] M. D. Skowronski and J. G. Harris, "Acoustic detection and classification of microchiroptera using machine learning: lessons learned from automatic speech recognition," *The Journal of the Acoustical Society of America*, vol. 119, no. 3, pp. 1817–1833, 2006.

[59] D. L. Colton, R. Kress, and R. Kress, *Inverse acoustic and electromagnetic scattering theory*, vol. 93. Springer, 1998.

[60] A. Kirsch and S. Ritter, "A linear sampling method for inverse scattering from an open arc," *Inverse problems*, vol. 16, no. 1, p. 89, 2000.

[61] A. Kirsch, "Characterization of the shape of a scattering obstacle using the spectral data of the far field operator," *Inverse problems*, vol. 14, no. 6, p. 1489, 1998.

[62] F. Collino, H. Haddar, *et al.*, "Numerical and analytical studies of the linear sampling method in electromagnetic inverse scattering problems," *Inverse problems*, vol. 19, no. 6, p. 1279, 2003.

[63] P. Meng, L. Su, W. Yin, and S. Zhang, "Solving a kind of inverse scattering problem of acoustic waves based on linear sampling method and neural network," *Alexandria Engineering Journal*, vol. 59, no. 3, pp. 1451–1462, 2020.

[64] W. W. Ahmed, M. Farhat, P.-Y. Chen, X. Zhang, and Y. Wu, "A generative deep learning approach for shape recognition of arbitrary objects from phaseless acoustic scattering data," *Advanced Intelligent Systems*, vol. 5, no. 5, p. 2200260, 2023.

[65] S. Afifi and M. Diaf, "Scattering by random rough surfaces: Study of direct and inverse problem," *Optics communications*, vol. 265, no. 1, pp. 11–17, 2006.

[66] A. Krynkin, K. Horoshenkov, A. Nichols, and S. Tait, "A non-invasive acoustical method to measure the mean roughness height of the free surface of a turbulent shallow water flow," *Review of Scientific Instruments*, vol. 85, p. 114902, Nov. 2014.

[67] A. Krynkin, K. V. Horoshenkov, and T. Van Renterghem, "An airborne acoustic method to reconstruct a dynamically rough flow surface," *The Journal of the Acoustical Society of America*, vol. 140, pp. 2064–2073, Sept. 2016.

[68] A. Krynkin, G. Dolcetti, and S. Hunting, "Acoustic imaging in application to reconstruction of rough rigid surface with airborne ultrasound waves," *Review of Scientific Instruments*, vol. 88, p. 024901, Feb. 2017.

[69] A. Nichols, *Free surface dynamics in shallow turbulent flows.* PhD thesis, University of Bradford, 2015.

[70] X. Liu, B. Zhang, and H. Zhang, "A direct imaging method for inverse scattering by unbounded rough surfaces," *SIAM Journal on Imaging Sciences*, vol. 11, no. 2, pp. 1629–1650, 2018.

[71] W. C. Chew and Y.-M. Wang, "Reconstruction of two-dimensional permittivity distribution using the distorted born iterative method," *IEEE transactions on medical imaging*, vol. 9, no. 2, pp. 218–225, 1990.

[72] M. V. Klibanov, "Phaseless inverse scattering problems in three dimensions," *SIAM Journal on Applied Mathematics*, vol. 74, no. 2, pp. 392–410, 2014.

[73] M. V. Klibanov and V. G. Romanov, "Two reconstruction procedures for a 3d phaseless inverse scattering problem for the generalized helmholtz equation," *Inverse Problems*, vol. 32, no. 1, p. 015005, 2015.

[74] G. Dolcetti, M. Alkmim, J. Cuenca, L. De Ryck, and A. Krynkin, "Robust reconstruction of scattering surfaces using a linear microphone array," *Journal of Sound and Vibration*, vol. 494, p. 115902, 2021.

[75] K. Xu, L. Wu, X. Ye, and X. Chen, "Deep learning-based inversion methods for solving inverse scattering problems with phaseless data," *IEEE Transactions on Antennas and Propagation*, vol. 68, no. 11, pp. 7457–7470, 2020.

[76] L. Deng, "The mnist database of handwritten digit images for machine learning research [best of the web]," *IEEE signal processing magazine*, vol. 29, no. 6, pp. 141–142, 2012.

[77] Y. Chen and M. Spivack, "Rough surface reconstruction at grazing angles by an iterated marching method," *JOSA A*, vol. 35, no. 4, pp. 504–513, 2018.

[78] C. Qian, B. Zheng, Y. Shen, L. Jing, E. Li, L. Shen, and H. Chen, "Deep-learning-enabled self-adaptive microwave cloak without human intervention," *Nature photonics*, vol. 14, no. 6, pp. 383–390, 2020.

[79] A. Antona, "Remote fish species and size identification using broadband echosounders," *Institute for Marine Resources and Ecosystem Studies (IMARES), Wageningen University. http://edepot. wur. nl/378294*, 2016.

[80] R. M. Goldade, *Towards real-time sea-floor surface reconstruction and classification using 3-D side-scan sonar*. PhD thesis, Applied Sciences: School of Engineering Science, 2014.

[81] J. B. Mendieta, "An efficient and semiautomatic segmentation method for 3d surface reconstruc-tion of the lumbar spine from magnetic resonance imaging (mri)," *Brisbane.*, 2016.

[82] J. Adler and O. Öktem, "Solving ill-posed inverse problems using iterative deep neural networks," *Inverse Problems*, vol. 33, no. 12, p. 124007, 2017.

[83] F. Wang, A. Eljarrat, J. Müller, T. R. Henninen, R. Erni, and C. T. Koch, "Multi-resolution convolutional neural networks for inverse problems," *Scientific reports*, vol. 10, no. 1, pp. 1–11, 2020.

[84] Y. Kim and N. Nakata, "Geophysical inversion versus machine learning in inverse problems," *The Leading Edge*, vol. 37, no. 12, pp. 894–901, 2018.

[85] S. Sonoda and N. Murata, "Neural network with unbounded activation functions is universal approximator," *Applied and Computational Harmonic Analysis*, vol. 43, no. 2, pp. 233–268, 2017.

[86] S. Ren, G. Chen, T. Li, Q. Chen, and S. Li, "A deep learning-based computational algorithm for identifying damage load condition: an artificial intelligence inverse problem solution for failure analysis," *Computer Modeling in Engineering & Sciences*, vol. 117, no. 3, pp. 287–307, 2018.

[87] M. Prato and L. Zanni, "Inverse problems in machine learning: an application to brain activity interpretation," in *Journal of Physics: Conference Series*, vol. 135, p. 012085, IOP Publishing, 2008.

[88] Y. Fan and L. Ying, "Solving inverse wave scattering with deep learning," *arXiv preprint arXiv:1911.13202*, 2019.

[89] B. Engquist, C. Frederick, Q. Huynh, and H. Zhou, "Seafloor identification in sonar imagery via simulations of helmholtz equations and discrete optimization," *Journal of Computational Physics*, vol. 338, pp. 477–492, 2017.

[90] Y. Gao, H. Liu, X. Wang, and K. Zhang, "On an artificial neural network for inverse scattering problems," *Journal of Computational Physics*, vol. 448, p. 110771, 2022.

[91] T. Song, L. Kuang, L. Han, Y. Wang, and Q. H. Liu, "Inversion of rough surface parameters from sar images using simulation-trained convolutional neural networks," *IEEE Geoscience and Remote Sensing Letters*, vol. 15, no. 7, pp. 1130–1134, 2018.

[92] W. Yin, W. Yang, and H. Liu, "A neural network scheme for recovering scattering obstacles with limited phaseless far-field data," *Journal of Computational Physics*, vol. 417, p. 109594, 2020.

[93] N. J. Nagelkerke *et al.*, "A note on a general definition of the coefficient of determination," *biometrika*, vol. 78, no. 3, pp. 691–692, 1991.

[94] P. Hennig, M. A. Osborne, and H. P. Kersting, *Probabilistic Numerics: Computation as Machine Learning*. Cambridge University Press, 2022.

[95] N. Krämer, J. Schmidt, and P. Hennig, "Probabilistic numerical method of lines for time-dependent partial differential equations," in *International Conference on Artificial Intelligence and Statistics*, pp. 625–639, PMLR, 2022.

[96] K. P. Murphy, *Machine learning: a probabilistic perspective*. MIT press, 2012.

[97] A. McHutchon and C. Rasmussen, "Gaussian process training with input noise," *Advances in neural information processing systems*, vol. 24, 2011.

[98] C. Andrieu, N. De Freitas, A. Doucet, and M. I. Jordan, "An introduction to mcmc for machine learning," *Machine learning*, vol. 50, no. 1, pp. 5–43, 2003.

[99] S. Yu, B. Liu, K. Yu, Z. Yang, G. Kan, and L. Zong, "Inversion of bottom parameters using a backscattering model based on the effective density fluid approximation," *Applied Acoustics*, vol. 182, p. 108187, 2021.

[100] A. E. Fouda and F. L. Teixeira, "Bayesian compressive sensing for rough surface reconstruction," in *2021 IEEE 19th International Symposium on Antenna Technology and Applied Electromagnetics (ANTEM)*, pp. 1–2, IEEE, 2021.

[101] J. Antoni, Q. Leclere, and T. Lemagueresse, "Sparse holography from iterated bayesian focusing," in *INTER-NOISE and NOISE-CON Congress and Conference Proceedings*, vol. 257, pp. 648–659, Institute of Noise Control Engineering, 2018.

[102] T. Le Magueresse, J.-H. Thomas, J. Antoni, and S. Paillasseur, "Instantaneous bayesian regularization applied to real-time near-field acoustic holography," *The Journal of the Acoustical Society of America*, vol. 142, no. 2, pp. 924–934, 2017.

[103] Z. Li, Y. Liu, J. Sun, and L. Xu, "Quality-bayesian approach to inverse acoustic source problems with partial data," *SIAM Journal on Scientific Computing*, vol. 43, no. 2, pp. A1062–A1080, 2021.

[104] Z. Yang, X. Gui, J. Ming, and G. Hu, "Bayesian approach to inverse time-harmonic acoustic scattering with phaseless far-field data," *Inverse Problems*, vol. 36, no. 6, p. 065012, 2020.

[105] Z. Yang, X. Gui, J. Ming, and G. Hu, "Bayesian approach to inverse time-harmonic acoustic obstacle scattering with phaseless data generated by point source waves," *Computer Methods in Applied Mechanics and Engineering*, vol. 386, p. 114073, 2021.

[106] A. Palafox, M. A. Capistrán, and J. A. Christen, "Effective parameter dimension via bayesian model selection in the inverse acoustic scattering problem," *Mathematical Problems in Engineering*, vol. 2014, 2014.

[107] M.-H. Chen, Q.-M. Shao, and J. G. Ibrahim, *Monte Carlo methods in Bayesian computation*. Springer Science & Business Media, 2012.

[108] T. Hong and M. K. Sen, "A new mcmc algorithm for seismic waveform inversion and corresponding uncertainty analysis," *Geophysical Journal International*, vol. 177, no. 1, pp. 14–32, 2009.

[109] I. Smal, N. Carranza-Herrezuelo, S. Klein, W. Niessen, and E. Meijering, "Trans-dimensional mcmc methods for fully automatic motion analysis in tagged mri," in *International Conference on Medical Image Computing and Computer-Assisted Intervention*, pp. 573–580, Springer, 2011.

[110] I. Smal, N. Carranza-Herrezuelo, S. Klein, P. Wielopolski, A. Moelker, T. Springeling, M. Bernsen, W. Niessen, and E. Meijering, "Reversible jump mcmc methods for fully automatic motion analysis in tagged mri," *Medical image analysis*, vol. 16, no. 1, pp. 301–324, 2012.

[111] M. Niskanen, J.-P. Groby, A. Duclos, O. Dazel, J. Le Roux, N. Poulain, T. Huttunen, and T. Lähivaara, "Deterministic and statistical characterization of rigid frame porous materials from impedance tube measurements," *The Journal of the Acoustical Society of America*, vol. 142, no. 4, pp. 2407–2418, 2017.

[112] H. Haario, E. Saksman, and J. Tamminen, "Adaptive proposal distribution for random walk Metropolis algorithm," *Computational Statistics*, vol. 14, pp. 375–396, 1999.

[113] H. Haario, E. Saksman, and J. Tamminen, "An adaptive metropolis algorithm," *Bernoulli*, pp. 223–242, 2001.

[114] M. Betancourt, "A conceptual introduction to hamiltonian monte carlo," *arXiv preprint arXiv:1701.02434*, 2017.

[115] J. Salvatier, T. V. Wieckiâ, and C. Fonnesbeck, "Pymc3: Python probabilistic programming framework," *Astrophysics Source Code Library*, pp. ascl–1610, 2016.

[116] B. Carpenter, A. Gelman, M. D. Hoffman, D. Lee, B. Goodrich, M. Betancourt, M. A. Brubaker, J. Guo, P. Li, and A. Riddell, "Stan: A probabilistic programming language," *Journal of statistical software*, vol. 76, 2017.

[117] G. B. Airy, *Tides and waves*. B. Fellowes, 1845.

[118] T. Sarpkaya, *Wave forces on offshore structures*. Cambridge university press, 2010.

[119] K. Hasselmann, T. P. Barnett, E. Bouws, H. Carlson, D. E. Cartwright, K. Enke, J. Ewing, A. Gienapp, D. Hasselmann, P. Kruseman, *et al.*, "Measurements of wind-wave growth and swell decay during the joint north sea wave project (jonswap).," *Ergaenzungsheft zur Deutschen Hydrographischen Zeitschrift, Reihe A*, 1973.

[120] W. J. Pierson Jr and L. Moskowitz, "A proposed spectral form for fully developed wind seas based on the similarity theory of sa kitaigorodskii," *Journal of geophysical research*, vol. 69, no. 24, pp. 5181–5190, 1964.

[121] R. Reid and C. Bretschneider, "Surface waves and offshore structures," *The Agricultural and Mechanical College of Texas, Department of Oceanography*, 1953.

[122] K. V. Horoshenkov, A. Nichols, S. J. Tait, and G. Maximov, "The pattern of surface waves in a shallow free surface flow," *Journal of Geophysical Research: Earth Surface*, vol. 118, no. 3, pp. 1864–1876, 2013.

[123] C. J. Legleiter, C. D. Mobley, and B. T. Overstreet, "A framework for modeling connections between hydraulics, water surface roughness, and surface reflectance in open channel flows," *Journal of Geophysical Research: Earth Surface*, vol. 122, no. 9, pp. 1715–1741, 2017.

[124] G. Dolcetti and A. Krynkin, "Doppler spectra of airborne ultrasound forward scattered by the rough surface of open channel turbulent water flows," *The Journal of the Acoustical Society of America*, vol. 142, no. 5, pp. 3122–3134, 2017.

[125] R. Savelsberg and W. Van De Water, "Experiments on free-surface turbulence," *Journal of Fluid Mechanics*, vol. 619, pp. 95–125, 2009.

[126] M. Teixeira and S. Belcher, "On the initiation of surface waves by turbulent shear flow," *Dynamics of atmospheres and oceans*, vol. 41, no. 1, pp. 1–27, 2006.

[127] F. Muraro, G. Dolcetti, A. Nichols, S. J. Tait, and K. V. Horoshenkov, "Free-surface behaviour of shallow turbulent flows," *Journal of Hydraulic Research*, vol. 59, no. 1, pp. 1–20, 2021.

[128] I. Nezu, H. Nakagawa, and G. H. Jirka, "Turbulence in open-channel flows," *Journal of Hydraulic Engineering*, vol. 120, no. 10, pp. 1235–1237, 1994.

[129] G. Alfonsi, "Reynolds-averaged navier–stokes equations for turbulence modeling," 2009.

[130] P. J. Mason, "Large-eddy simulation: A critical review of the technique," *Quarterly Journal of the Royal Meteorological Society*, vol. 120, no. 515, pp. 1–26, 1994.

[131] R. Golshan, A. E. Tejada-Martínez, M. J. Juha, and Y. Bazilevs, "Les and rans simulation of wind-and wave-forced oceanic turbulent boundary layers in shallow water with wall modeling," *Computers & Fluids*, vol. 142, pp. 96–108, 2017.

[132] R. J. Adrian, "Twenty years of particle image velocimetry," *Experiments in fluids*, vol. 39, pp. 159–169, 2005.

[133] I. Grant, "Particle image velocimetry: a review," *Proceedings of the Institution of Mechanical Engineers, Part C: Journal of Mechanical Engineering Science*, vol. 211, no. 1, pp. 55–76, 1997.

[134] M. R. Abdulwahab, Y. H. Ali, F. J. Habeeb, A. A. Borhana, A. M. Abdelrhman, and S. M. A. Al-Obaidi, "A review in particle image velocimetry techniques (developments and applications)," *Journal of Advanced Research in Fluid Mechanics and Thermal Sciences*, vol. 65, no. 2, pp. 213–229, 2020.

[135] J. Westerweel, G. E. Elsinga, and R. J. Adrian, "Particle image velocimetry for complex and turbulent flows," *Annual Review of Fluid Mechanics*, vol. 45, pp. 409–436, 2013.

[136] M. Muste, I. Fujita, and A. Hauet, "Large-scale particle image velocimetry for measurements in riverine environments," *Water resources research*, vol. 44, no. 4, 2008.

[137] M. Khalid, L. Pénard, and E. Mémin, "Optical flow for image-based river velocity estimation," *Flow Measurement and Instrumentation*, vol. 65, pp. 110–121, 2019.

[138] M. Khalid, L. Pénard, and E. Mémin, "Application of optical flow for river velocimetry," in *2017 IEEE International Geoscience and Remote Sensing Symposium (IGARSS)*, pp. 6243–6246, IEEE, 2017.

[139] L. Mendes, A. Ricardo, A. Bernardino, and R. Ferreira, "Comparison of piv and optical flow for river flow applications," in *River Flow 2020*, pp. 891–900, CRC Press, 2020.

[140] J. Jyoti, H. Medeiros, S. Sebo, and W. Mcdonald, "Remote sensing of river velocity using drone video and optical flow algorithm," in *Watershed Management Conference 2020*, pp. 197–204, American Society of Civil Engineers Reston, VA, 2020.

[141] M. Streßer, R. Carrasco, and J. Horstmann, "Video-based estimation of surface currents using a low-cost quadcopter," *IEEE Geoscience and Remote Sensing Letters*, vol. 14, no. 11, pp. 2027–2031, 2017.

[142] S. Molnar, S. E. Dosso, and J. F. Cassidy, "Bayesian inversion of microtremor array dispersion data in southwestern british columbia," *Geophysical Journal International*, vol. 183, no. 2, pp. 923–940, 2010.

[143] M. Carley, "Some notes on acoustics," *University of Bath, UK*, 2001.

[144] D. Thompson, "The reciprocal lattice as the fourier transform of the direct lattice," *American Journal of Physics*, vol. 64, no. 3, pp. 333–334, 1996.

[145] C. Mack, *Fundamental principles of optical lithography: the science of microfabrication*. John Wiley & Sons, 2007.

[146] M. Abramowitz and I. A. Stegun, *Handbook of mathematical functions with formulas, graphs, and mathematical tables*, vol. 55. US Government printing office, 1968.

[147] A. Sommerfeld, "Die greensche funktion der schwingungsgleichung," *J.-Ber. Deutsch Math.-Verein*, vol. 21, pp. 309–353, 1912.

[148] E. I. Thorsos, "The validity of the kirchhoff approximation for rough surface scattering using a gaussian roughness spectrum," *The Journal of the Acoustical Society of America*, vol. 83, no. 1, pp. 78–92, 1988.

[149] J. J. Stoker, *Water waves: The mathematical theory with applications*, vol. 36. John Wiley & Sons, 1992.

[150] W. A. Strauss, *Partial differential equations: An introduction*. John Wiley & Sons, 2007.

[151] H. Lamb, "Hydrodynamics dover publications," *New York*, no. 260-261, p. 445, 1945.

[152] O. M. Phillips, "The dynamics of the upper ocean," *(No Title)*, 1977.

[153] L. Breiman, J. Friedman, C. J. Stone, and R. A. Olshen, *Classification and regression trees*. CRC press, 1984.

[154] T. Hastie, R. Tibshirani, J. H. Friedman, and J. H. Friedman, *The elements of statistical learning: data mining, inference, and prediction*, vol. 2. Springer, 2009.

[155] J. R. Quinlan, "Induction of decision trees," *Machine learning*, vol. 1, no. 1, pp. 81–106, 1986.

[156] J. Ali, R. Khan, N. Ahmad, and I. Maqsood, "Random forests and decision trees," *International Journal of Computer Science Issues (IJCSI)*, vol. 9, no. 5, p. 272, 2012.

[157] E. Fix and J. L. Hodges, "Discriminatory analysis. nonparametric discrimination: Consistency properties," *International Statistical Review/Revue Internationale de Statistique*, vol. 57, no. 3, pp. 238–247, 1989.

[158] G. A. Seber and A. J. Lee, *Linear regression analysis*, vol. 330. John Wiley & Sons, 2003.

[159] C. P. Robert, G. Casella, and G. Casella, *Monte Carlo statistical methods*, vol. 2. Springer, 1999.

[160] E. Çinlar and E. ðCınlar, *Probability and stochastics*, vol. 261. Springer, 2011.

[161] E. Parzen, *Stochastic processes*. SIAM, 1999.

[162] S. Chib and E. Greenberg, "Understanding the metropolis-hastings algorithm," *The american statistician*, vol. 49, no. 4, pp. 327–335, 1995.

[163] D. Aldous and J. Fill, "Reversible markov chains," *To appear*, 2001.

[164] H. Haario, E. Saksman, and J. Tamminen, "An adaptive Metropolis algorithm," *Bernoulli*, vol. 7, pp. 223–242, 2001.

[165] G. D'Agostini, "On the use of the covariance matrix to fit correlated data," *Nuclear Instruments and Methods in Physics Research Section A: Accelerators, Spectrometers, Detectors and Associated Equipment*, vol. 346, no. 1-2, pp. 306–311, 1994.

[166] T. Lähivaara, L. Kärkkäinen, J. M. Huttunen, and J. S. Hesthaven, "Deep convolutional neural networks for estimating porous material parameters with ultrasound tomography," *The Journal of the Acoustical Society of America*, vol. 143, no. 2, pp. 1148–1158, 2018.

[167] N. J. Joslyn and D. R. Dowling, "Recovery of coherent reflection from rough-surface scattered acoustic fields via the frequency-difference autoproduct," *The Journal of the Acoustical Society of America*, vol. 151, no. 1, pp. 620–633, 2022.

[168] M. Kleiner, H. Gustafsson, and J. Backman, "Measurement of directional scattering coefficients using near-field acoustic holography and spatial transformation of sound fields (p)," *Journal of the Audio Engineering Society*, vol. 45, no. 5, pp. 331–346, 1997.

[169] A. Richard, D. Fernández Comesaña, J. Brunskog, C.-H. Jeong, and E. Fernandez-Grande, "Characterization of sound scattering using near-field pressure and particle velocity measurements," *The Journal of the Acoustical Society of America*, vol. 146, no. 4, pp. 2404–2414, 2019.

[170] G. Dolcetti, A. Krynkin, and K. V. Horoshenkov, "Doppler spectra of airborne sound backscattered by the free surface of a shallow turbulent water flow," *The Journal of the Acoustical Society of America*, vol. 142, no. 6, pp. 3387–3401, 2017.

[171] C. Strobl, A.-L. Boulesteix, A. Zeileis, and T. Hothorn, "Bias in random forest variable importance measures: Illustrations, sources and a solution," *BMC bioinformatics*, vol. 8, no. 1, pp. 1–21, 2007.

[172] W. Zhou, H. Yang, L. Xie, H. Li, L. Huang, Y. Zhao, and T. Yue, "Hyperspectral inversion of soil heavy metals in three-river source region based on random forest model," *Catena*, vol. 202, p. 105222, 2021.

[173] K. E. Atkinson, *An introduction to numerical analysis*. John wiley & sons, 2008.

[174] D. Zhang, "A coefficient of determination for generalized linear models," *The American Statistician*, vol. 71, no. 4, pp. 310–316, 2017.

[175] T. M. Oshiro, P. S. Perez, and J. A. Baranauskas, "How many trees in a random forest?," in *International workshop on machine learning and data mining in pattern recognition*, pp. 154–168, Springer, 2012.

[176] P. Probst and A.-L. Boulesteix, "To tune or not to tune the number of trees in random forest," *The Journal of Machine Learning Research*, vol. 18, no. 1, pp. 6673–6690, 2017.

[177] A. L. Beam, A. K. Manrai, and M. Ghassemi, "Challenges to the reproducibility of machine learning models in health care," *Jama*, vol. 323, no. 4, pp. 305–306, 2020.

[178] M. McDermott, S. Wang, N. Marinsek, R. Ranganath, M. Ghassemi, and L. Foschini, "Reproducibility in machine learning for health," *arXiv preprint arXiv:1907.01463*, 2019.

[179] M. B. McDermott, S. Wang, N. Marinsek, R. Ranganath, L. Foschini, and M. Ghassemi, "Reproducibility in machine learning for health research: Still a ways to go," *Science Translational Medicine*, vol. 13, no. 586, p. eabb1655, 2021.

[180] W. K. Hastings, "Monte carlo sampling methods using markov chains and their applications," 1970.

[181] F. Y. Kuo and I. H. Sloan, "Lifting the curse of dimensionality," *Notices of the AMS*, vol. 52, no. 11, pp. 1320–1328, 2005.

[182] G. Dolcetti, A. Krynkin, K. V. Horoshenkov, and S. J. Tait, "An acoustic technique to measure the velocity of shallow turbulent flows remotely," in *Free Surface Flows and Transport Processes*, pp. 181–194, Springer, 2018.

[183] A. Nichols, S. Tait, K. Horoshenkov, and S. Shepherd, "A non-invasive airborne wave monitor," *Flow Measurement and Instrumentation*, vol. 34, pp. 118–126, 2013.

[184] S. P. Walstead and G. B. Deane, "Reconstructing surface wave profiles from reflected acoustic pulses using multiple receivers," *The Journal of the Acoustical Society of America*, vol. 136, no. 2, pp. 604–613, 2014.

[185] L. Hellequin, J.-M. Boucher, and X. Lurton, "Processing of high-frequency multibeam echo sounder data for seafloor characterization," *IEEE Journal of Oceanic Engineering*, vol. 28, no. 1, pp. 78–89, 2003.

[186] M.-D. Johnson, A. Krynkin, G. Dolcetti, M. Alkmim, J. Cuenca, and L. D. Ryck, "Surface shape reconstruction from phaseless scattered acoustic data using a random forest algorithm," *Journal of the Acoustical Society of America*, vol. Accepted, 2022.

[187] S. G. Konarski, C. A. Rohde, R. Gotoh, S. N. Roberts, and C. J. Naify, "Acoustic measurement and statistical characterization of direct-printed, variable-porosity aluminum foams," *The Journal of the Acoustical Society of America*, vol. 149, no. 6, pp. 4327–4336, 2021.

[188] C. Andrieu and J. Thoms, "A tutorial on adaptive mcmc," *Statistics and computing*, vol. 18, no. 4, pp. 343–373, 2008.

[189] J. Kaipio and E. Somersalo, *Statistical and Computational Inverse Problems*. Springer-Verlag, 2005.

[190] E. I. Thorsos, "The validity of the kirchhoff approximation for rough surface scattering using a gaussian roughness spectrum," *The Journal of the Acoustical Society of America*, vol. 83, pp. 78–92, Jan. 1988.

[191] O. M. Phillips, "The equilibrium range in the spectrum of wind-generated waves," *Journal of Fluid Mechanics*, vol. 4, no. 4, pp. 426–434, 1958.

[192] D. R. Jackson, D. P. Winebrenner, and A. Ishimaru, "Application of the composite roughness model to high-frequency bottom backscattering," *The Journal of the Acoustical Society of America*, vol. 79, no. 5, pp. 1410–1422, 1986.

[193] M. T. Stewart, S. M. Cameron, V. I. Nikora, A. Zampiron, and I. Marusic, "Hydraulic resistance in open-channel flows over self-affine rough beds," *Journal of Hydraulic Research*, vol. 57, no. 2, pp. 183–196, 2019.

[194] D. Foreman-Mackey *et al.*, "corner. py: Scatterplot matrices in python.," *J. Open Source Softw.*, vol. 1, no. 2, p. 24, 2016.

[195] G. A. Korn and T. M. Korn, *Mathematical handbook for scientists and engineers: definitions, theorems, and formulas for reference and review*. Courier Corporation, 2000.

[196] M. Brocchini and D. Peregrine, "The dynamics of strong turbulence at free surfaces. part 1. description," *Journal of Fluid Mechanics*, vol. 449, pp. 225–254, 2001.

[197] A. Nichols, S. J. Tait, K. V. Horoshenkov, and S. J. Shepherd, "A model of the free surface dynamics of shallow turbulent flows," *Journal of Hydraulic Research*, vol. 54, no. 5, pp. 516–526, 2016.

[198] G. Dolcetti and H. García Nava, "Wavelet spectral analysis of the free surface of turbulent flows," *Journal of Hydraulic Research*, vol. 57, no. 2, pp. 211–226, 2019.

[199] M. A. Donelan, W. M. Drennan, and A. K. Magnusson, "Nonstationary analysis of the directional properties of propagating waves," *Journal of Physical Oceanography*, vol. 26, no. 9, pp. 1901–1914, 1996.

[200] B. K. Smeltzer, E. Æsøy, and S. Å. Ellingsen, "Observation of surface wave patterns modified by sub-surface shear currents," *Journal of Fluid Mechanics*, vol. 873, pp. 508–530, 2019.

[201] Q. Luo, G. Dolcetti, T. Stoesser, and S. Tait, "Water surface response to turbulent flow over a backward-facing step," *Journal of Fluid Mechanics*, vol. 966, p. A18, 2023.

[202] K. Fukami, T. Yamaguchi, H. Imamura, and Y. Tashiro, "Current status of river discharge observation using non-contact current meter for operational use in japan," in *World Environmental and Water Resources Congress 2008: Ahupua'A*, pp. 1–10, 2008.

[203] E. Walsh, D. Hancock III, D. Hines, R. Swift, and J. Scott, "Directional wave spectra measured with the surface contour radar," *Journal of physical oceanography*, vol. 15, no. 5, pp. 566–592, 1985.

[204] M. Gharib and A. Weigand, "Experimental studies of vortex disconnection and connection at a free surface," *Journal of Fluid Mechanics*, vol. 321, pp. 59–86, 1996.

[205] J. Wu, A. Nichols, A. Krynkin, and M. Croft, "Digital image correlation for stereoscopic measurement of water surface dynamics in a partially filled pipe," *Acta Geophysica*, vol. 70, no. 5, pp. 2451–2467, 2022.

[206] B. Jähne, J. Klinke, and S. Waas, ". imaging of short ocean wind waves: A critical theoretical review," *Journal of the Optical Society of America A*, vol. 11, no. 8, pp. 2197–2209, 1994.

[207] B. Pan, "Digital image correlation for surface deformation measurement: historical developments, recent advances and future goals," *Measurement Science and Technology*, vol. 29, no. 8, p. 082001, 2018.

[208] W. Peters and W. Ranson, "Digital imaging techniques in experimental stress analysis," *Optical engineering*, vol. 21, no. 3, pp. 427–431, 1982.

[209] B. Pan, K. Qian, H. Xie, and A. Asundi, "Two-dimensional digital image correlation for in-plane displacement and strain measurement: a review," *Measurement science and technology*, vol. 20, no. 6, p. 062001, 2009.

[210] T. Chu, W. Ranson, and M. A. Sutton, "Applications of digital-image-correlation techniques to experimental mechanics," *Experimental mechanics*, vol. 25, no. 3, pp. 232–244, 1985.

[211] A. Robert, "Boundary roughness in coarse-grained channels," *Progress in physical geography*, vol. 14, no. 1, pp. 42–70, 1990.

[212] R. Ferguson, "Flow resistance equations for gravel-and boulder-bed streams," *Water resources research*, vol. 43, no. 5, 2007.

[213] D. E. Turney, A. Anderer, and S. Banerjee, "A method for three-dimensional interfacial particle image velocimetry (3d-ipiv) of an air–water interface," *Measurement Science and Technology*, vol. 20, no. 4, p. 045403, 2009.

[214] Y. Akutina, *Experimental investigation of flow structures in a shallow embayment using 3D-PTV*. McGill University (Canada), 2016.

[215] C. Tropea, A. L. Yarin, J. F. Foss, *et al.*, *Springer handbook of experimental fluid mechanics*, vol. 1. Springer, 2007.

[216] B. Jean-Yves, "Pyramidal implementation of the lucas kanade feature tracker description of the algorithm," *http://sourceforge. net/projects/opencvlibrary/*, 2000.

[217] J. David, "Fleet and yair weiss," optical flow estimation"," 2006.

[218] H. E. Krogstad and K. Trulsen, "Interpretations and observations of ocean wave spectra," *Ocean Dynamics*, vol. 60, no. 4, pp. 973–991, 2010.

[219] J. Dugan, C. Piotrowski, and J. Williams, "Water depth and surface current retrievals from airborne optical measurements of surface gravity wave dispersion," *Journal of Geophysical Research: Oceans*, vol. 106, no. C8, pp. 16903–16915, 2001.

[220] C. Action, *Measuring and analysing the directional spectra of ocean waves*. Office for Official Publications of the European Communities, 2005.

[221] J. V. Toporkov and G. S. Brown, "Numerical simulations of scattering from time-varying, randomly rough surfaces," *IEEE Transactions on Geoscience and Remote Sensing*, vol. 38, no. 4, pp. 1616–1625, 2000.

[222] S. Tamari, F. García, J. Arciniega-Ambrocio, and A. Porter, "Testing a handheld radar to measure water velocity at the surface of channels," *La Houille Blanche*, no. 3, pp. 30–36, 2014.

[223] S. Tamari *et al.*, "Laboratory and field testing of a handheld radar to measure the water velocity at the surface of open channels," 2013.

[224] F. Alimenti, S. Bonafoni, E. Gallo, V. Palazzi, R. V. Gatti, P. Mezzanotte, L. Roselli, D. Zito, S. Barbetta, C. Corradini, *et al.*, "Noncontact measurement of river surface velocity and discharge estimation with a low-cost doppler

radar sensor," *IEEE Transactions on Geoscience and Remote Sensing*, vol. 58, no. 7, pp. 5195–5207, 2020.

[225] J. W. Fulton, C. A. Mason, J. R. Eggleston, M. J. Nicotra, C.-L. Chiu, M. F. Henneberg, H. R. Best, J. R. Cederberg, S. R. Holnbeck, R. R. Lotspeich, *et al.*, "Near-field remote sensing of surface velocity and river discharge using radars and the probability concept at 10 us geological survey streamgages," *Remote Sensing*, vol. 12, no. 8, p. 1296, 2020.

[226] J. Fulton and J. Ostrowski, "Measuring real-time streamflow using emerging technologies: Radar, hydroacoustics, and the probability concept," *Journal of Hydrology*, vol. 357, no. 1-2, pp. 1–10, 2008.

[227] M. Born and E. Wolf, *Principles of optics: electromagnetic theory of propagation, interference and diffraction of light*. Elsevier, 2013.